OPEN ACCESS document

Analysis of ESAFORM 2021 cup drawing benchmark of an Al alloy, critical factors for accuracy and efficiency of FE simulations

Anne Marie Habraken[1]*,

Toros Arda Aksen[2], José L. Alves[3], Rui L. Amaral[4], Ehssen Betaieb[1], Nitin Chandola[5], Luca Corallo[6], Daniel J. Cruz[4], Laurent Duchêne[1], Bernd Engel[7], Emre Esener[8], Mehmet Firat[2], Peter Frohn-Sörensen[7], Jesús Galán-López[9], Hadi Ghiabakloo[10], Leo Kestens[11], Junhe Lian[12], Rakesh Lingam[13,14], Wencheng Liu[15], Jun Ma[16], Luís F. Menezes[17], Tuan Nguyen-Minh[11], Sara S. Miranda[4], Diogo M. Neto[17], André F.G. Pereira[17], Pedro A. Prates[17,22], Jonas Reuter[7], Benoit Revil-Baudard[5], Carlos Rojas-Ulloa[1], Bora Sener[18], Fuhui Shen[12], Albert Van Bael[10], Patricia Verleysen[6],

Frederic Barlat[13], Oana Cazacu[5], Toshihiko Kuwabara[19], Augusto Lopes[20], Marta C. Oliveira[17], Abel D. Santos[4,21], Gabriela Vincze[22]

[1] University of Liège, ArGEnCo dpt, MSM team, 9 Allée de la Découverte, 4000 Liège, Belgium

[2] Mechanical Engineering Department, University of Sakarya, Esentepe Campus, M7, 54050 Serdivan, Sakarya, Turkey

[3] CMEMS, Microelectromechanical Systems Research Unit, University of Minho, Campus de Azurém, Guimarães, 4800-058, Portugal

[4] Institute of Science and Innovation in Mechanical and Industrial Engineering (INEGI), R. Dr. Roberto Frias 400, 4200-465 Porto, Portugal

[5] Department of Mechanical and Aerospace Engineering, University of Florida, REEF, 1350N. Poquito Rd., Shalimar, FL 32579, USA

[6] Department of Electromechanical, Systems and Metal Engineering, MST-DyMaLab Research Group, Ghent University, Technologiepark 46, 9052 Zwijnaarde, Belgium

[7] Forming Technologies (UTS), Institute for Production Technology, University of Siegen, Breite Strasse 11, 57076 Siegen, Germany

[8] Mechanical Engineering Department, Bilecik Seyh Edebali University, Pelitozu, 11230, Bilecik, Turkey

[9] MSE, Faculty 3mE, Delft University of Technology, Mekelweg 2, 2628 CD Delft, The Netherlands

[10] KU Leuven, Department of Materials Engineering, Leuven, Belgium

[11] Ghent University, Department of Electromechanical, Systems and Metal Engineering, Ghent, Belgium

[12] Advanced Manufacturing and Materials, Department of Mechanical Engineering, Aalto University, Puumiehenkuja 3, 02150 Espoo, Finland

[13] Graduate Institute of Ferrous Technology (POSTECH), Pohang University of Science and Technology, 166-5 Hyogok-dong, Nam-gu, Pohang-si, Gyeongsangbuk-do, South Korea

14 Indian Institute of Technology Dharwad, P.B. Road, Dharwad, Karnataka 580011, India

[15] School of Civil Aviation, Northwestern Polytechnical University, Taicang, 215400, China

[16] Department of Mechanical and Industrial Engineering, Norwegian University of Science and Technology, 7491, Trondheim, Norway

[17] CEMMPRE, Department of Mechanical Engineering University of Coimbra, Polo II, Pinhal de Marrocos, 3030-788 Coimbra, Portugal

[18] Mechanical Engineering Department, Yildiz Technical University, Yildiz Campus, Barbaros, 34349, Istanbul, Turkey

[19] Division of Advanced Mechanical Systems Engineering, Institute of Engineering, Tokyo University of Agriculture and Technology, 2-24-16 Nakacho, Koganei-shi, Tokyo, 184-8588, Japan

[20] Department of Materials and Ceramic Engineering, CICECO, Universidade de Aveiro, 3810-193 Aveiro, Portugal

[21] University of Porto, Faculty of Engineering, R. Dr. Roberto Frias 400, 4200-465 Porto, Portugal

[22] Center for Mechanical Technology and Automation (TEMA), Department of Mechanical Engineering, University of Aveiro, Portugal

* Corresponding author: anne.habraken@uliege.be, marta.oliveira@dem.uc.pt

Abstract

This article details the ESAFORM Benchmark 2021. The deep drawing cup of a 1mm thick, AA 6016-T4 sheet with a strong cube texture was simulated by 11 teams relying on phenomenological or crystal plasticity approaches, using commercial or self-developed Finite Element (FE) codes, with solid, continuum or classical shell elements and different contact models. The material characterization (tensile tests, bi-axial tensile tests, monotonic and reverse shear tests, EBSD measurements) and the cup forming steps were performed with care (redundancy of measurements). The Benchmark organizers identified some constitutive laws but each team could perform its own identification. The

methodology to reach material data is systematically described as well as the final data set. The ability of the constitutive law and of the FE model to predict Lankford and yield stress in different directions is verified. Then, the simulation results such as the earing (number and average height and amplitude), the punch force evolution and thickness in the cup wall are evaluated and analysed. The CPU time, the manpower for each step as well as the required tests *versus* the final prediction accuracy of more than 20 FE simulations are commented. The article aims to guide students and engineers in their choice of a constitutive law (yield locus, hardening law or plasticity approach) and data set used in the identification, without neglecting the other FE features, such as software, explicit or implicit strategy, element type and contact model.

1. Introduction

Why to launch a series of Benchmarks within European Scientific Association for material FORMing (ESAFORM) community? Still today, in the United States of America, the National Institute of Standards and Technology (NIST) founded in 1901 provides data for engineers and materials scientists to develop accurate simulations and processes. This fact demonstrates that benchmarking is a long-term need. Since 1986, NAFEMS provides sets of independent "standard" tests that can be applied to any Finite Element System. In the specific field of sheet forming, a 1st congress with benchmark (the precursor of Numisheet series) called VDI 1991 in Zurich gathered international teams eager to compare their results and to discuss them within a conference. Since the nineties, the Numisheet benchmarks are references in the sheet forming community.

ESAFORM association promotes applied research in University and Industry, spreads scientific information and develops education. These objectives explain why this new Benchmark series is launched. An ESAFORM Benchmark is not seen as a competitive event but as an opportunity to gather senior and young researchers to discuss and bring a state-of-the-art information about any scientific challenge related to material forming. The target of ESAFORM Benchmarks can be focused on any materials (polymers, composites, metals…), based on experimental work or applied simulations, software developments or forming process innovations, forming processes impact and sustainability, etc. The specificity of ESAFORM benchmark is the intention to provide data, but also to exchange about how they are treated or collected. For instance within this article, the generation of data, the identification method of the material model parameters and the mandatory choices within the simulations (friction, element type, constitutive laws…) are analysed and published.

This state-of-the-art article constitutes a deliverable of the EXACT Benchmark (Experiment and Analysis of Aluminium Cup Drawing Test). For this first ESAFORM Benchmark edition, the ESAFORM board selected the proposal of a group of senior scientists either dedicated on numerical or experimental metal fields (*Frederic Barlat*. *Oana Cazacu*, *Anne Marie Habraken*, *Toshihiko Kuwabara, Augusto Lopes, Marta Oliveira*, *Abel Santos*, *Gabriela Vincze)*. They worked a large part of their career developing new yield locus formulations, crystal plasticity simulations, measuring textures, trying to validate sheet model predictions vs. experimental tests. However, they still need to interact among them and with young researchers to understand and analyse the advantages and drawbacks of the different constitutive models. This article deals with a strong texture aluminium sheet which enhances the challenge for the phenomenological yield *loci* as it generates interesting curvatures within the plastic surface description.

The Artificial Intelligence (AI) algorithms are now entering within material science problems [Rov2018, Hsu2020, Yam2020, WuL2020]. Sheet forming can benefit from these new approaches, saving computation time at various steps of the classical 'old fashion' way of simulations. However, Deep

Learning methods cannot only be fed by experimental data. Therefore, more than ever, this review paper will help to develop FE models and to point where AI can help. Success stories are already present as for instance, [Gor2020] where Recurrent Neural Networks model the behaviour of AA5182 aluminium alloy and DC05 steel. The Deep Learning surrogate model predicts accurate results for arbitrary loading paths, after a training step based on FE simulation results. In this specific case, a Barlat Yld2000-2d yield locus coupled with Homogeneous Anisotropic Hardening was selected to model the material behaviour. So, let us be prepared for these new approaches.

Hereafter, the article tries to answer interrogations such as: is the final discrepancy between experimental and numerical results related to measurement errors, model inaccuracies or phenomena forgotten in the simulation? Which model to choose under time constraint or lack of data? After all these years of debates about solid, shell, solid-shell elements (Kai1995, Sch2009, Abe2013, Cha2021), constitutive laws (Hil1948, Kar1993, Caz2001, Hab2004a, Bar2004, Plu2008, Van2011, Sch2018, Che2020), after all the Numisheet Benchmarks dedicated to folding, deep drawing or incremental forming etc. of different steel, aluminium, magnesium grades, what can be added?

The current article gathers information allowing industries and young researchers to easily select a rheological model as well as perhaps a multiscale modelling strategy. For instance, the interest of the identification of macroscopic material parameters based on microscopic computations is presented vs. the classical approach (tensile tests and phenomenological laws). Within the sheet forming simulation process, the constitutive law is not the only key feature. The finite element type (shell, solid-shell, solid element), the mesh refinement and the contact models are parts of the finite element simulation accuracy. These choices are however not the main focus of this benchmark, even if they are somehow included in the discussion.

The ESAFORM Benchmark organizing team has attracted many other colleagues within this Benchmark adventure and Table 1 provides the acronyms used hereafter for their institutions.

Table 1 The participants and the organizers of ESAFORM 2021 Benchmark, their affiliation and single acronym for each group

Team members affiliation	Acronym
Katholieke Universiteit Leuven and Ghent University (Belgium) Hadi Ghiabakloo, Albert Van Bael (Leuven), Tuan Nguyen-Minh, Leo Kestens (Ghent)	KUL
Norwegian University of Science and Technology (Norway) and Northwestern Polytechnical University (China) Jun Ma (Trondheim), Wencheng Liu (Taicang)	NTNU
Pohang University of Science and Technology and Indian Institute of Technology Dharwad (Korea) Rakesh Lingam, Frederic Barlat (Pohang)	POSTECH
University of Florida (US) Benoit Revil-Baudard, Oana Cazacu, Nitin Chandola (Shalimar)	REEF
Aalto University (Finland) Junhe Lian, Fuhui Shen (Espoo)	UAalto
University of Coimbra and University of Minho (Portugal) Marta C. Oliveira, André F.G. Pereira, Pedro A. Prates, Diogo M. Neto, Luís F. Menezes (Coimbra), José L. Alves (Minho)	UCoimbra
Ghent University (Belgium) and Delft University of Technology (Netherlands) Luca Corallo, Patricia Verleysen (Ghent), Jesus Galan Lopez (Delft)	UGent
University of Liege (Belgium) Ehssen Betaieb, Carlos Rojas, Laurent Dûchene, Anne Marie Habraken (Liege)	ULiege
University of Porto (Portugal)	UPorto

130

Rui L. Amaral, Daniel J. Cruz, Sara S. Miranda, Abel D. Santos (Porto)	
University of Sakarya, Bilecik Seyh Edebali University and Yildiz Technical University (Turkey) Bora Sener (Yildiz), Emre Esener (Bilecik), Toros Arda Aksen, Mehmet Firat (Sakarya)	USakarya
University of Siegen (Germany) Jonas Reuter, Bernd Engel, Peter Frohn-Sörensen (Siegen)	USiegen
University of Aveiro Gabriela Vincze, Augusto Lopes (Aveiro)	UA
Tokyo University of Agriculture and Technology Toshihoko Kuwabara (Tokyo)	TUAT

As explained above, this ESAFORM 2021 Benchmark article offers a holistic story, from the data generation to the final simulation validations:

1) the material characterization behaviour by macroscopic classical mechanical tests (tensile tests, monotonic and reverse simple shear tests, biaxial tensions) is the result of the collaboration of 3 laboratories that duplicated some tests (Section 2.2);
2) the analysis of the initial and updated textures by EBSD maps (Section 2.1 and 2.2.4);
3) the cup forming process description as well as the measurement techniques used to characterize earing profile and thickness evolution (Section 3)
4) some considerations about friction and how it affects simulation results (Section 4)
5) the summary of the simulation features performed by the Benchmark participants (Section 5)
6) a short description of all the constitutive laws used, either phenomenological ones or based on crystal plasticity (Section 6)
7) the clear identification methodology followed to reach the material parameter sets for each constitutive model as well as a model validation step through the predictions of Lankford coefficient and the evolution of initial yield limit with tensile directions (Section 7);
8) the comparisons between the FE predictions (cup average height, number of ears and their average amplitude, thickness in the cup wall and punch force) vs. the experimental results and their analysis (Section 8).

The ratio between the Central Processing Unit (CPU) time, the results accuracy as well as the ratio between the engineering time, to prepare and post process the data, vs. the confidence in the results are also commented. The conclusion (Section 9) summarizes the interesting points emerging from this Benchmark study.

2. Material experimental characterization

2.1 Material and initial texture

The material studied in this work is an aluminium alloy 6016-T4 produced by the UACJ Co., Japan and supplied in a sheet form with 1 mm thickness. A Bruker CrystAlign QC 400 EBSD system interfaced to a Hitachi SU-70 SEM was employed in UA to map the crystallographic orientations of the grains. From the EBSD raw data (Figure 1(a)), a set of 1000 orientations representing the crystallographic texture were extracted using the MTEX Matlab Toolbox [Bac2010]. The pole figures are shown in Figure 1(b) and the main texture components present in the microstructure are given in Table 2, where ϕ_1, Φ, ϕ_2 are the Euler angles (Bunge convention). Considering a misorientation of 3°, it is obtained that 52% volume fraction of grains are spread around the {100}<001> orientation (cube component). This material selection with a strong cube texture enhancing anisotropy is seen as an ideal example to test the capability of the constitutive models. Note also that the material presents equiaxed grains with an average size of around 50 μm.
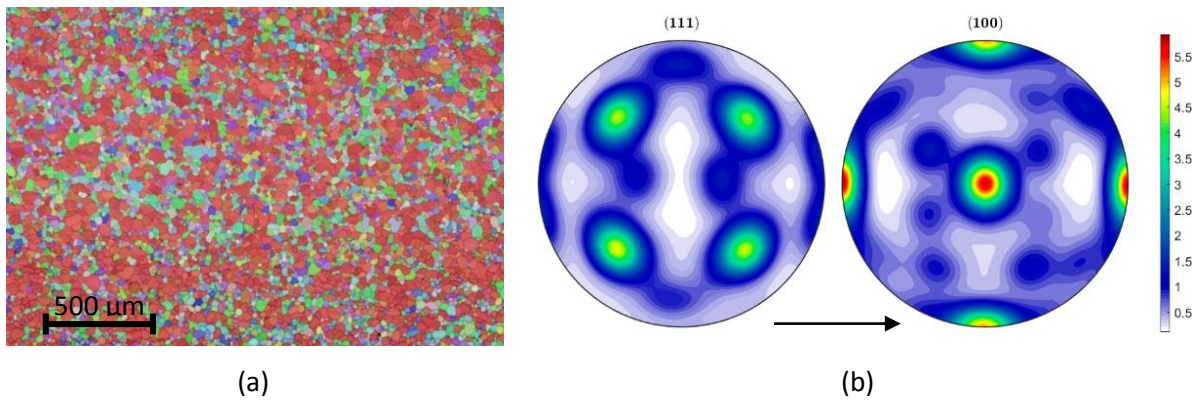
(a)   (b)

Figure 1 Initial texture of the 6016-T4 aluminium alloy: (a) EBSD map; (b) {111} and {100} pole figures; the arrow indicates the rolling direction (RD)

Table 2 The volume fractions for the main texture components for the AA 6016-T4 sheet

ϕ_1°	Φ°	ϕ_2°	Volume
204.96	0.05885	155.608	52%
330.862	56.1717	72.9679	16%
238.861	35.9114	156.439	13%
210.481	58.1962	108.63	11%
300.531	34.0291	27.1024	8%

2.2   Mechanical characterization tests

The material has been characterized in 2018 at Tokyo University of Agriculture and Technology (TUAT) based on uniaxial tensile and biaxial tensile tests on flat specimens and multiaxial tube expansion tests. Sheets from the same batch were provided for this benchmark, which enabled to further investigate the mechanical response for other loading paths, by performing simple and reverse shear tests and conducting additional cup drawing tests. Four laboratories have been involved in the mechanical characterization campaign conducted in 2020, which was aimed at: (i) generating complementary data and (ii) assessing the influence of the testing procedures by replicating some of the tests in at least two laboratories. This section is organized in subsections corresponding to each type of test conducted. In each subsection are presented succinctly the equipment used and a summary of the test results.

2.2.1   Uniaxial tensile tests

Uniaxial tensile tests have been conducted at TUAT in 2018 and 2020. Standard specimens (JIS Z 2241) with 50 mm gauge length and 12.5 mm width were used. In 2018, samples were cut at each 15° from the rolling direction (RD) or 0° orientation, in the plane of the sheet. All the tests were conducted at a strain rate 10^{-3} s^{-1} using a Shimadzu tensile test machine AUTOGRAPH AG-250kNG (Shimazu Co., Japan). The strain up to fracture was measured with a mechanical extensometer SG50-100 (Shimazu Co.). To measure the Lankford coefficients, additional tests were conducted up to 10% nominal strain, and measurements were done with a high-resolution extensometer SG25-10 (Shimazu Co.). In 2020, additional tests were conducted at TUAT using the same equipment and testing procedure for samples cut at 0°, 45° and 90° orientations to RD, respectively. In 2020, at the University of Aveiro (UA), for the 0°, 45° and 90° orientations, uniaxial tensile tests were conducted at the same strain rate (10^{-3} s^{-1}) on specimens of the same size (50 mm gauge length and 12.5 mm width) using a Shimadzu tensile test machine AUTOGRAPH AG-X100kN (Shimadzu Co., Japan). For the strain measurements, UA used a Digital Image Correlation (DIC) system and Aramis 5M software of GOM (Germany) (see Figure 2).
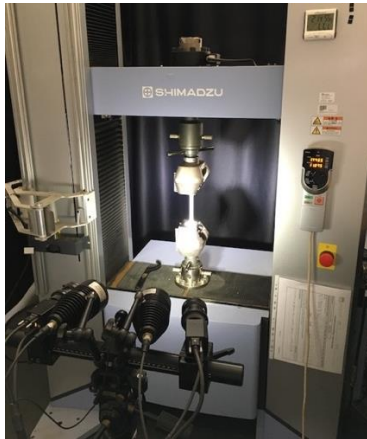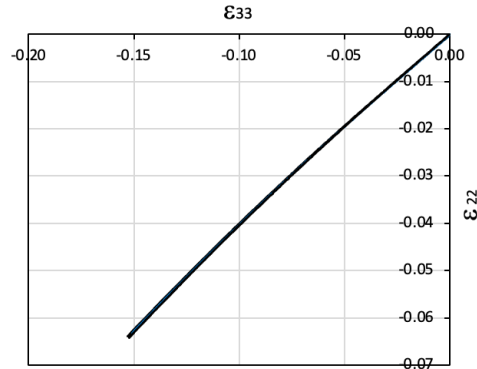
130

Figure 2 Shimadzu AG-X100kN and DIC (GOM)

Figure 3. Width strain vs. thickness strain measured by DIC in a uniaxial tensile test along 90° direction

From the DIC data up to necking obtained at UA, the Lankford coefficient in any given orientation was estimated from the slope between the width strain (ε_{22}), monitored during the whole test, and the thickness strain (ε_{33}) based on volume conservation, as exemplified in Figure 3 for a test at 90°. In addition, for the 0°, 45° and 90° orientations, the respective *r*-values were estimated from the slope of the width vs. thickness strains corresponding to the following plastic strain ranges: 5-10%, 10-15% and 15-20%. Note that r_0 and r_{90} are practically constant while for r_{45} the variation with the axial strain is larger (see Figure 5(c)).

To complement the characterization of the material anisotropy in the plane of the sheet, additional tests were performed in UA for the 15°, 30°, 60° and 75° orientations from the RD. Due to constraints related to material availability, these tests were conducted on smaller specimens with 25 mm gauge length and 9 mm width. It is worth mentioning that this geometry was verified in previous work [Vin2013] and it was found that this specimen geometry does not affect the results. That conclusion can also be driven from the current results for the 6016-T4 material as checked for the 90° orientation (see Figure 4).

To summarize, the uniaxial tensile tests conducted in TUAT and UA are listed Table 3 while the stress-strain curves corresponding to each specimen orientation are given in Figure 4. It is to be noted the very good reproducibility of the test results.
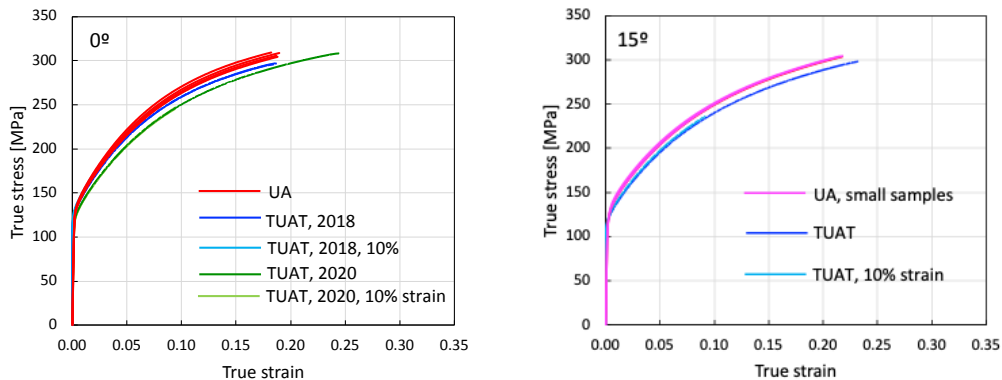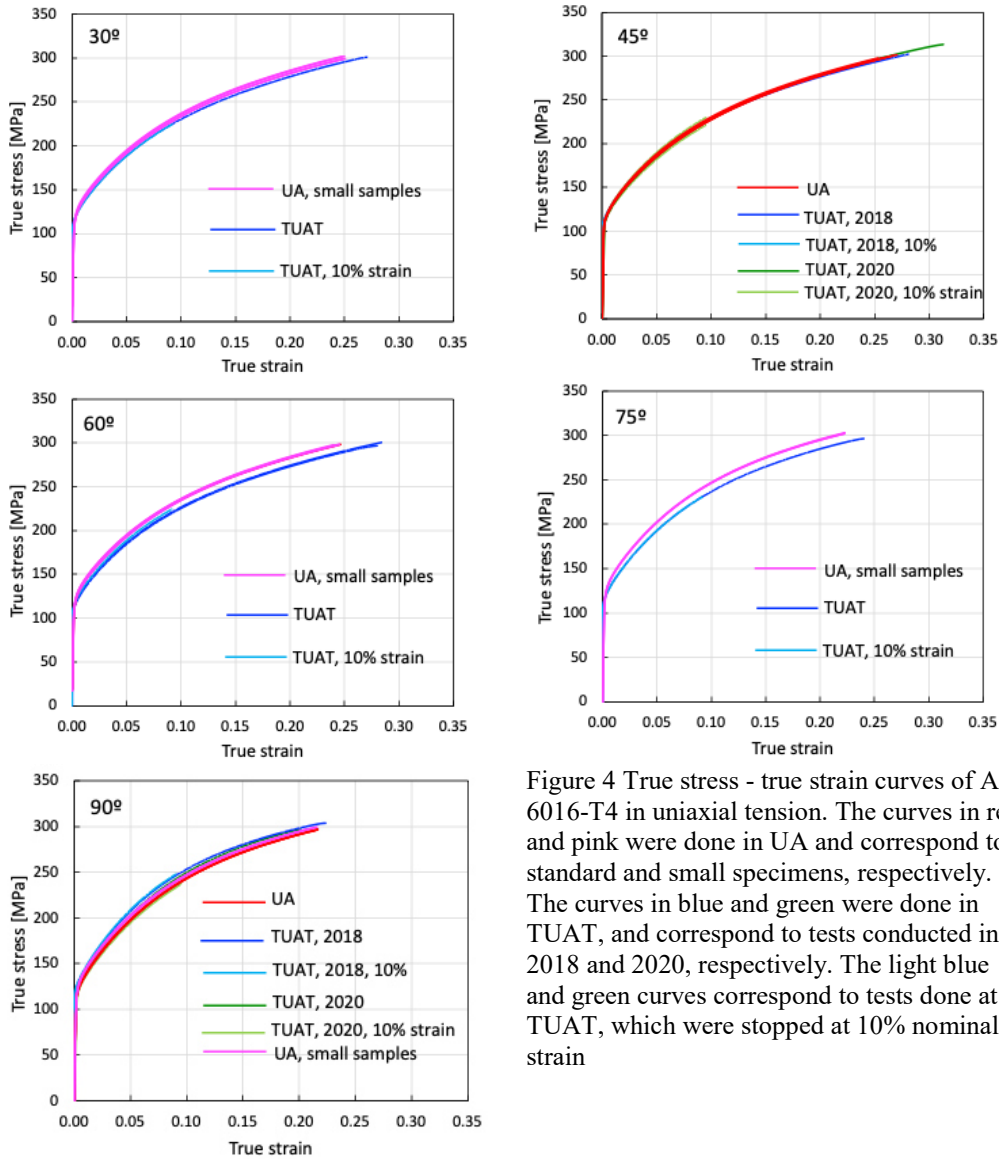
Figure 4 True stress - true strain curves of AA 6016-T4 in uniaxial tension. The curves in red and pink were done in UA and correspond to standard and small specimens, respectively. The curves in blue and green were done in TUAT, and correspond to tests conducted in 2018 and 2020, respectively. The light blue and green curves correspond to tests done at TUAT, which were stopped at 10% nominal strain

Table 3 Summary of the uniaxial tests and number of replicates for each orientation conducted in each laboratory

| Angle from RD	TUAT (2018)	TUAT (2020)	UA (2020)	UA (2020) - small sample
0°	4	3	4	-
15°	3	-	-	3
30°	3	-	-	4
45°	3	3	4	-
60°	4	-	-	5
75°	3	-	-	3
90°	3	3	4	3

Figure 5 shows the experimental evolution of the *r*-values and yield stresses with the loading orientation. The corresponding numerical values and spread are given in Tables 4-5. The data indicate that the material displays a very little anisotropy in yield stresses and a pronounced anisotropy in *r*-values.

130
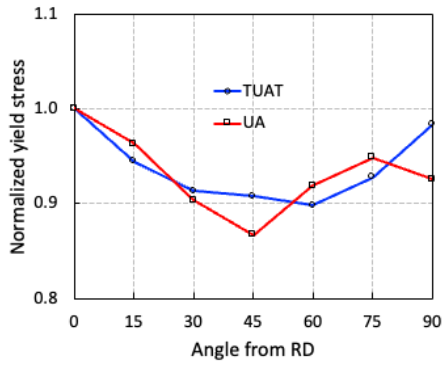
(a)
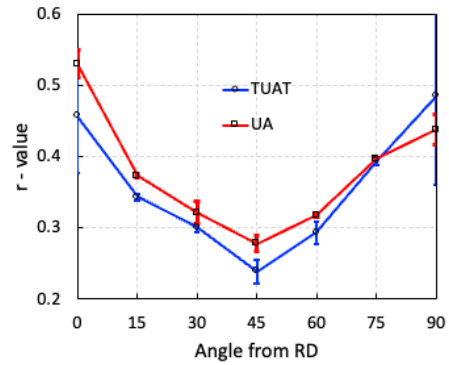
(b)
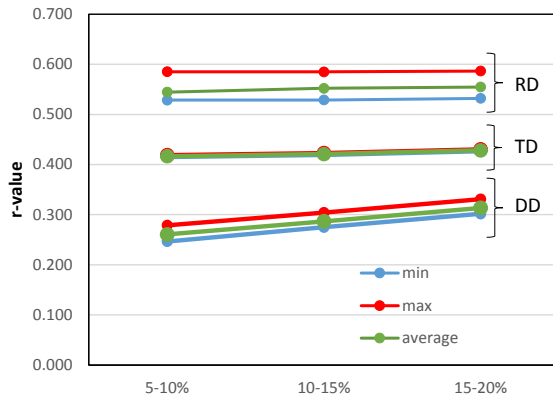
(c)

Figure 5 Anisotropy of the 6016-T4 sheet: (a) Experimental normalized yield stresses corresponding to ε_0^p=0.08 at TUAT and ε_0^p=0.002 at UA; (b) Experimental r-values obtained at UA from DIC data up to necking and at 10% of strain measured at TUAT in 2018 and 2020; (c) Experimental r-values based on UA tests for 3 plastic strain ranges

Table 4 Summary of the experimental r-values for AA 6016-T4 estimated from tests performed at UA and TUAT. For each orientation the average values from repeated tests (bold), the respective minimum and maximum values (in brackets) are given

Angle between RD and tensile direction	TUAT		UA
	2018	2020	2020
0°	**0.526** [0.499-0.553]	**0.384** [0.371-0.396]	**0.525** [0.505-0.554]
15°	**0.344** [0.339-0.348]		**0.359** [0.357-0.361]
30°	**0.301** [0.294-0.307]		**0.303** [0.277-0.320]
45°	**0.253** [0.253-0.254]	**0.229** [0.217-0.24]	**0.248** [0.236-0.267]
60°	**0.294** [0.278-0.309]		**0.297** [0.294-0.301]
75°	**0.393** [0.389-0.397]		**0.387** [0.384-0.390]
90°	**0.601** [0.580-0.621]	**0.368** [0.351-0.384]	**0.429** [0.404-0.454]

Table 5 Summary of the normalized experimental yield stresses for AA 6016-T4 obtained at UA and TUAT

Angle between RD and tensile test	0°	15°	30°	45°	60°	75°	90°
Normalized yield stress TUAT	1.000	0.944	0.913	0.908	0.898	0.928	0.983
Normalized yield stress UA	1.000	0.963	0.904	0.867	0.919	0.948	0.926

To further examine whether there is evolution in the material anisotropy induced by uniaxial tension loading, EBSD measurements were performed on post-test samples from the RD and transversal direction (90° or TD) tests conducted at UA. The results are presented in Figure 6. Note that no clear

texture evolution occurred during uniaxial tension tests. There is only a small increase of the intensity value for the material stretched in the RD direction.
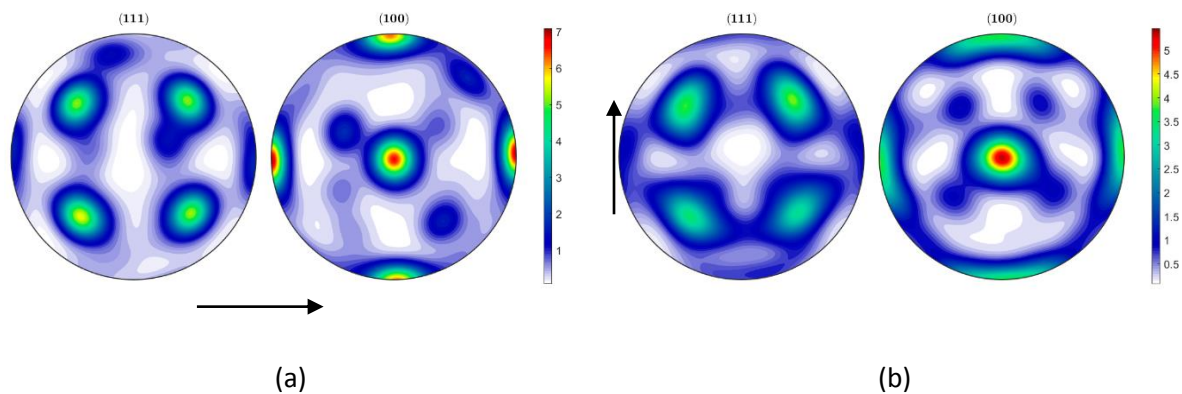

(a)   (b)

Figure 6 {111} and {100} pole figures of the material after uniaxial tensile tests conducted up to fracture: (a) along RD and (b) along TD. The arrows indicate the RD

2.2.2 Biaxial tensile tests

Figure 7(a) shows the geometry of the cruciform specimen used in the biaxial tensile tests. The specimen geometry and testing procedures have been established as an international standard: ISO 16842 [ISO2014]. A couple of strain gauges (YFLA-2, Tokyo Sokki Kenkyujo Co.) were mounted at ±21 mm from the centre along the maximum loading directions x and y (see Figure 7) to measure the normal strain components ε_x and ε_y. Using Finite Element analyses, Hanabusa et al. [Han2010, Han2013] estimated that the stress measurement error is less than 2%, when the strain components are measured at the positions shown in Figure 7(a). True stress increments were controlled and applied to the specimens so that the von Mises equivalent plastic strain rate became roughly constant at $5 \times 10^{-4} \, s^{-1}$ for all stress paths.

Moreover, multiaxial tube expansion tests (MTETs) were performed to precisely measure the work hardening characteristics of the test samples for larger strain ranges than those obtainable from cruciform specimens. True stress increments were controlled and applied to the specimens so that the von Mises equivalent plastic strain rates became roughly constant at $5 \times 10^{-4} \, s^{-1}$ for all stress paths. The details of the testing apparatus and procedures of the MTET are given in [Kuw2013]. Figure 7(b) shows the geometry of the tubular specimens used in the MTETs. The as-received sheet samples were uniformly bent to form a cylinder and the sheet edges were welded using YAG laser. The inner diameter of the tubular specimen was 53.9 mm, and the gauge length (distance between the chucking areas at either end) was 170 mm. The maximum principal stress direction was always taken to be in the axial direction of the tubular specimens in the MTETs, as the strength of the heat-affected zone (HAZ) is lower than that of the base material. Therefore, two types of tubular specimens were made; the specimens of type I had the RD in the axial direction and were used for tests with $\sigma_x > \sigma_y$, and the specimens of type II had the RD in the circumferential direction and were used for tests with $\sigma_x < \sigma_y$.
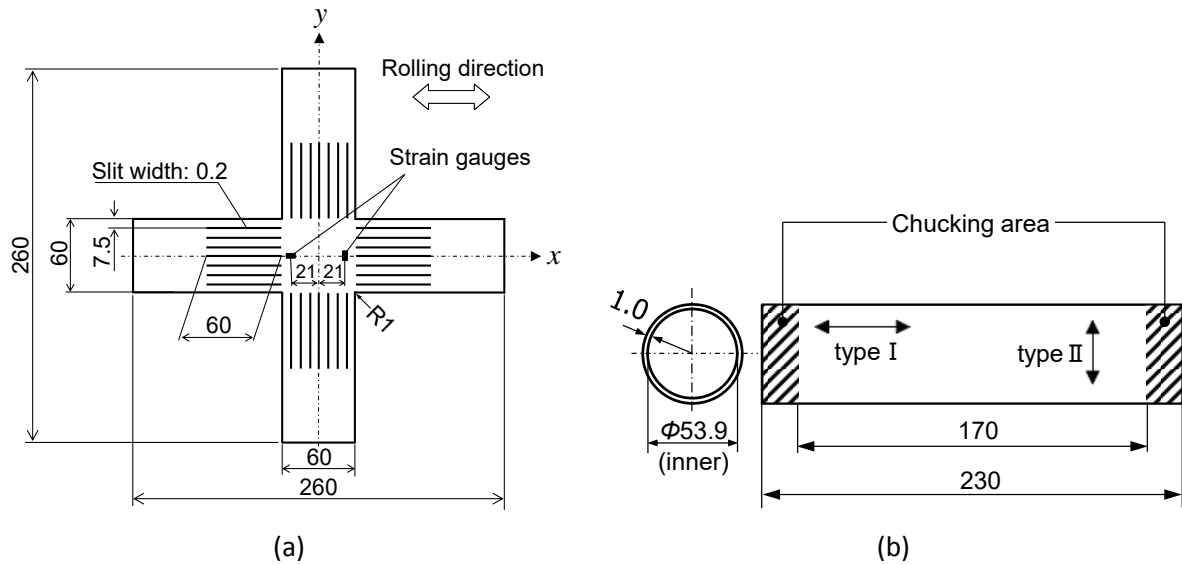
130

Figure 7 Geometry of cruciform specimen (a) and tubular specimen (b) used in biaxial tensile tests. Dimensions are in millimetres. The arrows indicate the RD

Slight differences between the true stress vs. logarithmic plastic strain (s-s) curves obtained with the cruciform and tubular specimens were observed for all stress ratios, due to the influence of the prestrain applied to the sheet samples during tube fabrication. The prestrain, distributed linearly in the thickness direction, is equal to 0 at mid-thickness and takes the maximum and minimum values, ±0.018, at the outer and inner surfaces of the tube, respectively for the geometry shown in Figure 7(b). The influence of the prestrain on the s-s curves measured using the MTETs was compensated using the procedures as described in [Kuw2013].

Contours of plastic work in the stress space were measured to identify proper material models for the test samples subjected to biaxial tension. The true stress vs. logarithmic plastic strain curve ($\sigma_0 - \varepsilon_0^{\mathrm{p}}$ curve) measurements for the RD were selected as reference data for work hardening; the plastic work per unit volume W_0^{p} associated with particular values of $\varepsilon_0^{\mathrm{p}}$ were determined. The stress point that gives the same plastic work as W_0^{p} on each linear stress path forms a contour of plastic work associated with $\varepsilon_0^{\mathrm{p}}$.

Figure 8 shows the stress points that form contours of plastic work. Two specimens were used per loading path. The maximum value of $\varepsilon_0^{\mathrm{p}}$ for which the work contour has a full set of stress points for nine linear stress paths was 0.11.
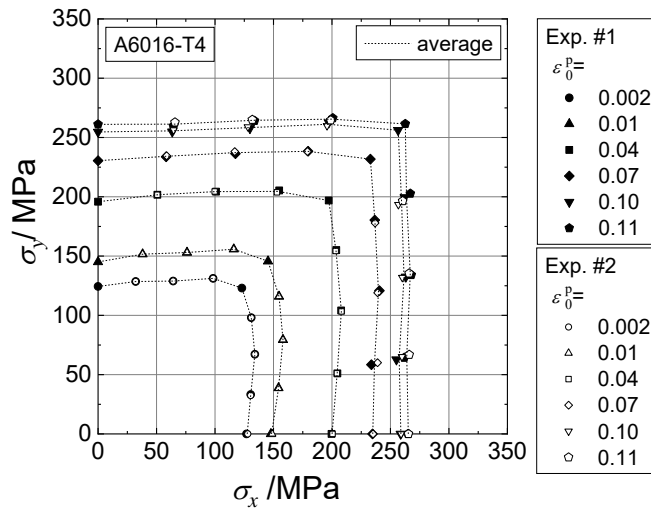
Figure 8 Stress points forming contours of plastic work at different levels of ε_0^p

Figure 9 shows the directions of the plastic strain rates measured at different levels of ε_0^p and points that texture evolution during these biaxial tensile tests is either weak or does not affect the direction of the plastic strains. Let us remind that uniaxial tensile tests were characterized by a low texture evolution (see Figure 6).
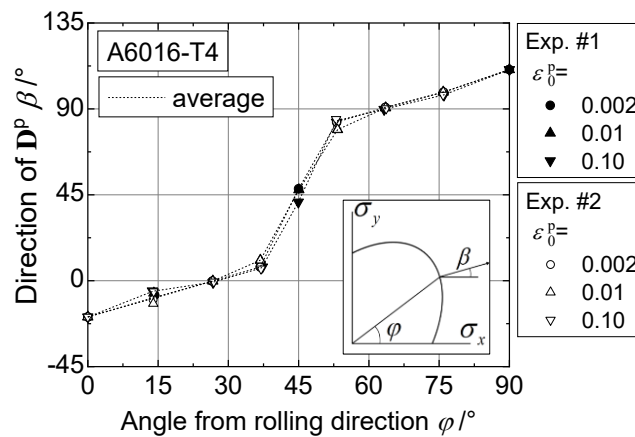

Figure 9 Direction of plastic strain rate at different levels of ε_0^p

2.2.3 Monotonic and reverse simple shear test

Shear test have been done in two laboratories, namely at the University of Liège (ULiege) and at the University of Aveiro (UA). Although the systems were very different, the common and favourable point is that the deformation volume is nearly identical, namely 30x3x1 mm³ in ULiege and 35x3x1 mm³ in UA.

To perform the simple shear tests in UA, the same equipment as in the case of the tensile test, namely AUTOGRAPH AG-X100kN (Shimazu Co., Japan) was used and a dedicated shear device was mounted. DIC coupled with Aramis 5M software of GOM (Germany) was used to measure the strains. Details about the simple shear device can be found in [Vin 2016] and in Figure 10. The specimen size was 35x13x1 mm³ corresponding to length, width and thickness respectively.
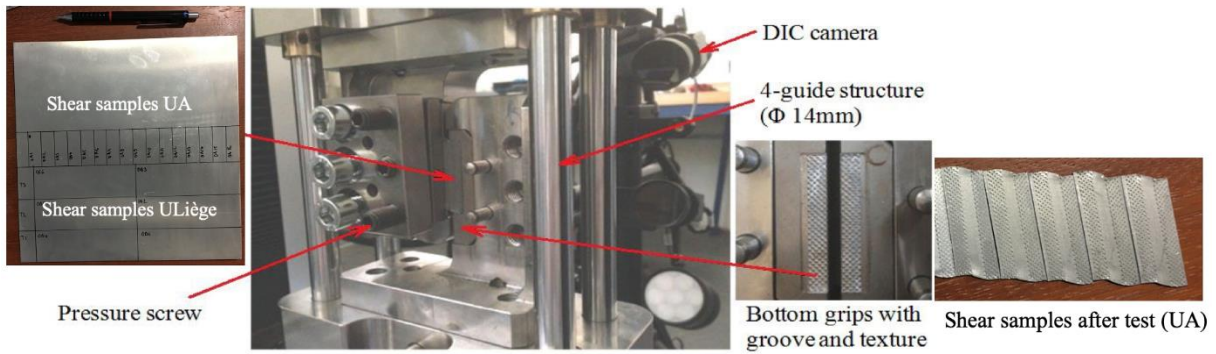
Figure 10 The dedicated shear device in UA as well as initial and deformed samples
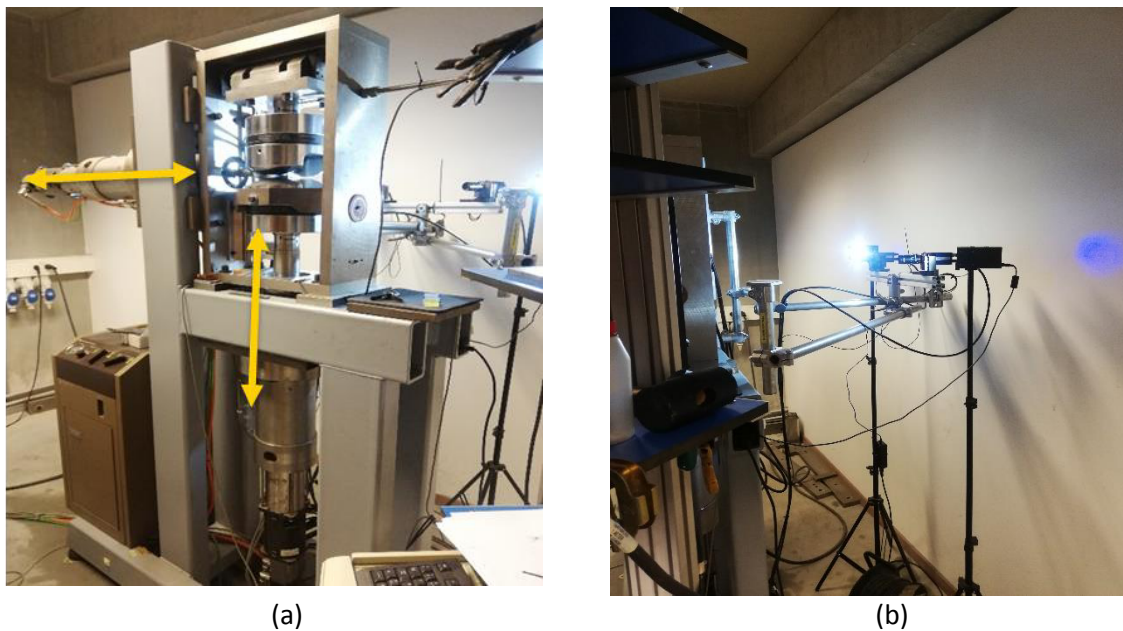

(a)

(b)

Figure 11 (a) Home-made bi-axial machine and (b) optical system allowing to measure both the in-plane and out of plane displacement (ULiege)

The equipment used in ULiege is a bi-axial in-house machine (Figure 11). It has an optical system with 2 cameras to measure the strain, one computer to command the pistons connected to the software "Tema" and one computer for image acquisition from the optical system. The force and displacement acquisition from the bi-axial machine are connected to the software "VIC 3D". The size of the specimen used for the Benchmark was 100x30x1 mm^3. The need for a large specimen is related to the hydraulic grips. The list of all the shear tests performed in both laboratories is given in Table 6.

Table 6 List of simple shear tests and number of replicates conducted in each laboratory

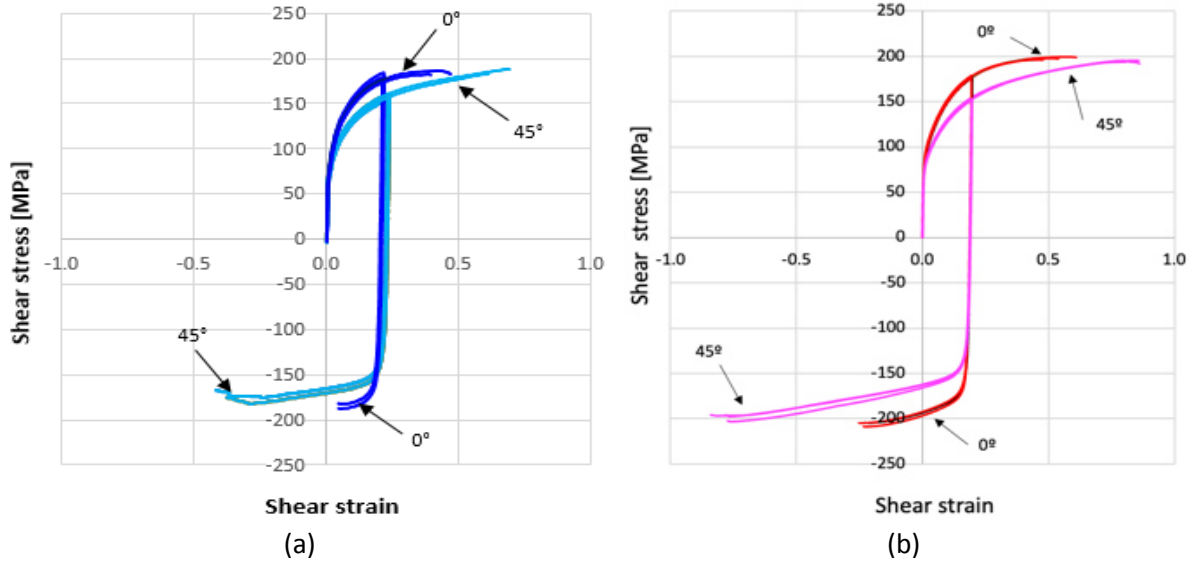| Angle from RD	Type of test	ULiege	UA
0°	Simple shear	3	5
0°	Reverse shear	2	3
45°	Simple shear	2	5
45°	Reverse shear	2	3

130

Figure 12 Shear stress - shear strain curves: (a) data from ULiege and (b) data from UA

As shown in Figure 12, the presence of a kinematic hardening is clear and the scattering of the shear tests in each laboratory is very low. The results of tests in 2 different directions enhance an anisotropic behaviour. Figure 13 compares the laboratory results, showing a reasonable agreement; the difference could be associated with the way each DIC system expresses the shear strain. This latter was calculated through the shear angle in Aramis software (used in UA), while Vic 3D software (used in ULiege) directly provided the Lagrange strain. Both measurements (shear angle and Lagrange strain) were calculated and an average was computed over the sheared area to generate the data shown in Figure 12 (another source of potential differences).
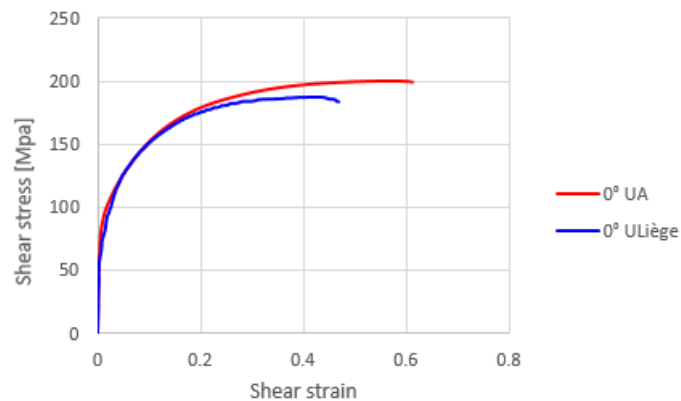

Figure 13 Comparison of test results from UA and ULiege

2.2.4 EBSD measurements of the fully drawn cup of AA 6016-T4

EBSD measurements were also performed after cup drawing. Samples were taken from two locations of the fully drawn cup, namely at the middle and the top of the cup along RD, 45° to RD and TD, respectively (see Figure 14). As in the case of uniaxial tensile loading, no significant texture evolution is observed. Note that the maximum changes with respect to the initial texture were observed at the top of the cup.
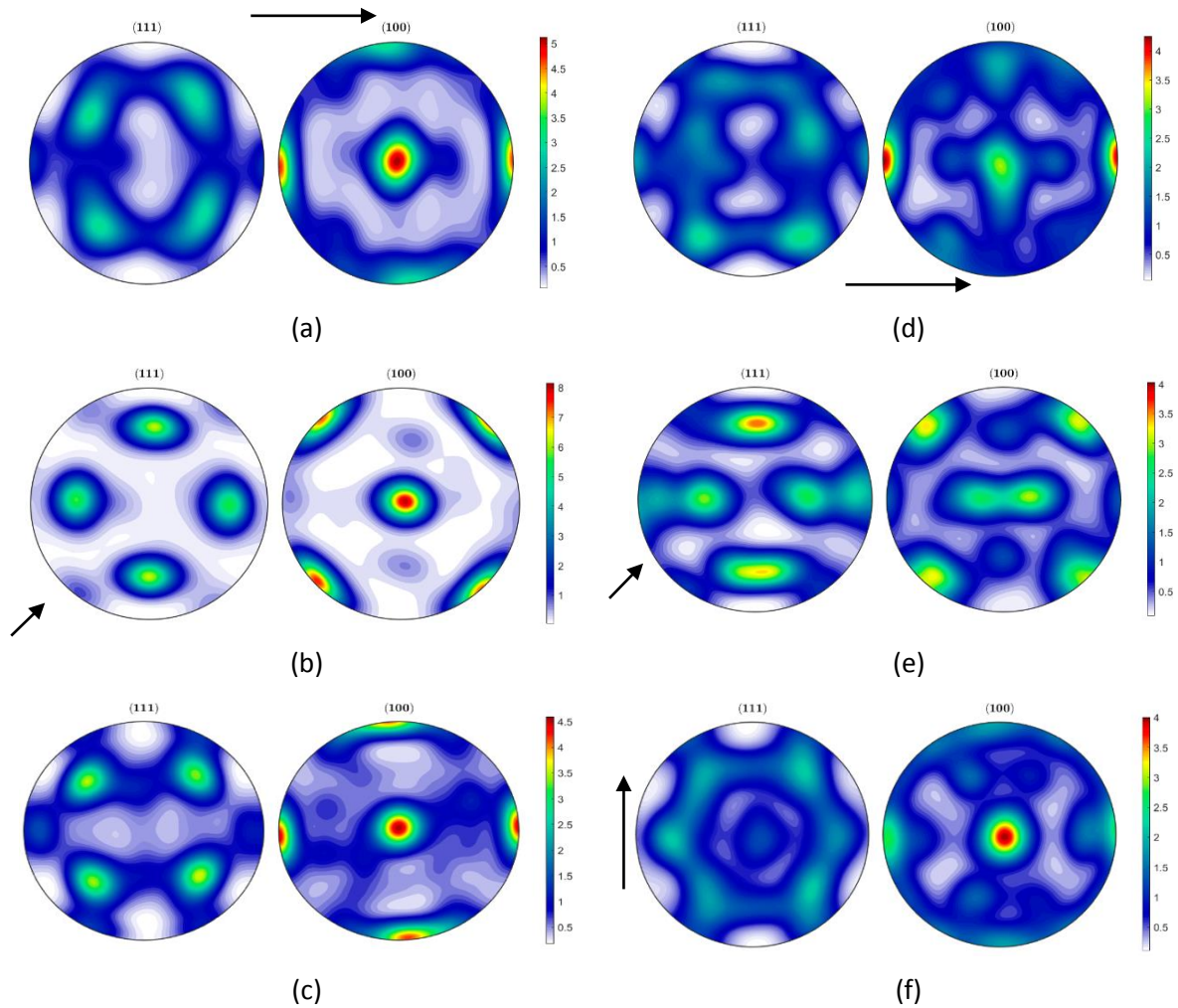
130

Figure 14 {111} and {100} pole figures obtained from the EBSD measurements performed on samples taken at the middle (left column) and at the top of fully draw cup (right column) respectively along RD (see (a) and (d)); 45 to RD (see (b) and (e)) and along TD (see (c) and (f)). The arrows indicate the RD direction

3. Cup forming and measurements

The proposed cylindrical cup drawing benchmark is used to investigate the anisotropic behaviour of an aluminium alloy AA 6016-T4 by measuring the earing profiles after cup forming. It will be the experimental reference result to compare with the numerical simulation predictions. Additional measurements are also considered, including punch force vs. punch stroke and the final thickness along the cylindrical perimeter from the sidewall of a drawn cylindrical cup for sections at different heights.

3.1 Experimental forming tools and process conditions

The cup test was performed in a hydraulic (250 bar) in house 300 kN Universal testing machine [Sou2019], as shown in Figure 15. The tool configuration consisting of four parts: a die, a blank holder, a cylindrical punch and a stopper, which has the same thickness as the blank (see Figure 16).
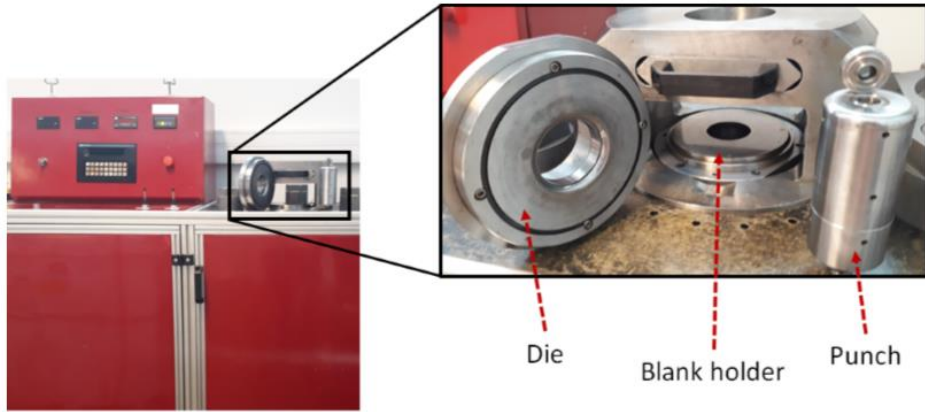
Figure 15 Universal testing machine and tools used for cylindrical cup benchmark
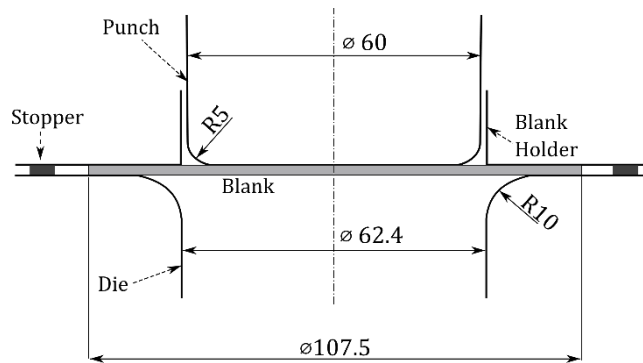

Figure 16 Cylindrical cup test schematic representation and tool dimensions

The delivered material was a single sheet of AA 6016 with the size of 220x220x1 mm³, from which three circular blanks were extracted for testing, with a nominal diameter of 107.5 mm, thus giving a drawing ratio of 1.79 for cup drawing. The blank dimensions were measured (diameter and thickness) by using a micrometre, as shown in Figure 17 and the corresponding results are presented in Table 7.

Figure 17 Methodology for measurement of blanks

Table 7 Blank diameters and sheet thicknesses for AA 6016-T4 samples

Sample ID	Diameter [mm]	Thickness [mm]
1	107.54 ± 0.005	0.98 ± 0.004
2	107.54 ± 0.003	0.98 ± 0.004
3	107.53 ± 0.009	0.98 ± 0.006

Preliminary tests were performed also with AA 6016-T4 material of identical thickness but from a different supplier. Such trials were used to test and tune the experimental conditions, such as the drawing ratio to be used, blank holder conditions, output data and even the earing measurements and the lubrication conditions. Regarding the blank holder conditions, a stopper with the same thickness of the blank was used (see Figure 16) and a constant force of 40 kN was selected in order to maintain the gap between the blank holder and the die.

3.2   Punch force

To fully draw the cup, a punch displacement of 54 mm is considered and a constant punch travel speed of 0.5 mm/s was defined. The punch force and the punch stroke are recorded during the test. The data acquisition was 50 Hz. Figure 18(a) shows the resulting evolution of the punch force vs. displacement for the cup test. The final drawn cup is presented in Figure 18(b). As observed in this figure, the upper part of the cylindrical cup shows some polished regions, thus denoting the occurrence of ironing, which is also related with the *plateau* observed in the punch force-displacement curve.
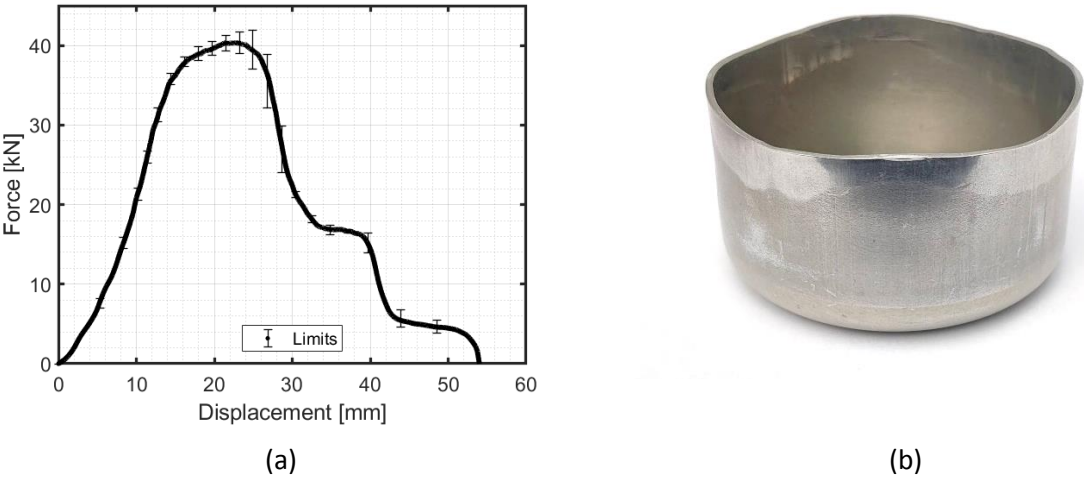

(a)   (b)

Figure 18 (a) Evolution of punch force vs. displacement and (b) final drawn cup

3.3   Cup height and earing profile

The samples of cylindrical cups were measured to obtain the earing profile along the perimeter of the top part of cup. Such measurement was performed using a Mitutoyo digital dial gauge micrometre with a resolution of 0.001 mm, as shown in Figure 19(a). Rotation of cup was done by means of an electric motor. The measurements acquired with this digital dial gauge micrometre were relative measurements, with the zero-height defined for 0° to RD. The total cup height was performed with an additional setup using a high precision height gauge, Mitutoyo Heightmatic 600 mm, shown in Figure 19(b).

(a)   (b)

Figure 19 (a) Setup for measuring the earing height evolution (b) equipment to measure the total cup height

The direction of rotation for the motor and the sample was defined as clockwise rotation, as presented in Figure 20. Therefore, the x-values on the results correspond to angle measurements, represented in Figure 20, defined with anti-clockwise direction. Three complete rotations were considered for each sample, in order to assure repeatability. The average earing profile and the corresponding error limits are represented in Figure 21.
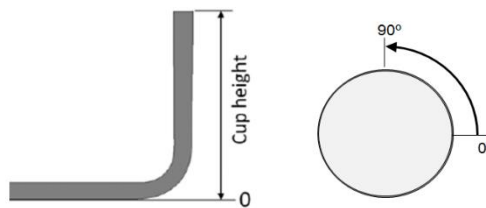

Figure 20 The earing profile evolution was measured around the cup circumference, starting from rolling direction (RD=0°) and three anti-clockwise rotations (full 360°) were performed for each cylindrical cup
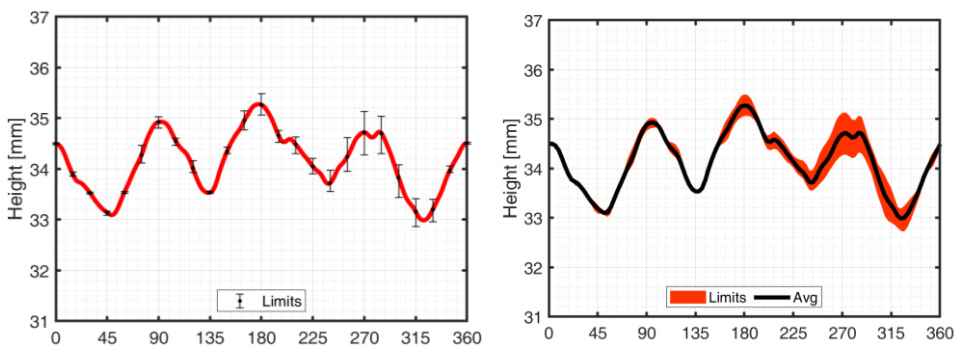
Figure 21 Evolution of average cup height for different angles

3.4   Cup thickness

The thickness distribution was measured using an Industrial 3D Measuring System - ATOS Triple Scan as presented in Figure 22. This equipment is a non-contact high-resolution optical digitizer, delivering three-dimensional data points. Figure 23 shows the evolution of thickness according to the cup perimeter considering different measurement heights.
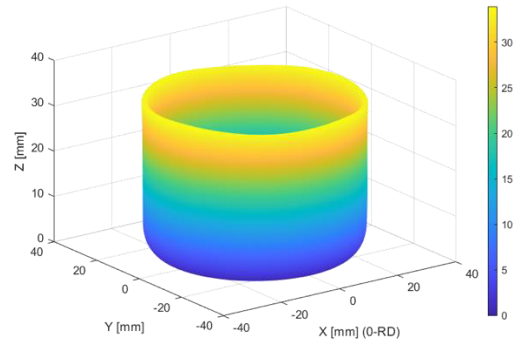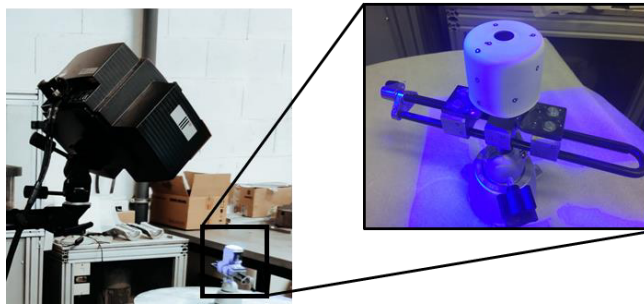
(a)   (b)

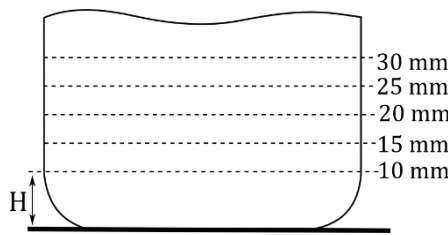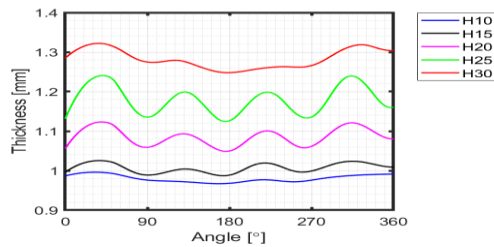Figure 22 (a) Experimental 3D measuring system (b) Cup geometry by point cloud

(a)   (b)

Figure 23 (a) Reference heights for the thickness measurements and (b) Evolution of thickness-angle for different cup heights

It can be noticed that the measured thickness in the upper part of the cup is larger than the die-punch clearance of 1.2 mm (cf. Figure 16). To confirm this finding, the tool dimensions have been re-measured with other techniques; all confirmed the dimensions in Figure 16. Elastic deformations of the tools during the ironing stage could explain these observations.

3.5   Measurement of tools and cup thickness by different methods

The results of thickness for the cup height of 30 mm, as seen in Figure 23, gives rise to questions on tool dimensions (as defined in Figure 16) and specially on the tool clearance between punch and die. As seen in Figure 23, the average values of thickness for such cup height (30 mm) correspond to 1.3 mm, while the tool clearance is defined as 1.2 mm (Figure 16).

It is clear that ironing occurs for this cup drawing, but the question follows: how can the sheet thickness be higher than the space between punch and die?

The first step to answer this question it is to verify and to confirm the measurements, for both tools and cup thickness. Accordingly, different strategies were used for new measurements:

- **Tools** were measured by two methods:
  - *Method T1* – measurement of **Punch** by using an outside micrometre (Mitutoyo Digimatic, 50-75 mm, 0.001 mm resolution); measurement of **Die** by using a digital 3-point internal micrometre (Mitutoyo, 0.001 mm resolution);
  - *Method T2* - 3D measuring system (ATOS Triple Scan e GOM Inspect) for both **Punch** and **Die**;
- **Cup thickness** was confirmed by three methods:
  - *Method C1* –ATOS Triple Scan, as already presented in Section 3.4;

130

- o *Method C2* – rotational system using an extensometer (Epsilon 3542), for data acquisition along the cup perimeter (height=30 mm);
- o *Method C3* – discrete point measurements using an outside digital micrometre (Mitutoyo, 0.001 mm resolution) for points every 45°.

Results for tool measurements are presented in Table 8 and Figure 24, respectively, for *Method T1* and *T2*. As seen, tool dimensions correspond to the defined dimensions, as presented in Figure 16. Deviations on dimensions are in the order of ± 0.001 mm, using *Method T1*, and ± 0.01 mm, using *Method T2*. There is an evident higher deviation only for die radius, which is detected when using *Method T2*, but this deviation is not affecting the current concern on tool clearance.

Table 8 Method T1 for tool measurements using a digital micrometre

	Calibration Reference [mm]	Measurement [mm]	Diameter [mm]
Punch	50.000	+ 10.002	60.00 ± 0.001
		+ 10.001	
		+ 10.000	
Die	59.998	+ 2.415	62.41 ± 0.01
		+ 2.415	
		+ 2.416	

(a)   (b)
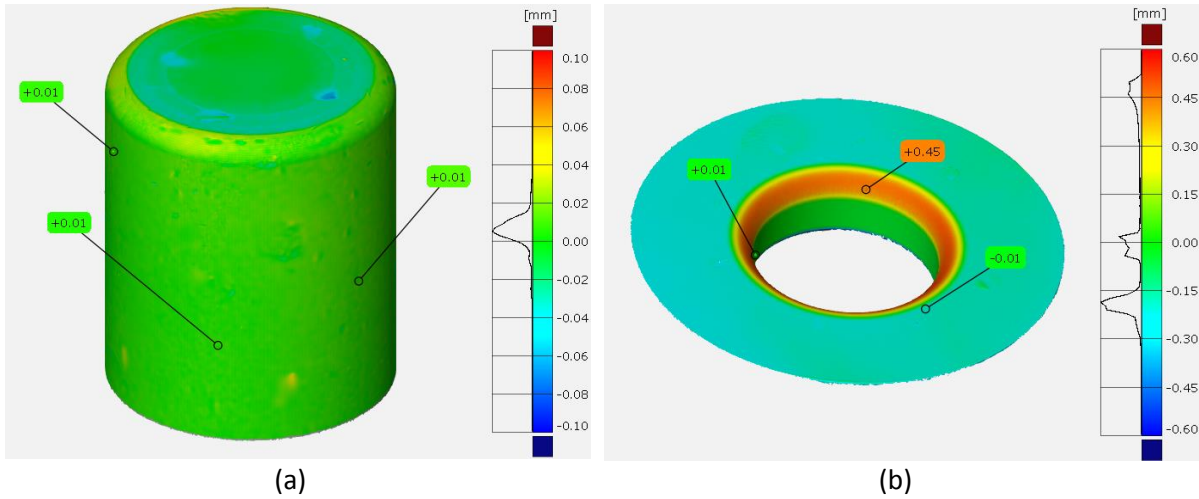
Figure 24 *Method T2* for tool measurements; results of differences to CAD data, using 3D measuring system (ATOS Triple Scan e GOM Inspect); (a) punch; (b) die

Results for cup thickness are presented in Figure 25, were the previous measurements (Figure 23, using ATOS Triple Scan) are compared with two additional methods (extensometer and micrometre). They are consistent among them, thus validating measurements by ATOS Triple Scan (Figure 23).
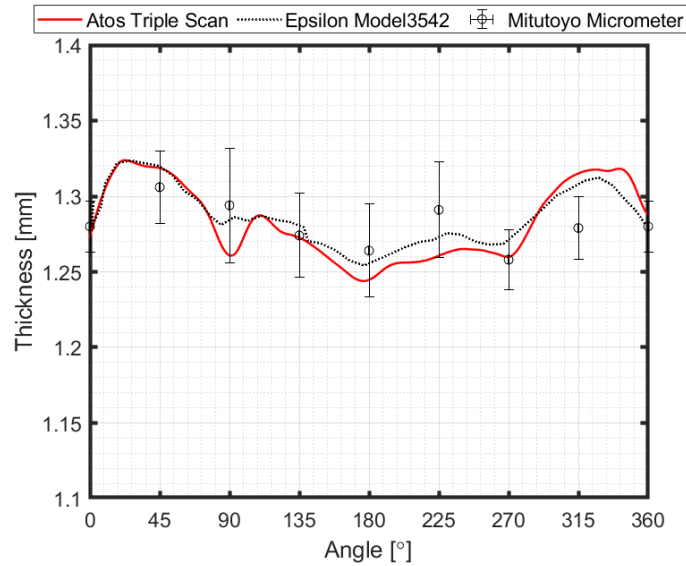
Figure 25 Thickness evolution for a cup height of 30 mm, using three methods

These experimental results show that ironing occurs for cup drawing and it is indeed observed that the final sheet thickness is higher than the clearance between punch and die. These observations suggest that elastic deformation of the tools during the ironing stage can be a direction for an explanation of what our intuition would not tell us. Note that hereafter, the usual common approach to model tools as rigid bodies in FE drawing simulations is applied by all the Benchmark participants.

4. Discussion about friction coefficient

In sheet metal forming processes, friction between the work piece and the tools is an important factor influencing the process behaviour such as material flow and forming forces, and further affecting the quality of formed products and tooling life [Nie2018]. In particular, for forming of aluminium alloys, the friction-induced galling phenomenon may commonly occur, leading to a significant impact on the quality of formed parts and the tool maintenance [Gro2008].

The frictional behaviour varies with different metal forming operations due to various tooling/constraints, deformation characteristics, loading steps, etc. For cup drawing, as illustrated in Figure 26(a), the friction occurring between the tools and the sheet has different characteristics depending on the respective zones, which can be summarized as follows:

Flange zone (zone 1 and 2), in which a blank holder force is normally applied to prevent wrinkling. A relatively lower strain level is experienced. The severe friction in this zone is mainly characterized by abrasive and adhesive wear. The lubrication condition in the flange zone influences the thickness distribution in the sidewall of the formed parts as it affects the drawing force and stretching strain.

Corner zone of lower die (zone 3), in which the sheet is forced to bend along the die radius and higher strain level is experienced. The contact stress in this zone is much higher and the wear pattern is similar to that of the flange zone; however, galling could possibly occur.

Cup wall zone (zone 4), in which the sheet is stretched and punch-sheet contact is occurring. As the deformation progresses, the sheet further stretches and gradually sets apart from the interaction with the punch. However, if wrinkles form, a die-sheet contact and galling may occur in the wrinkling area.

130

Corner zone of punch (zone 5), in which the interaction between sheet and punch corner exists, and wear characteristics are similar to those at the die corner zone.

Bottom zone (zone 6), where the biaxial stress determines the stretch forming process. Under the action of the drawing force, the punch bottom contacts the sheet but with relatively small sliding.
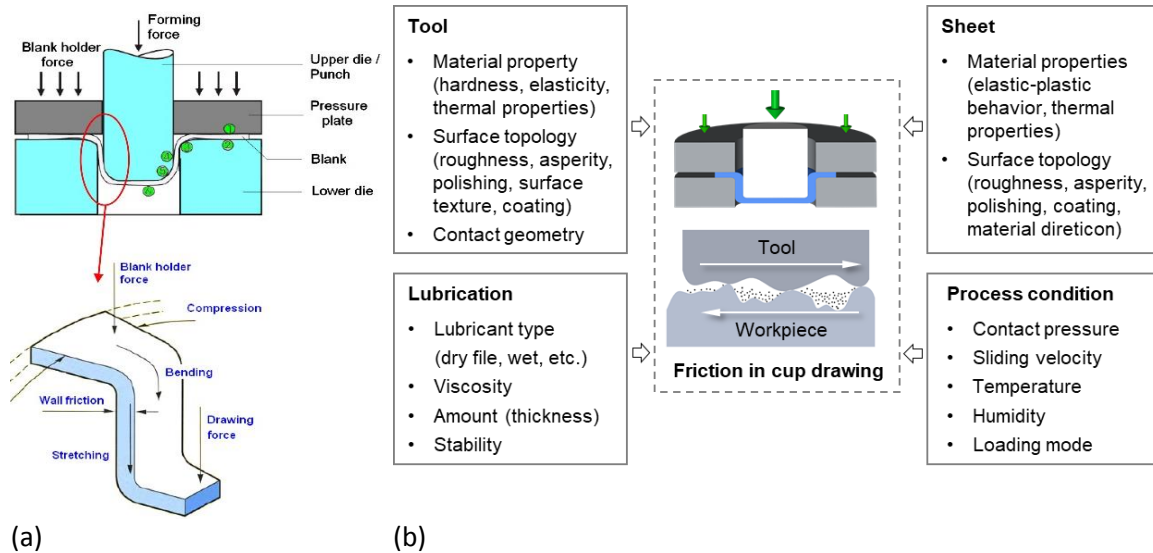

(a)   (b)

Figure 26 Friction in cup drawing process: (a) frictional characteristic [Shi2021]; (b) influential factors.

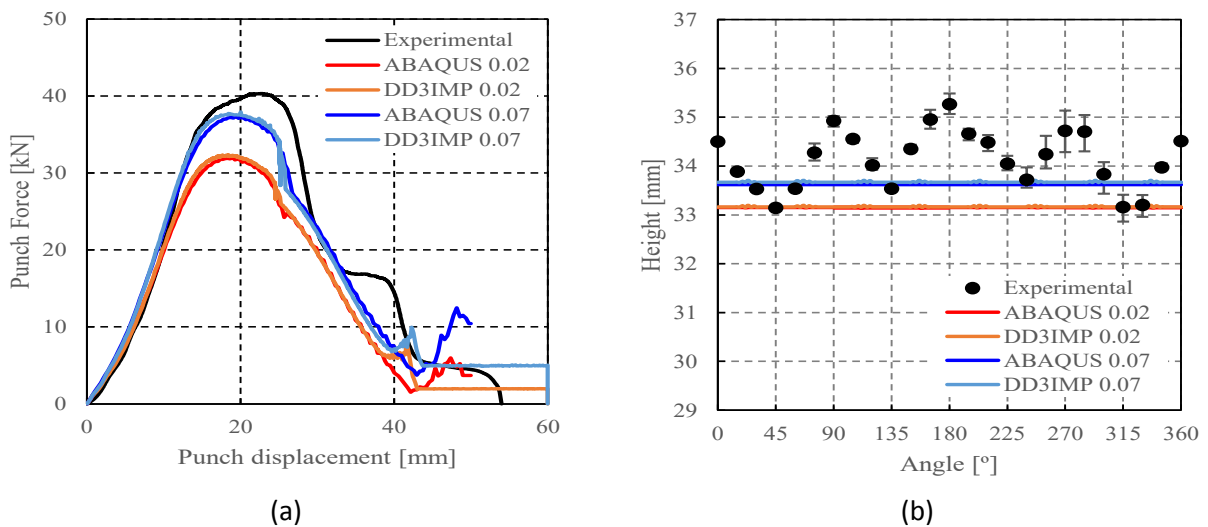(a)   (b)

Figure 27 Effect of the value of the friction coefficient in cup drawing simulations obtained with FE codes DD3IMP and ABAQUS using von Mises yield criterion in comparison with experimental results for 6016-T4, (a) punch force evolution and (b) earing profile

Because of its complexity and the related difficulties associated with measurements of the friction coefficient, in FE simulation Coulomb's law with a constant coefficient is used [Lee2015]. However, different friction regimes (e.g. dry friction and mixed lubrication) may concurrently occur depending on the lubrication conditions and surface topography of the tools and sheet [Shi2021, Hol2013]. Indeed, it has been reported that the lubrication affects the contact conditions at the sheet-tool interface [Shi2021, Lee2015, Hol2013, MaJ2018]. The different factors that affect the contact conditions and thus the frictional behaviour are depicted in Figure 26(b) (see also [Lee2015]). Each contributing factor includes many variables that change during the forming process, so that the value of the friction coefficient may also evolve. For example in the case of lubricated deep drawing, it was reported in [Rec2017] that the friction coefficient is likely to vary in the range μ=0.1~0.2. The material orthotropic behaviour also contributes to an uneven distribution of the contact pressure between the

blank and the tools [Bar2015]. To account for this, some authors use a different value of the friction coefficient in RD and TD and in this way manage to improve the agreement between FE predictions and experimental earing profile [Trz2017]. Friction tests, with particular regard to influence of process parameters such as lubrication, e.g. [Gal2021; Sig2015] or normal pressure, e.g. [Fro2021; Pre2013] can provide a better compliance between experiments and simulations, however the influence of evolving friction coefficient was not studied in this benchmark.

Numerical simulations of the present benchmark were performed, using the von Mises yield criterion and two constant values for the friction coefficient: 0.02 and 0.07. As shown in Figure 27(a), the value considered for the friction coefficient affects the predicted punch force throughout the cup drawing process. Setting a higher friction coefficient (from 0.02 to 0.07) leads to a predicted maximum punch force roughly 20% higher and a very slight increase of the corresponding punch displacement. As shown in Figure 27(b), this is related with the increase in the predicted overall cup height of 0.5 mm, i.e. 1.5%. In fact, for the higher value of friction coefficient the predicted height is 33.8 mm against the experimental average of 34.1 mm (1.3% difference). These FE results show that for this material the von Mises yield criterion enables a good prediction of the average cup height, and that the prediction can be further "tuned" by changing the value of the friction coefficient. Nevertheless, with the von Mises criterion the thickening of the cup wall is underestimated. Indeed, the results in Figure 27(a) indicate that irrespective of the value considered for the friction coefficient, a lower value is predicted for the ironing force as compared to the experimental data. Note that in Figure 27 are presented results obtained with two FE codes: ABAQUS standard (conducted by REEF) and DD3IMP (performed by UCoimbra). Further details about the FE modelling (e.g. contact algorithm, type of elements) are presented in Section 5. Irrespective of the code adopted, the punch force and the cup height increase if a higher value of the friction coefficient is considered; the differences between the predictions obtained with the two codes being negligible. For more examples and further discussion on the influence of the modelling strategies, including the algorithms used for the treatment of the contact conditions in different FE codes, the reader is referred to Section 8.

5. Summary of features of FEM simulations

A total of 11 teams contributed with results to the benchmark, as summarized in Table 9. Some teams provided more than one result, to enrich the discussion. Table 9 presents the codes adopted, highlighting that the majority adopted ABAQUS code, which is connected with the possibility to integrate user-defined material subroutines. In this context, two teams used their own in-house codes (ULiege with Lagamine and UCoimbra with DD3IMP). Regarding the time integration scheme, ABAQUS, and MSC.MARC allow the selection of either the implicit or the explicit strategy. As shown in Table 9, 5 teams adopted the implicit scheme, while 5 used the explicit one. One team selected the approach in function of the chosen code. This table also presents the selected element type, often solid. Only one team opted for continuum-shell elements and another for shell. USakarya and USiegen contributed with results using shell and solid elements. Their choice reflects the difficulties in predicting the ironing of the cup wall (see Section 3.5) with shell elements.

Only two teams adopted a full mesh to model the 360° geometry: KUL and USakarya, but the latter used this approach only with MSC.MARC code. KUL used the full model to impose some deviation to the initial blank positioning of the blank on the tools, in order to improve the correlation with the experimental results. In Table 9, the mesh refinement is described: the total number of elements used to discretise the blank and the number of layers (number in brackets) through the thickness, in case of solid elements. In case of shell or continuum-shell elements, it is presented the number of integration points through the thickness (in brackets). The dispersion in the total number of elements is very high, reflecting different options concerning the average in-plane finite element size. In fact, the full models

are not the ones using the highest number of elements in the sheet plane. The average in-plane element area was determined based on the initial area of the blank and the total number of elements used in the sheet plane. The results shown in Figure 28 highlight that this value is typically lower (~1.9 mm^2) for shell elements than for solid or continuum-shell (~4.0 mm^2).

Table 9 Choice(s) of FE code(s) and element type(s) by each team. Total number of finite elements used to discretise the blank (for solid elements, the number of through-thickness layers is shown in brackets, while for shell or continuum-shell elements the number of integration points through the thickness is between brackets)

| Acronym	Code	Element type	Total FE
KUL	ABAQUS (explicit) 2019	Continuum Shell (SC8R)	9743 (5)
NTNU	ABAQUS (implicit) 6.14	Solid (C3D8R)	7401 (3)
POSTECH	ABAQUS (explicit) 6.13	Solid (C3D8R)	1344 (2)
REEF	ABAQUS (implicit) 6.14	Solid (C3D8R)	10900 (3)
			15660 (3)
UAalto	ABAQUS (explicit) 2020	Solid (C3D8R)	40143 (2)
UCoimbra	DD3IMP (implicit)	Solid (Selective Reduced Integration)	15982 (2)
UGent	ABAQUS (implicit) 6.13	Shell (S4R)	11027 (5)
ULiege	Lagamine (implicit)	Solid (BWD3D one integration point)	2904
UPorto	ABAQUS (explicit)	Solid (C3D8R)	2128 (2)
USakarya	LS-DYNA R5.1 (explicit)	Quadrilateral shell (elform=16), Fully integrated	3072 (7)
	MSC.MARC (implicit)	Solid Hexahedral, Fully integrated	3072 (1)
USiegen	LS-DYNA R10/R12 (explicit)	Quadrilateral shell based on Hu-Washizu Three Field Principle, Fully integrated	11112
		Hexahedral solid (elform= -2), Fully integrated	55560 (5)
	PAMSTAMP 2020 (explicit)	Belytschko-Tsai quadrilateral shell, Fully integrated	9558
		Flanagan-Belytschko hexahedral solid, Fully integrated	55560 (5)
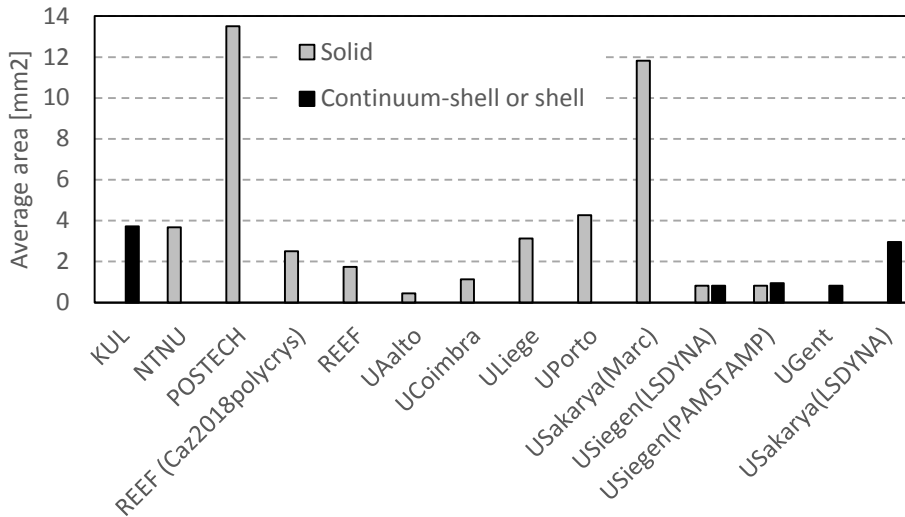
Figure 28 FE average in-plane size for the models adopted by each team

All teams considered the tools as rigid. Since their geometry is quite simple, the analytical description of the tools was adopted by UGent, UPorto and USakarya (when using LS-DYNA). Remaining teams adopted a description with rigid elements, except UCoimbra that uses Nagata surfaces. In terms of contact search algorithm, most teams resort to the surface-to-surface approach. In terms of method to enforce the contact constraints, most of the teams used the penalty method. All teams adopted the Coulomb friction model, with a constant value for the friction coefficient, indicated in Table 10. USakarya also considered a shear stress limit of 70 MPa (when using MSC.MARC). In general, the teams selected the constant friction coefficient based on the prediction of the punch force, during the drawing stage. This resulted in a value in the range of 0.075-0.1. Nevertheless, as previously mentioned in Section 4, this leads to an overestimation of the force in the ironing stage, which explains the use of a lower value by other teams. Moreover, in order to avoid the ironing effect, USakarya altered the clearance between the punch and the die to 1.4mm.

The teams reported different strategies to control the blank holder, in order to mimic the presence of the stopper used in the experimental setup (see Figure 16). In some cases, this involved the modelling of a rigid body stopper. UPorto considered a constant distance of 1.2 mm between the die and the blank holder.

Table 10 FE code, contact algorithm and friction coefficient adopted in the Coulomb law

Acronym	Code	Contact algorithm	Friction coefficient
KUL	ABAQUS	Surface-to-surface, Penalty contact method, Tangential (friction: penalty), Normal (hard contact)	0.09
NTNU	ABAQUS	Finite sliding	0.09
POSTECH	ABAQUS	Penalty contact	0.1/0.07
REEF	ABAQUS	ABAQUS built-in contact pressure-overclosure (linear)	0.02
UAalto	ABAQUS	Penalty contact	0.01
UCoimbra	DD3IMP	Node-to-surface; Augmented Lagragian	0.02/0.07/0.10
UGent	ABAQUS	Surface-to-surface, Tangential (penalty) and hard contact	0.07
ULiege	Lagamine	Penalty contact method at integration points with a surface layer of elements (CFI3D)	0.082
UPorto	ABAQUS	Penalty contact	0.05
USakarya	LS-DYNA	Forming one way surface-to-surface	0.10
	MSC.MARC	Segment-to-segment	
USiegen	LS-DYNA	Forming one way surface-to-surface	0.075
	PAMSTAMP	Surface-to-surface	

The list of the yield criteria selected by the teams is presented in Table 11, confirming the enormous variety of options. Some yield criteria appear frequently, because the anisotropy parameters were supplied by the benchmark committee. This is not the case of the Yld2000-2D and the Yld2004-18p, which were also selected by two of the teams using crystal plasticity models: UGent and NTNU, respectively. Regarding the hardening law, the summary is presented in Table 12. Only one team modelled the kinematic component of the hardening behaviour, USakarya (when using the MSC.MARC). Many teams adopted the Swift isotropic hardening law since its parameters were supplied by the benchmark committee. Note that ULiege team chose Voce isotropic hardening law coupled with Hill48 criterion and Swift hardening law coupled with their Crystal plasticity law Minty.

Table 11 FE code and yield criterion used with (A) for an associated law, (NA) for a non-associated choice or polycrystalline model used for identification (I) or forming simulations (F). The source of the set of anisotropy parameters used (benchmark committee, own identification) is also indicated

Acronym	Code	Yield criterion	Benchmark set	Own set	CP model
KUL	ABAQUS	Facet-3D		X	ALAMEL (I)
NTNU	ABAQUS	Yld2004-18p (A)		X	DAMASK (I)
		Yld2004-18p (A)		X	
POSTECH	ABAQUS	Yld2004-18p (A)	X		
		Caz2018singlecrys		X	
REEF	ABAQUS	Hill48 (A)	X		
		Caz2018-Orth (A)	X		
		Caz2018singlecrys		X	
		Caz2018polycrys		X	Taylor (F)
UAalto	ABAQUS	Hill48 (NA)		X	
UCoimbra	DD3IMP	Hill48 (A)	X		
		CB2001 (A)		X	
		CPB06ex2 (A)		X	
		Caz2018-Orth (A)	X		
UGent	ABAQUS	Yld2000-2D (A)		X	VPSC (I)
ULiege	Lagamine	Hill48 (A)		X	
		Minty		X	Taylor (F)
UPorto	ABAQUS	Hill48 (A)	X		
		Hill48 (NA)		X	
USakarya	LS-DYNA	Yld2000-2D (A)	X		
		Yld89 (A)		X	
		HomPol4 (A)		X	
		HomPol6 (A)		X	
	MSC.MARC	HomPol4 (A)		X	
		HomPol6 (A)		X	
USiegen	LS-DYNA	Hill48 (A)	X		
		Yld2000-2D (A)	X		
		Yld2004-18p (A)	X		
	PAMSTAMP	Hill48 (A)	X		
		Hill48 (NA)	X		
		Yld2000-2D (A)	X		

Table 12 For each team, choice of FE code and hardening law used; the source of the set of parameters (benchmark committee, own identification) is also indicated

Acronym	Code	Hardening law	Benchmark set	Own set
KUL	ABAQUS	Swift, isotropic		X
NTNU	ABAQUS	Voce, isotropic		X
POSTECH	ABAQUS	Voce, isotropic		X
REEF	ABAQUS	Swift, isotropic	X	
UAalto	ABAQUS	Voce, isotropic		X
UCoimbra	DD3IMP	Swift, isotropic	X	
		Voce, isotropic		X
UGent	ABAQUS	Voce, isotropic		X
ULiege	Lagamine	Voce, for Hill48 law Swift for Minty law		X
UPorto	ABAQUS	Swift, isotropic	X	
USakarya	LS-DYNA	Swift, isotropic	X	
	MSC.MARC	Swift, isotropic		X
		Swift, isotropic + Chaboche, kinematic		X
USiegen	LS-DYNA	Swift, isotropic	X	
	PAMSTAMP	Swift, isotropic	X	

6. Main features of constitutive laws

Hereafter all the constitutive laws used by the Benchmark participants are presented.

To account for the observed anisotropy in the plastic deformation of the AA 6016-T4 polycrystalline sheet alloy, both polycrystalline models and macroscopic phenomenological elastoplastic models were adopted. Crystal plasticity models and Fast Fourier Transformation approach (FFT) were for instance used to generate virtual tests or material features. The anisotropic yield functions and plastic potentials involved in the elastoplastic models were identified either using only mechanical data (POSTECH, UCoimbra, USiegen, USakarya) or using a combination of mechanical data and results of polycrystalline simulations (KUL, UGent, NTNU, ULiege, REEF).

For simulation of the cup forming process, most of the participating teams have used phenomenological elastoplastic models. However, some teams also directly exploited crystal plasticity simulations. UGent applied a Visco-Plastic-Self-Consistent (VPSC) model, ULiege an interpolation model based on the yield locus concept, where points of this surface are computed by a crystal plasticity approach. In addition, direct FE simulations of cup drawing using a single crystal plasticity law were performed by POSTECH, while a polycrystalline model based on the same single crystal plasticity law was reported by REEF.

We begin with the presentation of the general form of the governing equations for modelling rate-independent elastoplastic deformation. Next, in Section 6.1, are presented the 2-D and 3-D macroscopic orthotropic yield functions (phenomenological laws identified by classical mechanical tests), while Section 6.2 describes the polycrystalline models. They rely for their identification either on crystal plasticity models, like FACET-3D yield surface, associated with ALAMEL crystal plasticity model (see Section 6.2.1) or directly use crystal plasticity models within the constitutive law as the elasto visco-plastic-self-consistent approach implemented by UGent (see Section 6.2.5).

The set of equations governing elastoplastic behaviour are:

$$
\begin{cases}
\mathbf{D} = \mathbf{D}^e + \mathbf{D}^p \\[4pt]
\dot{\boldsymbol{\sigma}} = \mathbf{C}^e{:}\mathbf{D}^e \\[4pt]
f\left(\boldsymbol{\sigma},\mathbf{X},\xi\right) = \bar{\sigma}\left(\mathbf{s}-\mathbf{X}\right) - Y\left(\xi\right) \leq 0 \\[4pt]
\mathbf{D}^p = \dot{\lambda}\dfrac{\partial g}{\partial \boldsymbol{\sigma}} \\[8pt]
\dot{\lambda} \geq 0 \text{ and } f\dot{\lambda} = 0
\end{cases}
\tag{1}
$$

where **s** is the Cauchy stress deviator $s = \boldsymbol{\sigma} - \sigma_m \mathbf{I}$ with $\sigma_m = \frac{1}{3}\mathrm{tr}\left(\boldsymbol{\sigma}\right)$, where **I** is the second-order identity tensor while "tr" denotes the trace operator, $\mathbf{D}$ is the strain-rate tensor with $\mathbf{D}^e$ and $\mathbf{D}^p$ being its elastic and plastic part, respectively.

Eq. (1)$_2$ is the hypo-elastic law defining the stress rate with respect to the elastic strain rate, $\mathbf{C}^e$ is the elastic fourth-order stiffness tensor while ":" denotes the double contracted product between the two tensors. Assuming linear isotropic elastic response, with respect to any coordinate system, $\mathbf{C}^e$ is given as:

$$
C^e_{ijkl} = G\left(\delta_{ik}\delta_{jl} + \delta_{il}\delta_{jk}\right) + \left(K - \frac{2}{3}G\right)\delta_{ij}\delta_{kl}
\tag{2}
$$

with $i,j,k,l = 1...3$, δ_{ij} is the Kronecker delta, while G and K are the shear and bulk modulus, respectively. Eq. (1)$_3$ defines the elastic domain with f denoting the yield function, $\bar{\sigma}$ the effective stress which depends on the Cauchy stress deviator **s** and hardening variables which can be scalar or tensorial (e.g. the back-stress **X**). Eq. (1)$_4$ defines the direction of the plastic flow with $\dot{\lambda} \geq 0$ being the plastic multiplier and g denotes the plastic potential. For associated flow rule, the yield function and the plastic potential are equal ($g = f$).

Isotropic hardening (i.e. a single scalar hardening variable) is widely used for description of the plastic behaviour under monotonic loadings or for modelling the plastic behaviour for processes that do not involve cyclic loading/unloading conditions. All participants assuming isotropic hardening, described it either by the Swift law [Swi1952], i.e.

$$
Y\left(\bar{\varepsilon}^p\right) = K_0\left(\varepsilon_0 + \bar{\varepsilon}^p\right)^n
\tag{3}
$$

where K_0, ε_0 and n are material parameters, or by the Voce law (1948) [Voc1948], given by,

$$
Y = Y_0 - B\exp\left(-n\bar{\varepsilon}^p\right)
\tag{4}
$$

where Y_0, B and n are parameters; $\bar{\varepsilon}^p$ is the effective plastic strain being the work-conjugate of the effective stress. In addition, the team from USakarya used a Chaboche type hardening law (also called Armstrong-Frederick law) [Cha1986, Chu2005, Chu2002] involving both a scalar variable and a second-order tensorial variable **X** (combined isotropic and kinematic hardening law) for which the evolution law is given as:

$$
\dot{\mathbf{X}} = C\left(2/3\right)\mathbf{D}^p - \gamma\mathbf{X}\dot{\bar{\varepsilon}}^p
\tag{5}
$$

where γ and C are parameters that were determined from the cyclic shear tests.

Most participants assumed an associated flow rule, $f=g$ in Eq. (1)$_4$).

UAalto, UPorto, USiegen (see Table 11) used in conjunction with Hill's yield function (see Eq.(12)) a non-associated flow rule. As in [Sto2009], it was assumed that the flow potential g has the same mathematical form as Eq.(12), but it is characterized by different values for the anisotropy coefficients. In this manner, in the elastoplastic model, there are six anisotropy coefficients denoted as F_σ, G_σ,

H_σ, L_σ, M_σ, N_σ associated with the yield function and six additional anisotropy coefficients denoted as F_r, G_r, H_r, L_r, M_r, N_r, associated with the flow potential (see [Sto2009]). Evolution of the anisotropy coefficients involved in either yield function or potential flow with the equivalent plastic strain can also be also considered (see for example, [Lia2018] and Section 7.2.9).

6.1   Orthotropic yield functions

Both 2-D orthotropic yield functions and general 3-D orthotropic yield functions that are applicable to any stress state were considered. The expressions of these yield functions are presented in Section 6.1.1 and 6.1.2, respectively, while details concerning the identification of these yield functions for the AA 6014-T4 are given in Section 7.2. In the following, (x, y, z) denotes the Cartesian coordinate system associated with the orthotropy axes; for a rolled sheet such as the material studied in this benchmark, x coincides with RD, y with TD and z is the normal direction to the sheet plane.

6.1.1   2-D orthotropic yield functions (Yld89, Yld2000-2d, HomPol4, HomPol6)

The 2-D yield functions Yld89 and Yld2000-2D proposed by [Bar1989] and [Bar2003] are extensions to orthotropy of the isotropic Hershey-Hosford yield function (see [Her1954], [Hos1990]) which is expressed as:

$$\phi_{H-H}(s_1, s_2, s_3) = \left|s_1 - s_2\right|^m + \left|s_2 - s_3\right|^m + \left|s_3 - s_1\right|^m \tag{6}$$

where s_1, s_2, s_3 denote the principal values of the stress deviator, and m is an exponent.

Specifically, Yld89 is a non-quadratic plane stress yield function containing a shear stress term,

$$a\left|k_1 + k_2\right|^m + a\left|k_1 - k_2\right|^m + \left(2 - a\right)\left|2k_2\right|^m = 2\bar{\sigma}^m \tag{7}$$

and $k_1 = \left(\sigma_{xx} + h\sigma_{yy}\right)/2$ and $k_2 = \sqrt{\left(\sigma_{xx} - h\sigma_{yy}\right)^2/4 + p^2\sigma_{xy}^2}$.

In the above equation, a, h, p are material parameters; the recommended values for the exponent m =6 for body centred cubic (BCC) materials and m=8 for face centred cubic (FCC) materials. In [Bar1989], in Eq. (7), a coefficient $c = \left(2 - a\right)$ is sometimes introduced. In the identification of the model parameters by POSTECH, the anisotropy coefficients are indeed a, h, p, m. (see Table 25 in Section 7.2.4).

The Yld2000-2d yield function was defined as:

$$\left|X_1' - X_2'\right|^m + \left|2X_2'' + X_1''\right|^m + \left|2X_1'' + X_2''\right|^m = 2\bar{\sigma}^m \tag{8}$$

with $X_{1,2}' = \frac{1}{2}\left(X_{xx}' + X_{yy}' \pm \sqrt{\left(X_{xx}' - X_{yy}'\right)^2 + 4X_{xy}'^2}\right)$ and similar expression with the appropriate double prime indices for $X_{1,2}''$. The relations giving the components of $\mathbf{X}'$ and $\mathbf{X}''$ in terms of the in-plane components of the Cauchy stress deviator are:

$$\begin{bmatrix} X_{xx}' \\ X_{yy}' \\ X_{xy}' \end{bmatrix} = \begin{bmatrix} \alpha_1 & 0 & 0 \\ 0 & \alpha_2 & 0 \\ 0 & 0 & \alpha_7 \end{bmatrix} \begin{bmatrix} s_{xx} \\ s_{yy} \\ s_{xy} \end{bmatrix} \quad \text{and} \quad \begin{bmatrix} X_{xx}'' \\ X_{yy}'' \\ X_{xy}'' \end{bmatrix} = \frac{1}{3}\begin{bmatrix} 4\alpha_5 - \alpha_3 & 2\alpha_6 - \alpha_4 & 0 \\ 2\alpha_3 - 2\alpha_5 & 4\alpha_4 - \alpha_6 & 0 \\ 0 & 0 & 3\alpha_8 \end{bmatrix} \begin{bmatrix} s_{xx} \\ s_{yy} \\ s_{xy} \end{bmatrix} \tag{9}$$

where α_j, j=1…8 denote the independent anisotropy coefficients involved in the formulation of Yld2000-2d (see [Bar2003]).

The polynomial plane stress yield functions developed by [Soa2007] and called hereafter HomPol4 and HomPol6, respectively, are expressed as:

$$\varphi = a_1\sigma_{xx}^4 + a_2\sigma_{xx}^3\sigma_{yy} + a_3\sigma_{xx}^2\sigma_{yy}^2 + a_4\sigma_{xx}\sigma_{yy}^3$$
$$+a_5\sigma_{yy}^4 + \left(a_6\sigma_{xx}^2 + a_7\sigma_{xx}\sigma_{yy} + a_8\sigma_{yy}^2\right)\sigma_{xy}^2 \qquad (10)$$
$$+a_9\sigma_{xy}^4$$

$$\phi = a_1\sigma_{xx}^6 + a_2\sigma_{xx}^5\sigma_{yy} + a_3\sigma_{xx}^4\sigma_{yy}^2 + a_4\sigma_{xx}^3\sigma_{yy}^3$$
$$+a_5\sigma_{xx}^2\sigma_{yy}^4 + a_6\sigma_{xx}\sigma_{yy}^5 + a_7\sigma_{yy}^6 +$$
$$\left(a_8\sigma_{xx}^4 + a_9\sigma_{xx}^3\sigma_{yy} + a_{10}\sigma_{xx}^2\sigma_{yy}^2 + a_{11}\sigma_{xx}\sigma_{yy}^3 + a_{12}\sigma_{yy}^4\right)\sigma_{xy}^2 \qquad (11)$$
$$+\left(a_{13}\sigma_{xx}^2 + a_{14}\sigma_{xx}\sigma_{yy} + a_{15}\sigma_{yy}^2\right)\sigma_{xy}^4 + a_{16}\sigma_{xy}^6$$

with a_i denoting anisotropy coefficients.

6.1.2   3-D orthotropic yield functions (Hill48, CB2001, Yld2004-18p, CPB06ex2, Caz2018-Orth)

The orthotropic extension of the isotropic von Mises yield criterion was introduced by Hill [Hill1948]. The effective stress associated to Hill's criterion is given by:

$$F\left(\sigma_{yy} - \sigma_{zz}\right)^2 + G\left(\sigma_{zz} - \sigma_{xx}\right)^2 + H\left(\sigma_{xx} - \sigma_{yy}\right)^2 + 2\left(L\sigma_{yz}^2 + M\sigma_{zx}^2 + N\sigma_{xy}^2\right) = \bar{\sigma}^2 \qquad (12)$$

where F, G, H, L, M and N are parameters describing the material anisotropy.

The orthotropic yield functions developed by [Caz2001] and [Caz2018a] are expressed in terms of the orthotropic invariants J_2^0, J_3^0. In this manner it is ensured that these formulations automatically satisfy the orthotropy requirements (i.e. correct combinations of stress components). The condition of independence of yielding on hydrostatic pressure is fulfilled and the anisotropy coefficients are independent. Specifically, the expressions of the orthotropic invariants were developed using rigorous representation theorems for tensor functions, imposing that they are respectively homogeneous polynomials of degree two, and three in stresses, pressure-insensitive, and for isotropy reduce to the isotropic invariants J_2 and J_3, respectively. In the coordinate system (x, y, z) associated with the orthotropy axes (i.e. RD, TD, ND), these orthotropic invariants are expressed as follows:

$$J_2^o = \frac{a_1}{6}\left(\sigma_{xx} - \sigma_{yy}\right)^2 + \frac{a_2}{6}\left(\sigma_{yy} - \sigma_{zz}\right)^2 + \frac{a_3}{6}\left(\sigma_{xx} - \sigma_{zz}\right)^2 + a_4\sigma_{xy}^2 + a_5\sigma_{xz}^2 + a_6\sigma_{yz}^2 \qquad (13)$$

$$J_3^o = \frac{1}{27}(b_1 + b_2)\sigma_{xx}^3 + \frac{1}{27}(b_3 + b_4)\sigma_{yy}^3 + \frac{1}{27}\left[2(b_1 + b_4) - b_2 - b_3\right]\sigma_{zz}^3$$
$$-\frac{1}{9}\left(b_1\sigma_{yy} + b_2\sigma_{zz}\right)\sigma_{xx}^2 - \frac{1}{9}\left(b_3\sigma_{zz} + b_4\sigma_{xx}\right)\sigma_{yy}^2$$
$$-\frac{1}{9}\left[(b_1 - b_2 + b_4)\sigma_{xx} + (b_1 - b_3 + b_4)\sigma_{yy}\right]\sigma_{zz}^2$$
$$+\frac{2}{9}(b_1 + b_4)\sigma_{xx}\sigma_{zz}\sigma_{yy} - \frac{\sigma_{xz}^2}{3}\left[2b_9\sigma_{yy} - b_8\sigma_{zz} - (2b_9 - b_8)\sigma_{xx}\right] \qquad (14)$$
$$-\frac{\sigma_{xy}^2}{3}\left[2b_{10}\sigma_{zz} - b_5\sigma_{yy} - (2b_{10} - b_5)\sigma_{xx}\right] - \frac{\sigma_{yz}^2}{3}\left[(b_6 + b_7)\sigma_{xx} - b_6\sigma_{yy} - b_7\sigma_{zz}\right]$$
$$+2b_{11}\sigma_{xy}\sigma_{xz}\sigma_{yz}$$

where a_k (k = 1...6) and b_j, j = 1...11 are anisotropy coefficients (see book [Caz2019]).

The yield function [Caz2001], denoted hereafter as CB2001 is of the form:

130

$$f = \left(J_2^o\right)^3 - c\left(J_3^o\right)^2 \tag{15}$$

where *c* is a parameter. For isotropic conditions (i.e. all anisotropy coefficients set equal to unity), the isotropic yield function proposed by Drucker [Dru1949] is recovered.

The effective stress according to the orthotropic yield function of [Caz2018a], called hereafter Caz2018-Orth is expressed as:

$$\bar{\sigma} = B\left[\left(J_2^o\right)^4 - \alpha\left(J_2^o\right)\left(J_3^o\right)^2\right]^{1/8} \tag{16}$$

with α being a parameter and B defined such as for uniaxial tension in the *x*-direction the effective stress reduces to the yield stress, i.e.:

$$B = \frac{3\sqrt{2}}{\left\{\left[27\left(a_1 + a_3\right)^3 - 8\alpha\left(b_1 + b_2\right)^2\right]\left(3a_1 + 3a_3\right)\right\}^{1/8}} \tag{17}$$

A 3-D orthotropic extension of Hershey-Hosford isotropic yield function given by Eq. (6) is the yield function Yld2004-18p proposed in [Bar2005]:

$$\phi\left(s_{\alpha\beta}\right) = \Phi\left(\tilde{s}_i', \tilde{s}_j''\right) = \sum_{i,j}^{1,3}\left|\tilde{s}_i' - \tilde{s}_j''\right|^m = 4\bar{\sigma}^m \tag{18}$$

In the above equation $\tilde{s}_i', \tilde{s}''$ being the principal values of two transformed stress deviators $\tilde{\mathbf{s}}' = \mathbf{C}'\mathbf{s}$ and $\tilde{\mathbf{s}}'' = \mathbf{C}''\mathbf{s}$. These transformed tensors are written in a matrix form as:

$$\tilde{\mathbf{s}} \equiv \begin{bmatrix} \tilde{s}_{xx} \\ \tilde{s}_{yy} \\ \tilde{s}_{zz} \\ \tilde{s}_{yz} \\ \tilde{s}_{zx} \\ \tilde{s}_{xy} \end{bmatrix} = \begin{bmatrix} 0 & -c_{12} & -c_{13} & 0 & 0 & 0 \\ -c_{21} & 0 & -c_{23} & 0 & 0 & 0 \\ -c_{31} & -c_{32} & 0 & 0 & 0 & 0 \\ 0 & 0 & 0 & c_{44} & 0 & 0 \\ 0 & 0 & 0 & 0 & c_{55} & 0 \\ 0 & 0 & 0 & 0 & 0 & c_{66} \end{bmatrix} \begin{bmatrix} s_{xx} \\ s_{yy} \\ s_{zz} \\ s_{yz} \\ s_{zx} \\ s_{xy} \end{bmatrix} \tag{19}$$

with the appropriate symbols (prime and double prime) for each transformation, i.e., C_{ij}' for $\tilde{\mathbf{s}}'$ and C_{ij}'' for $\tilde{\mathbf{s}}''$ (for more details, see [Bar2005]). Note that the two tensors $\mathbf{C}'$ and $\mathbf{C}''$ are not symmetric ($C_{ij}' \neq C_{ji}'$ and $C_{ij}'' \neq C_{ji}''$).

To account for yielding asymmetry between tension and compression associated either with deformation twinning or non-Schmid effects at single crystal level, in [Caz2006] it was proposed an isotropic criterion of the form:

$$G\left(s_1, s_2, s_3, k, a\right) = \left(\left|s_1\right| - ks_1\right)^a + \left(\left|s_2\right| - ks_2\right)^a + \left(\left|s_3\right| - ks_3\right)^a \tag{20}$$

where k is a parameter. Furthermore, this isotropic yield criterion was further extended to orthotropy by applying a fourth-order symmetric and orthotropic tensor $\mathbf{C}$ on the stress deviator $\mathbf{s}$, i.e. in Eq.(20), s_1, s_2, and s_3 were substituted by the principal values of the transformed tensor $\boldsymbol{\Sigma} = \mathbf{Cs}$. Thus, the resulting anisotropic yield criterion, denoted, CPB06 is of the form:

$$F_1 = \left(\left|\Sigma_1\right| - k\Sigma_1\right)^a + \left(\left|\Sigma_2\right| - k\Sigma_2\right)^a + \left(\left|\Sigma_3\right| - k\Sigma_3\right)^a = \bar{\sigma}^a \tag{21}$$

where Σ_i are the principal values of $\boldsymbol{\Sigma}$ and $\bar{\sigma}$ is the effective stress associated with this criterion. If two linear transformations operating on the Cauchy stress deviator $\mathbf{s}$ are considered, namely $\boldsymbol{\Sigma} = \mathbf{Cs}$

130

and $\Sigma' = \mathbf{C's}$ with $\mathbf{C}$ and $\mathbf{C'}$ being symmetric and orthotropic, the general form of the orthotropic criterion, called CPB06ex2, is:

$$F_2 = G \ (\ \Sigma_1, \Sigma_2, \Sigma_3, k, a) + G \ (\ \Sigma'_1, \Sigma'_2, \Sigma'_3, k', a) = \overline{\sigma}^a \qquad (22)$$

where k, k' are parameters and Σ_i and Σ'_i the principal values of the respective transformed tensors (for more details, see [Plu2008]).

6.2 Crystal plasticity based constitutive models

To describe the macroscopic plastic anisotropy of a polycrystalline metallic materials, in crystal plasticity based constitutive models, the deformation of the constituent crystals is explicitly simulated. Generally, for FCC materials, the plastic deformation of the crystals is modelled with the Schmid law, i.e. it is assumed that a critical value of the resolved shear stress is required for the initiation of the slip. Furthermore, the same critical resolved shear stress is considered for all twelve slip systems (e.g. see review of [Van2004]). The slip rate on each slip system is generally described by a power-law (e.g. see Eq. (35)). Recently, a new single-crystal law [Caz2018b] called hereafter "Caz2018singlecrys" that is defined for any stress-state was developed (see Eq. (28-30)).

To obtain the macroscopic stress-strain response of the polycrystal from the response of the individual constituent crystals, different assumptions are made among the Benchmark participants:

- the homogeneous strain assumption of Taylor [Tay1938] referred hereafter as the Full Constraints Taylor model is used in the models developed by REEF (section 6.2.2), ULiege (section 6.2.3), NTNU (section 6.2.4);

- more relaxed grain interaction constraints, such in the ALAMEL model [Van2005] is applied by KUL (see Section 6.2.1);

-a self-consistent homogenization method (see Section 6.2.5) is used by UGent.

Finally, the simplified approach of POSTECH is to assume that only the cubic component is present in the texture of the AA 6016-T4 material (i.e. 100% of the crystals are oriented along the <100> crystallographic directions) and use the cubic single-crystal law of Cazacu [Caz2018b] to model the yielding behaviour of the polycrystalline material.

6.2.1 Facet-3D model linked to ALAMEL crystal plasticity model

The FACET approach presented in [Van2009] defines a phenomenological yield surface in the stress space based on rates of plastic work per unit volume, obtained with the ALAMEL model. The Facet expression for this plane-stress yield surface in stress space is given by [Van2009]:

$$\phi(\boldsymbol{s}) = (\textstyle\sum_{k=1}^{m} c_k (\boldsymbol{s}.\boldsymbol{a}_k)^n)^{\frac{1}{n}} = 1 \qquad (23)$$

where for Facet-3D, which is a generalized plane stress model, $\boldsymbol{s}$ is a 3D stress vector such that $\boldsymbol{s} = [s_1 \quad s_2 \quad s_3]^{\mathrm{T}}$ in which $s_1 = \frac{1}{\sqrt{2}}(s_x - s_y)$, $s_2 = \sqrt{\frac{3}{2}}(s_x + s_y)$, and $s_3 = \sqrt{2}s_{xy}$, with s_x, s_y, and s_{xy} being the components of stress deviator. m represents the number of Facet terms, n is the order of the Facet expression, c_k are coefficients to be determined during the fitting procedure, and $\boldsymbol{a}_k$ are normal vectors to hyperplanes or "facets" in 3D stress space to ensure convexity of the yield surface. The order n should be an even number, and the coefficients c_k must be non-negative.

The 3D plastic strain rate vector $\dot{\boldsymbol{e}}^{\mathrm{P}} = [\dot{e}_1^{\mathrm{P}} \quad \dot{e}_2^{\mathrm{P}} \quad \dot{e}_3^{\mathrm{P}}]^{\mathrm{T}}$ that corresponds to a given yield stress is calculated by:

$$\dot{e}^{\mathrm{P}} = \dot{\lambda}\frac{\partial \phi(s)}{\partial s} = \dot{\lambda}(\sum_{k=1}^{m} c_k (s.a_k)^n)^{\frac{1}{n}-1} \sum_{k=1}^{m} c_k (s.a_k)^{n-1} a_k \tag{24}$$

in which $\dot{\lambda}$ is an arbitrary non-negative number, called the plastic multiplier. Note that rate-insensitivity is assumed. The components of the plastic strain rate vector are then calculated by:

$$\dot{e}_x^{\mathrm{P}} = \frac{1}{\sqrt{2}}\dot{e}_1^{\mathrm{P}} + \frac{1}{\sqrt{6}}\dot{e}_2^{\mathrm{P}}$$
$$\dot{e}_y^{\mathrm{P}} = -\frac{1}{\sqrt{2}}\dot{e}_1^{\mathrm{P}} + \frac{1}{\sqrt{6}}\dot{e}_2^{\mathrm{P}} \tag{25}$$
$$\dot{e}_z^{\mathrm{P}} = -\dot{e}_x^{\mathrm{P}} - \dot{e}_y^{\mathrm{P}}$$
$$\dot{e}_{xy}^{\mathrm{P}} = \frac{1}{\sqrt{2}}\dot{e}_3^{\mathrm{P}}$$

The Facet expression is further used within a VUMAT user material routine of ABAQUS/Explicit [Gaw2013] for the cup drawing simulations. As already mentioned, and further explained in Section 7.1.2.1, for this benchmark the ALAMEL model was used to identify the Facet-3D yield locus. ALAMEL [Van2005] is a statistical crystal plasticity model that accounts for short-range interaction of the grains. In ALAMEL model, pairs of grains are considered as a cluster with a common boundary plane of a certain orientation. While in the full constraints Taylor model all the grains are assumed to undergo the same velocity gradient as that imposed on the aggregate of crystals (a.k.a. the macroscopic deformation), in ALAMEL certain deviations from the macroscopic deformation are allowed for each pair of grains.

In particular, two shear strain components parallel to the boundary plane of each pair of grains are relaxed from the full constrains Taylor theory. If the macroscopic velocity gradient is given by L, then the local velocity gradient l is calculated by:

$$l_i = L + (-1)^i \sum_{j=1}^{2} T_j^{\mathrm{R}} \dot{\gamma}_j^{\mathrm{R}} \tag{26}$$

where $i = 1,2$ represents the number of grain in the cluster, $\dot{\gamma}^{\mathrm{R}}$ is a "cooperative" shear deformation which is equal for both grains and operates on "pseudo slip systems", and T^{R} are relaxation matrices which in the local coordinate system with a normal in z direction are defined as:

$$T_1^{\mathrm{R}} = \begin{bmatrix} 0 & 0 & 1 \\ 0 & 0 & 0 \\ 0 & 0 & 0 \end{bmatrix}$$
$$T_2^{\mathrm{R}} = \begin{bmatrix} 0 & 0 & 0 \\ 0 & 0 & 1 \\ 0 & 0 & 0 \end{bmatrix}. \tag{27}$$

More details about ALAMEL and its comparison with Taylor and other models can be found in [Van2005]. For the virtual experiments with ALAMEL, the latent hardening of the grains was neglected. Therefore, only the texture data was necessary to generate 10,000 orientations to assign to the grains. These grains were then randomly grouped into 5,000 clusters to make the input for ALAMEL. In the present work, the virtual tests are performed with the initial texture, assuming identical critical resolved shear stresses for all slip systems in all grains. No hardening is considered at the microscopic scale. The virtual yield stresses define the shape of the yield locus. This is normalized to yield stress of one for the tensile test in the rolling direction. Further scaling of the yield locus to account for hardening is done at the macroscopic level (i.e. the FE simulations), where isotropic hardening is assumed using the Swift hardening law described in Section 7.3 (see Table 32).

6.2.2 Caz2018polycrys, a polycrystalline model based on Cazacu single crystal law Caz2018singlecrys

The polycrystal is represented by a finite set of grains characterized by orientation and volume fraction to reproduce the material texture. Elastic deformations are modelled using Hooke's law for the type of symmetry shown by cubic crystals.

With Caz2018polycrys law, the plastic behaviour of the constituent crystals is modelled using the single crystal law of [Caz2018b], called Caz2018singlecrys, normality rule, and isotropic hardening described by a Swift-type law. The single-crystal law is defined for any stress-state. It is written in terms of cubic stress-invariants that were deduced using rigorous theorems of representation of tensor functions (see Eq. (28-30)). Consequently, the exact number of anisotropy coefficients that ought to be involved in the formulation, in order to satisfy the symmetries of the cubic lattice and the condition of insensitivity of plastic deformation to hydrostatic pressure are satisfied (for full mathematical proofs and further details, see [Caz2018b] and book [Caz2019]).

Relative to the Cartesian coordinate system $Ox_1x_2x_3$ associated with the crystal axes (i.e., the <100> crystal directions), the expression of the cubic invariants are:

$$J_2^c = \frac{1}{2} m_1 \left(s_{11}^2 + s_{22}^2 + s_{33}^2 \right) + m_2 \left(s_{12}^2 + s_{13}^2 + s_{23}^2 \right)$$

$$J_3^c = n_1 s_{11} s_{22} s_{33} - n_3 \left(s_{33} s_{12}^2 + s_{11} s_{23}^2 + s_{22} s_{13}^2 \right) + 2 n_4 s_{12} s_{13} s_{23}$$

(28)

The single crystal law writes,

$$\left(J_2^c \right)^3 - c \left(J_3^c \right)^2 = k^6$$

(29)

the effective stress of the crystal, $\bar{\sigma}_{grain}$, being given by:

$$\bar{\sigma}_{grain} = \frac{3}{\left(27 - 4cn_1^2 \right)^{1/6}} \left[\left(J_2^c \right)^3 - c \left(J_3^c \right)^2 \right]^{1/6}$$

(30)

where **s** denotes the deviator of the applied Cauchy stress, k is the yield limit in simple shear m_1, m_2, n_1, n_3, n_4 are anisotropy coefficients and c is a parameter that describes the relative importance of the second-order and third-order cubic stress-invariants on yielding. The plastic strain-rate of each crystal $\mathbf{d}_{grain}^p$ is uniquely defined for any stress state and can be easily calculated as:

$$\mathbf{d}^P = \dot{\lambda} \frac{\partial \bar{\sigma}_{grain}}{\partial \boldsymbol{\sigma}}$$

(31)

where $\dot{\lambda}$ is the plastic multiplier, and $\bar{\sigma}_{grain}$ is given by Eq.(30).

While all the simulations presented hereafter were done using Caz2018polycrys polycrystalline model implemented in the commercial FE solver ABAQUS Standard (implicit solver), the same approach can be used to do calculations in any FE solver. The model is called Caz2018polycrys, as already introduced in Table 11, to have a clear distinction with Caz2018singlecrys.

A polycrystalline aggregate is associated with each FE integration point. The FE code provides the deformation gradient at the integration point. The elasto-plasticity problem is solved in each grain (crystallite level). The orientation, the equivalent plastic strain and stress of the individual grains are updated depending on the deformation of the element, and the calculated individual crystallite stresses are homogenized to give the stress at the integration point, for use in the solution of the

continuum equilibrium equations. The isostrain homogenization scheme is used (the total strain-rate of each grain is equal to the overall strain-rate $\mathbf{D}$).

It is considered that the total strain-rate of each grain belonging to a given element is equal to the overall strain-rate $\mathbf{D}$. At the time increment *(n)*, the stress in each grain is computed by solving the governing equations, namely:

$$\mathbf{D}_{grain}^{(n)} = \left(\mathbf{R}^{(n)}\right)^{T}\mathbf{D}^{(n)}\mathbf{R}^{(n)}$$

$$\mathbf{D}_{grain}^{(n)} = \mathbf{D}_{grain}^{e(n)} + \mathbf{D}_{grain}^{p(n)}$$

$$\boldsymbol{\sigma}_{grain}^{(n)} = \boldsymbol{\sigma}_{grain}^{(n-1)} + \left(\mathbf{C}^{el}{:}\mathbf{D}_{grain}^{e(n)}\right)dt \qquad (32)$$

$$\bar{\sigma}_{grain}^{(n)} - Y\left(\bar{\varepsilon}_{grain}^{p\,(n)}\right) \leq 0$$

$$\mathbf{D}_{grain}^{p(n)} = \dot{\lambda}_{grain}\frac{\partial\bar{\sigma}_{grain}^{(n)}}{\partial\sigma}$$

where $\mathbf{D}_{grain}^{(n)}$, $\mathbf{D}_{grain}^{p(n)}$ and $\mathbf{D}_{grain}^{e(n)}$ are respectively the total strain-rate, the plastic and elastic strain-rate, $\boldsymbol{\sigma}_{grain}^{(n-1)}$ and $\boldsymbol{\sigma}_{grain}^{(n)}$ are the stress tensors at the beginning and end of the increment, respectively, $Y\left(\bar{\varepsilon}_{grain}^{p\,(n)}\right)$ is the hardening law while $\bar{\varepsilon}_{grain}^{p\,(n)}$ is the equivalent plastic strain in the given grain.

The stress of the polycrystal at the end of the increment is given by:

$$\boldsymbol{\sigma}^{(n)} = \left(\sum_{i} w_{i}\mathbf{R}_{i}^{(n)}\left(\boldsymbol{\sigma}_{grain}^{(n)}\right)_{i}\left(\mathbf{R}_{i}^{(n)}\right)^{T}\right) / \left(\sum_{i} w_{i}\right) \qquad (33)$$

where $\left(\boldsymbol{\sigma}_{grain}^{(n)}\right)_{i}$ is the stress tensor of grain *i*, and $\mathbf{R}_{i}^{(n)}$ is the transformation matrix for passage from the crystal axes of grain *i* to the loading frame axes, while w_{i} is the weight of the grain *i*. Note that to increase readability, in Eqs.(29) the index '*i*', designating the local field variables associated to the grain *i*, has been dropped.

6.2.3 MINTY model, an interpolation approach

The main specificity of the Minty model is that it uses a local yield locus approach based on a direct stress-strain interpolation method. In this respect, it does not use a classical yield locus formulation neither for the interpolation nor in the stress integration scheme. Instead, a linear stress-strain interpolation is employed:

$$\boldsymbol{\sigma} = \tau\boldsymbol{Cu} \qquad (34)$$

In the above equation, $\boldsymbol{\sigma}$ is a 5-D vector containing the deviatoric part of the stress, its hydrostatic part being elastically computed according to Hooke's law. The 5-D vector $\boldsymbol{u}$ is the deviatoric plastic strain rate direction; it is a unit vector. τ is the critical resolved shear stress describing the work hardening according to the Swift type exponential relationship of Eq. (35), where the strength coefficient *K*, the offset Γ^{0} and the hardening exponent *n* are material parameters, fitted to experimental data (further explanations in Section 7.1.2.3) and Γ is the accumulated polycrystal induced slip.

$$\tau = K\left(\Gamma^{0} + \Gamma\right)^{n} \qquad (35)$$

The stress-strain interpolation is included in the matrix C of Eq. (34). For its construction, 5 directions: $\underline{u}_i$ (*i*=1…5) in the deviatoric strain rate space are advisedly chosen. The associated deviatoric stresses: $\underline{s}_i$ (*i*=1…5) are computed by a full constraints Taylor's model. These stress vectors lie on the yield surface according to Taylor's model. These points define the interpolation domain; they are located at the vertices of the domain and are called 'stress nodes'. The mathematical details about the construction of the C matrix from the 5 stress nodes can be found in [Hab2004a and b].

With this method, only a small part of the yield locus is known. As long as the interpolation is achieved in the domain delimited by the 5 stress nodes, the interpolation matrix C is valid. When the stress direction explored during the finite element computation falls out of the domain, updating of the stress nodes must take place; a new interpolation matrix is computed. The classical updating method consists in finding 5 new stress nodes defining a new domain containing the current stress direction. An enhanced updating method makes use of the adjacent domain. Therefore, only 1 new stress node is computed with Taylor's model and 4 of the 5 old stress nodes are kept for the interpolation. The main advantages of this method are that updating requires only 1 (instead of 5) call to Taylor's model and that it improves the continuity of the resulting yield locus and the continuity of its normal.

The texture of the material is represented at each integration point of the finite element mesh by a set of crystallographic orientations. Texture evolution can be computed at each integration point on the basis of the strain history using Taylor's model. To include its effects in the computations, the interpolation matrix must be updated when texture evolution took place.

6.2.4 Crystal plasticity model used in DAMASK solver

The usual constitutive assumptions are considered. Namely, it is assumed a local multiplicative decomposition of the deformation gradient $\mathbf{F} = \mathbf{F_e F_p}$, where $\mathbf{F_e}$ and $\mathbf{F_p}$ are elastic and plastic component, respectively. The evolution of deformation gradients is obtained from $\mathbf{L} = \mathbf{L_e} + \mathbf{F_e L_p (F_e)}^{-1}$. It is assumed that plastic deformation is due to slip over N slip systems. Each deformation system (α) is characterized by the unit vectors $\mathbf{n}^\alpha$ (normal to the slip plane) and a vector $\mathbf{b}^\alpha$ (shear direction), their dyadic product defining the Schmid tensor of the system, $\mathbf{S}_0^\alpha$. It is considered that the plastic velocity gradient $\mathbf{L_p}$ is expressed as:

$$\mathbf{L_p} = \dot{\mathbf{F}}_\mathbf{p} \mathbf{F_p}^{-1} = \sum_\alpha^N \dot{\gamma}^\alpha \mathbf{S}_0^\alpha \tag{36}$$

with $\dot{\gamma}^\alpha$ is the shear on the slip system (α).

The usual power-law [Soc1976, Pei1983] is used to define the plastic shear rate $\dot{\gamma}^\alpha$:

$$\dot{\gamma}^\alpha = \dot{\gamma}^0 \left|\frac{\tau_\alpha}{g^\alpha}\right|^{1/m} \text{sign}(\tau_\alpha) \tag{37}$$

where τ_α is the applied shear stress, $\dot{\gamma}^0$ is a reference shear strain rate and the exponent *m* defines the rate sensitivity of slip system, g^α is the slip resistance which accounts for the strain hardened state of the crystal in the current configuration [Bro1989]. The evolution of g^α is governed by:

$$\dot{g}^\alpha = \sum_\beta^N h_{\alpha\beta} \dot{\gamma}^\beta g^\alpha \tag{38}$$

where $g^\alpha(0) = \tau_0$ is the initial hardness, assumed the same for each slip system and $h_{\alpha\beta}$ is the instantaneous strain hardening matrix, which is given by:

$$h_{\alpha\beta} = h_0 \left[q + (1-q)\delta_{\alpha\beta}\right] \left|1 - \frac{g^\beta}{g_\infty}\right| sign\left(1 - \frac{g^\beta}{g_\infty}\right) \tag{39}$$

130

where q is a latent hardening parameter. For a coplanar slip system $q=1$, and for a non-coplanar slip system $q=1.4$, where h_0, α and g_∞ are hardening parameters.

The applied shear stress τ_α is related to the Cauchy stress tensor $\boldsymbol{\sigma}$ as [Rot2010]:

$$\tau_\alpha = \boldsymbol{\sigma} : (\mathbf{F_e} \mathbf{S}_0^\alpha \mathbf{F_p^{-1}}) = (\mathbf{F_e^T} \mathbf{F_e} \mathbf{S}) : \mathbf{S}_0^\alpha \tag{40}$$

where $\mathbf{S}$ is the second-order Piola-Kirchhoff stress calculated using the small elastic strain assumption:

$$\mathbf{S} = \ \mathbf{C} : \mathbf{E}_e \text{ with } \mathbf{E}_e = (\mathbf{F_e^T} \mathbf{F_e} - \mathbf{I})/2 \tag{41}$$

where $\mathbf{C}$ is the elasticity matrix in the sample coordinate system. With respect to the crystal axes, this matrix for the case of a cubic crystal is fully specified by three material constants, C11, C12 and C44.

This model has been implemented into the open-source spectral method solver DAMASK [Rot2019]. Details on the numerical spectral method using the Fast Fourier transformation (CPFFT) can be found in Shanthraj et al. [Sha2015]. For this benchmark, DAMASK is used to predict yield stress points in both in-plane and out-of-plane uniaxial loadings and other multi-axial loadings.

6.2.5 Viscoplastic Self Consistent Model (VPSC)

The viscoplastic self-consistent (VPSC) model, developed by Lebensohn and Tomé [Leb1993], uses a mean-field approach for the simulation of plastic deformation of polycrystals. Each grain is treated as an anisotropic, viscoplastic, ellipsoidal inclusion embedded in a uniform matrix having the unknown properties (to be determined) of the polycrystal. In this work, the VPSC90 implementation [Gal2014] is employed. VPSC90 differs from the original VPSC version [Leb1993] in that it also considers elastic deformation and uses a different algorithm to find the self-consistent solution. The main assumptions are as follows:

1) Grain constitutive equation: the plastic strain rate of each grain is calculated using the strain rate sensitivity approach of Asaro and Needleman [Asa1985], which correlates the plastic strain rate of the grain, $\dot{\varepsilon}_g$, with its stress, σ_g, through the relationship:

$$\mathbf{D}_{\text{grain}}^{\text{p}} = \sum_s \mathbf{m}^s \ \dot{\gamma}^s = \dot{\gamma}_o \sum_s \mathbf{m}^s \left(\frac{\left| \mathbf{m}^s : \boldsymbol{\sigma}_{grain} \right|}{\tau_c^s} \right)^{n_s} sgn\left(\mathbf{m}^s : \boldsymbol{\sigma}_{grain} \right) \tag{42}$$

where $\dot{\gamma}^s$, $\mathbf{m}^s$, and n_s are respectively, the shear rate, the symmetric part of the Schmid tensor, the strain-rate sensitivity exponent of the slip system (s), and $\dot{\gamma}_0$ is a normalization constant (usually taken equal to unity). The critically resolved shear stress of the slip system (s), τ_c^s, is calculated according to an extended Voce-type hardening law [Tom1984],

$$\tau_c^s(\Gamma) = \tau_0^s + (\tau_1^s + \theta_1^s \, \Gamma) \left(1 - \exp\left(-\Gamma \left| \frac{\theta_0^s}{\tau_1^s} \right| \right) \right) \tag{43}$$

where Γ is the accumulated shear in all slip systems and τ_0, τ_1, θ_0 and θ_1 are parameters.

2) Micro-macro relationships: the overall stress and strain are calculated as the weighted averages over all the constituent grains:

$$\mathbf{D} = \sum_g w_g \mathbf{D}_{grain}^p \tag{44}$$

$$\boldsymbol{\sigma} = \sum_g w_g \boldsymbol{\sigma}_{grain} \tag{45}$$

with w_g the volumetric fraction of grain g.

130

3) Interaction equation: the Eshelby inclusion problem [Esh1957, Leb1993] is solved and the grain interaction tensor $\tilde{M}_g$ is found. This tensor is used to correlate the overall (polycrystal) and grain level stresses and strains:

$$\mathbf{D} - \mathbf{D}^{p}_{grain} = -\tilde{\mathbf{M}}_{g} \left(\mathbf{\sigma} - \mathbf{\sigma}_{grain} \right) \tag{46}$$

In addition, the obtained solution must fulfil the boundary conditions of the problem. At the macroscopic level, it is imposed that certain components of the stress or total strain (adding the elastic contribution) reach predefined values. The solution is found using an iterative algorithm, which is based on the gradient descent method in VPSC90. Namely, the total deformation of the polycrystal is obtained by imposing successive strain increments and calculating the resulting shears in the active deformation systems in the grains. The final texture is given by the grain reorientations associated with these shears.

7. Parameter identification and validation of constitutive models

Since all the plasticity anisotropic constitutive laws are non-linear, the determination of the parameters involved in the models often needs to be done in an iterative way and in general, multiple sets of parameters (i.e. solutions) can be obtained for the same law. The identification methodology involves minimizing the error between theoretical predictions and experimental data. To eliminate parametrizations that are not valid, additional constraints can be imposed to ensure that the yield surface is well-defined (e.g. the transformations tensors should not be singular) and convex.

The benchmark committee has provided a set of parameters for several orthotropic yield criteria. Specifically, POSTECH organizers supplied the values of the parameters for Yld2000-2D and Yld2004-18p (see Table 27 and Table 28); Univ. Florida-REEF supplied the values of the Caz2018-Orth yield criterion (see Table 30); UCoimbra supplied the parameters values for Hill 48 yield criterion (stress- r-based identification, see Table 22). The benchmark committee has also supplied the parameter values for the Swift and Voce isotropic hardening law (Table 32). Participants could use these material parameters or chose to perform their own identification based on experimental data of Section 2. Some participants selected other 2-D and 3-D yield criteria and/or models (see Table 11).

In this section, the ESAFORM benchmark organizers and participants have provided the information about their parameter identification methodology. In their procedure, they used mechanical tests of Section 2 or virtual ones, simulated with their crystal plasticity laws. The parameter values provided in this section are referenced when presenting and discussing the FE cup drawing results of Section 8.

Note that each participant had to provide the set of parameters used and to show the predictions of the Lankford coefficients, elastic limits (yield stresses), and the yield locus cross-section in the (RD-TD) plane. In this manner, the accuracy of the parameterization and the capacity of the models to describe the basic features of the plastic behaviour of the material can be evaluated. For the yield functions that have analytic expressions, the variation in yield stresses, Lankford coefficients and respectively yield surfaces was simply done by using the respective equations presented in Section 6.1. For the polycrystalline multi-scale models, these properties can be calculated only numerically.

Furthermore, to verify the implementation of the various orthotropic yield functions in the respective FE codes, participants were asked to provide the Lankford coefficients calculated by performing uniaxial tensile tests, and to check the numerical *r*-values vs. the analytical ones.

Finally by calculating with the same code both tensile tests and cup drawing tests, it was possible to ascertain whether the respective models can capture the experimentally observed correlations

130

between the anisotropy in Lankford coefficients and the earing profile. Moreover, this approach helps to differentiate between the effects on the predictions associated with the choice of FE elements and FE mesh and those associated with the choice of the constitutive model and parametrization used.

Section 7.1 presents the methodology used for identification and verification of polycrystalline models. Section 7.2 details the procedures used to identify the orthotropic yield functions. The approach adopted to identify the hardening law is described in Section 7.3 while Section 7.4 points the effort required in all these identification steps.

7.1 Parameter identification, validation and use of crystal plasticity models

For any polycrystalline plasticity model, the texture data is an input. As underlined hereafter, the description of the texture derived from the same EBSD data (Section 2.1) can already present significant variations. So each team describes in section 7.1.1, its methodology to obtain the representative texture. Section 7.1.2 provides the parameter identification method and verifies the parameterizations.

7.1.1 Representative textures and microstructures

7.1.1.1 Texture description for ALAMEL

KUL team uses the so-called ALAMEL crystal plasticity model to generate data exploited to identify the material parameter set of their Facet-3D yield locus (see Section 6.2.1). First a continuous texture was generated in the form of spherical harmonic C-coefficients (with a certain maximum rank L_{max}) from the raw EBSD texture [Bun1982].This was done by assuming a Gaussian distribution (with a certain spread φ_0) on each of the 471,411 indexed pixels in the raw EBSD data. The continuous texture was then re-discretized into 10,000 orientations with the statistical method described in [Tot1992].

Figure 29 shows the orientation distribution function (ODF) maps of the discrete texture at three different sections, which compare well with the measured textures with the main components preserved in the discrete texture. For this visualization, the discrete texture was made continuous again with the same φ_0 and L_{max} values as those were used for converting the initial EBSD orientations into a continuous ODF.

It was observed that the Gaussian spread width, φ_0, and the maximum rank for the generalized spherical harmonics, L_{max}, are important parameters that affect the results of the virtual experiments. When φ_0 is too large (in practice above 6°), the virtual experimentation leads to a larger $\Delta r = r_0 - 2r_{45} + r_{90}$ than that in the physical experiments, and the results are almost insensitive to the number of grains, n_g, that are considered for the ALAMEL virtual tests. On the other hand, when φ_0 is 6° or smaller, the Δr value decreased and converged to the experimental value when n_g was increased (see Figure 30). For the aluminium alloy in the present study, a combination of $\varphi_0 = 3^\circ$, $L_{max} = 22$, and $n_g = 10,000$ was found to be sufficient for reproducing the r-values with the virtual experiments, as will be shown in Section 7.1.2.1 (see Figure 32). As shown by Hutchinson et al. [Hut1999], the Gaussian spread of $\varphi_0 = 3^\circ$ offers the best possible correspondence between XRD and EBSD derived ODFs.
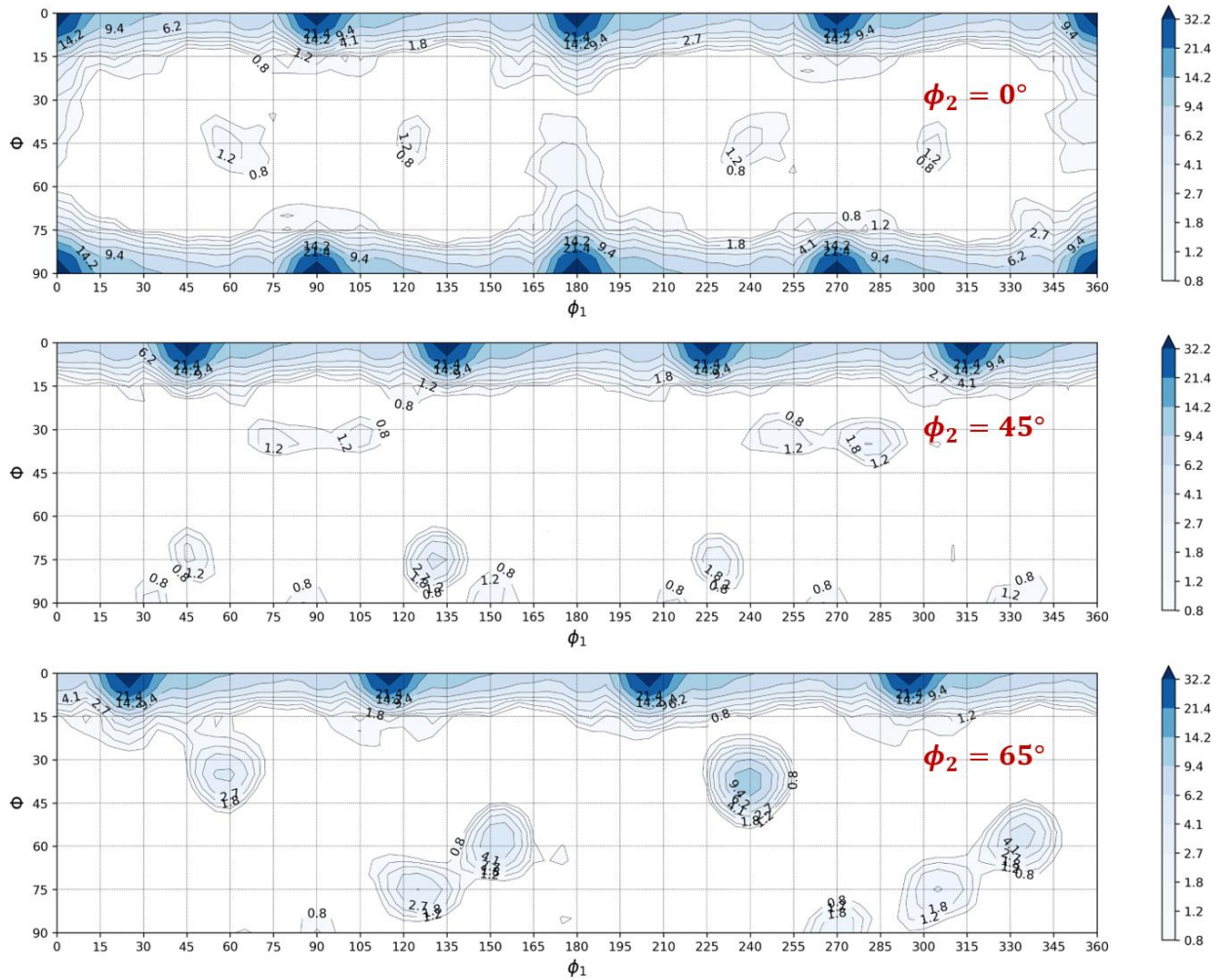
Figure 29 The ODF maps of the discrete texture used as the input for virtual experiments with ALAMEL crystal plasticity model
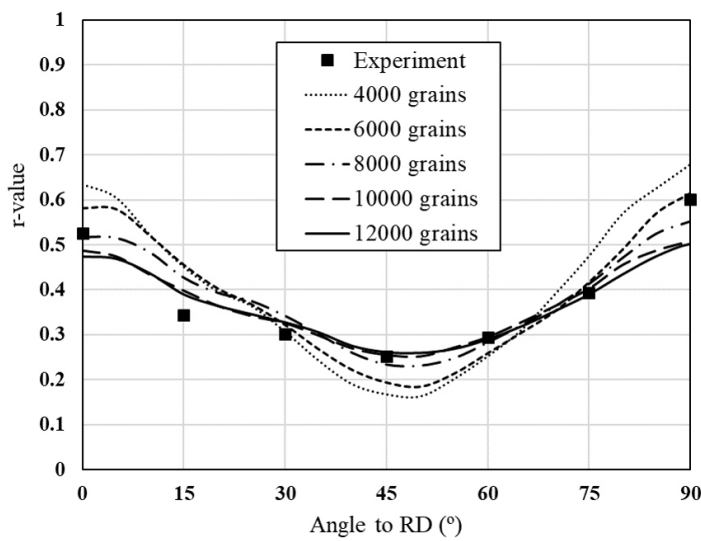
Figure 30 Effect of number of grains in the discrete texture on the r-values obtained by ALAMEL. This texture is generated by making the measured EBSD texture continuous with $\varphi_0 = 3°$ and $L_{max} = 22$ followed by a statistical discretization procedure described in [Tot1992]

130

7.1.1.2   *Texture description for Caz2018polycrys*

As mentioned in Section 2.1, the organizers at UA provided the measured ODF of the AA 6016-T4 aluminium alloy (see Figure 1 and Table 2). This ODF was first symmetrized to impose orthotropy and the MTEX Matlab Toolbox [Bac2010] software was used to generate 250 orientations representative of the material texture, which were further used as input in all the FE simulations with Caz2018polycrys, which relies on Caz2018singlecrys yield criterion for the description of the plastic behaviour of the constituent crystallites.

7.1.1.3   *Texture description for Minty*

For Minty law, the texture data provided by the benchmark committee was also used (see Section 2.1). From EBSD measurements, a set of 1000 crystal orientations in the form of Euler angles and weights was made available by the organizers. Such format can be directly used by Minty. It is worth to note that the orthotropic symmetry of the material (as shown in Figure 1(b)) is considered in the set of 1000 grains.

7.1.1.4   *Texture Description for Damask*

The 3D RVE crystal plasticity modelling used to predict the mechanical anisotropy of AA 6016-T4 needs texture data. First, the raw EBSD data in Section 2.1 was post-processed to remove the non-indexed points by their neighbouring orientations using the open-source MATLAB package, MTEX 5.6.0. As illustrated in Figure 31, 7509 grains in total were obtained from the post-processed EBSD map, among which the majority of the grains are aligned with cube orientation. Then, the orientations of the 7509 grains were assigned in the 3D RVE by using the open-source polycrystal generation software Neper, based upon the Voronoi tessellation method.
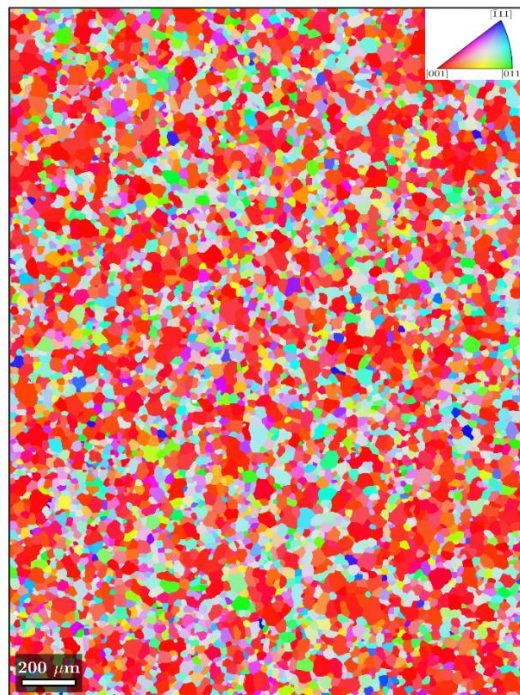
Figure 31 The EBSD map including the 7509 grains selected as input for the 3D RVE of AA 6016-T4 aluminium alloy sheet

7.1.1.5 *Texture description for VPSC model*

The microstructural information required by the VPSC model is the grain shape, expressed as the aspect ratios between the axes of the equivalent ellipsoid and a set of Euler angles indicating its spatial orientation (an average shape is commonly used for all grains in a phase), and a discrete crystallographic texture. Moreover, the model is used here in a particular way in order to take into account the influence of grain sizes. The capacity of VPSC to simulate multiphase materials is exploited to consider grains of different sizes as if they were different phases. The adopted approach by UGent team is similar to the one described in [GAL2020].

The microstructural data required by the model is extracted from the EBSD experimental data described Section 2.1. First, the raw data is processed with the help of the Dream3D software [GRO2014]. The data points with lower confidence index and image quality are removed, and the corresponding areas are filled extrapolating from adjacent grains. Then, using a grain boundary misorientation threshold of 5 degrees, the data is partitioned into different grains, and a grain list is generated with the grain area and the orientation obtained by averaging over all the data points of the grain. The list is then ordered by grain area and divided into three different sections, each corresponding to a different size range. For each of these sections, a different crystallographic texture and average grain shape are calculated. The different sections will be considered as different phases in the model, but, in fact, they correspond to the same material phase. The equivalent ellipsoids of each grain are calculated using Dream3D, and then the average lengths are calculated using the geometric average, while a discrete texture is calculated using the MTM-FHM software [Van1995]. First, an ODF is calculated (with triclinic symmetry, a Gaussian spread of 7 degrees, and $L_{max} = 22$), and then a discrete texture of 500 orientations is extracted. Thus, in total, for the three phases in the model, 1500 grains are considered in the simulation of Section 8.

7.1.1.6 *About the representative number of grains used to model the texture*

Let us already point the large discrepancy in the number of grains selected as representative of the texture (see Table 13). Each team made the choice based on their experience and focus on capturing the tensile test behaviour (yield stress variation and Lankford prediction in different direction from RD) and, sometimes, the shear test behaviour (see Section 7.1.2), before modelling the deep drawing process. The material chosen does not present an unusual earing profile (4 ears is a classical pattern). However, its strong cube texture with grains with different sizes already present some challenges. Therefore, a blind choice to model any material with a set of representative crystals, without any comparison with experiments, seems out of the scope. Nowadays, forgetting experiments and relying only on texture measurements and digital tools is still unreliable.

Table 13 Number of crystals used to model the texture and target model for each team

Team	Target constitutive law	Number of grains
KUL	ALAMEL model	10000
REEF	Caz2018polycrys	250
ULiege	Minty law	1000
NTNU	3D RVE for FFT (DAMASK)	7509
UGent	VPSC (own implementation)	1500

7.1.2 Parameter identification, validation and/or use of crystal plasticity models

7.1.2.1 *Facet-3D model*

The Facet-3D yield function was constructed based on 200 yield stresses computed by ALAMEL and the corresponding plastic strain rate directions obtained by virtual experiments on an equi-distant grid in 3D stress space. This grid was generated using the Spiral method [Saf1997] by evenly distributing 200 points on a sphere with a radius 1 and centred at the origin in a Cartesian coordinate system. Here,

the *x*, *y*, and *z* coordinates of each point were assumed to define the components of a stress mode $\boldsymbol{u} = [x \quad y \quad z]^T$, and the yield stress s^y, corresponding to this vector, was obtained from virtual experiment. Then, the coefficients of Facet-3D expression as defined in Eq. (24) were found by a non-negative least square (NNLS) fitting [Gaw2013] to make sure that all of them are positive.

In the present study, the Facet order was 8, and the fitted Facet-3D expression included 38 terms with the coefficients and normals to the facets given in Table 14.

Table 14 The coefficients and normal vectors to facets for the fitted Facet-3D with order 8

Facet number	Coefficient	Normal vector to the facet ($\boldsymbol{a}_k$)		
k	c_k	a_k^1	a_k^2	a_k^3
1	0.383	0.115	-0.003	0.403
2	0.056	-0.009	-0.381	0.304
3	0.227	0.267	-0.015	0.341
4	0.291	-0.294	0.001	0.308
5	0.025	0.336	0.015	0.279
6	0.283	0.186	0.393	0.239
7	0.266	-0.176	0.407	0.231
8	0.082	-0.193	-0.410	0.212
9	0.051	0.185	-0.418	0.207
10	0.554	0.245	-0.386	0.187
11	0.464	0.245	0.399	0.169
12	0.223	-0.274	0.383	0.140
13	0.141	-0.432	-0.028	0.086
14	0.578	0.444	0.006	0.043
15	0.147	0.332	0.338	0.042
16	0.264	-0.329	0.347	-0.013
17	0.057	-0.445	0.027	-0.021
18	0.003	-0.298	-0.384	-0.047
19	0.073	0.435	-0.060	-0.064
20	0.275	0.296	0.370	-0.108
21	0.056	-0.231	0.414	-0.157
22	0.001	-0.282	0.373	-0.145
23	0.058	-0.277	-0.366	-0.165
24	0.264	0.220	-0.402	-0.196
25	0.033	0.273	-0.349	-0.190
26	0.291	0.386	-0.028	-0.194
27	0.482	0.228	0.385	-0.208
28	0.303	-0.349	0.029	-0.262
29	0.081	0.139	-0.402	-0.258
30	0.034	0.117	0.397	-0.273
31	0.317	0.029	0.408	-0.283
32	0.287	-0.065	0.401	-0.284
33	0.210	-0.279	-0.013	-0.332
34	0.463	-0.013	-0.385	-0.300
35	0.228	0.233	-0.016	-0.353
36	0.259	0.152	-0.003	-0.390
37	0.102	0.055	-0.035	-0.409
38	0.166	0.016	0.031	-0.412

Figure 32 compares the experimental *r*-values, normalized tensile stresses, yield loci, and directions of the plastic strain rates with those obtained from the virtual experiments and the fitted Facet-3D.

130
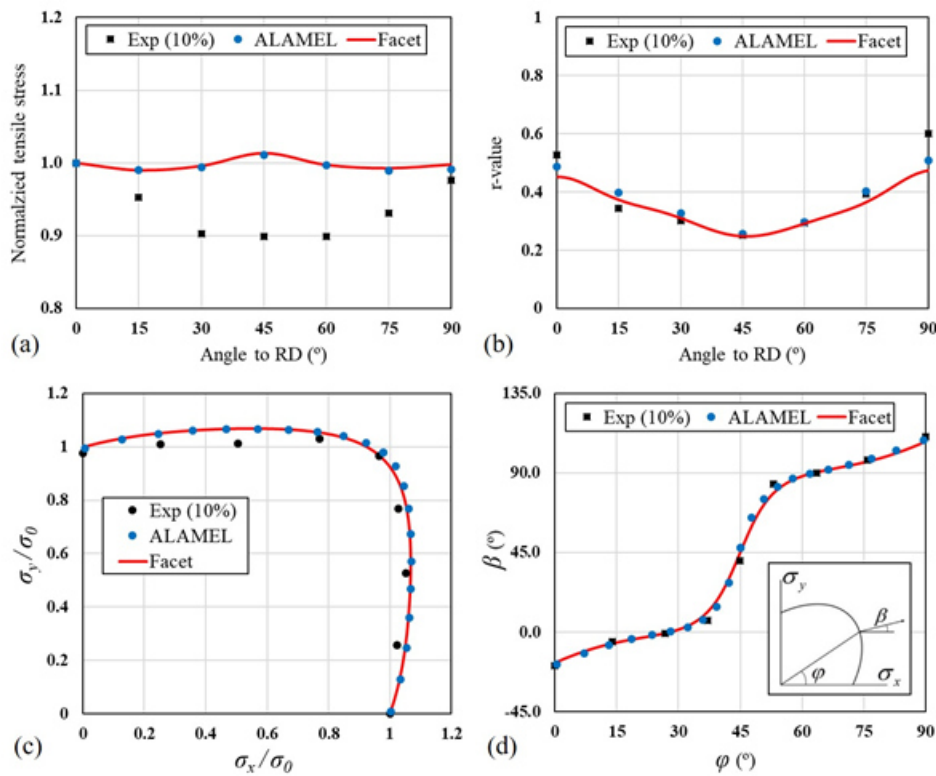
Figure 32 Comparison of (a) normalized tensile stresses, (b) *r*-values, (c) yield loci, and (d) directions of the plastic strain rates from experiment (TUAT values) , virtual experiment (ALAMEL), and Facet-3D

The maximum difference between the *r*-values predicted by ALAMEL virtual tests and the experimental ones is around 0.078; and between the Facet-3D approximation and the experiments it is around 0.064 (Figure 32(b)). The experimental normalized tensile yield stress values with a minimum at 45° is not predicted well by ALAMEL and Facet (Figure 32(a)). It needs to be taken into account that the yield stress anisotropy is not an exclusive function of the crystallographic texture, but may also be affected by spatial anisotropy of other microstructural elements, such as the morphology of grains and/or particles and the anisotropic distribution of particles. The ALAMEL yield surface (and the Facet approximation) is more rounded than the experimental one, with yield stresses that are up to 7% larger than the experimental values (Figure 32(c)). Whereas the ALAMEL normals to the yield surface pass through the experimental ones, the Facet-3D approximation shows deviations up to 14.5° (Figure 32(d)). Together with the previously mentioned computational efficiency, the resulting accuracy in reproducing the anisotropic plastic material behaviour makes the combination of ALAMEL and Facet highly suitable for multi-scale analysis of metal forming processes. A hierarchic framework for such a multi-scale analysis including full-field calculations of the evolution of texture and the associated anisotropy is described in [Gaw2013].

7.1.2.2 Caz2018polycrys

It is to be noted that the polycrystalline model Caz2018polycrys involves seven independent parameters which are associated with the description of the plastic behaviour of the crystals, namely the four independent parameters of the cubic Cazacu single-crystal law [Caz2018a], called here Caz2018singlecrys, which describes the yielding behaviour and respectively the three parameters associated with isotropic hardening (see Section 6.2.2). Since the determination of these parameters is done based on macroscopic plastic properties, only an inverse method using results of polycrystalline

simulations and macroscopic mechanical test data can be used for identification. The multi-step identification procedure used is outlined in the following. Given that this procedure does not require a very large number of FE simulations, the proposed approach enables a rapid/time efficient determination of the model parameters. While the computational approach was presented in Section 6.2.2, here we recall that in the FE simulations, a polycrystalline aggregate is associated with each FE integration point. The FE code imposes the computed macroscopic velocity gradient on the polycrystal. The orientation and the hardening of the individual grains depending on the deformation history of the element are updated, and the homogenization formula (Eq. (33)) predicts the macroscopic stress for use in the solution of the continuum equilibrium equations. The advantage of this approach is that it accurately accounts for material anisotropy and its evolution with texture development.

In general, the initial guess values of anisotropy coefficients (Lankford coefficient) are taken equal to unity (i.e. equal to the isotropic values). However, as within 30 degrees misorientation, the benchmark AA 6016-T4 material has almost 52% of the grains along the cube component (see Table 2); the first step of the applied identification procedure consists in considering that only the cube component is present in the texture, i.e. all the grains are oriented along the <100> directions. Each constituent crystal has the same response under the applied loadings, so the polycrystalline response is the same as the response of each single crystal. Only under this assumption that 100% of the grains have the [100] orientation, one can use a least square fit of the parameters of the cubic single crystal law of Eqs. (28-30) to predict mechanical data in uniaxial and biaxial tension, by comparison with the experimental results reported by UA and TUAT (see Section 2.2.1 and 2.2.2). The identified parameters by REEF of Eqs. (28-30) of this first step are defined in Table 15, line 1. With the assumption of ideal cube orientation [100], the variation obtained for the yield stress and r-values with respect to the angle from RD is given in Figure 33(a)-(b) while Figure 33(c) shows the projection of the yield surface in the biaxial plane $\left(\sigma_{RD}, \sigma_{TD}\right)$.

(a)   (b)

(c)

130
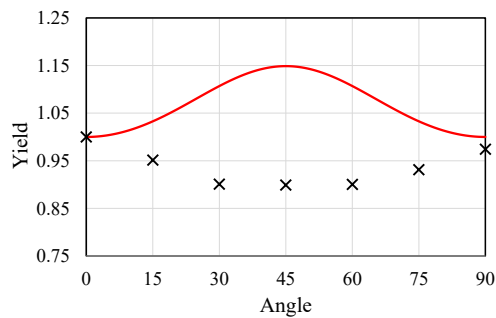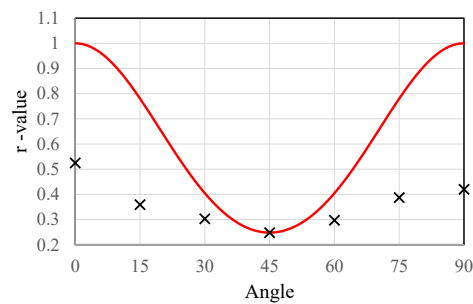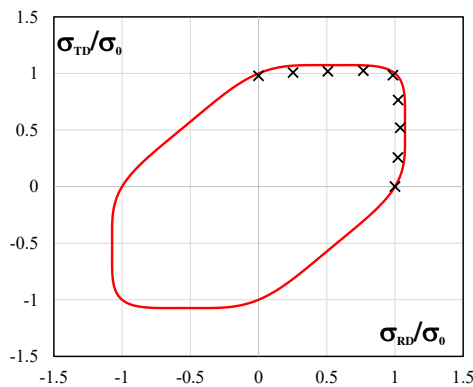
Figure 33 Predicted anisotropy for the AA 6016-T4 alloy assuming ideal cube orientation [100] using Eq. (28-30) (parameters values Table 15-line 1): (a) Uniaxial tensile flow stresses; (b) r-values; (c) Predicted yield surface section in the biaxial plane $(\sigma_{RD}, \sigma_{TD})$ (no shear). Data from UA (uniaxial data) and TUAT (biaxial data) are represented by cross symbols. All stresses are normalized by the yield stress along the rolling direction, σ_0

It is worth emphasizing that the assumption that all the grains have the [100] orientation implies that $r_0 = r_{90} = 1$. Thus, for the AA 6016-T4 material which has an average r_0= 0.525 and r_{90} =0.429 (see Table 4, results UA 2020), the assumption of ideal cube texture is only justifiable for determining an initial guess of the parameters. In the second step of the identification procedure, we use 250 grains to represent the texture of the AA 6016-T4 material (see Section 7.1.1.2). Specifically, we determine the model parameters by numerical minimization of an error function of the form:

$$ E = \sum_{k=1}^{7} \left[\frac{r_k^{\text{th}}}{r_k^{\text{exp}}} - 1 \right]^2 \tag{47} $$

In the above equation, k represents the number of available experimental r-ratios (k=7; data from UA) while the superscript indicates whether the corresponding value is experimental or theoretical. The theoretical r-value at an angle θ from the RD of the polycrystalline material (a single aggregate of 250 grains) is calculated as:

$$ r_\theta = -\frac{D_{xx}^p \sin^2\theta - D_{xy}^p \sin(2\theta) + D_{yy}^p \cos^2\theta}{D_{xx}^p + D_{yy}^p} \tag{48} $$

with the plastic strain-rate $\mathbf{D}^p$ expressed in the loading frame, given as

$$ \mathbf{D}^p = \frac{\dot{\lambda}}{N} \sum_{i=1}^{N} \mathbf{R}_i \frac{\partial \bar{\sigma}_{grain}^i \left(\mathbf{R}_i^T \boldsymbol{\sigma} \mathbf{R}_i \right)}{\partial \left(\mathbf{R}_i^T \boldsymbol{\sigma} \mathbf{R}_i \right)} \mathbf{R}_i^T \tag{49} $$

where $\dot{\lambda}$ is the plastic multiplier, $\boldsymbol{\sigma}$ denotes the applied stress tensor, N is the number of grains considered in the input texture, $\bar{\sigma}_{grain}^i$ is the effective stress of grain i according to Eq. (30) and $\mathbf{R}_i$ is the transformation matrix for passage from the crystal axes of grain i to the loading frame axes.

Note that in this second step of the identification procedure in the determination of the set of parameters, we took into consideration the main sources of the anisotropic response of the AA 6016-T4 material under uniaxial tension (measured Lankford coefficient and initial texture).

Finally, the last step of the identification procedure consists in fine-tuning the parameters determined in the previous step, to further improve the predictions of the anisotropy in r-values for this material. For this purpose, only a few FE simulations using the polycrystalline model described by Eqs. (32)-(33) in Section 6.2.2 were performed on uniaxial tension tests at θ =0°, 15°, 30°, 45°, 60°, 75° and 90°. In the FE simulations of any uniaxial tension test, the specimen is meshed with 570 ABAQUS C3D8R reduced integration elements (see Figure 34 for the FE mesh). As previously mentioned, a polycrystalline aggregate is associated with each FE integration point. The numerical r-value is extracted from the slope of the curve ε_w vs. ε_t, where $\varepsilon_w = \ln(w/w_0)$ and $\varepsilon_t = \ln(t/t_0)$ with w_0 and w being respectively the initial and current width, and t_0 and t being the initial and current thickness.
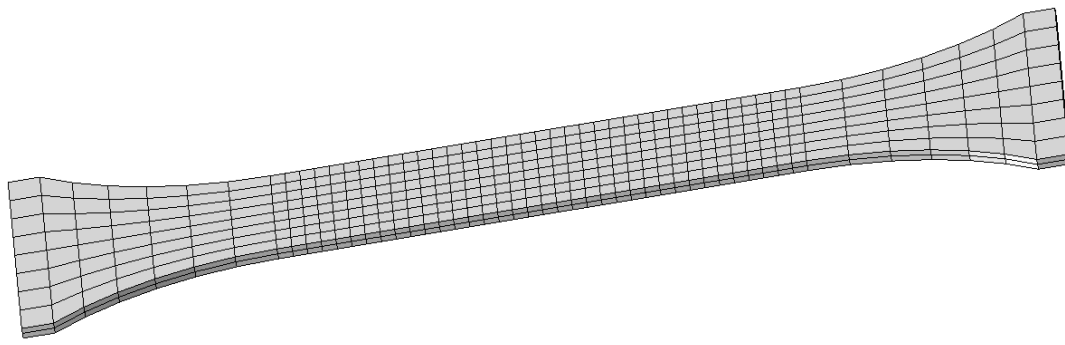
Figure 34 FE mesh used in the simulations of the uniaxial tension tests performed with the FE polycrystalline model

The final values of the identified parameters for the AA 6016-T4 polycrystalline material are provided in Table 15, line 2, and were further used to conduct the FE simulations with Caz2018polycrys model of cup drawing presented in Section 8. Figure 35(a) and (b) show the comparisons of the FE polycrystalline simulation results (circles) with the experimental data for the uniaxial yield stresses and *r*-values (cross) for the seven orientations in the plane of the sheet. The FE predicted yield surface cross-section in the RD, TD plane is shown in Figure 35(c).
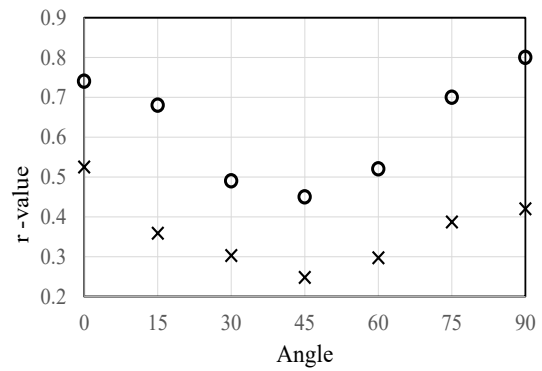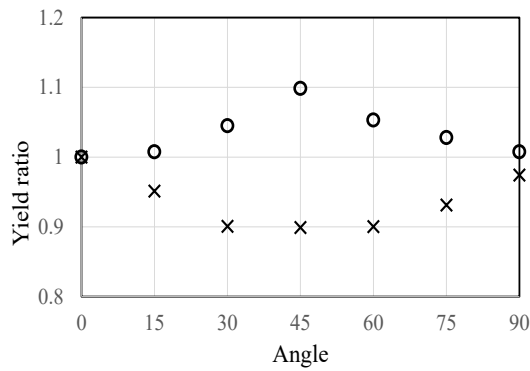
(a)

(b)
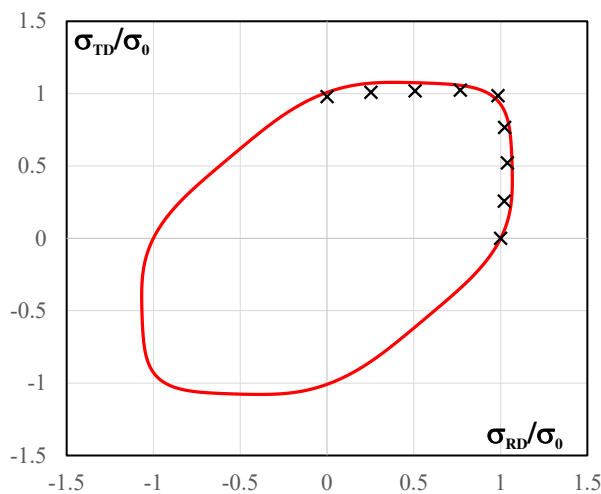
(c)

Figure 35 Predicted anisotropy using the polycrystalline FE model taking into account the texture of the AA 6016-T4 alloy (parameters values Table 15-line 2): (a) Uniaxial tensile flow stresses; (b) r-values; (c) Predicted yield

surface section in the biaxial plane $(\sigma_{RD}, \sigma_{TD})$ (no shear). Data (UA) are represented by cross symbols. All stresses are normalized by the yield stress along the rolling direction, σ_0

Table 15 REEF identified parameters for Caz2018singlecrys (Eqs.(28-30) of Section 6.2.2) at different steps of the identification method using the UA tensile test results (see Section 2.2.1)

Assumption	m_1	m_2	n_1	n_3	n_4	c
Only cube texture component	0.386	0.256	0.239	0.159	0.129	2.4
Polycrystal model (for minimization see (Eq. (47))	0.355	0.0973	0.341	0.103	0.0571	0.8

Finally, for Caz2018polycrys an isotropic Swift hardening law (see Eq. (3)) was considered at crystal plasticity level, the respective parameters being determined from the experimental stress-strain curve in uniaxial tension along θ =0° reported by UA (see Table 16).

Table 16 Parameters of the hardening law at crystal plasticity level in the polycrystalline model Caz2018polycrys

Hardening model	Set of parameters (REEF identification)		
	K_0 (MPa)	ε_0 (-)	n (-)
Swift	277	0.0089	0.285

We conclude the verification of the validity of the parametrization of the Caz2018polycrys model with a comparison between experimental stress-strain curves and polycrystalline predictions for uniaxial tension at RD and TD in

Figure **36**. Furthermore, illustrative examples of the predictive capabilities of the new FE polycrystalline model is done through comparison with shear tests at RD and 45° to RD (data obtained at UA) in Figure 37. It is worth noting that shear tests data were not used in the identification procedure and as such, the results serve for validation of the polycrystalline model.

(a)   (b)
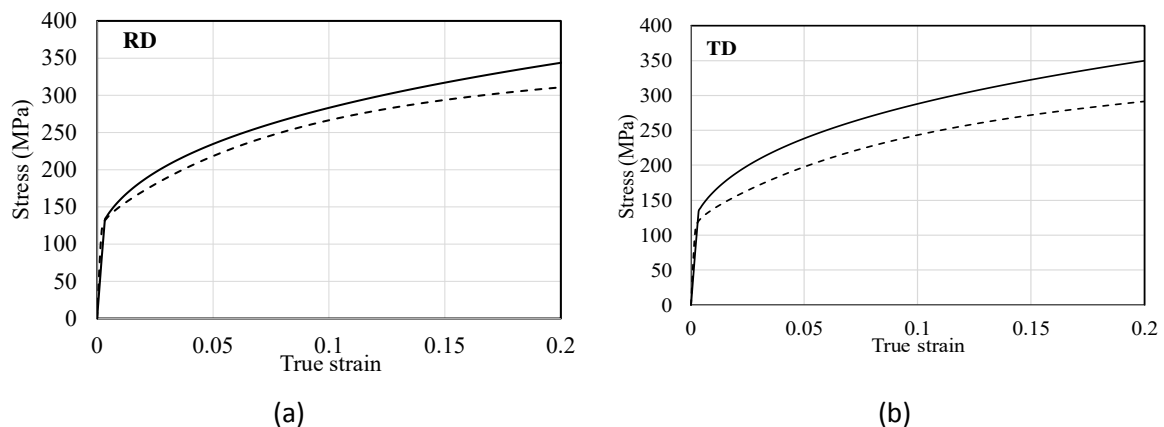
Figure 36 Comparison between experimental stress-strain curves (dashed line) in uniaxial tension and FE predictions obtained with the polycrystalline model (Eqs. (32)-(33), data set Table 15-line 2 and Table 16): (a) RD direction; (b) TD direction
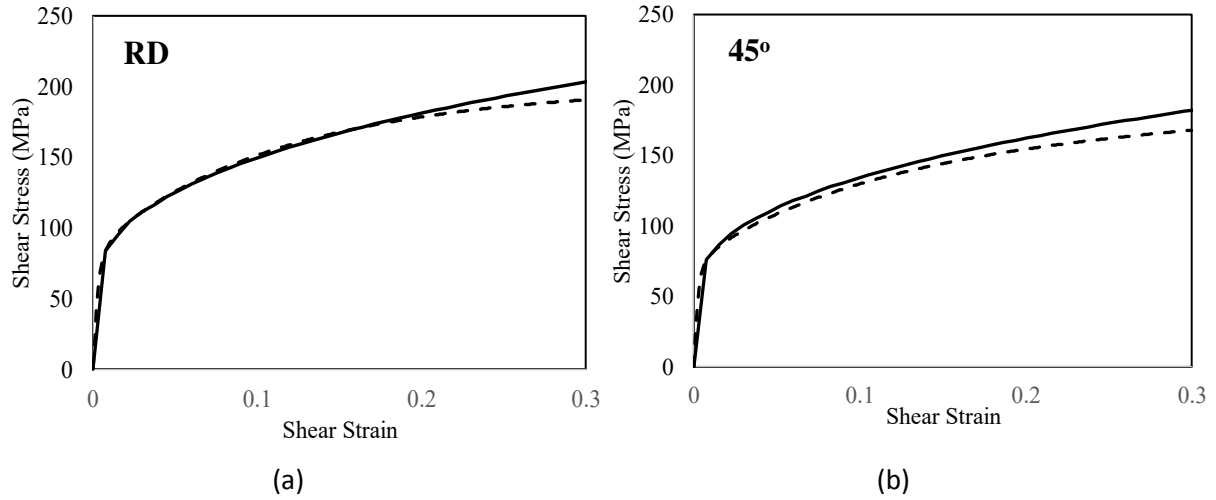
Figure 37 Comparison between experimental stress-strain curves (dashed line) in shear and FE predictions obtained with the polycrystalline model (Eqs. (32)-(33), data set Table 15-line 2 and Table 16): (a) RD direction; (b) at 45° to the RD direction

7.1.2.3 MINTY law

In Minty law, a type of interpolation law , the anisotropy of the material behaviour is solely determined from its texture description, as it uses a Taylor assumption where a set of crystals at one integration point has a single macroscopic strain value. For the present study, the texture was represented by the 1000 crystal orientations extracted from EBSD measurements as explained in Section 7.1.1.3.

The isotropic elastic behaviour is characterized by Young's modulus (E=70 000 MPa) and Poisson's ratio 0.33. As mentioned in Section 6.2.3, the isotropic hardening is modelled by a Swift type equation. However, the classical formulation of Swift hardening expressed as the yield stress as a function of the equivalent plastic strain (Eq. (3)) must be converted in the critical resolved shear stress τ vs. the accumulated polycrystalline induced slip Γ (Eq. (35)). As detailed in Eq. (50), adapted from [Duc2003], this conversion requires the computation of Taylor's factor $\overline{M}$ whose value is 2.8054 for the studied material.

$$K = \frac{K_0}{\overline{M}^{n+1}}$$
$$\Gamma^0 = \varepsilon_0 \cdot \overline{M}$$

(50)

In this equation n is unchanged compared with Eq. (35). Finally, the parameters involved in the isotropic Swift hardening law (see Eq. (3)) were determined by the benchmark committee, based on the experimental stress-strain curve in uniaxial tension along RD, and Eq. (50) allows to identify the hardening at the crystal level (see Table 17).

Table 17 Set of parameters for hardening Minty law

Hardening model	Set of parameters		
	K_0 (MPa)	ε_0 (-)	n (-)
Macroscopic Swift law Eq. (3) from UA	498.8	0.0089	0.285
	K (MPa)	Γ^0 (-)	n (-)
At the crystal plasticity level Eq. (35)	132.51	0.025	0.285

130

An important numerical parameter in the stress-strain interpolation of Minty law is the size of the interpolation domain, expressed as the angular gap between adjacent stress nodes in 5-D space (see Section 6.2.3). A small domain permits an accurate interpolation of the stress; however, it requires frequent updates of the domain leading to a larger computation time. Conversely, a large domain will remain valid longer, but is expected to provide less accuracy. As shown in [Hab2004a], an angular size of 5° is a good compromise between accuracy and computation time; it is the value used in this study.

Figure 38 presents the mechanical behaviour of AA 6016-T4 aluminium alloy as predicted by Minty law. As already observed in Figure 30, the Lankford coefficient curve (Figure 38(b)) has a similar shape as the experimental results, but with an overestimated amplitude. Conversely, the yield strength curve (Figure 38(a)) has an opposite trend to the experimental results with a low amplitude.

(a)   (b)
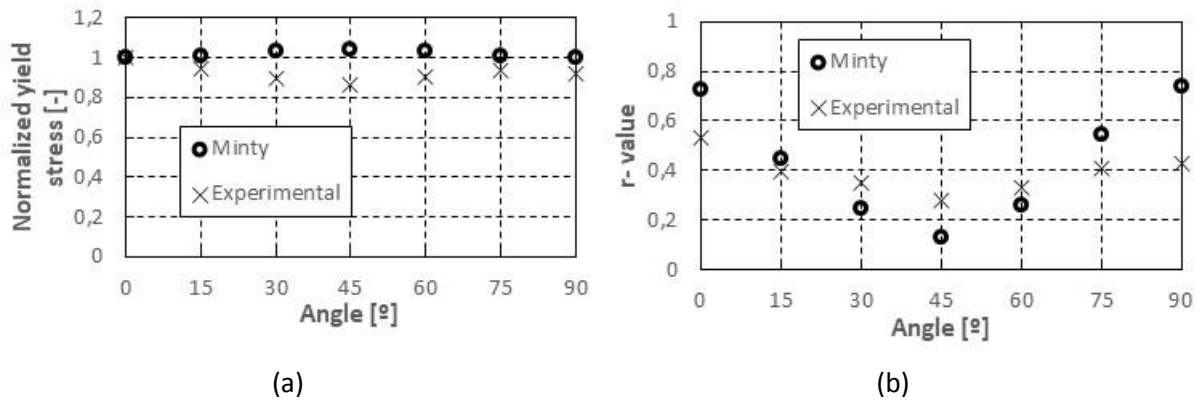
Figure 38 Comparison of normalized yield stress (a) and Lankford coefficients (b) predicted by Minty with experimental values obtained from tensile tests of UA

7.1.2.4   RVE Damask Simulations

(a)   (b)
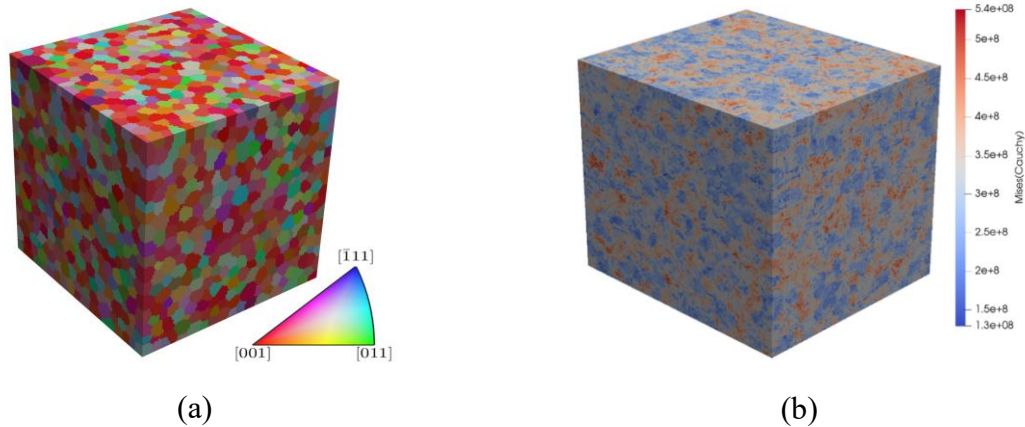
Figure 39 (a) 3D Representative Volume Element (RVE) with 7509 equiaxial grains generated by a Voronoi tessellation; (b) Distribution of equivalent Mises stress (Pa) of RVE in uniaxial tension simulation at RD direction for a macroscopic strain of 0.1

Figure 39 shows the established periodic cubic RVE that consists of 7509 equiaxial grains, with a high grid resolution of 120×120×120 Fourier points. This RVE was used to perform the virtual experiments [Liu2020], in the full-field crystal plasticity modelling kit DAMASK—an open-source spectral method solver [Rot2019], as described in Section 6.2.4. Twelve slip systems in FCC crystal structure including $<01\bar{1}>\{111\}$ slip system and its all symmetrically equivalent ones were taken into account in the

polycrystal modelling. The phenomenological power law was used to describe the hardening behaviour. The hardening parameters h_0, τ_0, τ_s, and a for the slip system described in Section 6.2.4 were determined by inverse modelling, focused on sets of stress-strain curves obtained from physical uniaxial tensile, pure shear, and plane-strain tensile tests in RD. The value of strain rate sensitivity, m=0.02 resulted in good agreement between the experimental (of TUAT 2018) and predicted uniaxial stress-strain curve and it was adopted in this work. The slip system references shear rate $\dot{\gamma}^0$, latent hardening parameter q and the cubic crystal elastic constants C_{11}, C_{12}, and C_{44} are typical values for cold-rolled FCC aluminium alloy [Liu2020]. The parameters of the crystal plasticity model are summarized in Table 18. By Damask simulations, the mechanical responding of the AA 6016-T4 RVE during the virtual uniaxial tensile tests at RD direction can be obtained and is illustrated in Figure 40.

Table 18 Damask crystal plasticity model parameters for the AA 6016-T4 aluminium sheet

C_{11}	C_{12}	C_{44}	$\dot{\gamma}_0$	h_0	τ_0	τ_s	m	a	q
82 GPa	62 GPa	29 GPa	$0.001 s^{-1}$	1140 MPa	48 MPa	140 MPa	0.02	2.0	1.4

Using the above RVE and Damask simulations, virtual experiments were performed for tensile and biaxial loading conditions. Figure 40(a) and (b), respectively, show the yield stresses and r-values of virtual and physical uniaxial tensile tests at 0, 15, 30, 45, 60, 75, and 90 degree with respect to RD at the nominal strain of 10%. Both virtual and physical experiments indicate that the r-value is relatively higher at 0 and 90 degree but the lowest at 45 degree. In addition, the lowest normalized yield stress is also observed at 45 degree which is about 0.90 and 0.95 obtained from physical and virtual experiments, respectively.

Figure 41(a) and (b) shows biaxial yield surfaces and directions of plastic strain rate, respectively, obtained from CP modelling and experiments. The plots show a good agreement between the CP predictions and experiment results.

(a)   (b)
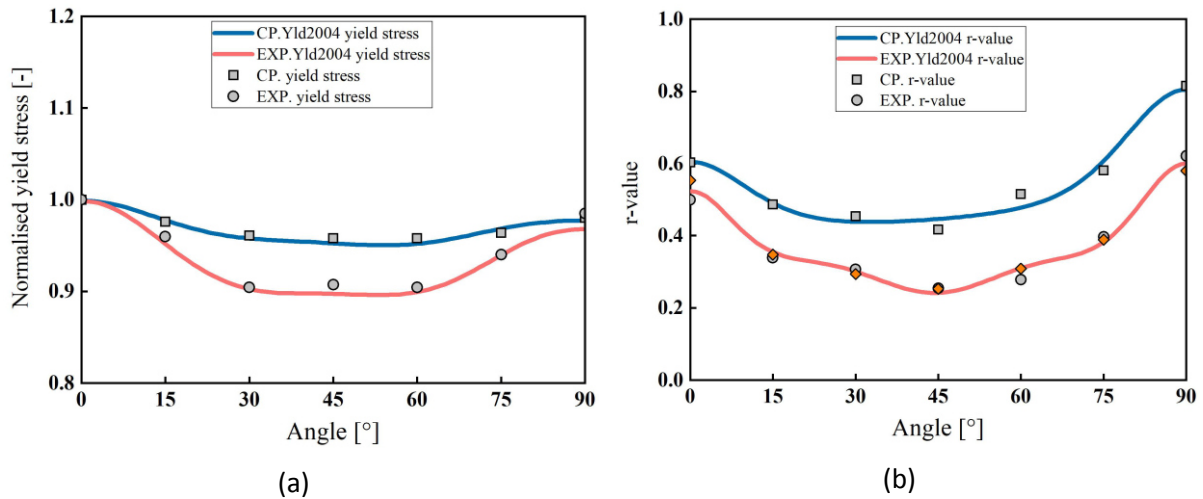
Figure 40 Comparison of mechanical anisotropy of AA 6016-T4 aluminium alloy sheet obtained from experiments, Damask simulations (CP) and Yld2004-18 yield function identified either on physical experiments or from CP results: (a) The directional normalized yield stresses; (b) r-values
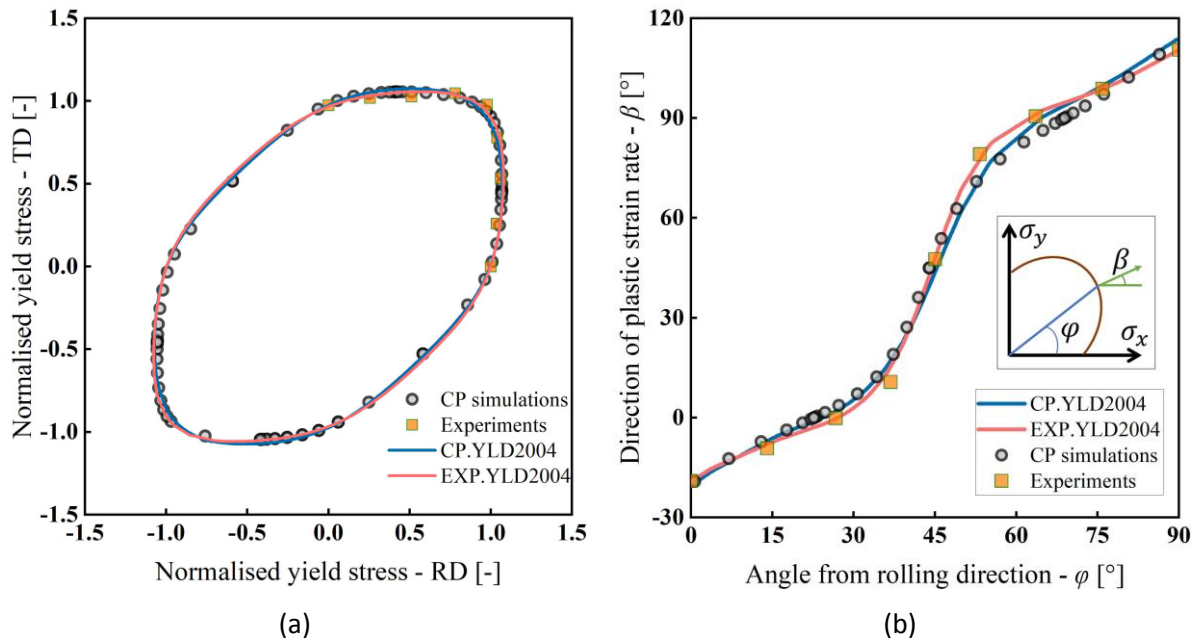
Figure 41 Measured experimental points, CP modelling results and Yld2004-18p yield function cut as well as plastic strain directions: (a) Yield surface of biaxial stress state in RD-TD plane; (b) Direction of plastic strain rate in biaxial tension

Note that both experimental and CP predicted uniaxial and biaxial material sampling points were used to calibrate the material parameters of Yld2004-18p yield function. The Matlab own least-squares function so-called 'lsqnonlin' was used to identify the parameters of Yld2001-18p. The identified parameters values are given in Section 7.2.6 with the other phenomenological identifications of this yield locus to allow easy comparison of anisotropic parameter values (see Table 28).

7.1.2.5   VPSC model

The simulations of the cup drawing test are performed considering three distinct phases within the set of crystals, as explained in Section 7.1.1.5. The model phases correspond to the same material phase and are defined based on grain size. For each model phase associated to a different grain size, different crystallographic textures and grain shapes are considered. The same strain rate sensitivity exponent and hardening parameters are employed for the three phases, but the τ_0 parameter is modified according to the Hall-Petch relationship (i.e. an additional term is added, proportional to the inverse of the grain diameter square root and a constant k_{HP}). In total, six parameters are fitted: the strain rate sensitivity exponent n_s, the Voce law parameters τ_0 (for the average grain size), τ_1, θ_0 and θ_1, (see Eq. (43)) and the Hall-Petch constant k_{HP}. The Levenberg-Marquadt algorithm is used for the fitting [Lev1944]. Having an initial estimation, a gradient value is calculated from simulations in which a small perturbation is applied to each parameter, and this gradient is then used to find an improved solution. The goal is to reproduce the uniform strain region of the tensile experiments in different directions described in Section 2.2.1 (TUAT tests in 0°, 15°, 30°, 45°, 60°, 70° and 90° directions). After several iterations, the method converges to the parameters shown in Table 19. Figure 42 compares the experimental and simulation results.

(a)

(b)
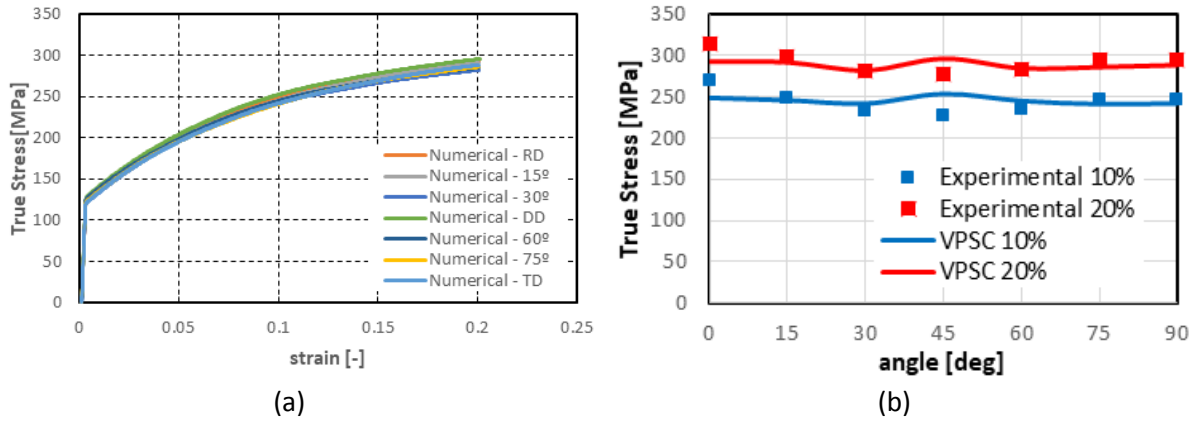
Figure 42 (a) Results from simulations used for fitting the VPSC model parameters; (b) Comparison of the model predictions (continuous line) with experimental values (squares) at specific strain levels

Table 19 VPSC fitted parameters

n_s $(-)$	τ_0 (MPa)	τ_1 (MPa)	θ_0 $(-)$	θ_1 $(-)$	k_{HP} (MPa$\sqrt{m}$)
44	54.2	33.2	171.0	0.12	14.0

Once the parameters are fitted, the VPSC model and its data set are validated using the monotonic and reverse shear tests of Section 2.2.3 not exploited in the identification method, as shown in Figure 43.

(a)

(b)
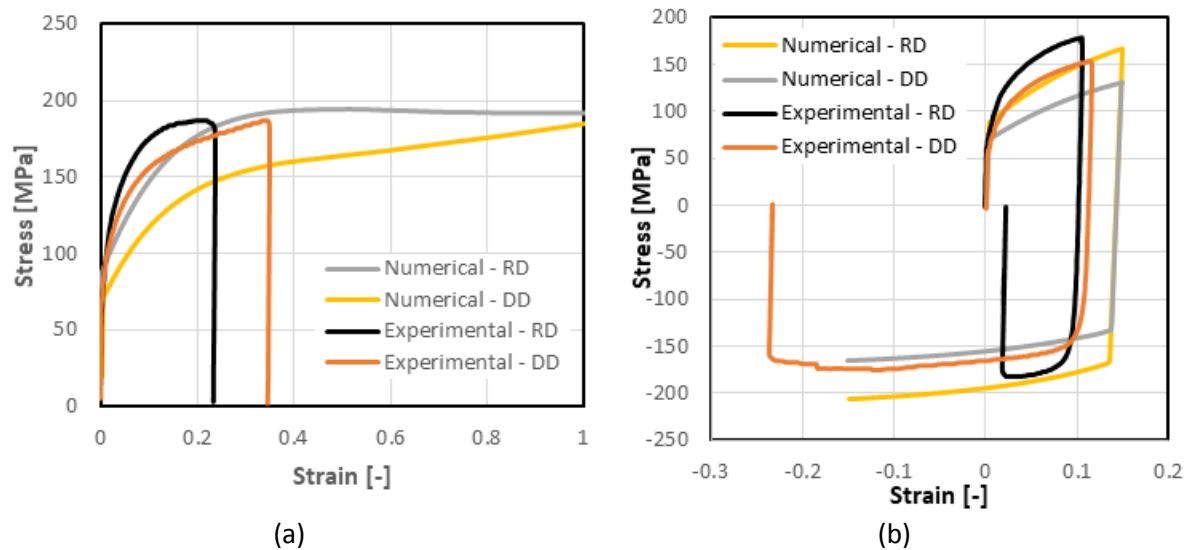
Figure 43 VPSC simulations compared with the: (a) monotonic and (b) reversed shear tests of ULiege, used for the validation of the model

Note that virtual uniaxial and biaxial tensile experiments performed by means of VPSC are used to calibrate the phenomenological yield criteria Yld2000-2d. From tensile tests in the 0°, 45° and 90° directions, the respective yield strengths σ_0, σ_{45}, σ_{90} and Lankford coefficients r_0, r_{45}, r_{90} are calculated. From an equibiaxial tension test, the yield strength σ_b and Lankford coefficient r_b are calculated. All values are computed at a fixed level of effective plastic strain of 10%. Figure 44 presents the comparison of experimental (UA) and simulated (VPSC) r-values.
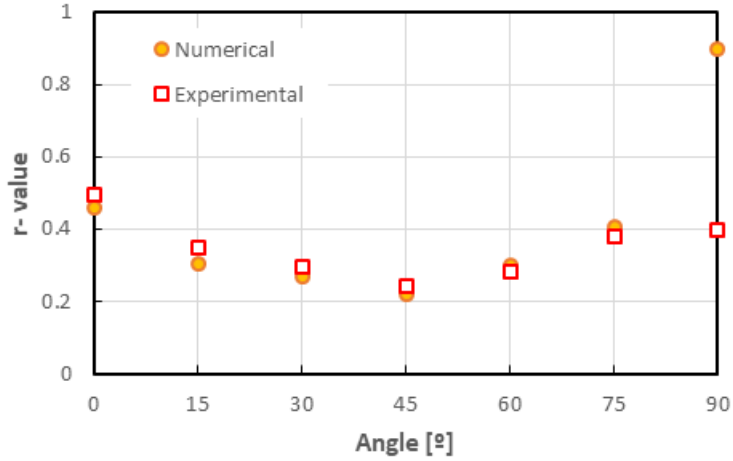
Figure 44 Comparison of experimental (UA) and simulated (VPSC) *r*-values

Using the VPSC yield strengths and Lankford coefficients, the Yld2000-2d model parameters α_i (i=1-8) are identified following the procedure described in [Kuw2017, Cop2019]. The identification of the anisotropic parameters is performed giving more weight to the *r*-values rather than to the stress amplitudes. This choice is made to enhance the capability of the model to predict the experimental earing profile. The identification of the exponent M is performed by a virtual work contour, the value 6.11 will be used. Data points in the $\sigma_x - \sigma_y$ principal plane are obtained carrying out virtual biaxial experiments with different, linear stress paths. The VPSC data points used are presented in Figure 45(a). The values are calculated at the moment when the same level of plastic work per unit volume is applied by σ_x and σ_y as in the tensile experiment along the RD at 10% of effective plastic strain. M is found minimizing the root mean square error δ_d between the virtual work contour and the numerical one predicted by Yld2000-2d [Kuw2017, Cop2019]:

$$\delta_d = \sqrt{\frac{\sum_i^N \left(d_i'(\varphi_i) - d_i(\varphi_i) \right)^2}{N}} \tag{51}$$

where d_i and d_i' are the distances between the origin of the principal stress space and the i-th VPSC data point and YLD2000-2d yield locus, respectively. The slope of the linear stress path is identified by the angle φ_i. N (=9) is the total number of data points considered for the minimization procedure. The following stress paths are considered $\sigma_x : \sigma_y = 1:0, 4:1, 2:1, 4:3, 1:1, 3:4, 1:2, 1:4, 0:1$. Figure 45(b) gives a schematic representation of the methodology used for the calculation of δ_d.

(a)

(b)

130
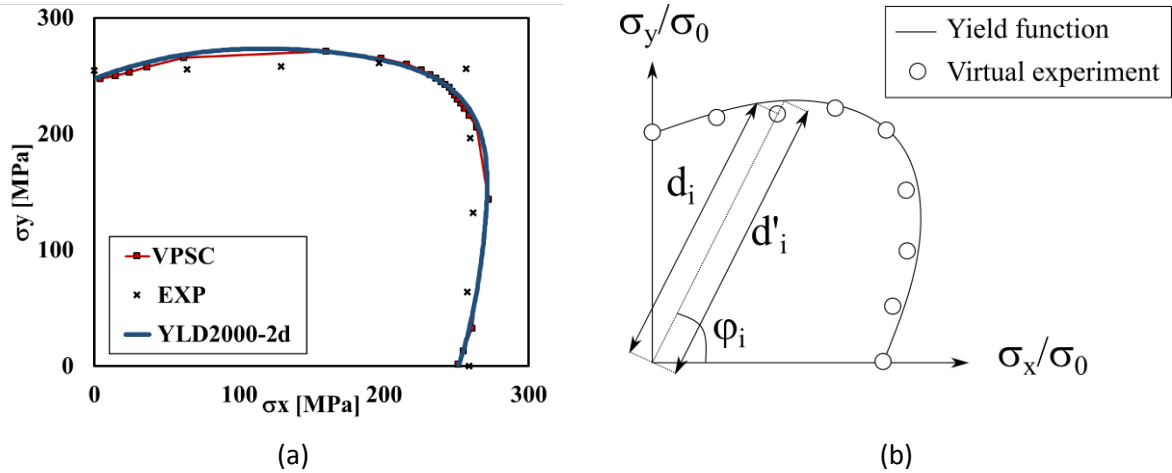
Figure 45 Identification method and validation of VPSC and Yld2000-2d predictions vs. experiments: (a) Experimental, virtual and predicted work contours at 10% of effective plastic strain and (b) Scheme of calibration procedure for M

The model constants obtained from the identification procedure of Yld2000-2d are summarized in Table 27 of section 7.2.6 to allow an easy comparison of the yield loci identified by classical tests or virtual ones. Finally, the Voce law parameters obtained by fitting the hardening curve for the tensile experiment performed along RD by UA are provided in Section 7.3 (see Table 32).

7.1.2.6 Caz2018singlecrys

If the texture is assumed to be a pure cube texture (simplified assumption based on Table 2), the Cazacu single crystal yield criterion could directly be applied. It was an interesting test performed by POSTECH team. The yield locus coefficients were determined with an optimization algorithm based on the Nelder-Mead Simplex algorithm, using the normalized flow stresses for different stress states obtained from UA test data (tensile and shear). An additional constraint about mainly plane stress assumption, explains that n_4 parameter can be seen as irrelevant. The normalized flow stresses are taken at 15 MPa plastic work per unit volume corresponding to 0.07 plastic strain in the RD tensile test (Figure 46(a)). Table 20 gives the identified coefficients for Cazacu single crystal yield criterion. The predicted yield locus (Figure 46(b)), normalized flow stress (Figure 47(a)) and r-values (Figure 47(b)) show considerable deviating from the experimental values, illustrating that the assumptions are too strong: the polycrystalline behaviour should take into account other components than the cube one and the identification method should include out of plane experiments allowing a correct n_4 calibration. The effect on deep drawing simulations is presented in Section 8.

Table 20 POSTECH identified set of parameters of single crystal yield locus Caz2018singlecrys (see Eqs. (28-30) of Section 6.2.2)

Assumption	m_1	m_2	n_1	n_3	n_4	c
Pure cube texture component	1	0.489	1.5	0.1	irrelevant	2.568

(a)   (b)
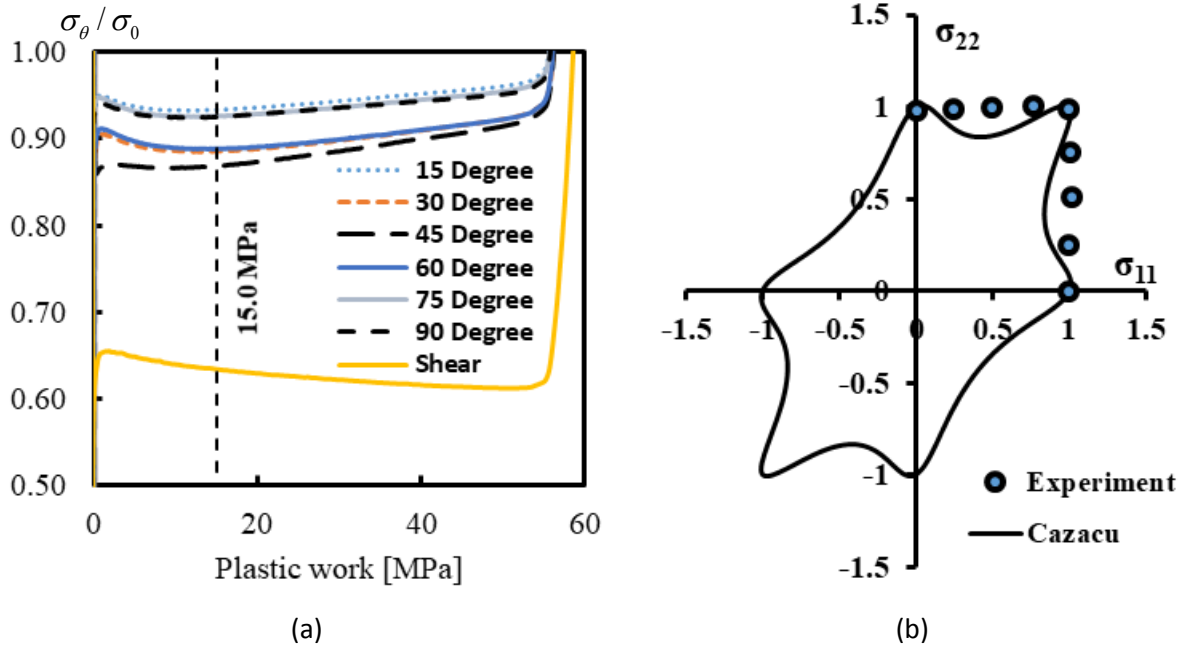
Figure 46 (a) Plastic work per unit volume vs. normalized flow stress in tests along different directions and in shear test in RD direction (UA tests) and (b) predicted Cazacu Single Crystal shape with the data set of Table 20 and experimental yield locus (UA and TUAT)

130

Note that the convexity issue of the yield locus for this set of parameter values is not a surprise. It happens for this function if c and n_1 are high, and n_3 is low. The same issue can be observed in Drucker's isotropic yield condition where a high coefficient c is assumed for the factor of the third stress invariant J_3 square. If an implicit FE solver is used for the FE simulations of Section 8, the identified yield locus of Figure 46(b) will be an issue, which explains why POSTECH has chosen an FE explicit solver.
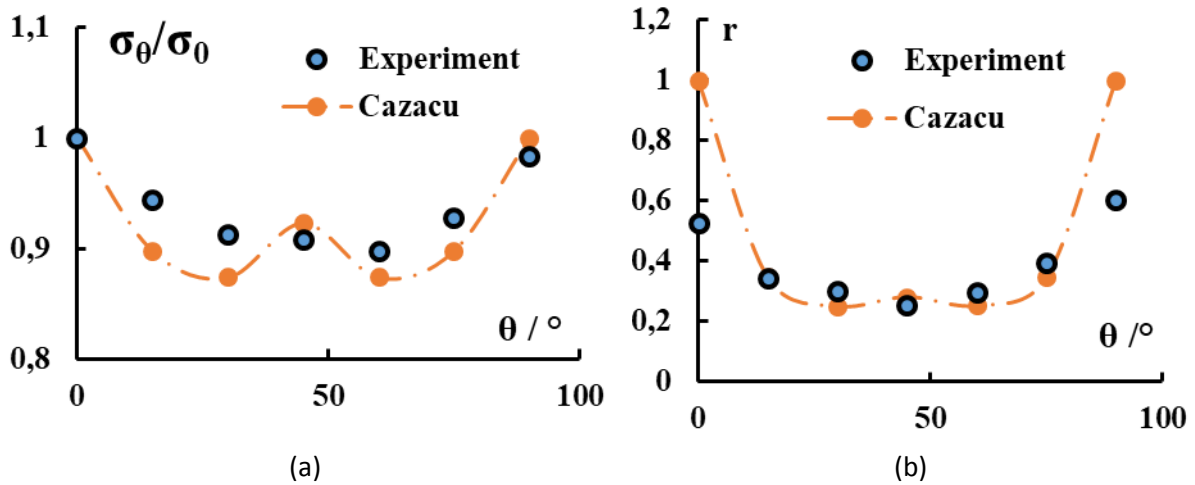
Figure 47 Comparison of (a) normalized flow stress and (b) r-values measured by UA tensile tests or predicted by Cazacu single crystal yield criterion identified by POSTECH

7.2 Parameter identification, validation of phenomenological models

7.2.1 Hill48 yield locus (associated law)

The determination of the anisotropic parameters associated to Hill48 model can be done analytically using as input either yield stresses corresponding to uniaxial loading along 0, 45, 90 orientations and equibiaxial yield stress or Lankford coefficients for 0, 45, 90 directions in the plane of the sheet. If the equivalent stress according to Hill48 yield criterion is given as in Eq. (12) of Section 6.1.2, the theoretical Hill stress is imposed to coincide with the yield stress along RD. If the assumption of associated flow rule is considered, the respective analytical formulae are given in Table 21 (see for example [Caz2019, Kaw1996]).

Table 21 Analytical determination of the anisotropy parameters in Hill48 model with effective stress given by Eq. (12)

Method	Input parameters	Equations	
Stress based	$\sigma_0, \sigma_{45}, \sigma_{90}, \sigma_b$	$2F = \frac{\sigma_0^2}{\sigma_{90}^2} - 1 + \frac{\sigma_0^2}{\sigma_b^2}$ $\quad 2H = 1 + \frac{\sigma_0^2}{\sigma_{90}^2} - \frac{\sigma_0^2}{\sigma_b^2}$	$2G = 1 - \frac{\sigma_0^2}{\sigma_{90}^2} + \frac{\sigma_0^2}{\sigma_b^2}$ $\quad 2N = \frac{4 \cdot \sigma_0^2}{\sigma_{45}^2} - \frac{\sigma_0^2}{\sigma_b^2}$
r-value based	r_0, r_{45}, r_{90}	$F = \frac{r_0}{r_{90} \cdot (1 + r_0)}$ $\quad H = \frac{r_0}{1 + r_0}$	$G = \frac{1}{1 + r_0}$ $\quad N = \frac{(r_0 + r_{90}) \cdot (r_{45} + 0.5)}{r_{90} \cdot (1 + r_0)}$

130

The shear coefficients in the planes RD-ND, TD-ND (where ND is the thickness direction) have analytical formulae in terms of the yield stresses in shear in these planes (see [Hill1948]). Due to the difficulty of measuring the through thickness shear, generally it is assumed that L=M=N (same shear behaviour in the planes of orthotropy). If for isotropic behaviour, this assumption is correct, for an anisotropic sheet severely deformed, like in incremental forming for instance, this assumption could be inadequate.

Depending on the input data used to identify the Hill48 yield locus, the predictions using Hill criterion are markedly different (for examples see [Kha2015, Caz2021]). Another methodology is to determine the parameters by numerical methods using both the experimental r-values and yield stresses in more than 3 orientations in conjunction with an objective function of the form

$$E = \sum_i \eta_i \left[\frac{(\sigma_\theta)_i^{\text{th}}}{(\sigma_\theta)_i^{\text{exp}}} - 1 \right]^2 + \sum_k \eta_k \left[\frac{r_k^{\text{th}}}{r_k^{\text{exp}}} - 1 \right]^2 \tag{52}$$

In the above equation, i and k represents respectively the number of available experimental normalized tensile stresses and r-ratios while the superscript indicates whether the corresponding value is experimental or predicted. As pointed in Section 7.2.7, the input experimental yield stresses can be extended such as to take into account shear and biaxial elastic limits. Most of the teams just look at one point per curve: elastic limit or yield value for a defined plastic work per unit volume or strain, while another possibility is to identify in a single optimization both hardening and yield locus shape by using the total stress-strain curves like again done in Section 7.2.7. In Eq. (52), the constants η_i and η_k are weight factors. Table 22 provides the parameter values either identified by analytical formulae or by numerical optimization based on tensile data.

Table 22 Parameters of Hill (1948) yield function obtained with different identification procedures

Hill 1948	F	G	H	N
Provided by Organizers (UCoimbra) Analytical formulae of Table 21 using r_0, r_{45}, r_{90} measured by UA	0.821	0.655	0.345	1.104
ULiege Set 1: Based on r-values at 0, 15, 30, 45, 75, 90° (UA data) η_i=0 , η_k =1 in Eq. (52)	0.756	0.669	0.330	1.119
ULiege Set 2: (used for deep drawing simulations) Based on UA tensile tests (0, 15, 30, 45, 75, 90°) and both yield stresses and r values; η_i=η_k =0.5 in Eq. (52)	0.815	0.666	0.334	1.184
ULiege Set 3: Based on yield stresses (0, 15, 30, 45, 75, 90°) η_i=1, η_k=0 in Eq. (52)	1.045	0.914	0.086	1.661

Figure 48(a) and (b) show the strong influence of the data used for the identification on the predictions of yield stresses and Lankford coefficients. Figure 48(b) serves to illustrate the reason why the identification based on Lankford coefficients is recommended for deep drawing simulations. The Lankford coefficient is representative of the sheet thinning during the forming process and if the data set identification is focused on the stress, one can generate Lankford prediction values very far from the experimental ones. Finally, the yield locus shape (Figure 49) reminds why more advanced anisotropic yield loci were defined. With Hill48 approach, one cannot model both the behaviour of uniaxial tensile tests and the biaxial states measured by TUAT.

130
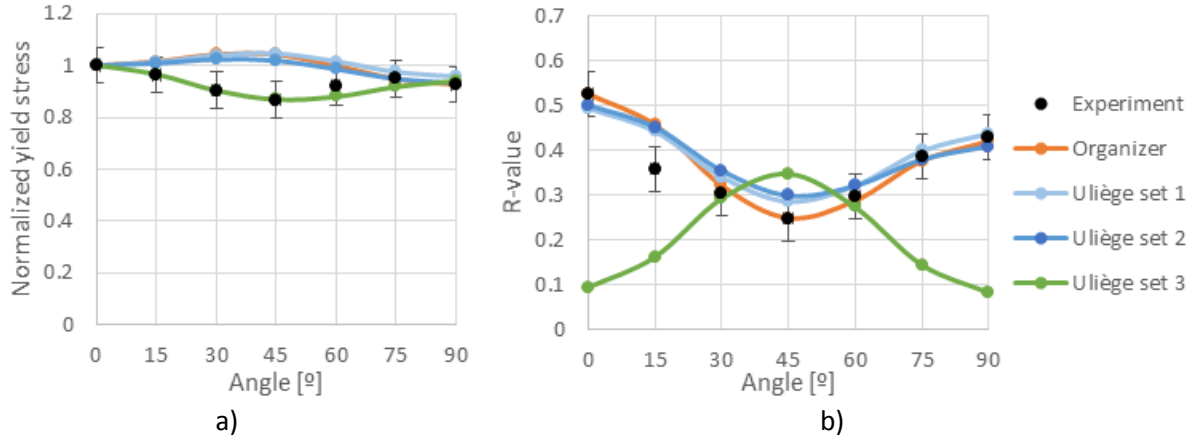
Figure 48 Experimental and predicted (a) directional normalized yield stresses, (b) *r*-values in uniaxial tensions (experimental data of UA) for chosen sets of parameters (in Table 20). Stresses are normalized by the yield stress along RD σ_0
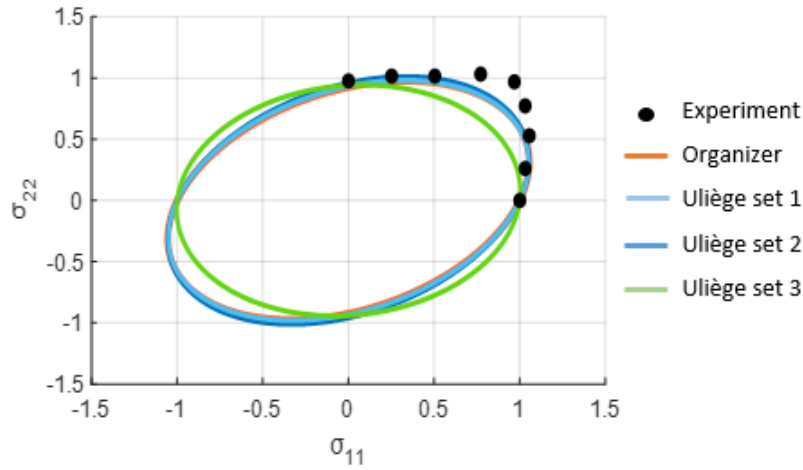
Figure 49 Hill yield locus cut in RD TD orthotropic plane stress based on different data sets (details in Table 20) and experimental points (work contour at 0.2% from TUAT). Stresses are normalized by the yield stress along RD σ_0

7.2.2   4th Order Polynomial Model (HomPol4)

In order to calibrate the anisotropic parameters of HomPol4 yield locus described by Eq. (10) in Section 6.1.1, the mechanical test data obtained by TUAT were used. The identified parameters of HomPol4 are listed in the Table 23.

Table 23 Anisotropy material parameters of HomPol4

α_1	α_2	α_3	α_4	α_5	α_6	α_7	α_8	α_9
1	-1.379	1.953	-1.608	1.071	6.865	2.966	6.899	5.790

Here, a_{1-9} are the parameters related to the anisotropy of the material. The parameters a_{1-5} are calibrated with yield stresses and *r*-values in rolling and transverse axes in uniaxial stress state, as well as biaxial yield stress [Soa2007]. Parameters a_{1-5} are determined with the equations given below:

$$a_1 = 1 \tag{53}$$

$$a_2 = -\frac{4r_0}{(1 + r_0)} \tag{54}$$

$$a_3 = \left(\frac{1}{\overline{\sigma}_b^4}\right) - (a_1 + a_2 + a_4 + a_5) \tag{55}$$

$$a_4 = -\frac{4a_5 r_{90}}{(1 + r_{90})} \tag{56}$$

$$a_5 = \frac{1}{\overline{\sigma}_{90}^4} \tag{57}$$

An optimization method was applied to determine the coefficients a_6 and a_8 with an objective function similar to Eq. (52), based on the error between predicted stress ratios and r-values and the corresponding the tensile experimental points of TUAT [Sen2021] at 15°, 30°,45°,60° and 75°. An equal weight was chosen for Lankford coefficients and yield limits. In addition, a_6 and a_8 have to satisfy the following inequalities to ensure the convexity conditions [Soa2007].

$$0 \leq a_6 \leq 6\sqrt{a_1 a_9} \tag{58}$$

$$0 \leq a_8 \leq 6\sqrt{a_5 a_9} \tag{59}$$

The parameter a_7 is calculated based on a_6 and a_8 by using following equation:

$$a_7 = \left(\frac{2}{(1+r_{45})\overline{\sigma}_{45}^4} - \frac{2}{\overline{\sigma}_b^4}\right) - (a_6 + a_8) \tag{60}$$

Regarding the convexity and the positivity measures, a_9 can be determined by:

$$a_9 = \frac{\left(\frac{2}{\overline{\sigma}_{45}}\right)^4 r_{45}}{1+r_{45}} + B_1 > 0 \tag{61}$$

where,

$$B_1 = a_1 + a_2 + a_3 + a_4 + a_5 = \left(\frac{1}{\overline{\sigma}_b}\right)^4 \tag{62}$$

Here, r_{45} should also ensure the following condition [Soa2007]:

$$\frac{-[5\left(2\frac{\overline{\sigma}_b}{\overline{\sigma}_{45}}\right)^4+8]+\left(\frac{3}{2}\right)\left(2\frac{\overline{\sigma}_b}{\overline{\sigma}_{45}}\right)^4[\left(2\frac{\overline{\sigma}_b}{\overline{\sigma}_{45}}\right)^4+8]^{1/2}}{[9\left(2\frac{\overline{\sigma}_b}{\overline{\sigma}_{45}}\right)^4+8]} \leq r_{45} \leq \frac{\left(2\frac{\overline{\sigma}_b}{\overline{\sigma}_{45}}\right)^4}{2} - 1 \tag{63}$$

The r-values and the initial yield stress in different tensile orientations are presented in Figure 50 together with experimental results, while the yield locus cuts obtained by HomPol4 criterion for different shear stress ratios are shown in Figure 51.

(a)   (b)
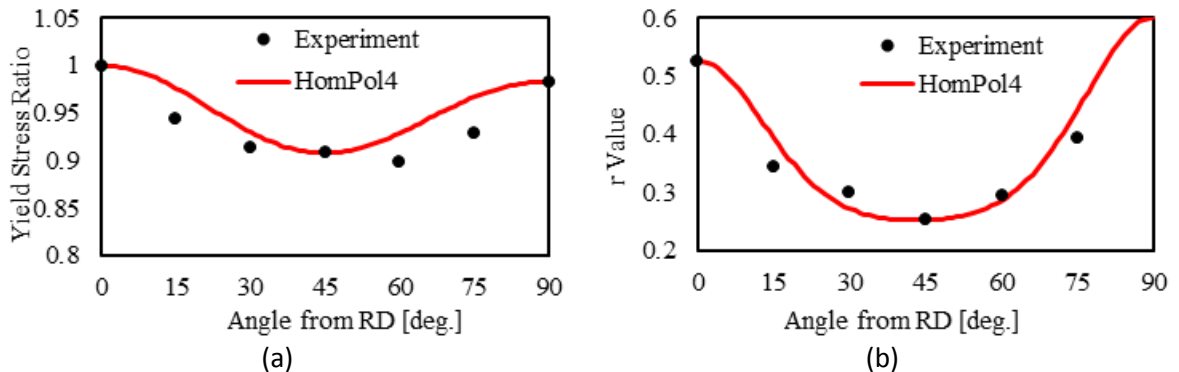
Figure 50 Predictions of (a) yield stress ratio and (b) Lankford coefficient values by HomPol4 with the data set of Table 23 compared with TUAT experimental values
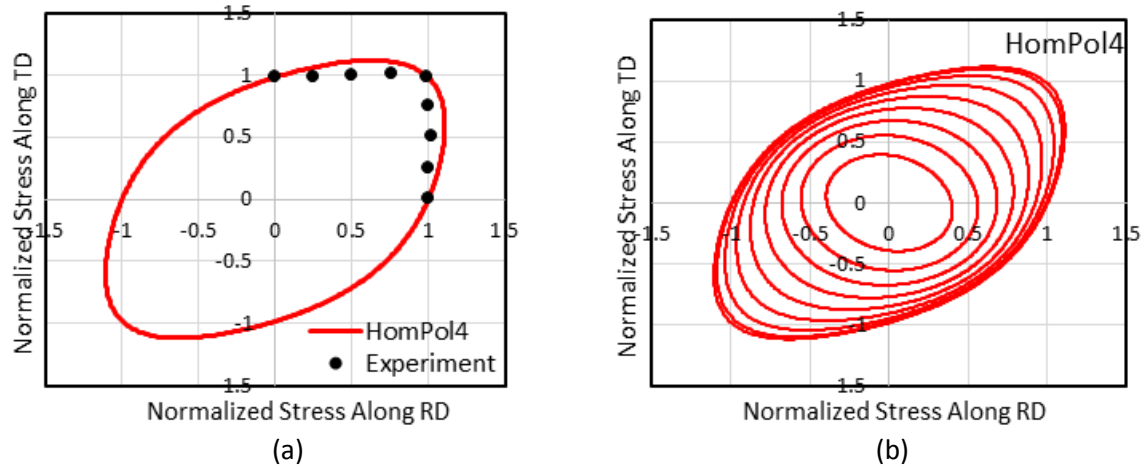
Figure 51 (a) Yield locus predicted by HomPol4 in principal stress space; (b) Yield loci contours predicted by HomPol4 for successive shear values of 0.1

7.2.3 6th order homogeneous polynomial model (HomPol6)

This yield locus described by Eq. (11) of Section 6.1.1 has 16 material parameters. In the identification procedure, the coefficients a_1, a_2, a_6 and a_7 are determined with the explicit formulae given in below:

$$a_1 = 1 \tag{64}$$
$$a_2 = -6r_0/(1 + r_0) \tag{65}$$
$$a_7 = (\sigma_0/\sigma_{90})^6 \tag{66}$$
$$a_6 = -6r_{90}\, a_7/(1 + r_{90}) \tag{67}$$

The other coefficients of the homogeneous polynomial model were determined with a minimization of an error function similar to Eq. (52). Experimental data of TUAT were used to identify the coefficients of HomPol6 for AA 6016-T4 alloy, which are given in Table 24.

Table 24 HomPol6 coefficients for AA 6016-T4

a_1	a_2	a_3	a_4	a_5	a_6	a_7	a_8
1.00000	-2.06815	3.53177	-3.93091	3.91107	-2.49639	1.10835	16.41230
a_9	a_{10}	a_{11}	a_{12}	a_{13}	a_{14}	a_{15}	a_{16}
-7.21657	11.92569	-5.02031	18.22988	22.46969	17.98091	24.43169	13.93065

Figure 52 show the predictions of planar variations of plastic properties (stress ratio and *r*-values). HomPol6 yield criterion can simultaneously predict planar variations of yield stress ratio and *r*-values. The computed yield locus contours are smooth and convex as observed in Figure 53, confirming that the determined coefficients satisfy the convexity condition.
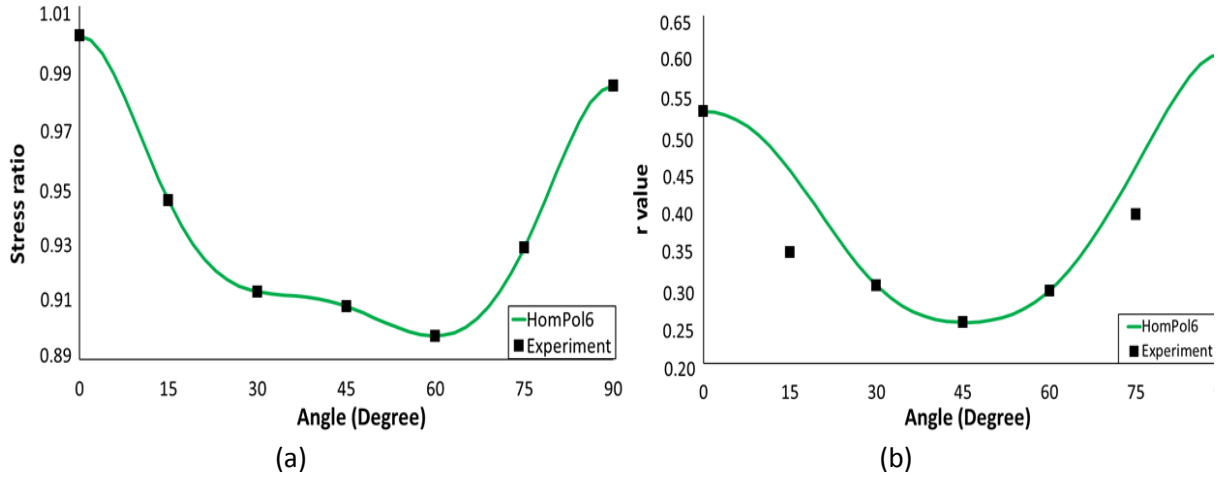
Figure 52 Predictions of stress ratios (a) and Lankford coefficients (b) for tensile tests in different directions based on HomPol6 yield locus and TUAT experimental results (angles measured from Rolling Direction)
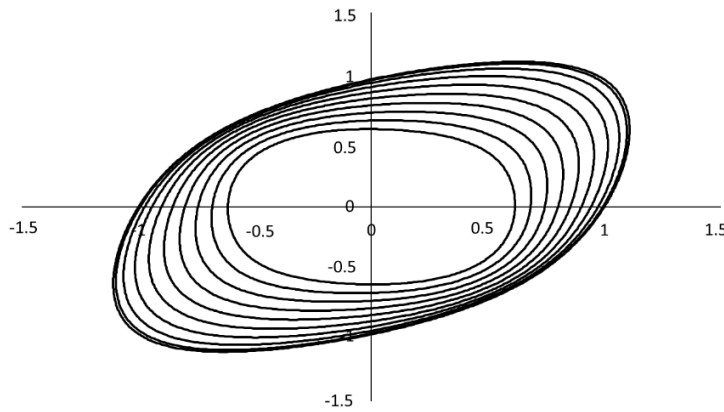
Figure 53 The computed contours of HomPol6 yield locus with the data set defined in Table 24

7.2.4   Non quadratic plane-stress yield locus Barlat (Yld89)

In this section, the identification methodology of Yld89 criterion (Eq. (7), Section 6.1.1) and the validation of its results for AA 6016-T4 aluminium alloy are described. As previously mentioned, it is recommended to select the m exponent in function of the crystal structure of the material, i.e. FCC m= 8 and BCC m= 6 [Liv2015]. The other material constants present in Eq. (7): a and h are obtained through r_0, r_{45}, and r_{90}:

$$a = 2 - 2\sqrt{\left(\frac{r_0}{1+r_0}\right)\left(\frac{r_{90}}{1+r_{90}}\right)} \tag{68}$$

$$h = \sqrt{\left(\frac{r_0}{1+r_0}\right)\left(\frac{1+r_{90}}{r_{90}}\right)} \tag{69}$$

while p parameter can be found by optimization. In this current benchmark, the tensile tests performed by TUAT were used and the objective function (Eq. (52)) was applied, with η_i=0, η_k =1, which means only the r-value error was minimized. Note this Yld89 model is often used in finite element analyses since its implementation is easy and it requires only a few numbers of material parameters.

The material parameters of the Yld89 criterion for the AA 6016-T4 alloy are given in Table 25. The Lankford coefficient and the normalized uniaxial flow stress for different directions defined by their angle with RD are presented in Figure 54(b), with the experimental results of TUAT. It can be seen that the directionality of r-values obtained with Yld89 has a good agreement with the experimental results except for 15° and 75°, while the criterion shows significantly poor performance for yield stress ratio

130

predictions (see Figure 54(a)). The yield locus cut shown in Figure 55 presents a close agreement with the biaxial-points measured by TUAT.

Table 25 Coefficients of Yld89 criterion for 6016-T4 aluminium alloy

a	h	p	m
1.2806	0.9582	0.86	8

(a)   (b)
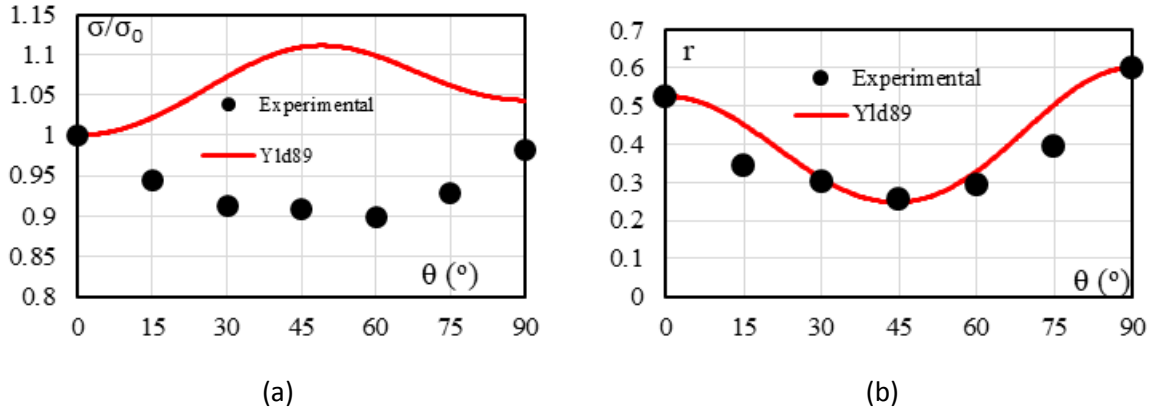
Figure 54 Prediction of angular variation of (a) normalized yield stress and (b) Lankford coefficient obtained with Yld89 compared with TUAT experimental points
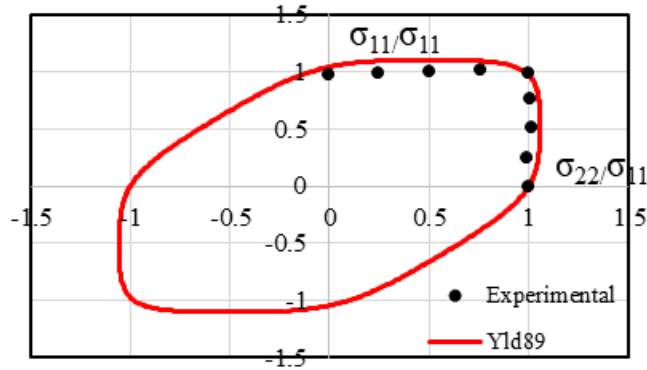
Figure 55 Yield locus cut of AA 6016-T4 obtained with Yld89

7.2.5   CB2001 by Cazacu and Barlat (2001)

The experimental data used for the identification of the CB2001 orthotropic yield criterion [Caz2001] for the benchmark material consisted of the uniaxial tensile data generated at UA. The anisotropy coefficients and parameter c involved in this criterion (see Eq. (15)) were determined by minimizing an error function of the form:

$$E = \sum_i \eta_i \left[\frac{(\sigma_\theta)_i^{\text{th}}}{(\sigma_\theta)_i^{\text{exp}}} - 1 \right]^2 + \sum_k \eta_k \left[\frac{r_k^{\text{th}}}{r_k^{\text{exp}}} - 1 \right]^2 + \sum_l \eta_l \left[\frac{\rho_l^{\text{th}}}{\rho_l^{\text{exp}}} - 1 \right]^2 \qquad (70)$$

In the above equation, i, k, l represent respectively the number of available experimental normalized tensile yield stresses and r-ratios (from UA) and biaxial data (from TUAT), while the superscript indicates whether the corresponding value is experimental or predicted. In Eq. (70), the

130

constants η_i, η_k and η_l are weight factors and were taken equal. To be recalled that a biaxial stress data point is represented by: $\rho = \sqrt{\left(\sigma_{xx}\, cos\,\varphi\right)^2 + \left(\sigma_{yy}\, sin\,\varphi\right)^2}$ with $\varphi = arctan\left(\sigma_{yy}\,/\,\sigma_{xx}\right)$ (see also Section 2.2.2). The parameters for the yield criterion are provided in Table 26.

Table 26 Values of material parameters of CB2001, the orthotropic Cazacu and Barlat [Caz2001] model

a_1	a_2	a_3	a_4	a_5	a_6	α				
1.000	1.900	1.391	0.870	1.000	1.000	1.2				
b_1	b_2	b_3	b_4	b_5	b_6	b_7	b_8	b_9	b_{10}	b_{11}
2.000	0.830	1.500	2.000	0.200	1.000	1.000	1.000	1.000	0.566	1.000

Comparison between experimental and predicted anisotropy in yield stresses and *r*-ratios obtained with CB2001 and associated flow rule are shown in Figure 56(a)-(b). The predicted yield surface cross-section in the plane (σ_{xx} , σ_{yy}) corresponding to constant levels of shear, namely $\sigma_{xy}/\sigma_0 = 0, 0.2, 0.3, 0.4, 0.5$ along with available biaxial stress data (TUAT) are shown in Figure 56(c). Moreover, Figure 57 shows the predicted direction of the plastic strain-rate $\beta = \arctan\left(D_{yy}^p\,/\,D_{xx}^p\right)$ for biaxial loading characterized by the angle $\varphi = \arctan\left(\sigma_{RD}\,/\,\sigma_{TD}\right)$ in comparison to the experimental data.

(a)

(b)

(c)
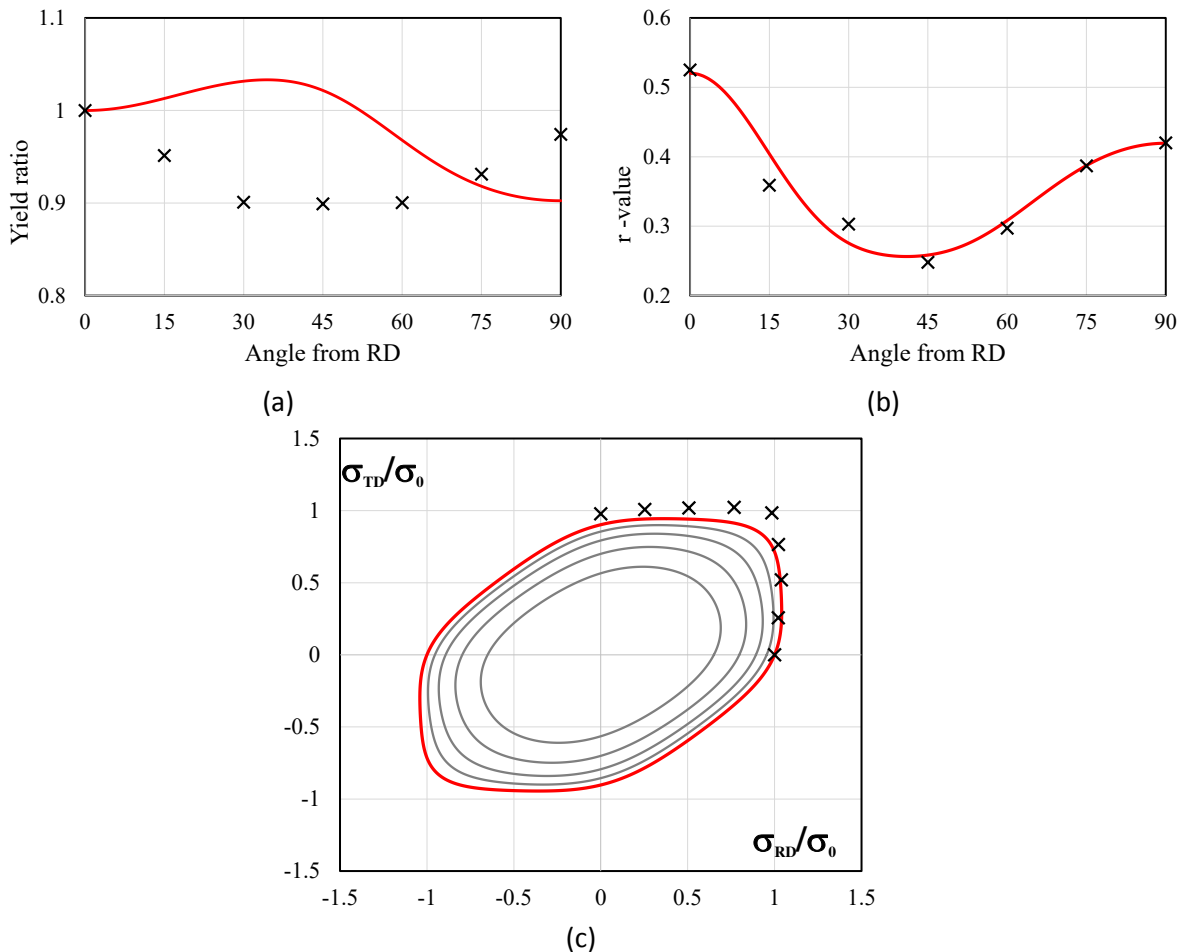
Figure 56 Predicted results by CB2001 criterion (Eq. (15)): (a) Tensile flow stresses; (b) Lankford coefficients; (c) Yield surface section in the biaxial plane $\left(\sigma_{RD},\sigma_{TD}\right)$ (with $\sigma_{xy}/\sigma_0 = 0, 0.2, 0.3, 0.4, 0.5$). Data represented by symbols. All stresses are normalized by the yield stress along the rolling direction, σ_0
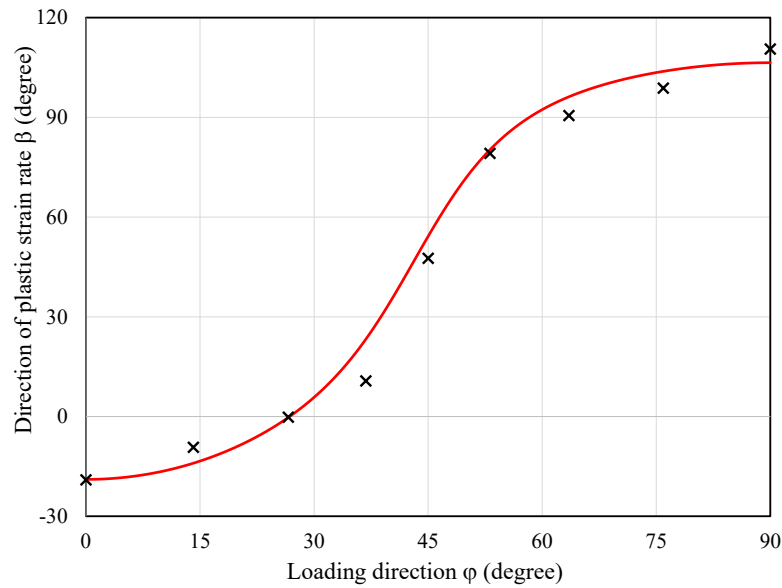
Figure 57 Predicted direction of the plastic strain-rate $\beta = \arctan\left(D_{yy}^{p}/D_{xx}^{p}\right)$ for biaxial loading at $\varphi = \arctan\left(\sigma_{RD}/\sigma_{TD}\right)$ by CB2001 criterion. Data represented by cross symbols

7.2.6 Yld2000-2d and Yld 2004-18p

POSTECH, as benchmark organizer provided dataset for the participants not performing their own identification. Based on the uniaxial tensile tests from TUAT, the Yld2000-2d and Yld2004-18p coefficients were determined with an optimization algorithm based on the steepest descent method with normalized flow stresses and r-values, for different stress states employed as input data. The normalized flow stress is taken at 20.6 MPa plastic work (corresponding to 0.1 plastic strain). The coefficients for Yld2000-2d (Eq. (8), Section 6.1.1) and Yld2004-18p (Eq. (18), Section 6.1.2), obtained by taking the yield function exponent m=8 are presented in Table 27 and Table 28, respectively. UGent approach to identify Yld2000-2d has already been described in Section 7.1.2.5, as virtual crystal plasticity tests are involved.

Table 27 Coefficients of Yld2000-2d (Line 1: POSTECH identification method based on classical experiments and Line 2: UGent identification method based on virtual tests)

α_1	α_2	α_3	α_4	α_5	α_6	α_7	α_8	M
0.9238	0.9967	0.9365	1.0227	1.0303	1.0075	0.8385	1.3761	8
0.6062	1.2813	1.2030	1.0214	1.0333	0.8686	0.7258	1.3764	6.11

Comparisons between the experimental and predicted (Yld2000-2d) yield stresses and r-values, with respect to the angle θ, based on the data sets of Table 27 are shown in Figure 58(a) and (b), respectively. Note that the UGent calibration procedure for Yld2000-2d by VPSC model is further

validated in Figure 59 by comparing the measured evolution of the direction of plastic strain rates with the predicted ones by VPSC and Yld2000-2d simulations.
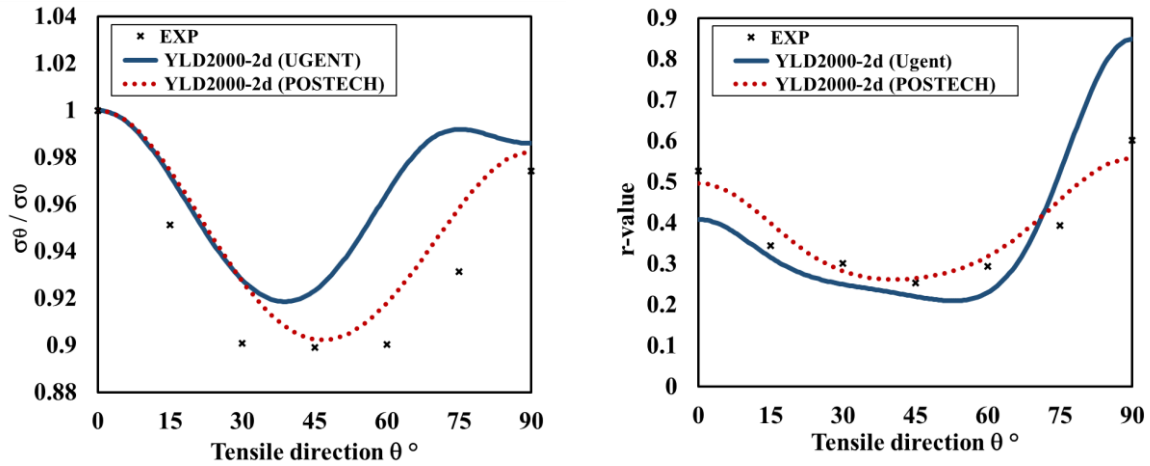
Figure 58 Validation of Yld2000-2d predictions by UGent and POSTECH vs. experiments at 10% of effective plastic strain: (a) normalized yield stresses and (b) *r*-values
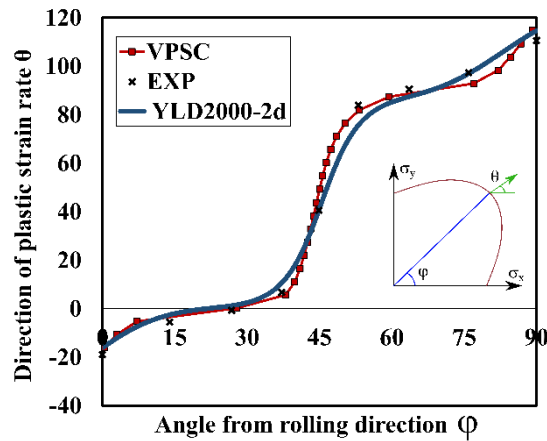
Figure 59 Directions of plastic strain rate obtained in the experimental tests and predicted by VPSC and Yld2000-2d as a function of the angle φ at 10% of effective plastic strain

The flexible model Yld2004-18p proposed in [Bar2005] and described by Eq. (18), Section 6.1.2, was identified by POSTECH based on physical experiments, but also by NTNU using the same kind of experimental data and also relying on crystal plasticity results (see Section 7.1.2.4). Their sets of parameters are provided in Table 28.

The results of POSTECH enhance a comparison between Yld2000-2d and Yld2004-18p predictions results (see yield locus cut in Figure 60 and anisotropy properties in Figure 61). Let us remind that the predicted anisotropic properties by NTNU were already presented in Section 7.1.2.4.They are directly based on virtual crystal plasticity experiments (Square Dots in Figure 40) or predicted by the Yld2004-18p identified from those virtual data (blue curves in Figure 40). The predictions based on the yield locus identified by crystal plasticity show some discrepancy with the experiments (overestimation, although the trends are good), while the results generated by Yld2004-18p directly identified by NTNU based on physical experiments (red curves in Figure 40) are similar to the experimental curves shown in Figure 61 and Figure 5.

130

Table 28 Coefficients of Yld2004-18p associated with the common choice of $m=8$ (Line 1 from POSTECH, Line 2 from NTNU, based on physical experiments, and Line 3 from NTNU based on virtual tests by Damask crystal plasticity simulations)

c'_{12}	c'_{13}	c'_{21}	c'_{23}	c'_{31}	c'_{32}	c'_{44}	c'_{55}	c'_{66}
1	1	-0.0870	0.4496	1.0192	1.1724	1.2801	1.1487	0
1.1998	1.2289	0.1315	0.8081	1.1386	0.2870	1.0000	1.0000	1.3739
1.1718	1.1284	-0.0403	0.6912	1.1030	0.4439	1.5916	0.0011	0.9922
c''_{12}	c''_{13}	c''_{21}	c''_{23}	c''_{31}	c''_{32}	c''_{44}	c''_{55}	c''_{66}
1.3329	1.2510	1.0948	1.0855	-0.0065	0.4812	0.5991	0.7366	1.5461
1.1510	-0.2576	0.4873	0.9934	0.9110	0.7965	1.0000	1.0000	0.2679
1.2910	-0.1740	0.7416	1.0787	1.0278	0.9367	-0.0021	1.5917	0.8146
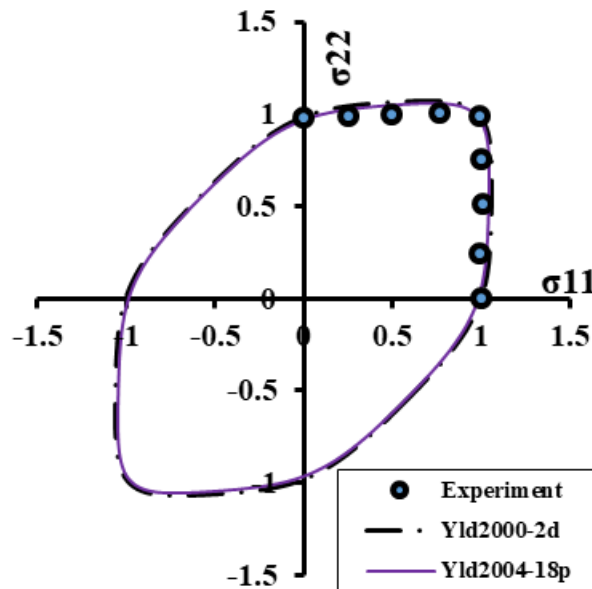
Figure 60: Comparison of the experimental yield locus and the predictions using Yld2000-2d and Yld2004-18p identified by POSTECH on physical experiments

(a)

(b)

7.2.7 CPB06 criterion by Cazacu, Plunket and Barlat (2006)

The procedure to determine the material parameters of the model developed by Cazacu, Plunket and Barlat [Caz2006] is described hereafter. The experimental data used for the simultaneous identification of the Voce hardening law (Eq. (4)) and the CPB06ex2 orthotropic yield locus (Eq. (22) of Section 6.1.2) consisted of the uniaxial tensile and shear tests performed by UA, as well as the biaxial data, generated at TUAT. These experiments assume uniform simple stress state, even if for simple shear and large shear strains, it is clearly more complex. These stress states can be implemented within an analytical integration of the constitutive law or computed by an element simulation with a FE software to identify associated equivalent anisotropy stress and strain values, stress-strain curves and Lankford coefficients.

The identification strategy consists in changing the parameters of the yield criterion and the hardening law, in order to minimize an error function similar to Eq. (52). Three differences are noted in this approach. Here, the whole stress-strain curve is taken into account using from 6 to 50 equivalent strain levels to compute the difference between the predicted and measured values. Another weight ponderation is applied: for tensile state, shear state, biaxial point and Lankford coefficient, values of 3, 1, 1, 1 are used, respectively. Note that seven bi-axial equivalent stress-strain curves were also included in the error function. The parameters for the Voce hardening law are reported in Table 32, which gathers all sets of hardening values, while the parameters for the yield criterion are provided in Table 29.

Table 29 Anisotropy parameter values of the CPB06ex2 yield criterion ($k = k' = 0$)

C_{11}	C_{22}	C_{33}	$C_{44} = C_{55}$	C_{66}	C_{12}	C_{13}	C_{23}	
1.0000	1.0610	0.1421	1.0000	1.0086	0.2321	-0.5621	-0.3188	
C'_{11}	C'_{22}	C'_{33}	$C'_{44} = C'_{55}$	C'_{66}	C'_{12}	C'_{13}	C'_{23}	a
1.1065	0.4034	1.1488	1.0000	1.1017	-0.3162	0.3983	-0.3531	8

The comparison between the experimental and predicted true stress vs. true strain curves for uniaxial tensile tests is presented in Figure 62(a) and (b), where it is possible to observe that the model underestimates the hardening behaviour for RD. Figure 62(c) presents the comparison between the experimental and predicted shear stress vs. shear strain curves, highlighting higher differences for shear strains lower than 0.25. In Figure 62(d), the comparison between the predicted equivalent stress vs. equivalent strain curve with the experimental results from biaxial tests, for different reference plastic strain values is performed. Globally, it is observed that the equibiaxial stress is underestimated by the model, while the others stress ratios and the hardening are overestimated.
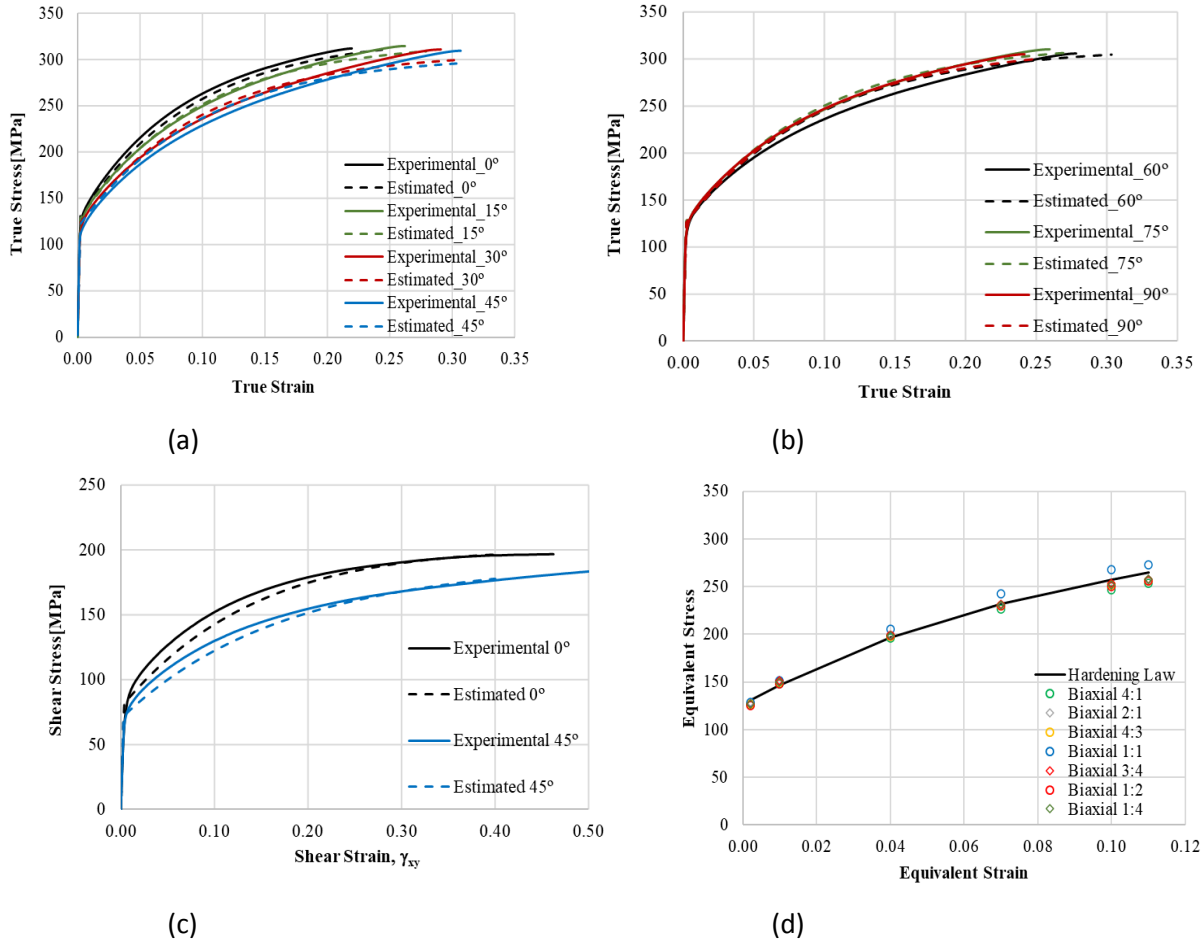
Figure 62 Comparison between the experimental and the CPB06ex2 predicted values: (a) and (b) true stress vs. true strain curves, for uniaxial tensile tests; (c) shear stress vs. shear strain curves; and (d) equivalent stress vs. equivalent strain curve, for biaxial tests

The comparisons between experimental and predicted anisotropy in yield stresses and *r*-ratios obtained with the CPB06ex2 yield criterion and associated flow rule are shown in Figure 63(a)-(b). The predicted yield surface cross-sections for constant levels of shear (normalized by the elastic limit in RD), namely 0, 0.2, 0.3, 0.4 and 0.5 along with available experimental biaxial stress data (from TUAT) are shown in Figure 63(c). Figure 63(d) shows the predicted direction of the plastic strain-rate for biaxial loading characterized by the angle β (see angle definition in Figure 41(b) in comparison to the experimental data. It is to be noted that the experimental data associated with the direction of the plastic strain-rate β for biaxial tests have not been used in the identification procedure. However, a very good agreement is observed.

130
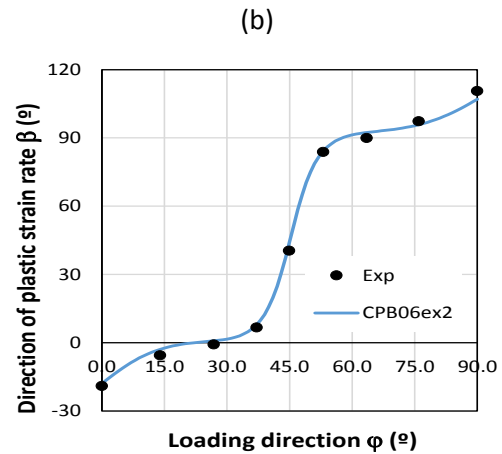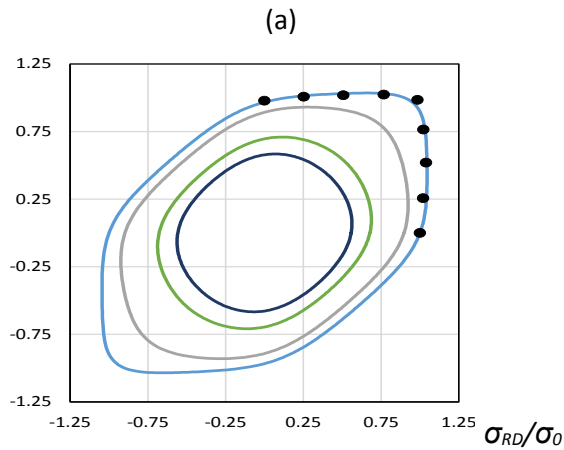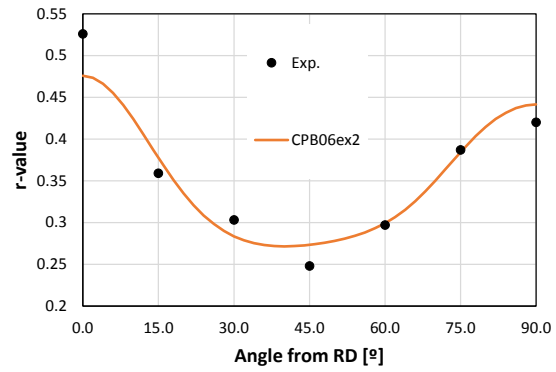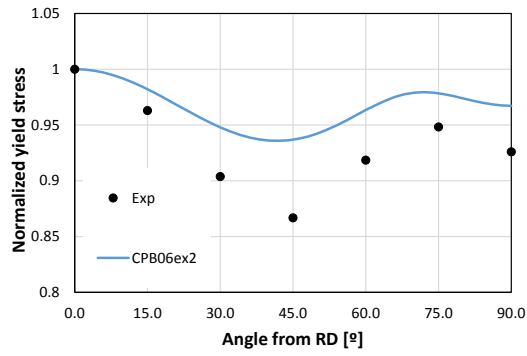
Figure 63. Predicted anisotropy by CPB06ex2 orthotropic yield criterion: (a) Uniaxial tensile flow stresses; (b) Lankford coefficients (*r*-values); (c) Predicted yield surface section in the biaxial plane σ_{RD} σ_{TD} (with $\sigma_{XY}/\sigma_0 = 0.$, 0.2, 0.3, 0.4 and 0.5). Data for the reference plastic strain of 0.002 are represented by symbols. All stresses are normalized by the yield stress along the RD σ_0; (d) Predicted direction of the plastic strain-rate β for biaxial loading at φ. Data are presented by symbols

7.2.8 Caz2018-Orth or Cazacu (2018) orthotropic yield criterion

For the benchmark material, the experimental data used for identification of the orthotropic yield criterion called Caz2018-Orth (details in [Caz2018a]) consisted of the uniaxial tensile data generated at UA. Specifically, the anisotropy coefficients a_k , k = 1...6 and b_j, j = 1...11 and parameter α (see Eq. (13), (14) and (16), in Section 6.1.2) were determined by the REEF organizers by minimizing the error function given by (Eq.(52)) with equal weights on stresses and Lankford coefficients. The parameters for the yield criterion are provided in Table 30.

Table 30 Values of material parameters of Caz2018-Orth, the orthotropic Cazacu (2018) model determined by the organizers REEF

a_1	a_2	a_3	a_4	a_5	a_6	α				
0.311	0.505	0.444	0.309	0.309	0.309	2.7				
b_1	b_2	b_3	b_4	b_5	b_6	b_7	b_8	b_9	b_{10}	b_{11}
0.253	0.206	0.223	0.288	0.220	0.174	0.205	0.220	0.213	0.213	0.172

Comparison between experimental and predicted anisotropy in yield stresses and *r*-ratios obtained with Caz2018-Orth yield locus and associated flow rule are shown in Figure 64(a)-(b). The predicted yield surface cross-section in the plane $(\sigma_{RD}, \sigma_{TD})$ corresponding to constant levels of shear, namely with $\sigma_{xy}/\sigma_0 = 0, 0.2, 0.3, 0.4, 0.5$ along with available biaxial stress data (from TUAT) are shown in Figure 64(c). Figure 65 presents the predicted direction of the plastic strain-rate β for biaxial loading at **φ.** (see angle definition Figure 41(b)) in comparison to the experimental data. It is to be noted that none of the experimental data for biaxial testing have been used for identification.
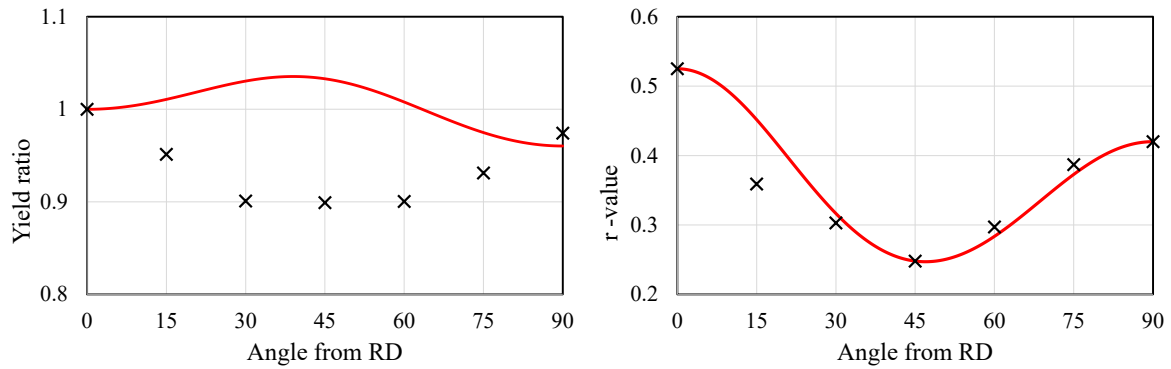
(a)

(b)
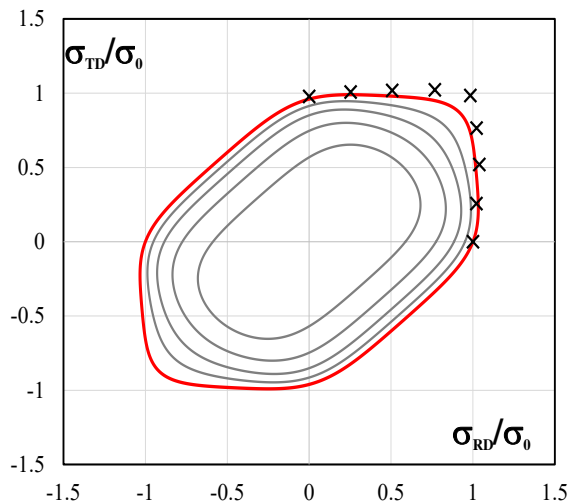
(c)

Figure 64 Predicted anisotropy by Caz2018-Orth yield criterion (Eq. (16)): (a) Uniaxial tensile flow stresses; (b) Lankford coefficients (*r*-values); (c) Predicted yield surface section in the biaxial plane $(\sigma_{RD}, \sigma_{TD})$ (with $\sigma_{xy}/\sigma_0 = 0, 0.2, 0.3, 0.4, 0.5$). Data are presented by cross symbols. All stresses are normalized by the yield stress along the rolling direction σ_0
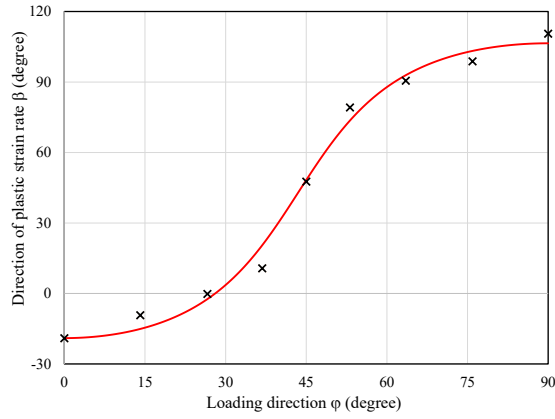
Figure 65 Predicted direction of the plastic strain-rate β for biaxial loading at φ by Caz2018-Orth yield criterion. Data are presented by cross symbols, angles β and φ are defined in Figure 41(b)

7.2.9   Hill48 and non-associated flow rule

For non-associative Hill model, as reminded at the end of the introduction of Section 6, 12 anisotropy parameters are necessary. Six for defining the yield stress function f and six for the flow potential g. The calibration for the anisotropy parameters is performed by analytical formulae defined hereafter by Eqs. (71), similar to the one described in associated Hill48 model (Table 21). They are reminded here to clearly define notations and to enhance that UAalto model assumes distortional hardening as explained hereafter.

The flow potential controls the update of strain components according to the non-associated flow rule Eq. (1)$_4$. This approach provides a new definition of the equivalent plastic strain rate $\dot{\bar{\varepsilon}}^{\mathrm{p}}$, which is not equal to the conventional non-negative plastic multiplier $\dot{\lambda}$, the details can be found in [Lia2018].

As shown by many experiments in the literature [Sto2009], during the monotonic and proportional plastic deformation process of anisotropic material, the hardening is not isotropic, but rather anisotropic and/or distortional. In addition to the hardening behaviour, the plastic anisotropy (r-values) is also not constant (see Figure 5(c)), as assumed by most of the benchmark participants which define an average value or a value associated to a specific stage of the strain (see Table 4). An evolving non-associated Hill48 model has been formulated with a straight updating of the anisotropic parameters, by the stress–strain curves and r-value evolution curves, as a function of the equivalent anisotropic plastic strain from uniaxial and biaxial tests [Lia2018]. Therefore, the parameters are defined as follows:

$$F_\sigma = \frac{\sigma_0^2(\bar{\varepsilon}^{\mathrm{p}})}{\sigma_{90}^2(\bar{\varepsilon}^{\mathrm{p}})} - 1 + \frac{\sigma_0^2(\bar{\varepsilon}^{\mathrm{p}})}{\sigma_{\mathrm{b}}^2(\bar{\varepsilon}^{\mathrm{p}})} \qquad\qquad G_\sigma = 1 - \frac{\sigma_0^2(\bar{\varepsilon}^{\mathrm{p}})}{\sigma_{90}^2(\bar{\varepsilon}^{\mathrm{p}})} + \frac{\sigma_0^2(\bar{\varepsilon}^{\mathrm{p}})}{\sigma_{\mathrm{b}}^2(\bar{\varepsilon}^{\mathrm{p}})}$$

$$H_\sigma = 1 + \frac{\sigma_0^2(\bar{\varepsilon}^{\mathrm{p}})}{\sigma_{90}^2(\bar{\varepsilon}^{\mathrm{p}})} - \frac{\sigma_0^2(\bar{\varepsilon}^{\mathrm{p}})}{\sigma_{\mathrm{b}}^2(\bar{\varepsilon}^{\mathrm{p}})} \qquad\qquad N_\sigma = \frac{4 \cdot \sigma_0^2(\bar{\varepsilon}^{\mathrm{p}})}{\sigma_{45}^2(\bar{\varepsilon}^{\mathrm{p}})} - \frac{\sigma_0^2(\bar{\varepsilon}^{\mathrm{p}})}{\sigma_{\mathrm{b}}^2(\bar{\varepsilon}^{\mathrm{p}})}$$

$$F_{\mathrm{r}} = \frac{2 \cdot r_0(\bar{\varepsilon}^{\mathrm{p}})}{r_{90}(\bar{\varepsilon}^{\mathrm{p}}) \cdot (1 + r_0(\bar{\varepsilon}^{\mathrm{p}}))} \qquad\qquad G_{\mathrm{r}} = \frac{2}{1 + r_0(\bar{\varepsilon}^{\mathrm{p}})}$$

$$H_{\mathrm{r}} = \frac{2 \cdot r_0(\bar{\varepsilon}^{\mathrm{p}})}{1 + r_0(\bar{\varepsilon}^{\mathrm{p}})} \qquad\qquad N_\sigma = \frac{2 \cdot (r_0(\bar{\varepsilon}^{\mathrm{p}}) + r_{90}(\bar{\varepsilon}^{\mathrm{p}})) \cdot (r_{45}(\bar{\varepsilon}^{\mathrm{p}}) + 0.5)}{r_{90}(\bar{\varepsilon}^{\mathrm{p}}) \cdot (1 + r_0(\bar{\varepsilon}^{\mathrm{p}}))}$$

(71)

The identification of N_σ was also performed considering the results from the simple shear test from UA at 0º. The results show that this approach lead to an improved description of the punch force and earing profile and, consequently, this data set will be the only one discussed here and in Section **Error! Reference source not found.**. The evolution of the yield stresses and r-values with the plastic strain was described using exponential type functions, but for the r-values, a linear increase is assumed for

130

plastic strain values higher than 0.025. Table 31 presents the values used for instance at four values of plastic strains. Figure 66 shows the comparison between the predicted and the experimental normalized yield stresses and *r*-values, for three values of plastic strain. The experimental results are the ones from UA. Figure 67 presents the yield surface section in the biaxial plane, only for two values of plastic strain, since the experimental data corresponds to the ones from TUAT. The model enables an accurate description of the in-plane anisotropy, including its evolution. For large strains, the *r*-values evolve with a linearly increasing trend, which is similar to the results presented in Figure 5(c). However, the model fails in capturing the shape of the yield locus and the directions of the plastic strain-rate β, for biaxial loadings. In the simulations of Section 8, the parameters are continuously updated with the equivalent strain values.

Table 31 Example of evolving parameters for Hill48 non-associated model at various plastic strain levels

Plastic strain value	F_σ	H_σ	G_σ	N_σ	F_r	G_r	H_r	N_σ
0.002	0.61	0.41	0.59	2.12	0.71	0.65	0.35	1.24
0.1	0.61	0.41	0.59	2.21	0.86	0.66	0.34	1.12
0.18	0.58	0.44	0.56	2.03	0.84	0.65	0.35	1.13
0.4	0.54	0.48	0.52	1.60	0.79	0.64	0.36	1.17

(a)   (b)
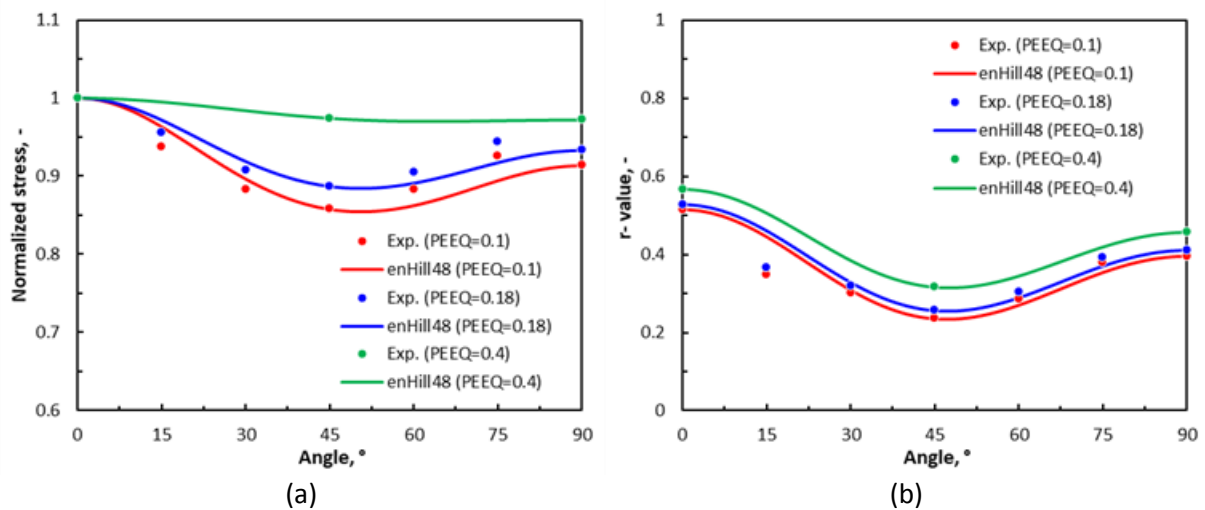
Figure 66 (a) Predicted anisotropy for the AA 6016-T4 alloy according to the evolving non-associated Hill48 yield locus (enHill48): (a) uniaxial tensile flow stresses at plasticity entrance; (b) Lankford coefficients (*r*-values) at equivalent plastic strain (PEEQ) of 0.10, 0.18, and 0.40; Symbols present the measured data of UA
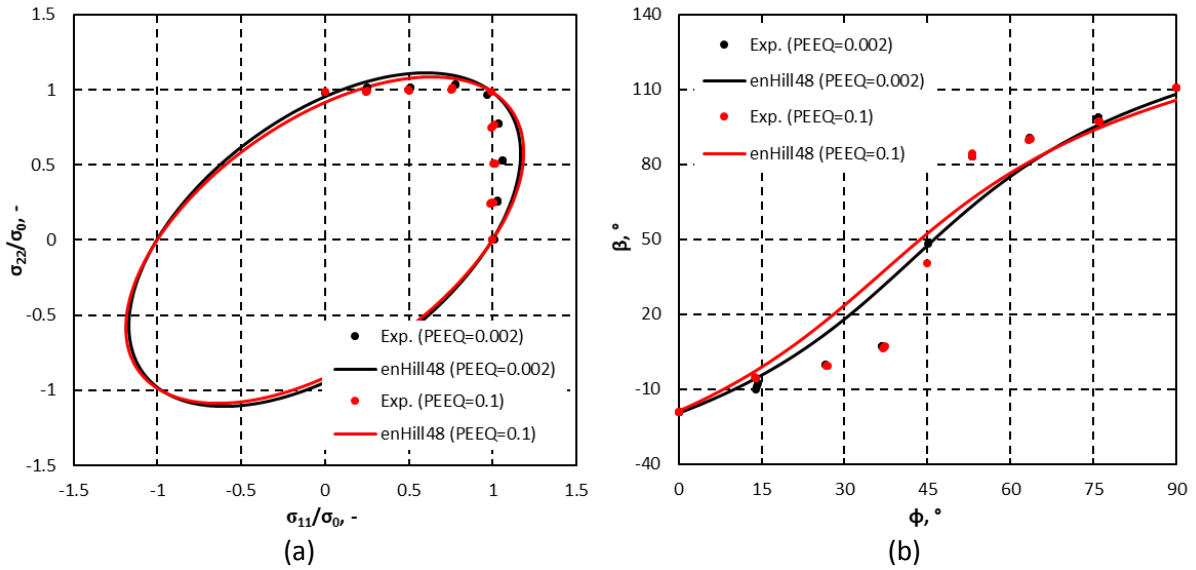
Figure 67 (a) Evolving non-associated Hill48 yield locus (enHill48) section in the biaxial plane $\sigma_{RD}\,\sigma_{TD}$ at equivalent plastic strain (PEEQ) of 0.002 and 0.1 All stresses are normalized by the yield stress along the rolling direction, σ_0, (b) Predicted direction of the plastic strain-rate β for biaxial loading at φ (see Figure 41 for angle definition)

7.3 Identification of hardening laws and data used

In this section, the identification procedures of isotropic hardening and combined isotropic – kinematic hardening parameters are briefly reminded. The benchmark organizers (REEF) provided the parameter values for the isotropic Swift and Voce hardening laws, identified using the UA tensile tests in RD and least-square fit (see Table 32). Other participants used different data and procedures. For instance, to determine the set of parameters of isotropic Swift law, USakarya approach was based on TUAT tensile tests in RD. Hardening curve parameters were obtained by using a curve fitting method from MATLAB Curve Fitting Tool software (Levenberg – Marquardt algorithm was selected). The values of the parameters used by all teams in the simulations presented in Section 8 are provided in Table 32. Figure 68 shows a comparison between modelling results and experimental RD tensile curves, designated as UA and TUAT.
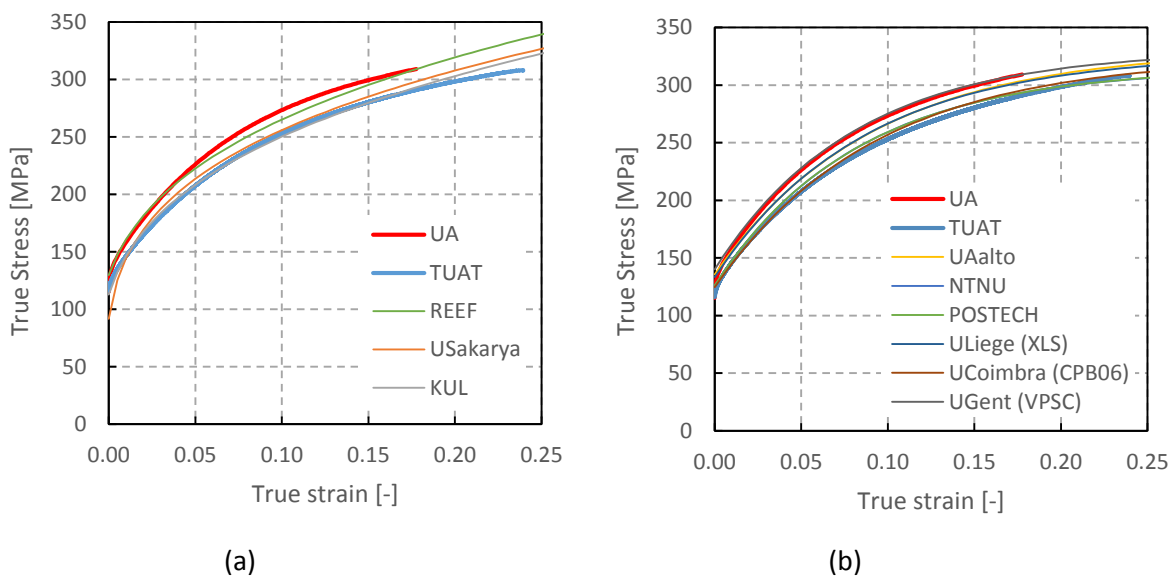
Figure 68 Experimental RD tensile curve of AA 6016-T4 of TUAT and UA along with the modelling results obtained with isotropic hardening laws: (a) Swift model and (b) Voce model

130

Kinematic hardening parameters of a mixed hardening model was obtained by USakarya, considering the reversal shear test data in RD of UA. Simulations of single element tests under reversal shear conditions were carried out to identify the values in Table 32 by inverse modelling. Figure 69 shows the boundary conditions of reversal shear conditions on a representative single element. Figure 70 presents the kinematic and isotropic parts of the hardening model, separately. In the curve fitting procedure, a slight decreased of the isotropic part of the mixed hardening model is observed, within a small range of small true strain values. Nevertheless, the isotropic part is globally well captured. The developed Hypela2 user subroutine code of USakarya considers this situation.
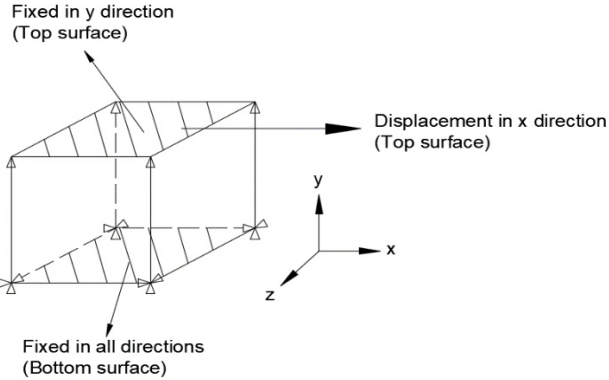
Figure 69 Reversal shear boundary conditions on a representative single element

(a)   (b)
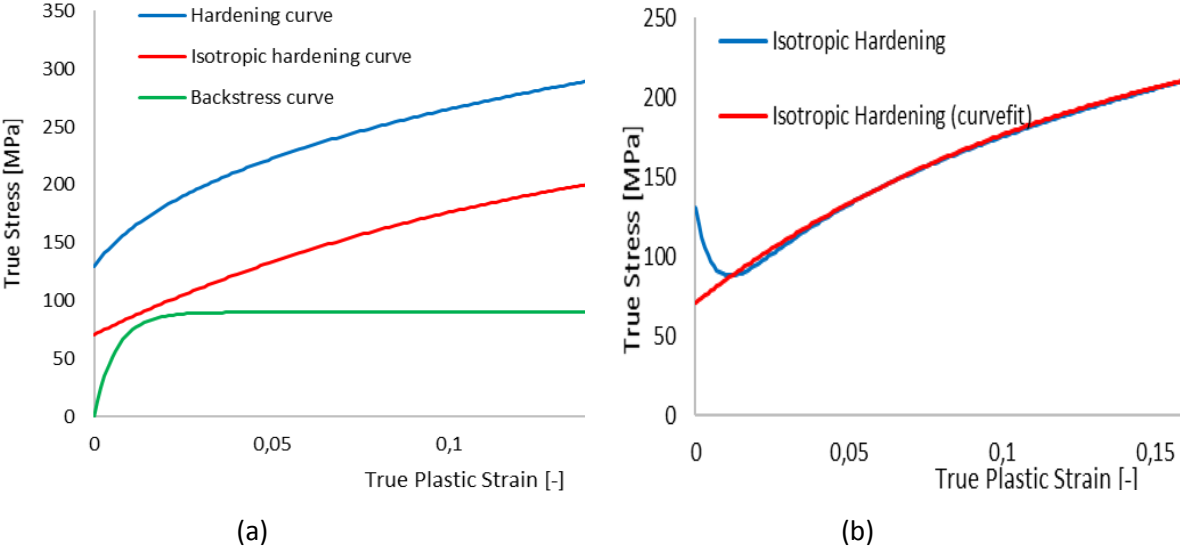
Figure 70 (a) Isotropic hardening, kinematic hardening and total hardening curves, (b) Curve fitting of isotropic part in combined hardening

Table 32 Values of hardening parameter data sets used by the participants, for phenomenological laws and if not presented in section 7.1, for polycrystalline models

Participant & Selected law & Identification Method	Hardening law

$Y\left(\bar{\varepsilon}^{\,p}\right)=K_0\left(\varepsilon_0+\bar{\varepsilon}^{\,p}\right)^n$	**Swift Isotropic Hardening**		
	Set provided by Benchmark organizer (REEF)		
	K_0 (MPa)	ε_0	n
Used by REEF, UCoimbra, UPorto, USiegen (LS-DYNA & PAMSTAMP)	498.8	0.0089	0.285
	Own identified dataset		
USakarya (MSC.MARC, LS-DYNA) Matlab Levenberg Marquardt, RD Tokyo tests	474.1	0.002299	0.2703
KUL (Tokyo test in RD – Fitted with Excel solver)	478.2	0.0068	0.2895
$Y = Y_0 - B\exp\left(-n\bar{\varepsilon}^{\,p}\right)$	**Voce Isotropic Hardening**		
	Set provided by Benchmark organizer (REEF)		
	Y_0 (MPa)	B (MPa)	n
	326.8	189.4	12.0
	Own identified dataset		
UAalto	331.18	195.46	11.04
NTNU	314.98	189.03	12.22
POSTECH	315.21	188.97	12.17
ULiege (XLS minimization)	326.99	193.60	11.64
UCoimbra (CPB06)	324.7	200.23	10.83
UGent (VPSC)	330.2	190.0	12.4

USakarya (MSC.MARC, LS-DYNA) See formulae hereafter*	**Mixed hardening**				
	$K_{0(iso)}$ (MPa)	$n_{(iso)}$	$\varepsilon_{0(iso)}$	C (MPa)	γ
	480	0.46	0.0089	15000	166.66

$$* \;\sigma = K_{0(\text{iso})}(\varepsilon_{0(\text{iso})} + \bar{\varepsilon}_p)^{n(\text{iso})} + \frac{C}{\gamma}\left(1 - \exp(-\gamma\bar{\varepsilon}^p)\right)$$

7.4   Discussion on the methodology for identification of the models

For polycrystalline models, we already pointed out the large differences in the number of grains considered in the final representative texture (FRT). Each team made its choice based on their experience and its focus, e.g. to model the tensile test behaviour (yield stress and Lankford predictions) or to take into account more stress states.

The results reported in Section 7.1.2 for the polycrystalline approach demonstrate the care required in the representative crystal data set and that the verification and comparison with experiments (yield stress and Lankford values in different directions from RD) is quite important to guide the user.

Table **33** summarizes these details as well as the CPU time required for performing the identification steps and the numerical simulation of the uniaxial test with the polycrystalline model. Note that the manpower required to generate, from EBSD data and mechanical tests, the final set of polycrystal model parameters, considers a skilled user.

Table 34 details the number of tests used for the phenomenological yield locus identification. Note that the analytical expression were used with the Hill48 yield criterion. Interestingly, most teams did not used all type of experimental data available. In particular, only two teams used the information from shear tests results, which can be related with the interpretation of the experimental results, as previously mentioned in Section 2.2.3. In addition, only two teams took into account the direction of the plastic strain-rate in the identification procedure.

Table 33 Effort required to model the texture and to identify the data set for the polycrystalline models including hardening data. In the last column, referring to the tensile test with the polycrystal model, the number of FE or FFT grids used is indicated in square brackets

Team	Target constitutive law and software used	Number of crystals in the FRT	Physical test used for calibration	Manpower to generate the final set of polycrystal model parameters	CPU time & hardware (PC or HPC configuration for identification steps)	CPU time to model one tensile test
KUL	ALAMEL model In-house code for virtual tests and Facet identification (FNG)	10 000	1 (EBSD) + tensile test along RD for hardening	~ 30 min	~ 10 s on HPC: Xeon Gold 6140 CPU@2.3 GHz – Skylake (7 s for generating discrete texture from EBSD data + 3 s for 200 virtual tests in stress space)	–
REEF	Caz2018polycrys ABAQUS, MTEX,	250	EBSD + tensile test along RD	~10 min	Total: 10 hr for complete identification (i.e. including the FE inverse analysis stage which requires calculation of 7 r-values (Section 7.1.1.2)	20 min on 1 PC [570 FE, see Figure 34] (Intel Core i7- 4770, 1 core, 16 GB RAM).
ULiege	Minty law, Lagamine, MTM MTM-FHM (1995)	1000	EBSD + tensile test along RD for hardening	~ 30 min	< 5 s	1.8 s [1 FE]
NTNU	3D RVE for FFT (DAMASK)	7509	EBSD + tensile test along RD	~ 30 min	120 min for the identification, PC (dual Intel Xeon E5-2696 v4, 88 core, 128GB RAM)	8 hours on 1, PC (dual Intel Xeon E5-2696 v4, 88 core, 128GB RAM), [120X120X120] FFT grids
UGent	VPSC (own implement.) ABAQUS	1500	EBSD + tensile tests in 7 different directions	~ 30 min	< 30 min (each step, the seven simulations are run at least once for each fitting parameter)	~ 45 seconds to run 7 simulations (one per direction) in parallel (i7-8650U)

Table 34 Mechanical tests used for the phenomenological yield locus identification

Team	Yield criterion	Lankford coef. (RD, TD and DD)	Tensile flow stress (RD, TD and DD)	Tensile test in 15, 30, 60, 75 from RD	Equibiaxial test point	More biaxial tests	Shear tests	Optim. tool =O Analy. Form. =A
ULiege	Hill48(A)	X	X	X	-	-	-	O
UCoimbra	Hill48(A)	X	Only RD	-	-	-	-	A
UAalto	Hill48(NA)	X	X	-	X	-	X	A
USakarya	Yld89	X	X	-	-	-	-	O
POSTECH	Yld2000-2d	X	X	X	X	-	-	O
USakarya	HomPol4	X	X	X	-	-	-	O
USakarya	HomPol6	X	X	X	-	-	-	O
UCoimbra	CB2001	X	X	X	X	X	-	O
POSTECH	Yld2004-18p	X	X	X	X	-	-	O
NTNU	Yld2004-18p	X	X	X	X	-	-	O
UCoimbra	CPB06ex2	X	X	X	X	X	X	O
REEF	Caz2018-Orth	X	X	X	-	-	-	O

8. Cup drawing simulations, analysis and discussion

The correlation between the predicted earing profile and *r*-values as well as the yield stresses directionalities has been shown in [Yoo2011] and [Caz2021]. In order to verify the implementation of the constitutive models, in commercial codes (PAMSTAMP, LS-DYNA) or done by the participants through user-subroutines (ABAQUS, DD3IMP, MSC.MARC, Lagamine), the participants were asked to perform uniaxial tensile tests for discrete values of the specimen orientation relatively to RD and report the estimated *r*-values and yield stresses. Therefore, the predicted *r*-values and yield stresses, obtained from FE simulations, as well as the earing profiles are reported in this section, for each yield function. The thickness distribution along the cup circumference at different heights was evaluated after unloading and it was an optional result, due to the work involved in its evaluation.

The result presentation is subdivided in four sections. The first and second ones concern simulations based on phenomenological models identified only by physical tests (Section 8.1) or also relying on virtual crystal plasticity computations (Section 8.2). The next section (Section 8.3) analyses the results of crystal plasticity simulations. Finally Section 8.4 presents a discussion of all these results.

8.1   Results of phenomenological models identified with physical tests

8.1.1   3-D orthotropic yield functions and solid or shell elements

8.1.1.1   Hill48 yield criterion

8.1.1.1.1   Hill48 with associated flow rule

Four teams reported results obtained using the Hill48 yield criterion and the Swift hardening law, with the set of parameters provided by the benchmark committee. These four teams are UCoimbra, UPorto, REEF and USiegen. As described in Section 5, UCoimbra used solid elements and the implicit code DD3IMP. UPorto also adopted solid elements and the simulations were performed with ABAQUS

(explicit). REEF used ABAQUS (implicit) also with solid elements. Finally, USiegen used both solid and shell elements, with the explicit codes LS-DYNA (DYNA) and PAMSTAMP (PAM). In this section, the results obtained by ULiege using the Hill48 yield criterion (Set 2 of Table 22, in Section 7.2.1) and the Voce hardening law are also presented. According to the information given in Section 5, ULiege used solid elements and its own FE implicit software Lagamine.

As reported in Table 9 and Figure 28, the finite elements adopted by USiegen have a smaller average in-plane size (nominal edge length of 0.5 mm). The velocity imposed to the punch in the explicit codes was 1 mm/ms; a constant friction coefficient of μ = 0.075 was applied to all tool surfaces in contact to the sheet metal blank. This value of the friction coefficient was adopted after performing a preliminary series of simulations using shell elements. Specifically, the friction coefficient value was taken such as to obtain the best fit for the first peak of the punch drawing force. UCoimbra considered a constant friction coefficient of μ = 0.020, while UPorto considered μ = 0.050 and REEF μ = 0.070. The simulations performed by ULiege considered a constant friction coefficient of μ = 0.082 applied to all tool surfaces in contact with the blank. ULiege used the same approach as USiegen to select the friction coefficient, by fitting the maximum punch force. The fact that ULiege attained a slightly higher value for the friction coefficient can be related with the different characteristics of the codes, but also with the adoption of the Voce hardening law, which tends to saturate for an equivalent plastic strain higher than 0.4. Note that the hardening presents an increasing trend when described with the Swift law (see Figure 68).

First, in Figure 71 are reported the results obtained by USiegen with shell elements. Next, comparison between simulation results with solid elements, obtained with the explicit and implicit codes, are presented in Figure 72. This enabled to compare the LS-DYNA and PAMSTAMP explicit code predictions obtained with the same process parameters, constitutive model, parametrization and FE meshes (for solid elements only (see Table 9)).

First, let us note that irrespective of the integration strategy (explicit vs. implicit) and irrespective of whether the simulations were conducted with shell or solid elements, Hill48 in conjunction with an isotropic hardening law correctly describes the overall experimental trends for both force vs. displacement and earing profile, i.e. 4 ears as observed experimentally.

For the first phase of the drawing operation (0 < displacement < 30 mm), the results obtained with shell elements are very close to the experimental ones. The results from LS-DYNA with solid elements show a larger error than the one with shell elements, although the r-value and yield stress anisotropies are identical, as shown in Figure 73. USiegen performed the simulations with a different type of integration scheme (elform=-1), in order to exclude the possibility that the element formulation might lead to this error. However, negligible differences were observed in the results. Because UCoimbra and UPorto used a smaller value for the friction coefficient, overall they predict a lower punch force.

Note that in the second phase of the drawing operation, where ironing of the initial flange area of the blank occurs in the drawing gap (displacement > 30 mm), a secondary peak is observed in all the simulations, while the experimental curve exhibits a brief plateau and subsequently drops towards a constant, very low force. These ironing forces are significantly lower when using solid element than shell element, but are quite sensitive to the value of the friction coefficient (μ range [0.02,0.082]). The evolution of the predicted punch force shows its sensitivity to the contact algorithm, FE strategy (implicit, explicit), particularly for the ironing stage. For instance, the results with DD3IMP (UCoimbra, implicit, μ=0.02) are close to the ones predicted by ABAQUS (UPorto, explicit, μ=0.05). While for the same element (C3D8R) and software (ABAQUS), but implicit or explicit strategy and different contact algorithms and values of the friction coefficient (μ =0.05 or 0.07), the ironing peak computed by REEF

is twice the one computed by UPorto. The single effect of a low or high friction coefficient value will be discussed in Figure 75.

Figure 72(a) shows that the evolution for the punch force predicted by Lagamine (ULiege) presents a sudden drop. This event occurs for a punch displacement for which the blank progressively starts to lose contact with blank holder. The control of the downward movement of the blank holder does not seem to fulfil the gap imposed by the stopper. This leads to issues in the punch force prediction and to the pinching of the ears located at 0° and 90° with the RD, as shown in Figure 72(b).

It is worth noting that the predicted amplitude of the ears obtained with shell elements is approximately 1 mm larger than the experimental one. In contrast, the amplitudes of the predictions obtained with solid elements are more accurate. The only exception is the profile obtained by UPorto, which can be related with the fact that the blank holder was controlled by a fixed position, leading to a much lower restraining force. In fact, the trend obtained by UPorto is identical to the one of DD3IMP at TD, but shows a lower height at RD. This observation is certainly related with the fact that UPorto considered a constant gap between the blank holder and the die, which reduces the friction effect induced by the blank holder, but it can also produce some wrinkles that influence the trend for the earing profile. Overall, the earing profile is being dictated by the in-plane distribution of the normalized yield stress and *r*-values, which are similar for all models, as shown in Figure 73.

The better prediction of the earing amplitude by solid element simulations can be explained by the fact that these elements can deform over thickness, within the drawing gap during ironing. The resulting transversal strain leads to an overall higher cup wall. Obviously, transverse strains are neglected when using shell elements. This fact also explains the lack of accuracy of the shell elements predictions for the thickness distribution along the cup circumference, for different heights, presented in Figure 74. For example, at a height of 30 mm, the predicted thickness value obtained with shell elements is higher than the gap between the punch and the die. On the other hand, for the simulations with solid elements the predictions of the thickness values for the same height are closer to the gap value, particularly the one obtained with DD3IMP. This indicates the stricter fulfilment of the normal contact constraint in the algorithm adopted in this code. Overall, the results obtained by DD3IMP present slightly higher thickness values for the lower heights of the cup, which can be related with the lower average cup height, i.e. with the fact that a lower friction coefficient was considered. The only exception for results obtained with solid elements is the one from Lagamine (ULiege), for which the thickness distribution predicted shows values higher than the gap between the punch and the die. Once again, this indicates either that the contact algorithm is not imposing the fulfilment of the gap or that the solid elements adopted are leading to an improper prediction of the transverse strains. The height predicted for RD is quite similar to the one obtained with DD3IMP, while at TD it is closer to the one obtained by UPorto and USiegen LS-DYNA. These results indicate that the earing trend is affected by the contact with friction algorithms, including the ones adopted to control the blank holder and by the formulation adopted for the solid element.

The influence of the value of the friction coefficient on the results is depicted in Figure 75, which shows the results obtained with two implicit codes: DD3IMP (UCoimbra) and ABAQUS (REEF), using solid elements. The value for the friction coefficient of 0.07 enables capturing the maximum drawing force, while the ironing force is clearly overestimated. Regarding the earing, the increase of the friction coefficient leads to an increase of the average height, as previously reported in Section 4 for the von Mises yield criterion. The increase of the friction coefficient also induces a slight increase on the earing amplitude. For instance, for the results obtained by REEF the amplitude increases from 2.62 mm to

83

2.65 mm (against the experimental value of 2.29 mm). This is also associated with the change in the location of the global maximum, from 90° (TD) to 0° (RD). This small effect is more pronounced in the results obtained by DD3IMP. This fact indicates that the earing trend is influenced by the contact algorithm adopted, since this effect is related with the uneven distribution of the blank holder force, resulting from the material orthotropic behaviour and the contact with friction conditions. The influence of the formulation adopted can also be observed in Figure 76, which shows the results obtained by different codes (Lagamine, LS-DYNA, ABAQUS, DD3IMP, PAMSTAMP), using similar values for the friction coefficient (μ=0.07 to 0.082) and solid elements. As shown in Figure 76(a), this high value for the friction coefficient enables to capture the maximum drawing force, except for LS-DYNA. Note the excellent correlation between the earing profiles predicted by ABAQUS (implicit, REEF) and LS-DYNA (USiegen) and between DD3IMP (UCoimbra) and PAMSTAMP (USiegen). Thus, Figure 76 highlights the small dispersion in the average height and amplitude of the earing profiles predicted by different codes, when using solid elements and the Hill48 yield criterion.

Figure 77 shows the isocontours of the equivalent plastic strain obtained in the simulations conducted with LS-DYNA and DD3IMP, with solid elements. Note that both codes can successfully predict/account for the high values of the plastic strains reached on the cup wall, due to the bending/unbending around the die radius, but also because of the ironing.

(a)   (b)
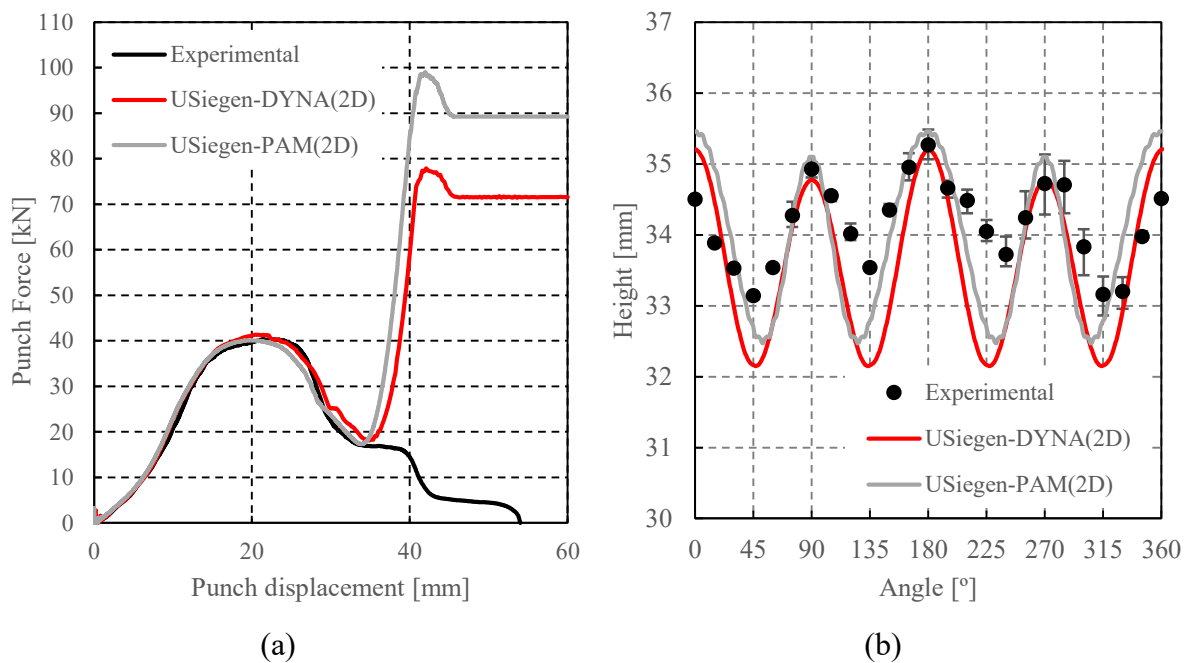
Figure 71 Comparison between experimental and predicted results by Hill48 criterion with the data set identified in Section 7.2.1 (Table 22) with shell elements: (a) punch force-displacement, (b) earing profile
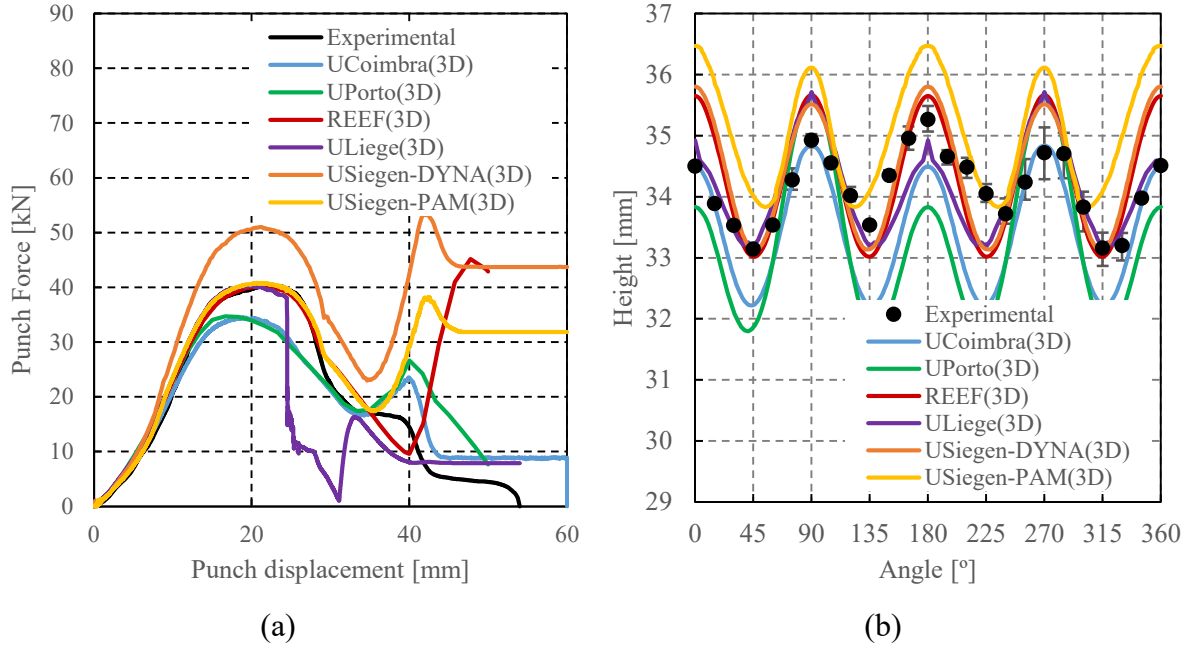
Figure 72 Comparison between experimental and predicted results by Hill48 criterion with the data set identified in Section 7.2.1 (Table 22) with solid elements: (a) punch force-displacement, (b) earing profile
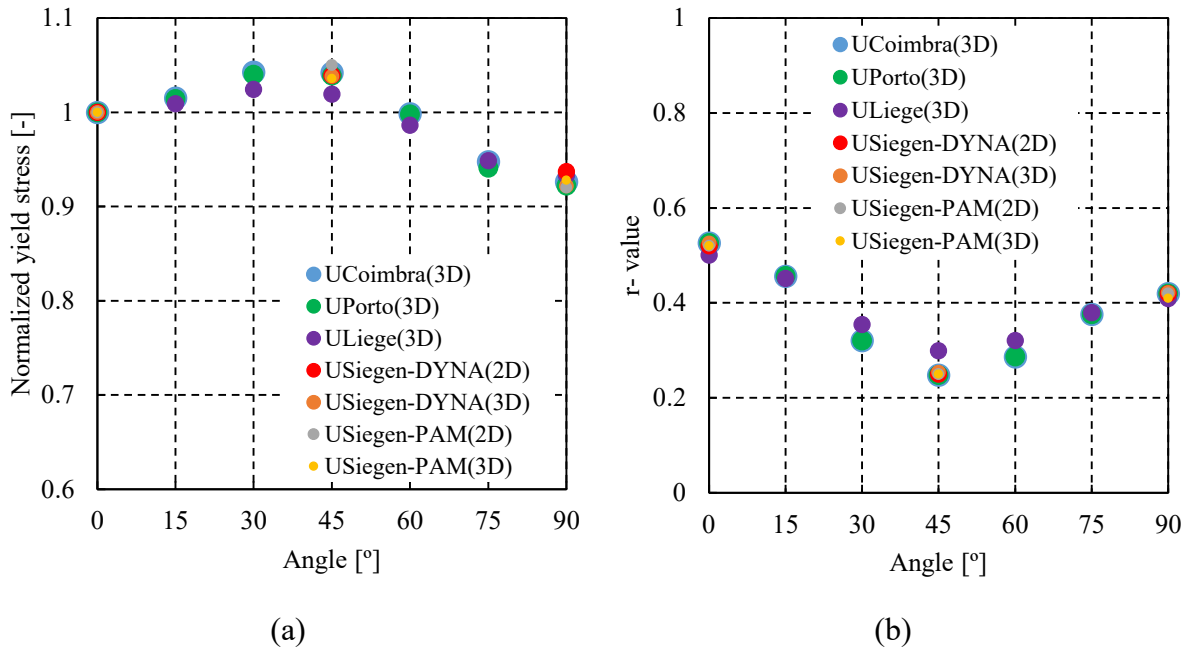
Figure 73 Predicted FE results by Hill48 criterion with the data set identified in Section 7.2.1 (Table 22): (a) uniaxial tensile flow stresses, (b) Lankford coefficients (*r*-values)

85

(a)

(b)

(c)

(d)

(e)   (f)
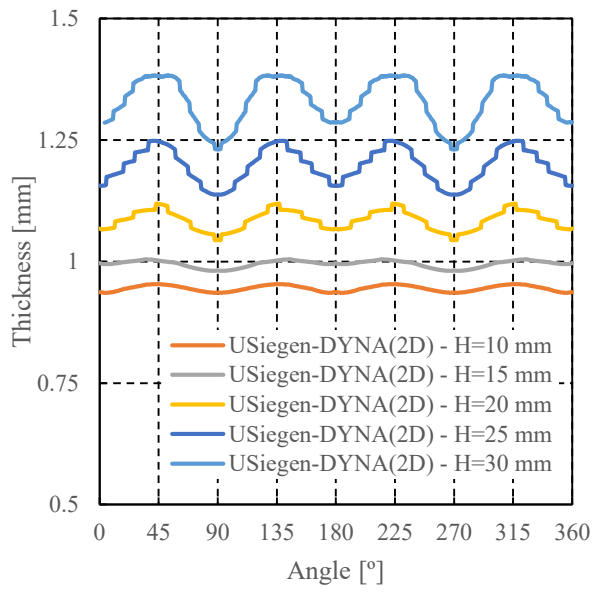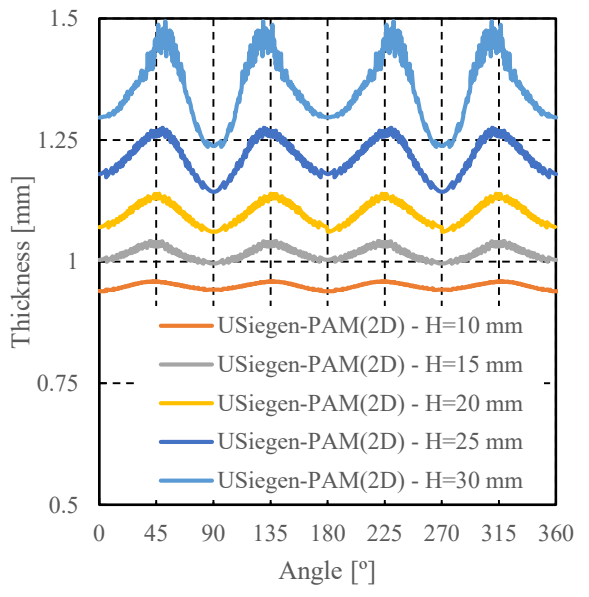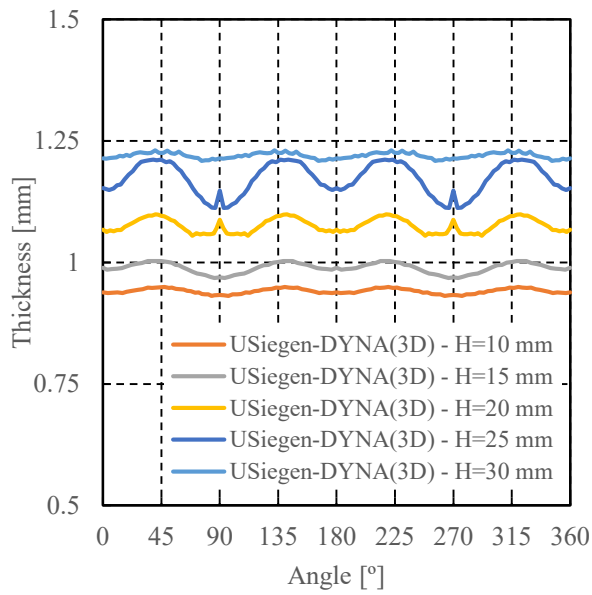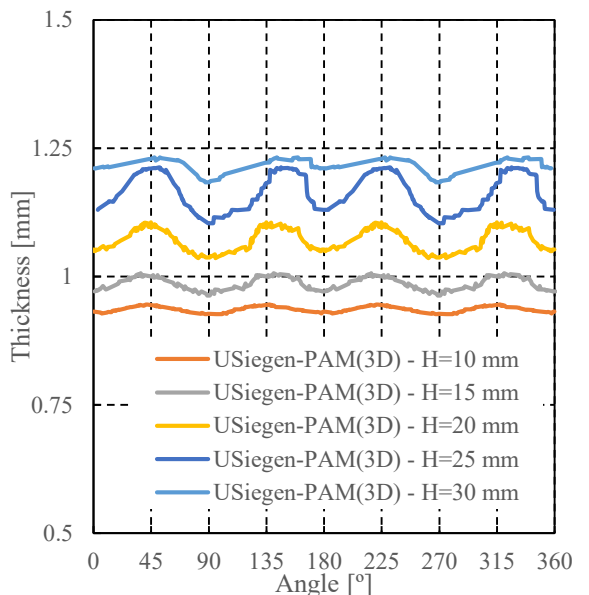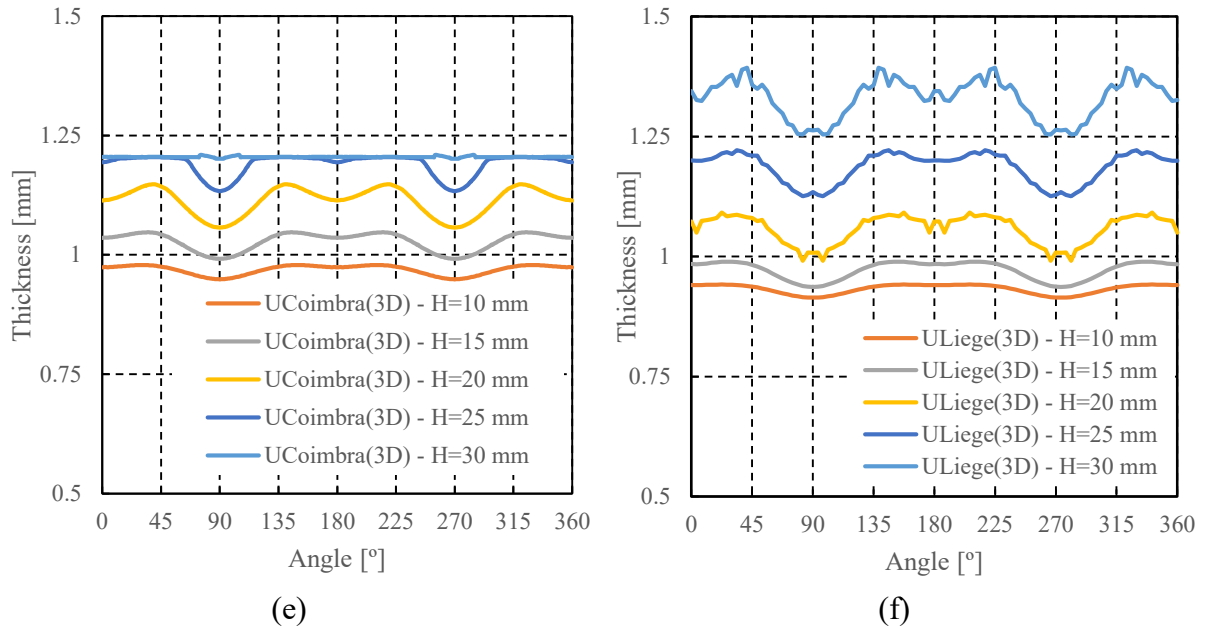
Figure 74 Evolution of the thickness along the cup circumference at different heights H = 15, 20, 25 and 30 mm from the cup bottom, by Hill48 criterion with the data set identified in Section 7.2.1 (Table 22): (a) LS-DYNA with shell elements, (b) PAM-STAMP with shell elements, (c) LS-DYNA with solid elements, (d) PAM-STAMP with solid elements, (e) DD3IMP with solid elements, and (f) Lagamine with solid elements

(a)   (b)
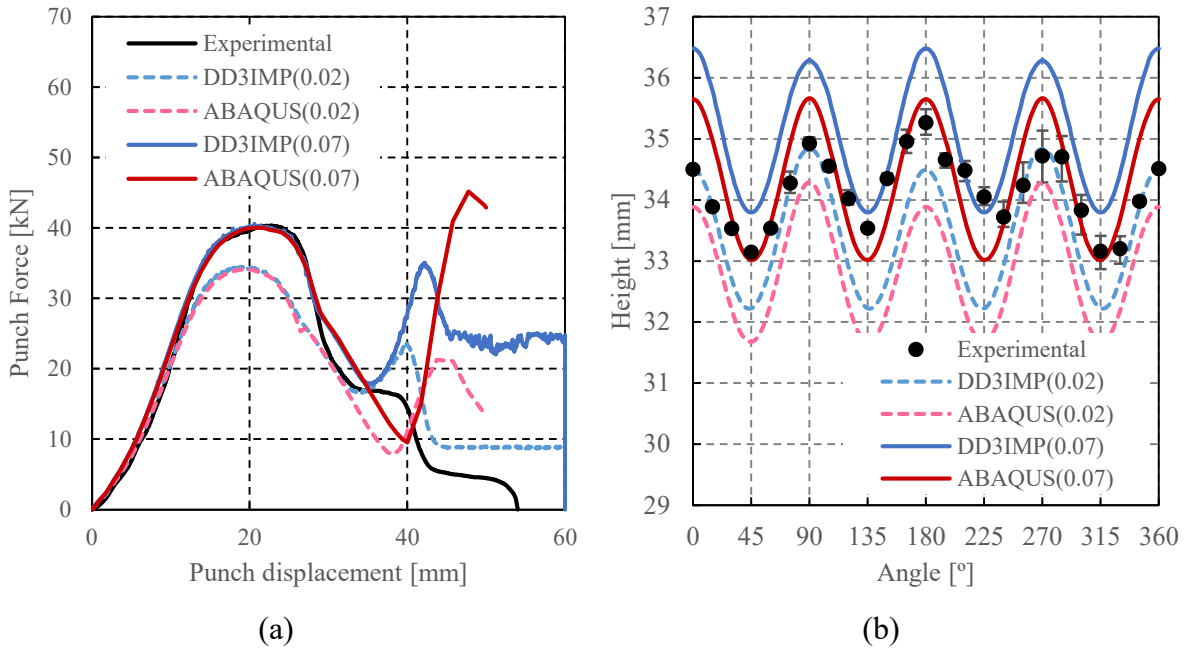
Figure 75 Comparison between experimental and predicted results by Hill48 criterion obtained with DD3IMP and built-in ABAQUS for the data set (Table 22 line1), solid elements and two different values of friction coefficient (0.02 and 0.07): (a) punch force-displacement, (b) earing profile

87
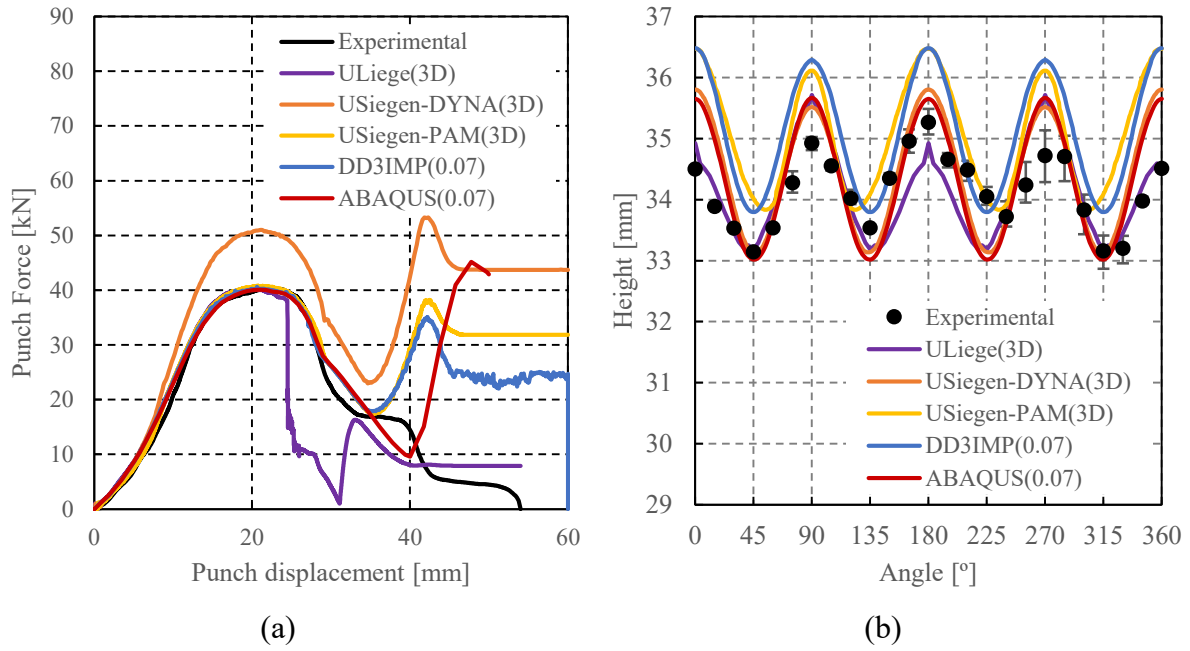
Figure 76 Comparison between experimental and predicted results by Hill48 criterion with the data set identified in Section 7.2.1 (Table 22) with solid elements and three similar values of friction coefficient (0.07, 0.075 USiegen and 0.082 ULiege): (a) punch force-displacement, (b) earing profile
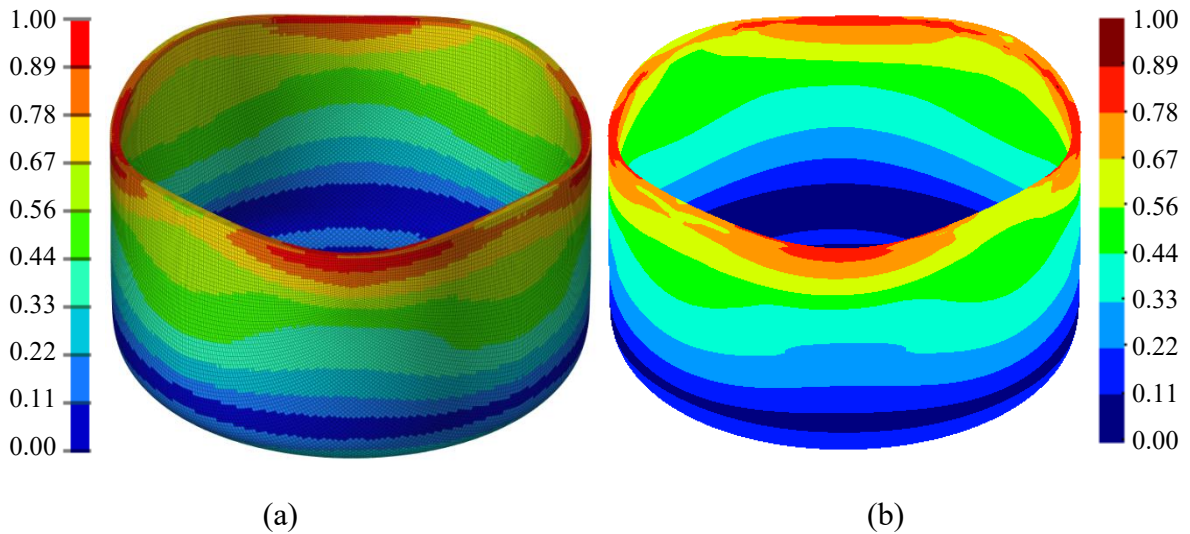
Figure 77 Distribution of the equivalent plastic strain predicted by Hill48 criterion for the data set (Table 22 line 1): (a) LS-DYNA with solid elements; (b) DD3IMP with solid elements

8.1.1.1.2 Hill48 with non-associated flow rule

As described in Section 6, the use of a non-associated flow rule with a potential of the same mathematical form as the Hill48 yield criterion allows increasing the number of anisotropy parameters in the elastoplastic model.

Three teams, USiegen, UPorto and UAalto used a non-associated flow rule in conjunction with the Hill48 yield criterion. While USiegen and UPorto used constant anisotropy properties (initial yield

88

stresses and Lankford coefficients) in Eqs. (71) to compute the input material data set, UAalto considered that both the parameters related with the plastic potential and the yield function evolve as a function of the equivalent anisotropic plastic strain (see Section 7.2.9). They also considered a different isotropic hardening law. Namely, USiegen and UPorto considered the Swift law (REEF parameters in Table 32), while UAalto adopted the Voce law (UAalto parameters in Table 32). USiegen adopted shell elements and the explicit code PAMSTAMP, while UAalto and UPorto used solid elements, with the implicit and explicit versions of ABAQUS, respectively. Moreover, the values adopted for the friction coefficient were μ = 0.075, μ = 0.05 and μ = 0.01, for USiegen, UPorto and UAalto, respectively.

The predicted punch force evolution with its displacement and the earing profiles are compared to the experimental ones in Figure 78(a). Regarding the punch force evolution, the differences between the predictions during the drawing phase reflect the use of a higher friction by USiegen. The differences between the predictions for the ironing stage are mainly related to the fact that USiegen used shell elements while UAalto and UPorto adopted solid elements (see also the discussion in Section 8.1.1.1 on the errors associated with performing simulations with shell elements and thus neglecting the thickness strains). Note that UAalto and UPorto adopted the same type of solid element and the same contact algorithm, which may allow some penetration (see Table 9 and Table 10). Interestingly, the numerical simulation performed by UAalto presents a lower ironing force, which is even slightly lower than the experimental one. This can be related with the very low friction coefficient (μ = 0.01), considering the very high contact pressure, which prevails during this stage of the cup drawing process. It can also be attributed to the use of the Voce type law, which saturates for an equivalent plastic strain higher than 0.40 (see Figure 68 for Voce and Swift stress-strain curves and the equivalent strain distribution, reaching values as high as 1.0 in Figure 77). However, in this particular case, the fact that the r-values present an increasing trend with the increase of the equivalent plastic strain (see Section 7.2.9) also modifies the plastic flow. It justifies a lower increase of the thickness in the outer edge of the vertical wall, similar to what is observed when adopting the von Mises yield criterion (see also Figure 27 in Section 4).

Regarding the prediction of the earing phenomenon, the results plotted in Figure 78(b) show that the use of non-associated plasticity, as implemented in PAMSTAMP, leads to a strong overestimation of the earing amplitude. The material at 45° with RD clearly shows a large resistance against plastic deformation, which correlates with the high value predicted for the normalized yield stress along this direction, as shown in Figure 79(a). Although the experimental stresses are used as input for the model, they are not properly described by the approach adopted in PAMSTAMP Shell case.

On the other hand, as shown in Figure 79, the solid element simulations with constant anisotropic parameters used by UPorto enable a proper description of both the normalized yield stresses and r-values in-plane distribution (see experimental reference in Figure 5(a) and (b)). UPorto results predict an earing amplitude closer to the experimental one, when compared with the one obtained by USiegen with PAMSTAMP, since the amplitude of the in-plane distribution of the normalized yield stress is lower. A high difference in the height predicted for RD and TD is observed in UPorto results, when compared with the one this team obtained with the associated flow rule (see Figure 72(b)). Finally, the approach adopted for the implementation of the non-associated flow rule by UPorto leads to a worse prediction of the earing profile than the one using Hill48 with an associated flow rule. Note that the difference between the height predicted along RD and TD is always higher for the simulations performed by UPorto, which can be related with the fixed gap between the die and the blank holder.

The UAalto simulation with solid element and evolving anisotropic parameters within the simulation (see Table 31) is able to provide a result closely related to the experimental profile.
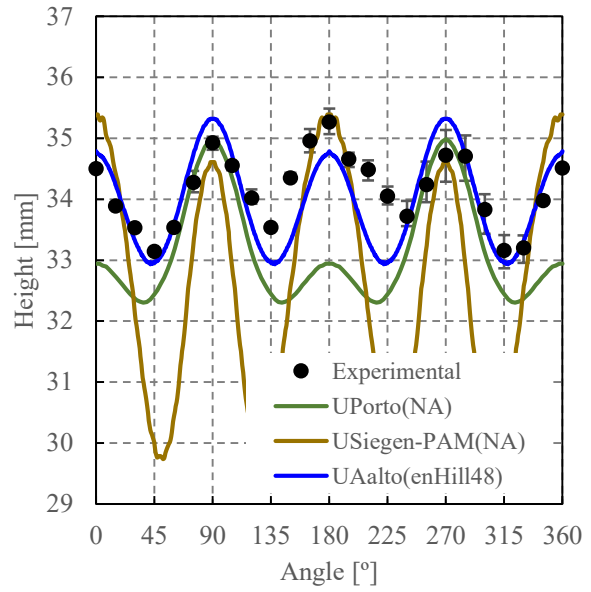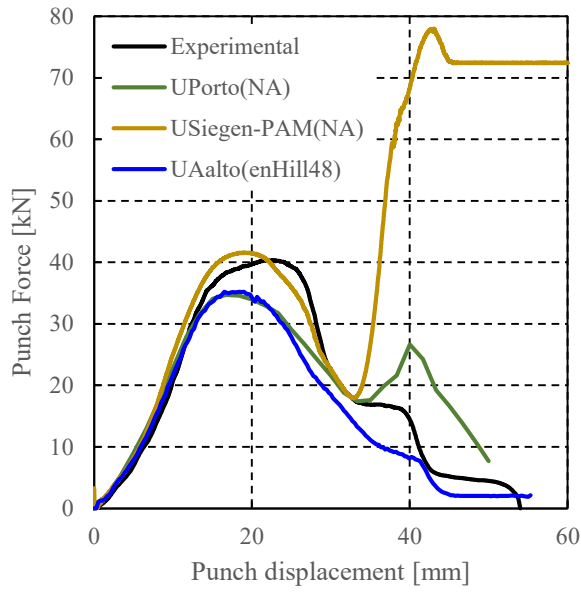
Figure 78 Comparison between experimental and predicted results by (NA) Hill48 criterion with constant or evolving anisotropy parameters identified in Section 7.2.9 (Eqs. (71)): (a) punch force-displacement, (b) earing profile
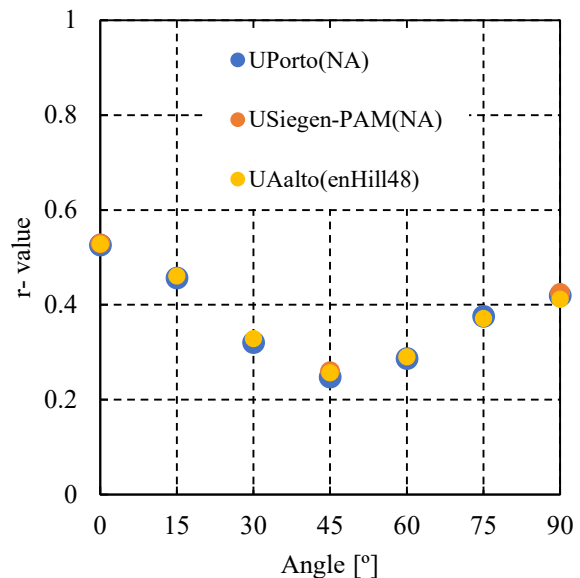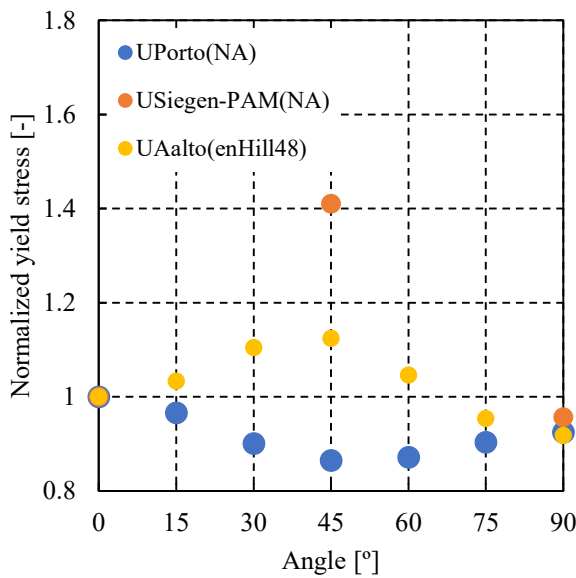
Figure 79 Predicted FE results by (non-associated flow rule) Hill48 criterion with constant or evolving anisotropy parameters identified in Section 7.2.9 (Eqs. (71)): (a) uniaxial tensile flow stresses, (b) Lankford coefficients (*r*-values). Note that for UAalto(enHill48) the results are plotted only for an equivalent plastic strain of 0.18

90

The results from the simulation performed with the associated flow rule by USiegen, using PAMSTAMP and shell elements are compared with the ones obtained with the non-associated flow rule in Figure 80. Both models enable a proper description of the in-plane distribution of the *r*-values (see Figures 73 and 79). However, unlike what was expected, for the non-associated flow rule the in-plane distribution of the normalized yield stress presents a higher amplitude then the one obtained with the associated flow rule (see Figure 73 and Figure 79). During the first part of the drawing stage, the force predicted with the non-associated flow rule is slightly higher, which correlates with the higher value predicted for the normalized yield stresses (see Figure 80(a)). The higher amplitude observed for the in-plane distribution of the normalized yield stress also justifies the increase in the earing amplitude observed in Figure 80(b).

(a)   (b)
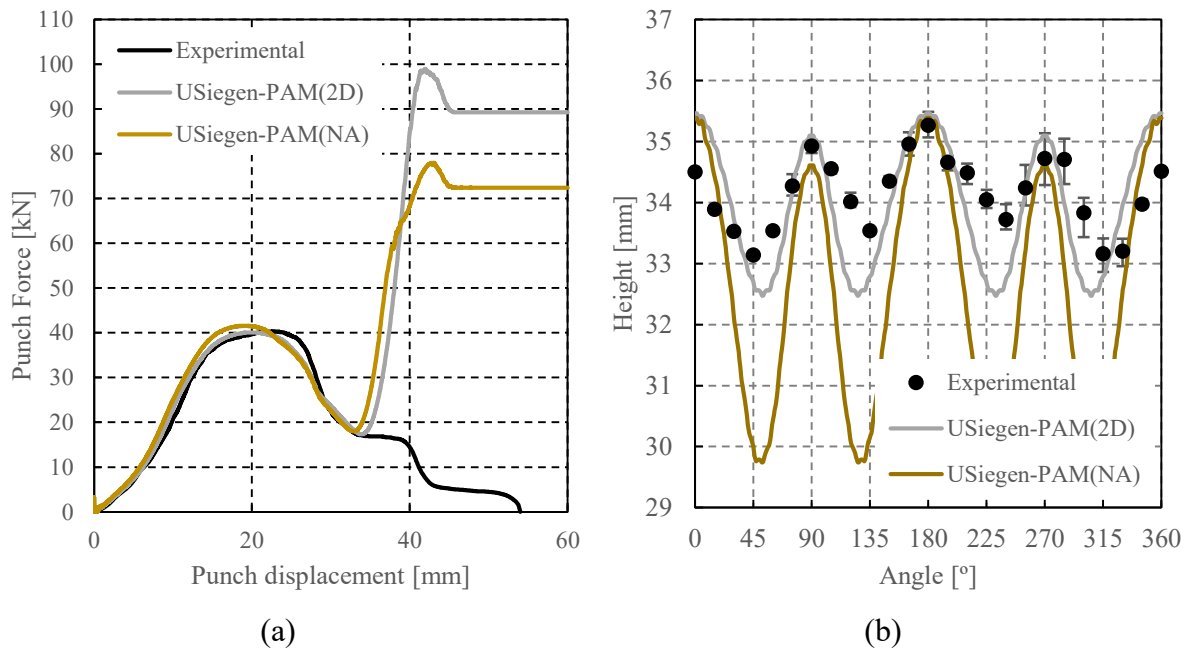
Figure 80 Comparison between experimental and predicted results with shell elements and Hill48 criterion with associated flow rule (data set Table 22-line 1) and non-associated flow rule (data set computed by Eqs. (71) for constant anisotropy properties (see Tables 4 and 5)): (a) punch force-displacement, (b) earing profile

8.1.1.2 *CB2001 yield criterion*

In the following, CB2001 or the Cazacu (2001) orthotropic yield criterion (Eq. (15)) was applied to model the cup drawing process, with the anisotropy coefficients identified in Section 7.2.5 (Table 26) and the Swift hardening law in Section 7.3 (Table 32) . UCoimbra performed the numerical simulation with DD3IMP code, using solid elements and a value of μ = 0.020 for the friction coefficient.

Figure 81(a) compares the predicted forming force vs. the punch stroke with the experimental data, while the earing profile prediction is plotted in Figure 81(b). It shows four ears, as observed in the experimental tests. The earing profile is similar to the one obtained with (A) Hill48 (see Figure 72). CB2001 predicts an average height of h_{avg}=33.14 mm against h_{avg}=34.10 mm in experiments (2.8% difference) and a cup profile amplitude of 3.82 mm, against 2.29 mm experimental value (67% difference) and 2.62 mm obtained with (A) Hill48, using the same friction coefficient and code with the data set of Table 22-line 1. The slightly higher amplitude of Hill48 results may be correlated with the

fact that CB2001 predicts a slighter more pronounced anisotropy in the yield stresses than Hill48 (see Figure 73(a) and Figure 82(a)).

Figure 83 shows the evolution of the wall thickness along the cup circumference (taken at different cup height from the cup bottom). The comparison with the results obtained with the Hill48 yield criterion (see Figure 74(e)), indicates that the CB2001 leads to a slightly sharper variation along the circumferential direction. For example, for H = 20mm, the thickness variation is 0.09 mm for Hill48 while for CB2001, it is 0.16 mm.

(a)   (b)
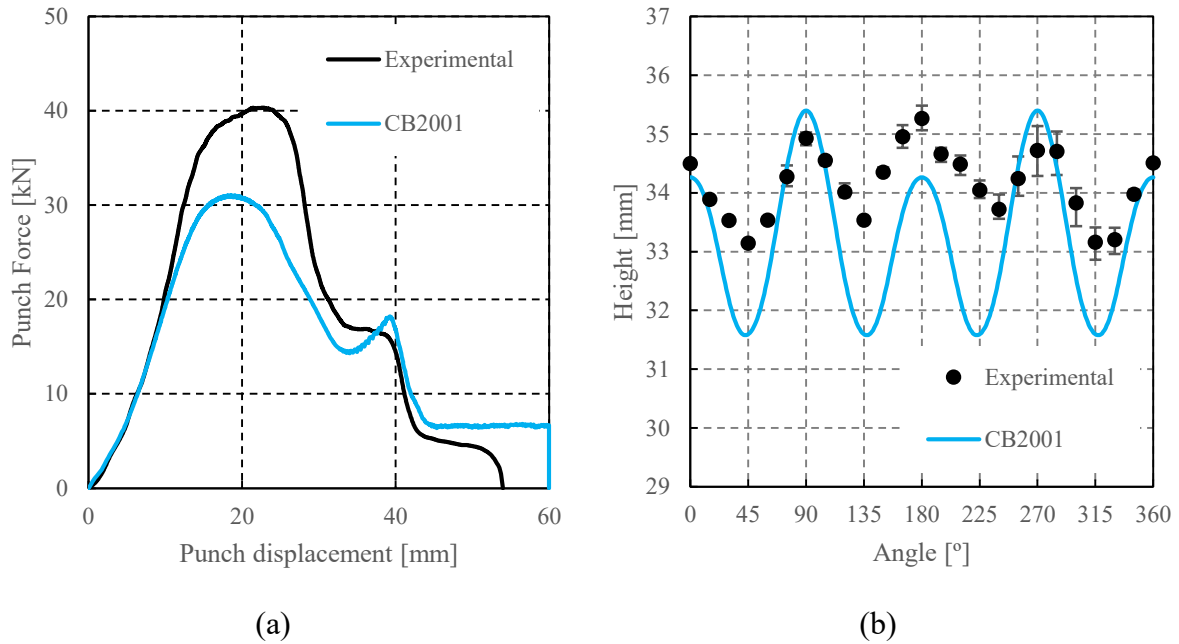
Figure 81 Comparison between experimental and predicted results by CB2001 with the anisotropy coefficients identified in Section 7.2.5 (Table 26): (a) punch force-displacement, (b) earing profile
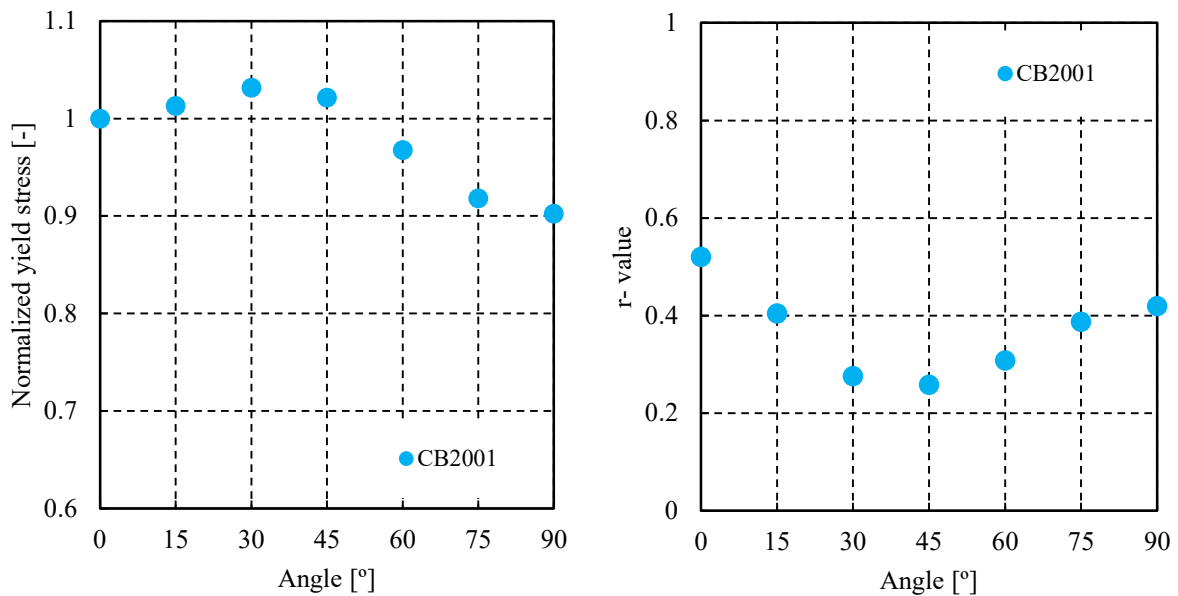
Figure 82 Predicted FE results by CB2001 criteria with the anisotropy coefficients identified in Section 7.2.5
(Table 26): (a) uniaxial tensile flow stresses, (b) Lankford coefficients (*r*-values)
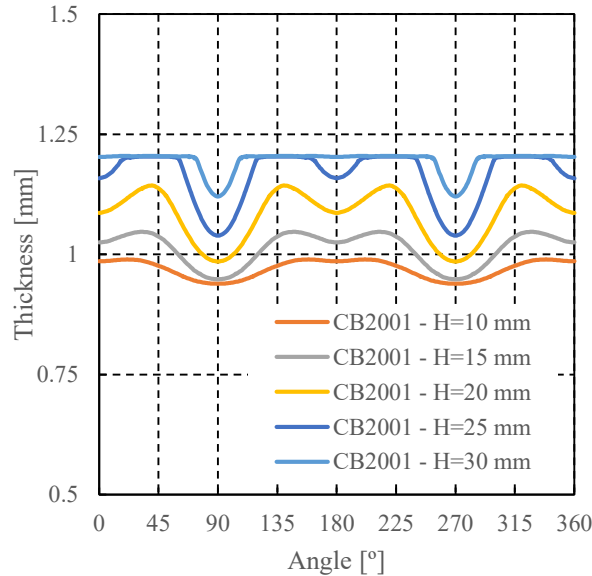
Figure 83 Evolution of the thickness along the cup circumference at different heights H = 15, 20, 25 and 30 mm
from the cup bottom, by CB2001 with the anisotropy coefficients identified in Section 7.2.5 (Table 26)

8.1.1.3 *Yld2004-18p yield criterion*

Two teams contributed with FE simulations for the Yld2004-18p yield criterion using POSTECH data set of anisotropy coefficients (Table 28-line 1) and solid elements. POSTECH used their own implementation in ABAQUS explicit solver (VUMAT), Voce hardening law (see Table 32) and $\mu = 0.100$, while USiegen used the built-in implementation of Yld2004-18p in LS-DYNA (explicit), the Swift hardening law (see Table 32 data set of REEF), and $\mu = 0.075$.

NTNU performed an identification of the parameters for the Yld2004-18p yield criterion based on the experimental data provided by TUAT (see Section 7.2.6 and Table 28, line 2). This team performed simulations using their own implementation of Yld2004-18p in ABAQUS implicit solver (UMAT), considering the same type of solid elements as POSTECH, a Voce hardening law (see Table 32) and $\mu = 0.090$. USiegen performed simulations using the same FE model for both data sets, the one of POSTECH and the one of NTNU.

The results with the FE code ABAQUS obtained for POSTECH and NTNU data sets and C3D8R solid elements are shown in Figure 84. The punch force evolution is well captured, although it is overestimated by POSTECH results, for both the drawing and the ironing stage (see Figure 84(a)). This can be related with the higher friction coefficient value but also with the coarse discretization adopted, when compared with the one used by UAalto using also an explicit strategy and the same solid element (see Table 9). Figure 84(b) shows that the cup drawing profiles obtained by POSTECH and NTNU, using their own implementations of Yld2004-18p in ABAQUS. Each team predicts 8 ears but their minimum and maximum locations in the cup height are opposite. However, the POSTECH and NTNU predictions for *r*-values and yield stresses are practically identical (see Sections 7.1.2.4 and 7.2.6), using their

93

respective sets of parameters for Yld2004-18p. Note that with both sets of anisotropy coefficients, the predicted earing amplitudes are similar and much smaller than the experimental one.

In Figure 85, the results obtained by USiegen, with the built-in Yld2004-18p in FE code LS-DYNA, for POSTECH and NTNU data sets of parameters are shown. Figure 85(a) shows that with POSTECH anisotropy coefficients and a friction coefficient slightly lower (USiegen μ=0.075, POSTECH μ=0.10), both the drawing and the ironing force are underestimated. On the other hand, for the set of anisotropy parameters identified by NTNU, the predicted trend during the drawing stage is the same irrespective of the code used (LS-DYNA or ABAQUS). The trend for the ironing stage is similar to the one observed with Hill48(A) (see Figure 72(a)), which can be related with the element type. Note also that the predicted trends for the earing profile obtained with the model built-in LS-DYNA are consistent with the predicted thickness distributions in the cup wall, as shown in Figure 86. The fact that the set of parameters provided by POSTECH leads to lower average values for the thickening of the cup wall can also help explaining the differences observed in the evolution of the punch force (see Figure 85(a)).

Note that with POSTECH anisotropy coefficients, the FE cup drawing results obtained with LS-DYNA show four ears, as in the experiments but the amplitude is strongly overestimated (see Figure 85(b)). For the same set of anisotropy coefficients, the number of ears is different and the maxima and minima in cup height are at opposite location with respect to the results reported by POSTECH (see Figure 84(b)).

For the NTNU anisotropy coefficients, the LS-DYNA profile shows 12 ears and the amplitude is underestimated. The comparison with the results obtained by NTNU, for the same data set, shows that although the number of ears is different (12 vs. 8), the amplitude and the location of the global maxima and minima are similar, but contrary to the experimental observations. However, for both sets of anisotropy coefficients for Yld2004-18p, the predictions for the anisotropy in yield stresses and r-values obtained with the LS-DYNA code are the same (see Figure 87) and are close to the experiments (Figure 5).

The analysis of the results obtained with other yield criteria with different FE models/codes, including different types of elements and contact algorithms, indicates that these parameters mainly affect the average height and the ears amplitude, but have no effect on the number of ears or on the location of the ears, which are driven by the yield locus. Therefore, the Yld2004-18p criterion seems to be very sensitive to the formulations adopted in its implementation.
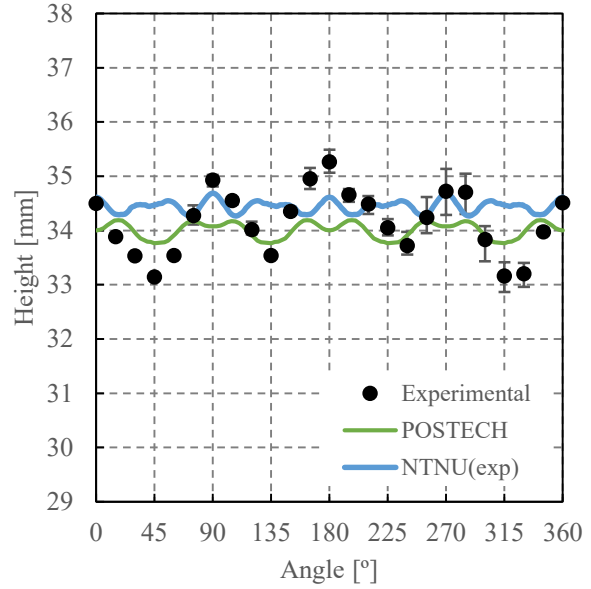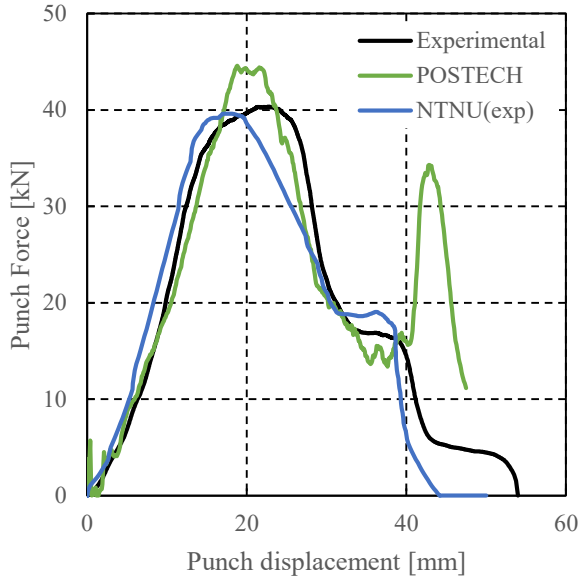
Figure 84 Comparison between experimental and predicted results by Yld2004-18p criterion with data set of POSTECH, using ABAQUS explicit (POSTECH VUMAT) and with data set of NTNU for their own UMAT implementation in ABAQUS (see Section 7.2.6 (Table 28)): (a) punch force-displacement, (b) earing profile
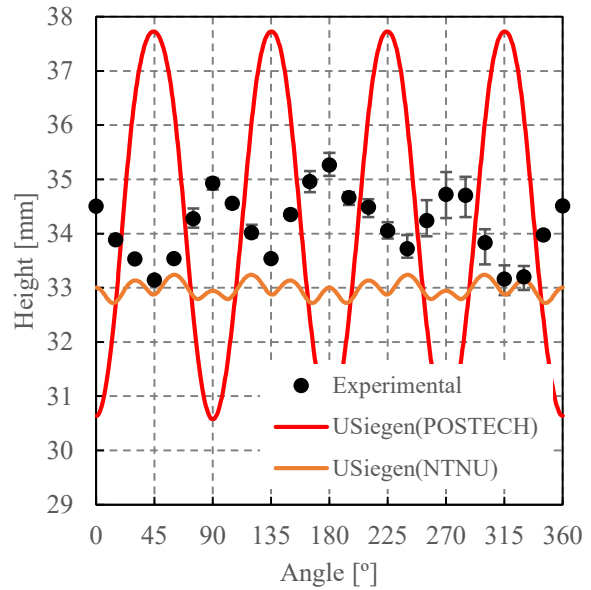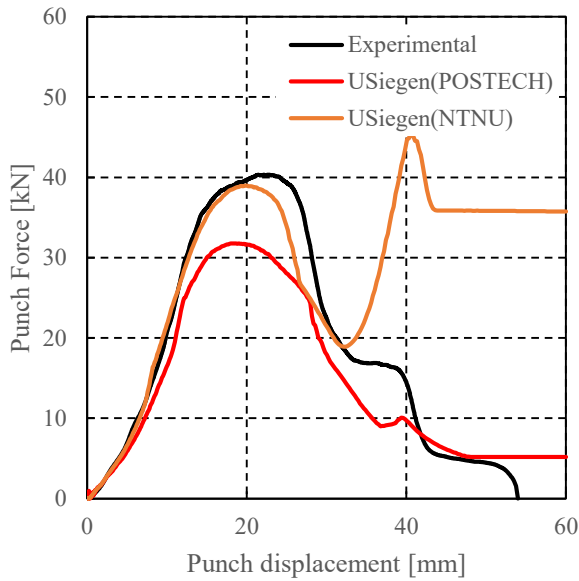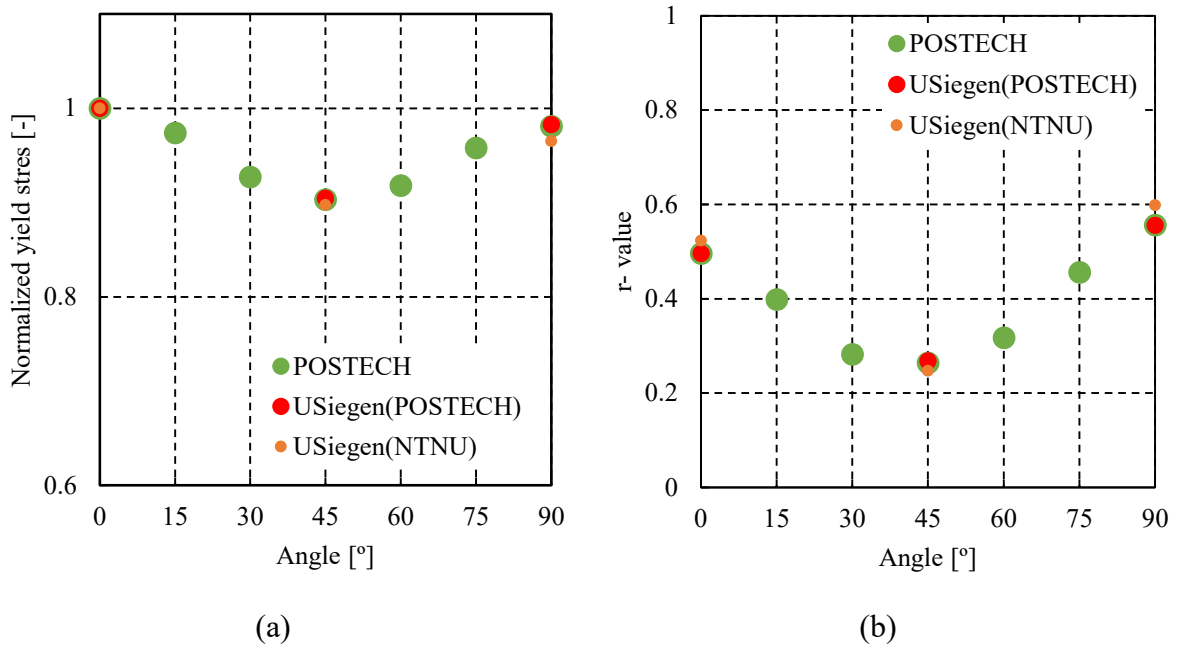

Figure 85 Comparison between experimental and predicted results by Yld2004-18p criterion with the anisotropy coefficients provided by POSTECH and NTNU (see Section 7.2.6 (Table 28)), using LS-DYNA (built-in; USiegen): (a) punch force-displacement, (b) earing profile
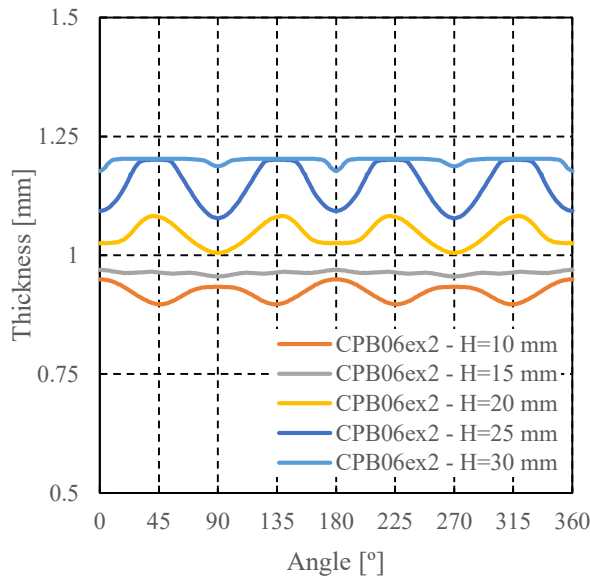
95
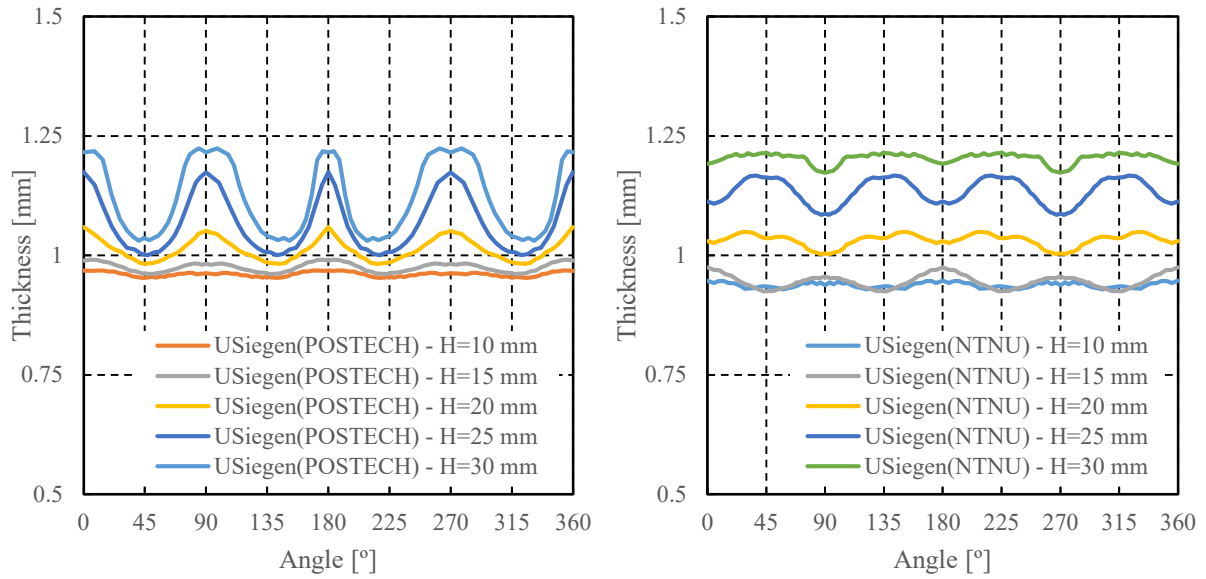
Figure 86 Evolution of the thickness along the cup circumference at different heights H = 15, 20, 25 and 30 mm from the cup bottom, using LS-DYNA (built-in; USiegen) and the set of anisotropy coefficients provided by: (a) POSTECH and (b) NTNU (see Section 7.2.6 (Table 28))

Figure 87 FE predictions of the anisotropy for uniaxial loadings according to Yld2004-18p criterion for the anisotropy coefficients, provided by POSTECH and NTNU (see Section 7.2.6 (Table 28)), using LS-DYNA (USiegen) and ABAQUS (POSTECH): (a) uniaxial tensile flow stresses, (b) Lankford coefficients (*r*-values)

96

8.1.1.4 CPB06ex2 yield criterion

The results presented in this section were obtained with DD3IMP (implicit) code, using the CPB06ex2 yield criterion (anisotropic parameters Table 29) and the Voce hardening law (Table 32, UCoimbra). In this case, a constant friction coefficient μ = 0.1 was used (see Table 10).

The predicted punch force evolution with its displacement and the earing profiles are compared to the experimental ones in Figure 88(a). The use of a high value for the friction coefficient enables a good prediction of the experimental drawing force (0.8% difference) while the ironing force is overestimated (see in Figures 72, 75 and 81 the light blue curves obtained for other yield criteria with DD3IMP and μ = 0.02 or 0.07). Regarding the earing, 4 ears are predicted, with an amplitude of 1.2 mm against the experimental value of 2.29 mm; the predicted minimum in cup height is deviated to approximately 25° from RD, which can be correlated to the predicted yield stress anisotropy shown in Figure 89(a) (i.e., an extra inflexion point in the yield stress distribution). Figure 90 presents the thickness distribution along the cup circumference, for different heights. The higher thinning predicted by CPB06ex2 for the lower heights (H = 10 and H = 15 mm), when compared to other results obtained with DD3IMP (see Figures 74(e) and 83), can be related with the higher value used for the friction coefficient.
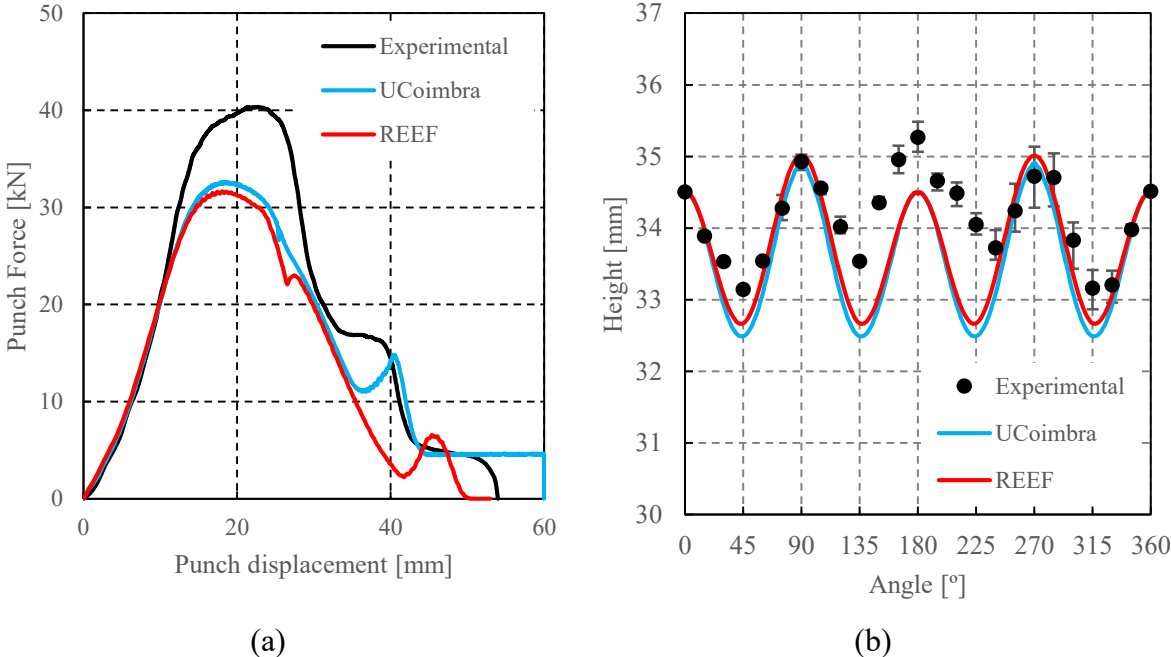

(a)   (b)
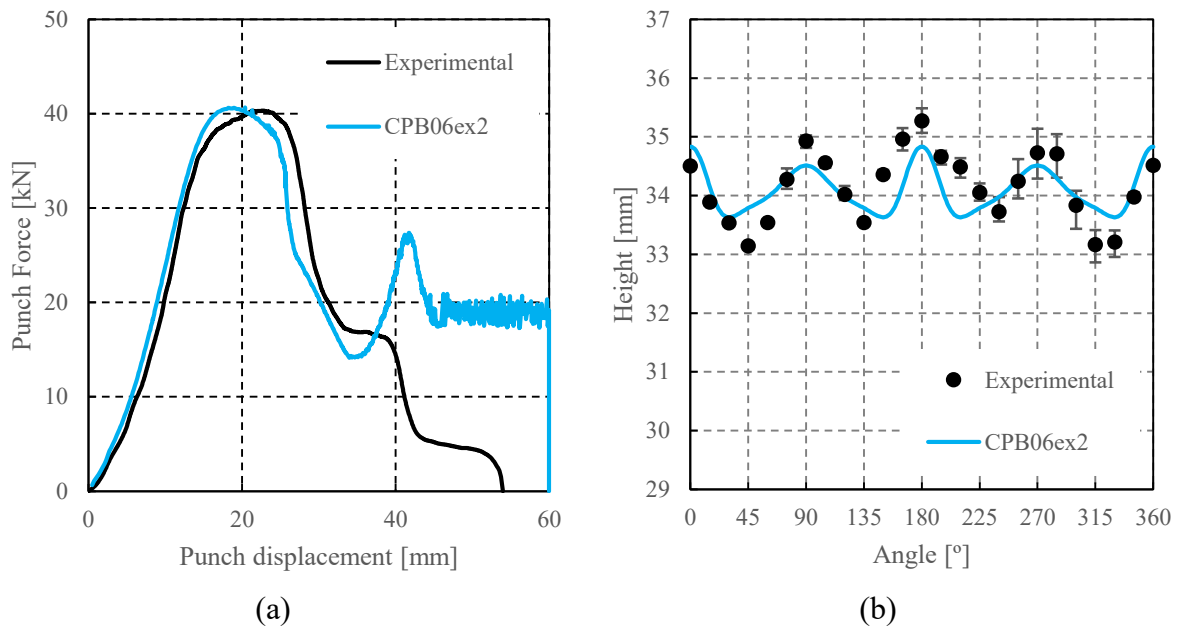
Figure 88 Comparison between experimental and predicted results by CPB06ex2 criterion with the anisotropy coefficients identified in Section 7.2.7 (Table 29): (a) punch force-displacement, (b) earing profile
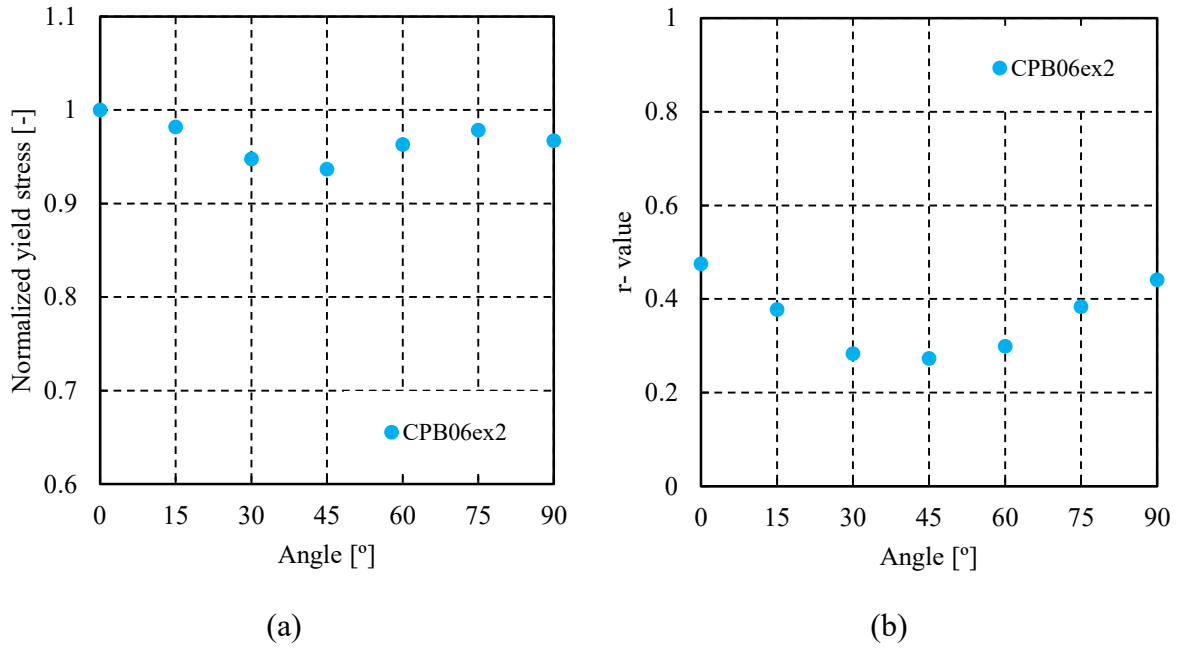
Figure 89 Predicted FE results by CPB06ex2 criterion with the anisotropy coefficients identified in Section 7.2.7 (Table 29): (a) uniaxial tensile flow stresses, (b) Lankford coefficients (*r*-values)

Figure 90 Evolution of the thickness along the cup circumference at different heights H = 10, 15, 20, 25 and 30 mm from the cup bottom, by CPB06ex2 criterion with the anisotropy coefficients identified in Section 7.2.7 (Table 29)

8.1.1.5 *Caz2018-Orth yield criterion*

In the following, Caz2018-Orth or the Cazacu (2018) orthotropic yield criterion (Eq. (16)) in conjunction with the anisotropy coefficients of Table 30, (see Section 7.2.8) will be applied to model cup drawing of the AA 6016-T4 alloy. Two teams reported results for this yield criterion using the same data set: UCoimbra and REEF. UCoimbra performed the numerical simulation with DD3IMP code, while REEF used ABAQUS (implicit). In this case, both teams used the Swift hardening law (Table 32), the same value of 0.020 for the friction coefficient and solid elements.

98

The predictions of Caz2018-Orth model for cup drawing are shown in Figure 91. Note that the cup-height profile is well described. A four-ear profile with ears located at RD and TD and a minimum cup height at 45° from RD is predicted, i.e. as observed in the test. The results obtained with ABAQUS (REEF) predict an average height of h_{avg}=33.70 mm against h_{avg}=34.70 mm experimentally (1.3% difference), a cup profile amplitude of 2.35 mm against 2.29 mm experimentally (2.5% difference). Furthermore, the predicted maximum height of the cup is 35.01 mm against 35.27 mm experimentally (0.8% difference) and the minimum height of the cup is 32.67 mm against 32.99 mm experimentally (1% difference). In this context, the excellent correlation in the results obtained for the earing profile by both codes should be noted. As shown in Figure 91(b), the results obtained with DD3IMP present a minimum height of the cup of 32.49 mm against 32.67 mm from ABAQUS, with negligible differences in the maximum height. Both codes predict the same in-plane yield stress and r-values evolutions, as shown in Figure 92.

Figure 93 presents the evolution of the wall thickness along the cup circumference (taken at different heights from the cup bottom). The slight differences observed in the earing profile can be related with the contact algorithms adopted in both codes (see Table 10). As previously mentioned, the algorithm adopted in DD3IMP imposes the normal constraint more strictly, leading to a higher ironing force (see Figure 91(a)) and a lower thickness value in the top of the vertical wall (see Figure 93). Nevertheless, for Caz2018-Orth the earing results are not as sensitive to the differences in the contact algorithm as in the case of Hill48 (see Figure 72(b)). Note that with von Mises (see Figure 27(b)) the cup height was also not sensitive to the differences between the codes.

The influence of the value of the friction coefficient on the results is depicted in Figure 94, which shows the results obtained with the implicit code DD3IMP (UCoimbra). As observed for the case of von Mises and Hill48, increasing the friction coefficient leads to an increase in maximum drawing force (for Caz2018-Orth a friction coefficient slightly higher than 0.07 may be required to give a perfect match with the experimental one). Likewise, the increase of the friction coefficient leads to the same number of ears (slight decrease in the earing amplitude from 2.42 mm to 2.38 mm, against the experimental value of 2.29 mm).

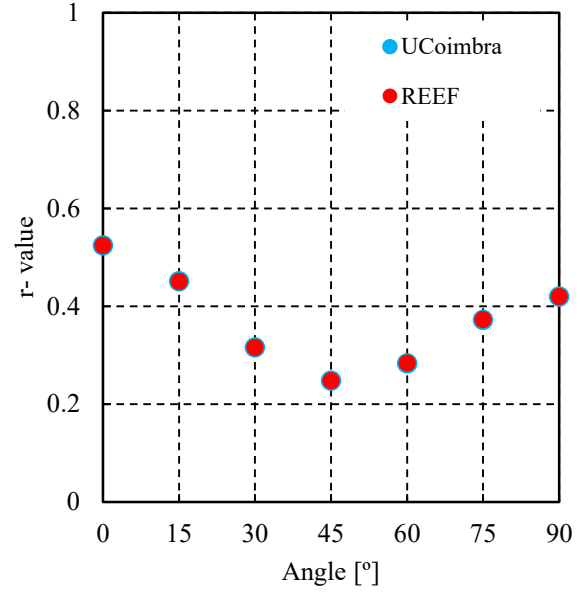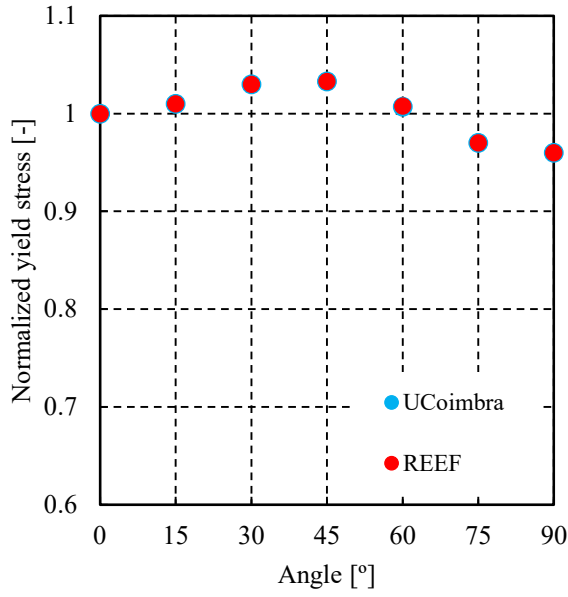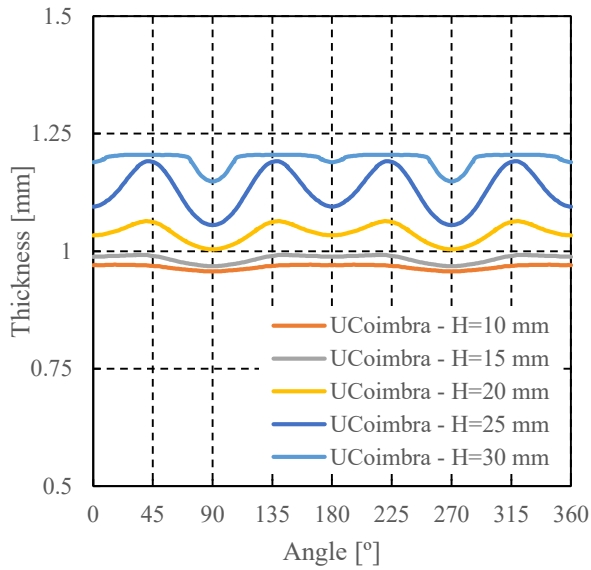(a)   (b)

Figure 91 Comparison between experimental and predicted results by Caz2018-Orth criterion with the anisotropy coefficients identified in Section 7.2.8 (Table 30): (a) punch force-displacement, (b) earing profile
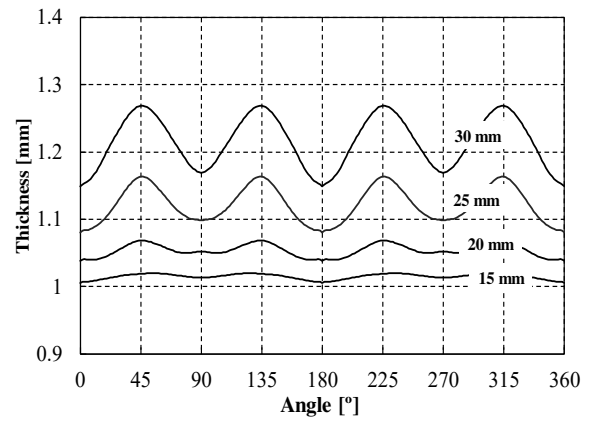
99

(a)

(b)

Figure 92 Predicted FEM results by Caz2018-Orth criterion with the anisotropy coefficients identified in Section 7.2.8 (Table 30): (a) uniaxial tensile flow stresses, (b) Lankford coefficients (*r*-values)

(a)

(b)

Figure 93 Evolution of the thickness along the cup circumference at different heights H = 15, 20, 25 and 30 mm from the cup bottom, by Caz2018-Orth criterion with the anisotropy coefficients identified in Section 7.2.8 (Table 30): (a) DD3IMP, (b) ABAQUS

100
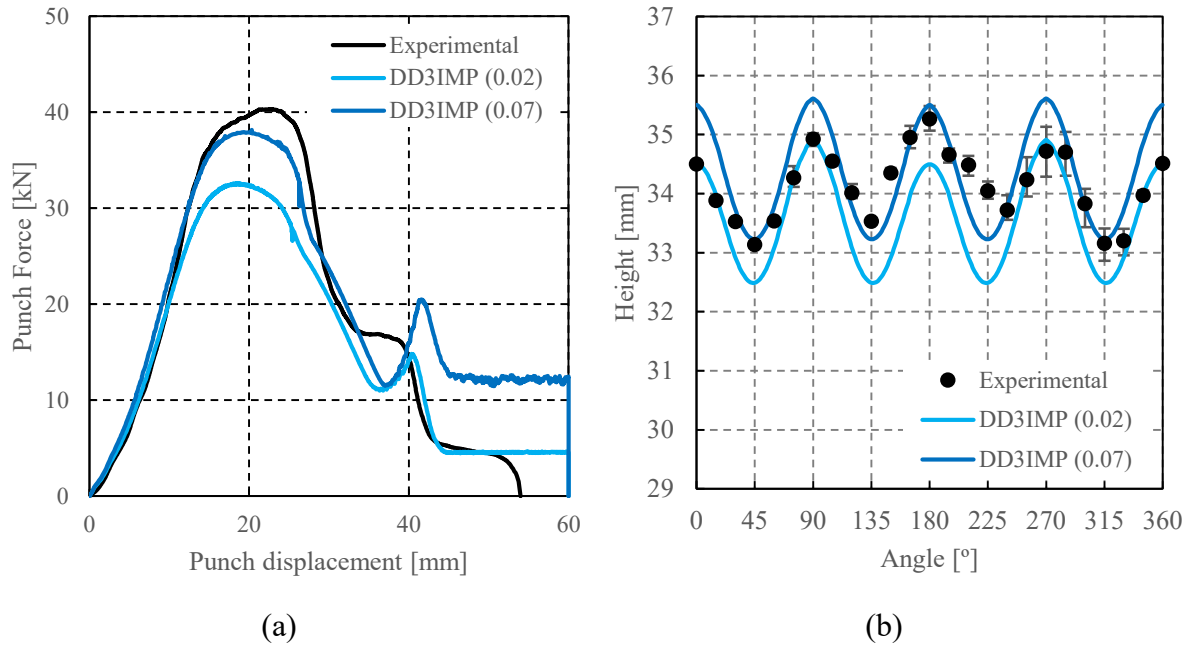
Figure 94 Comparison between experimental and predicted results by Caz2018-Orth criterion with the anisotropy coefficients provided by the organizers (Section 7.2.8 (Table 30)), obtained with DD3IMP for two values of the friction coefficient, 0.02 and 0.07 respectively: (a) punch force-displacement, (b) earing profile

8.1.2   2-D orthotropic yield functions and solid or shell elements
8.1.2.1   Yld89 yield criterion

USakarya performed the numerical simulation using the Yld89 yield criterion (anisotropy parameters in Table 25) and the Swift law (hardening parameters in Table 32), identified with the experimental data provided by TUAT, as described in Section 7.2.4. The simulation was performed with LS-DYNA code, using shell elements (see details in Section 5).

The predicted punch force evolution with its displacement and the earing profile are compared to the experimental ones in Figure 95. The drawing force is accurately predicted by using μ = 0.100. The fact that USakarya used a clearance between the punch and the die of 1.4 mm instead of 1.2 mm, explains the smoother evolution predicted for the punch force, although the ironing effect is not totally avoided.

Regarding the earing profile, the trend observed in Figure 95(b) shows 4 ears, with an amplitude higher than the experimental one. The comparison with the simulations performed with Hill48 (associated flow rule (see Figure 71), indicates that Yld89 predicts a similar amplitude for the ears. The sets of material parameters lead to an accurate in-plane distribution of the r-values, but overestimate the normalized yield stresses (Figure 96 and Figure 5(a) for experimental results). The average height predicted with Yld89 is closer to the one obtained with Hill48((A) and smaller values of friction coefficient (0.02 and 0.05 instead of 0.10). This can also be related with the higher value considered for the gap between the punch and die, which reduces the ironing effect and, consequently, the average height.
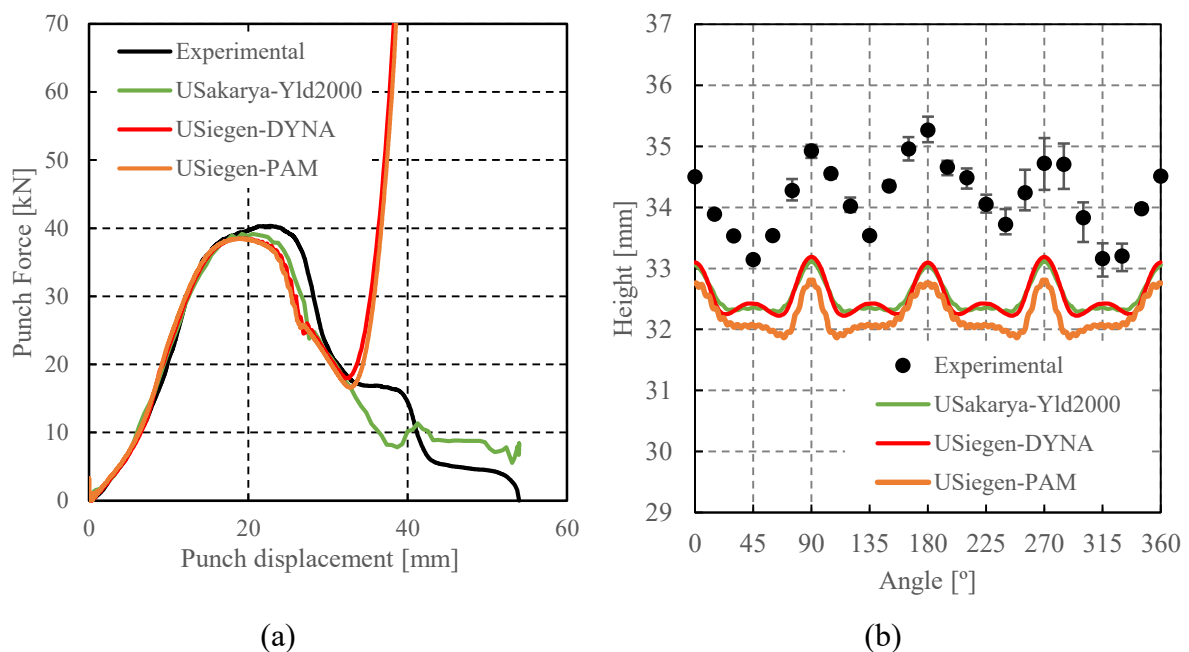
101
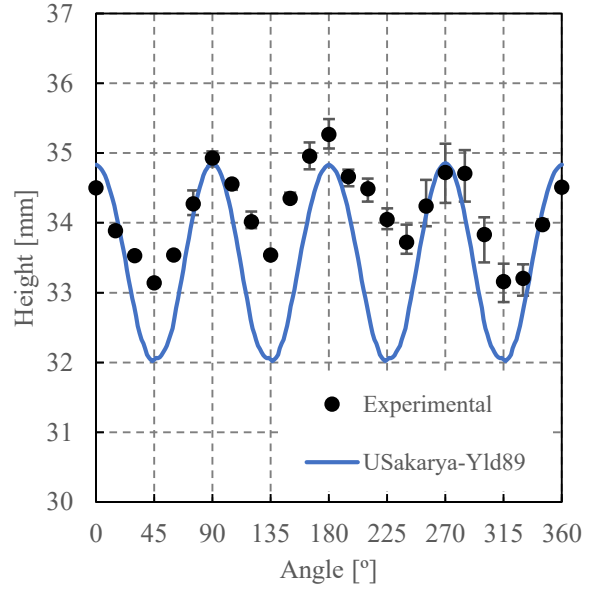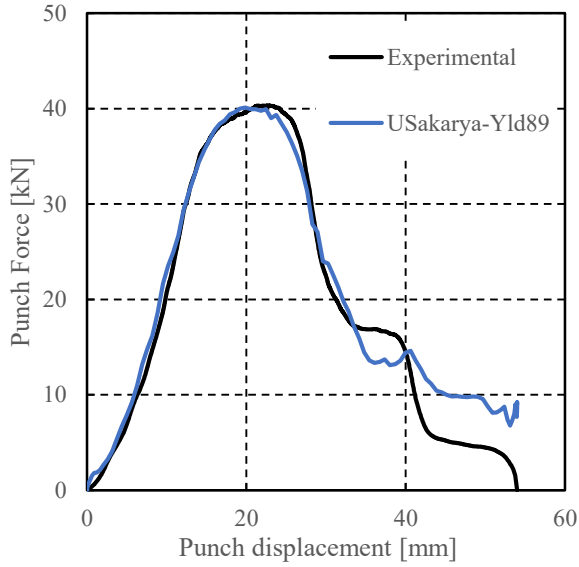
Figure 95 Comparison between experimental and predicted results by Yld89 criterion with the anisotropy coefficients identified in Section 7.2.4 (Table 25): (a) punch force-displacement, (b) earing profile
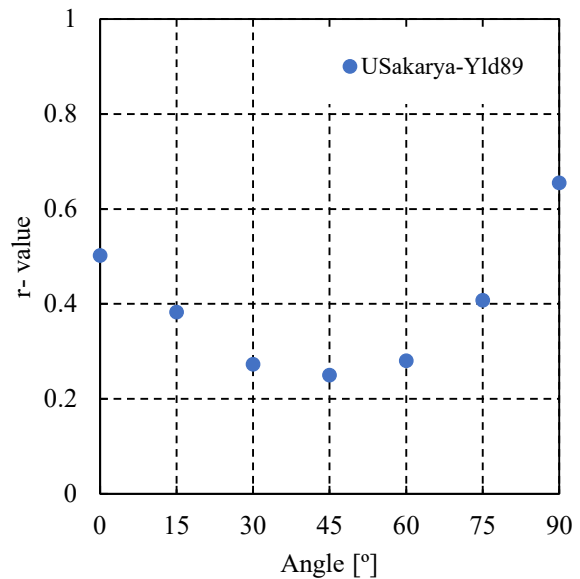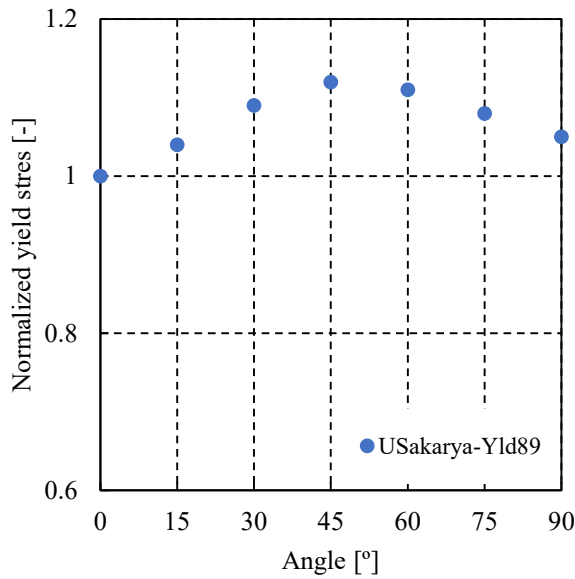
Figure 96 Predicted FEM results by Yld89 criterion with the anisotropy coefficients identified in Section 7.2.4 (Table 25): (a) uniaxial tensile flow stresses, (b) Lankford coefficients (*r*-values)

8.1.2.2 Yld2000-2D yield criterion

In this section, the contributions from two teams are analysed. The results presented by USakarya were all obtained using LS-DYNA FE code. USiegen performed numerical simulations using both LS-DYNA and PAMSTAMP. Both teams considered the Swift hardening law (Table 32) and the POSTECH

set of anisotropy parameters (see Section 7.2.6, Table 27). All numerical simulations were performed with shell elements, (the same type in the case of LS-DYNA (see Table 9)). Moreover, the contact algorithm adopted in LS-DYNA was also identical, although USakarya adopted a slightly higher friction value (μ = 0.100 instead of μ = 0.075). Moreover, USakarya used a clearance between the punch and the die of 1.4 mm instead of 1.2 mm.

The predicted punch force evolution with displacement and the earing profiles are compared to the experimental ones in Figure 97. All the models slightly underestimate the drawing force. The value predicted by LS-DYNA is slightly higher for the USakarya model, which can be related to the slightly higher value for the friction coefficient. Regarding the ironing force, the use of a higher clearance between the punch and the die, by USakarya, explains the smoother evolution predicted for the punch force in this stage. These results indicate that the effect of the clearance between the die and the punch is mainly visible in the ironing stage.

(a)   (b)

Figure 97 Comparison between experimental and predicted results by Yld2000-2D criterion with the anisotropy coefficients identified in Section 7.2.6 (Table 27): (a) punch force-displacement, (b) earing profile

Regarding the earing profile, 8 ears are predicted, with an amplitude lower than the experimental one, as for the Yld2004-18p with the POSTECH data set, although in that case solid element were used (see Figure 84(a)). USakarya and USiegen simulations provide a similar description of the normalized yield stress and r-values in-plane distribution (see Figure 98). Interestingly, the earing trend for Yld2000-2D presents maxima at 0°, 45° and 90° from RD, as the results obtained by NTNU with Yld2004-18p, identified using only experimental data (parametrization presented in Section 7.2.6). Both yield criteria underestimated the earing amplitude. In the case of Yld2000-2D, the average height of the cup is underestimated, although the drawing force is well described. Finally, the clearance between the die and the punch presents a negligible effect in the earing profile, which confirms the previously mentioned difficulties of shell elements in the analysis of the ironing process.
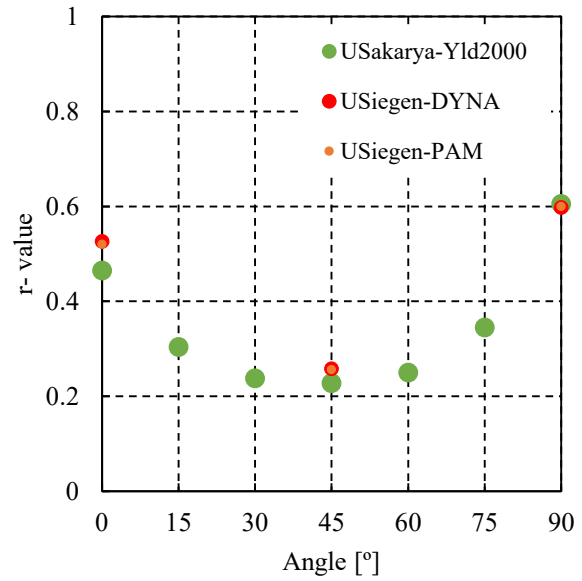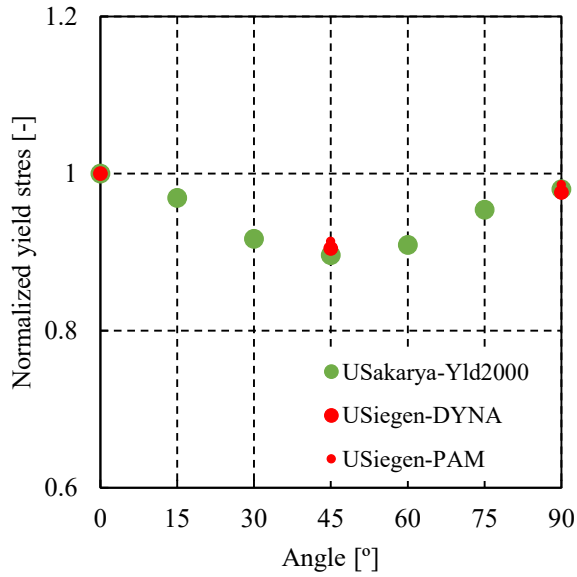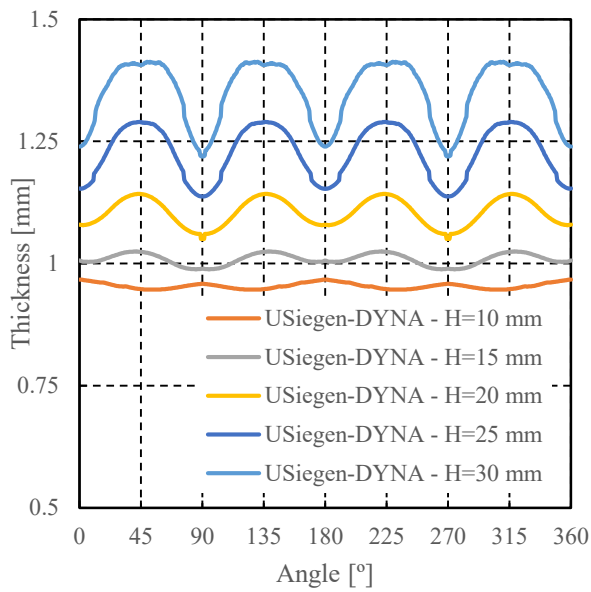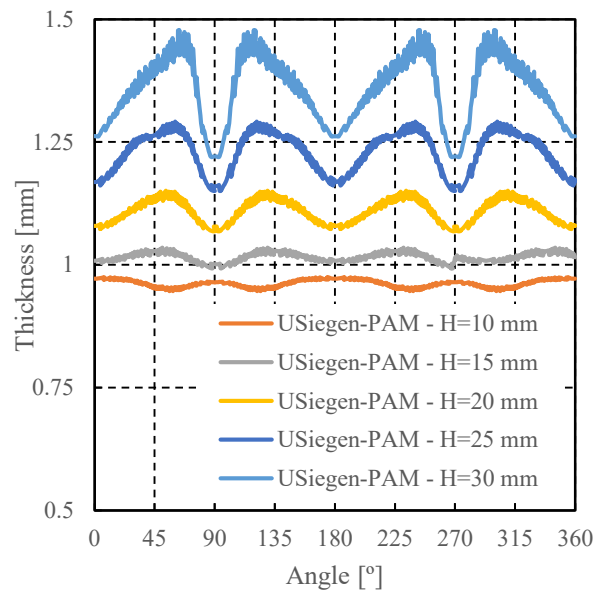
Figure 98 Predicted FE results according to the Yld2000-2D criterion with the anisotropy coefficients identified in Section 7.2.6 (Table 27): (a) uniaxial tensile flow stresses, (b) Lankford coefficients (*r*-values)

Figure 99 presents the thickness distribution along the cup circumference, for different heights, only for the results obtained with Yld2000-2D, by USiegen. Although the evolution predicted for each height is similar, the results obtained with PAMSTAMP present the maximum thickness height slightly away from the 45° from RD, which seems to correlate with the different trend for the earing profile close to this location (see Figure 97(b)).

Figure 99 Evolution of the thickness along the cup circumference at different heights H = 15, 20, 25 and 30 mm from the cup bottom, by Yld2000-2D criterion with the anisotropy coefficients identified in Section 7.2.6 (Table 27): (a) LS-DYNA, (b) PAM-STAMP

104

8.1.2.3 HomPol4 and HolmPol6 yield criteria

Hereafter, the contributions from the USakarya team, based on HomPol4 and HolmPol6 yield criteria (homogeneous polynomial yield functions described in Section 6.1.1) are presented. The anisotropy parameters were identified in Section 7.2.2 (Table 23) and Section 7.2.3 (Table 24), respectively. They were associated either with a Swift isotropic hardening or a single term Chaboche kinematic hardening (see Section 7.3). The models were separately implemented into LS-DYNA (explicit) and MSC.MARC (implicit) FE codes, using user defined material subroutines, UMAT and Hypela2, respectively. The blank was discretized with shell elements in the model built in LS-DYNA, while solid elements were used in MSC.MARC (see details in Table 9), although it may be arguable the use of 2-D orthotropic yield functions with solid elements. Moreover, in the LS-DYNA model, symmetry conditions were considered, while in MSC.MARC the complete geometry is meshed.

8.1.2.3.1   With isotropic hardening

For isotropic hardening law (Swift) case, the predicted punch force-displacement curves and earing profiles are compared with the experimental data in Figure 100. As observed in Figure 100(a), the slopes of the predicted punch force-displacement curves are compatible with each other and with the experimental data. All models approximately captured the maximum punch force. It should be mentioned that USakarya team avoided the ironing effect by increasing the gap between the punch and the die in the numerical model. Figure 100(b) shows that the cup height is underestimated as well as the earing amplitude, particularly in the simulations performed with LS-DYNA, i.e. with shell elements. A similar behaviour was observed in Figure 97(b) when the same type of elements, but the Yld2000-2D yield criterion was used. Only the numerical simulation performed with MSC.MARC and the homogeneous polynomial yield function of degree 4 enables the prediction of 4 ears, as in the experimental results.

In MSC.MARC code, FE analyses were also performed based on multiplicative decomposition theory, which considers the decomposition of the deformation gradient into elastic and plastic components. Mandel's intermediate isoclinic configuration was adopted for orthotropic plasticity model. Figure 101 shows the numerical results of punch force – displacement curve and earing profile predicted by multiplicative decomposition methodology. It can be seen from Figure 101(a) that the numerical punch force – displacement curves were consistent with the experimental curve. As for the earing profile, the multiplicative decomposition leads to an increase of the cup height. Nevertheless, the earing amplitude shows a decrease, particularly for HomPol4. Moreover, both the HomPol4 and the HomPol6 predict more than 4 ears. As shown in Figure 102, all models enable a similar description of the in-plane distribution of the normalized yield stress and r-values, but in this case it is very difficult to correlate these results with the earing profile.
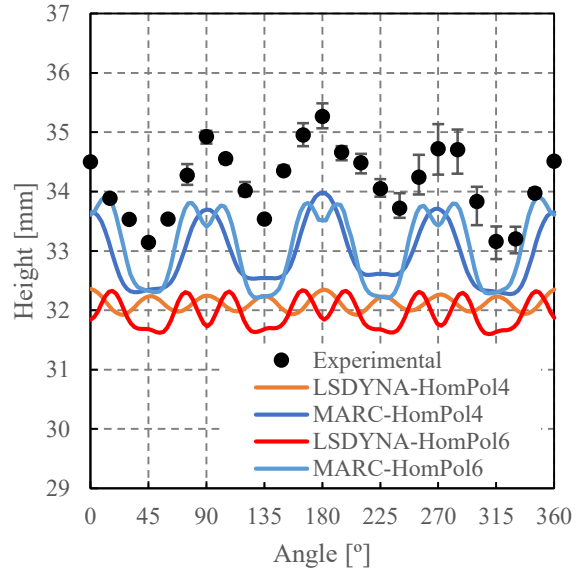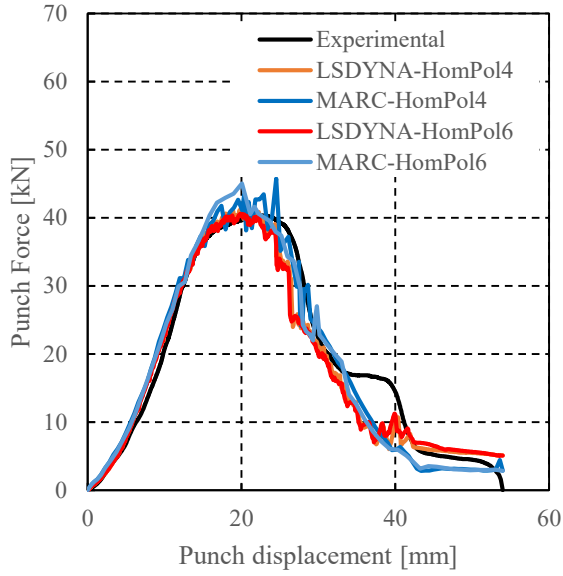
Figure 100 Comparison between experimental and predicted results by HomPol4 and HomPol6 criterion with the anisotropy coefficients identified in Sections 7.2.2 and 7.2.3 (Table 23 and Table 24), using LS-DYNA and MSC.MARC (additive decomposition): (a) punch force-displacement, (b) earing profile
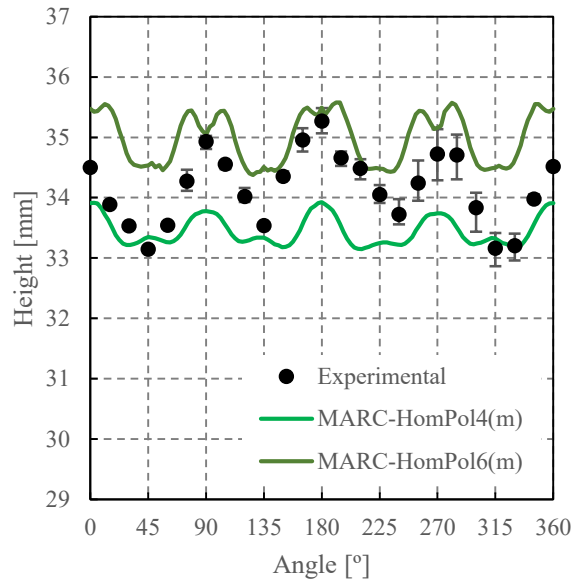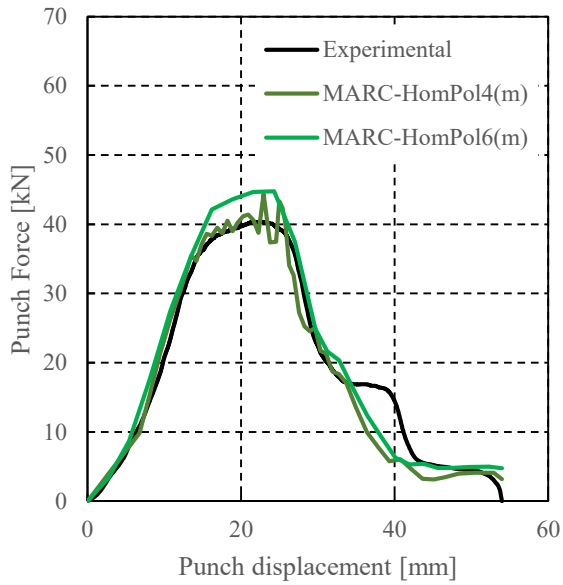
Figure 101 Comparison between experimental and predicted results by HomPol4 and HomPol6 criterion with the anisotropy coefficients identified in Sections 7.2.2 and 7.2.3 (Table 23 and Table 24), using MSC.MARC (multiplicative decomposition): (a) punch force-displacement, (b) earing profile
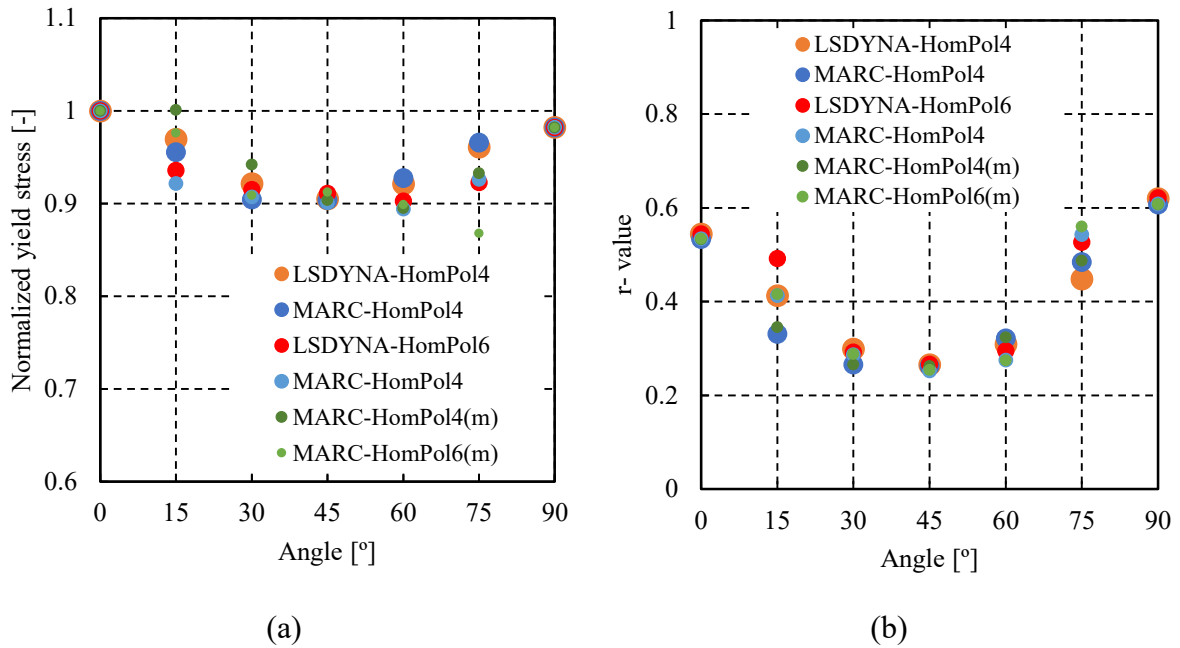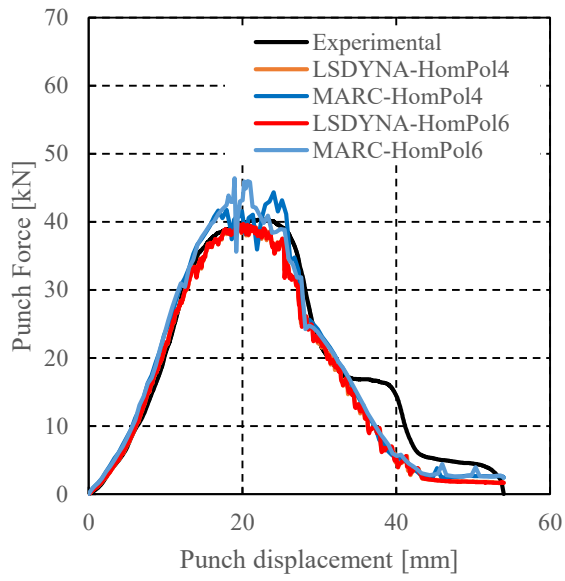
106

Figure 102 Predicted FEM results by HomPol4 and HomPol6 criterion with the anisotropy coefficients identified in Sections 7.2.2 and 7.2.3 (Table 23 and Table 24): (a) uniaxial tensile flow stresses, (b) Lankford coefficients (*r*-values). The label (m) corresponds to results obtained with MSC.MARC (multiplicative decomposition)

### 8.1.2.3.2   With isotropic and kinematic hardening

The results from USakarya team considering a combined hardening law relies on a Swift hardening law and the single term Chaboche nonlinear kinematic hardening rule, as described in Section 7.3, Table 32.

The predicted punch force-displacement curves and earing profiles are compared with the experimental results in Figure 103. Also in this case, the predicted punch force-displacement curves of both criteria are compatible with each other and with the experimental data (see Figure 100(a)). The comparison of Figure 100(b) with Figure 103(b) shows that the average cup height is better predicted when adopting the combined hardening law, particularly by the simulations performed with MSC.MARC. In fact, wrinkling was observed at several locations around the cup perimeter when the isotropic hardening rule was assumed. These wrinkles were substantially eliminated when the combined hardening rule was adopted.

Finally, the multiplicative decomposition theory was also tested in MSC.MARC FE code. Figure 104 shows the predictions of punch force – displacement curve and earing profile. As before, it can be seen from Figure 104(a) that the impact on the numerical punch force – displacement curves is marginal. As for the earing profile, combined hardening seems to affect the results positively. The cup height values were increased for HomPol4 and decreased for HomPol6, in comparison with the results based on isotropic hardening. It is seen that the predicted results from multiplicative decomposition with combined hardening were in best agreement with experimental data. Furthermore, the predicted cup profiles obtained from HomPol4 and HomPol6 with combined hardening are almost identical with each other. Nevertheless, it should be mentioned that while the HomPol4 predicts four ears, the HomPol6 results in a higher number. Finally, the trend predicted for the normalized yield stress and *r*-value directionalities is shown in Figure 105. The comparison with Figure 101 highlights small differences, particularly for the *r*-values. Previous results indicate that taking into account the kinematic hardening behaviour has small impact on the earing trend [Vla2011].
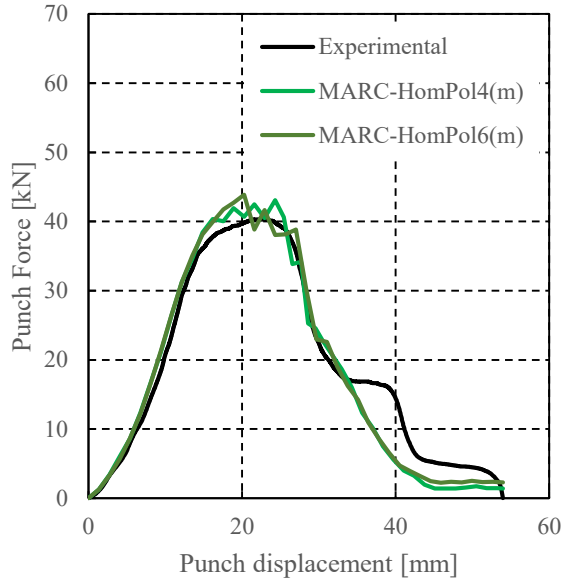
107
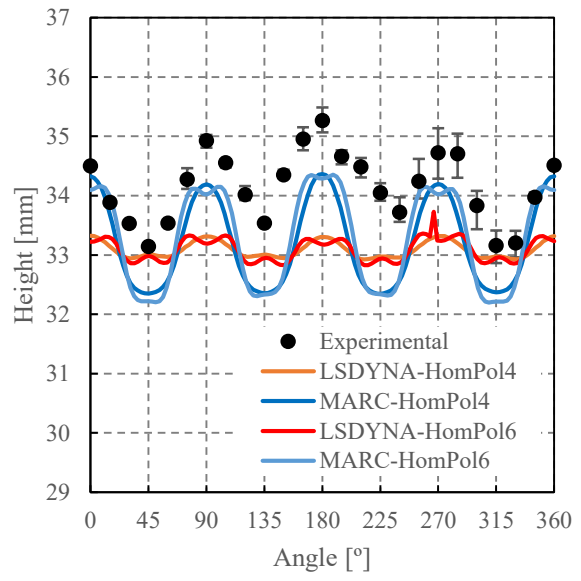
Figure 103 Comparison between experimental and predicted results by HomPol4 and HomPol6 criterion with the anisotropy coefficients identified in Sections 7.2.2 and 7.2.3 (Table 23 and Table 24), using LS-DYNA and MSC.MARC (additive decomposition): (a) punch force-displacement, (b) earing profile
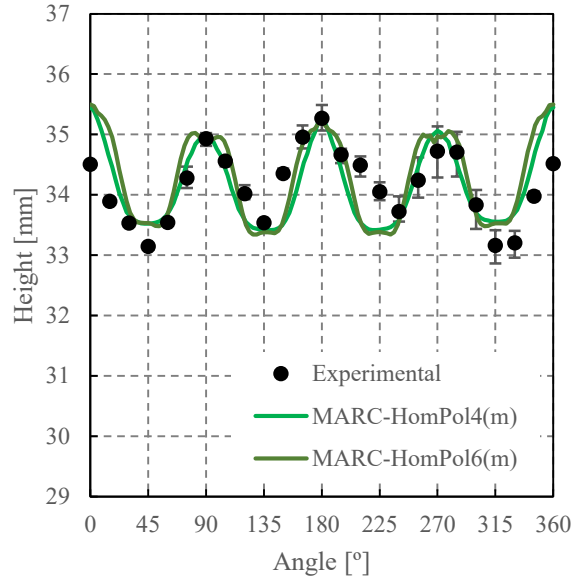

Figure 104 Comparison between experimental and predicted results by HomPol4 and HomPol6 criterion with the anisotropy coefficients identified in Sections 7.2.2 and 7.2.3 (Table 23 and Table 24), using MSC.MARC (multiplicative decomposition): (a) punch force-displacement, (b) earing profile
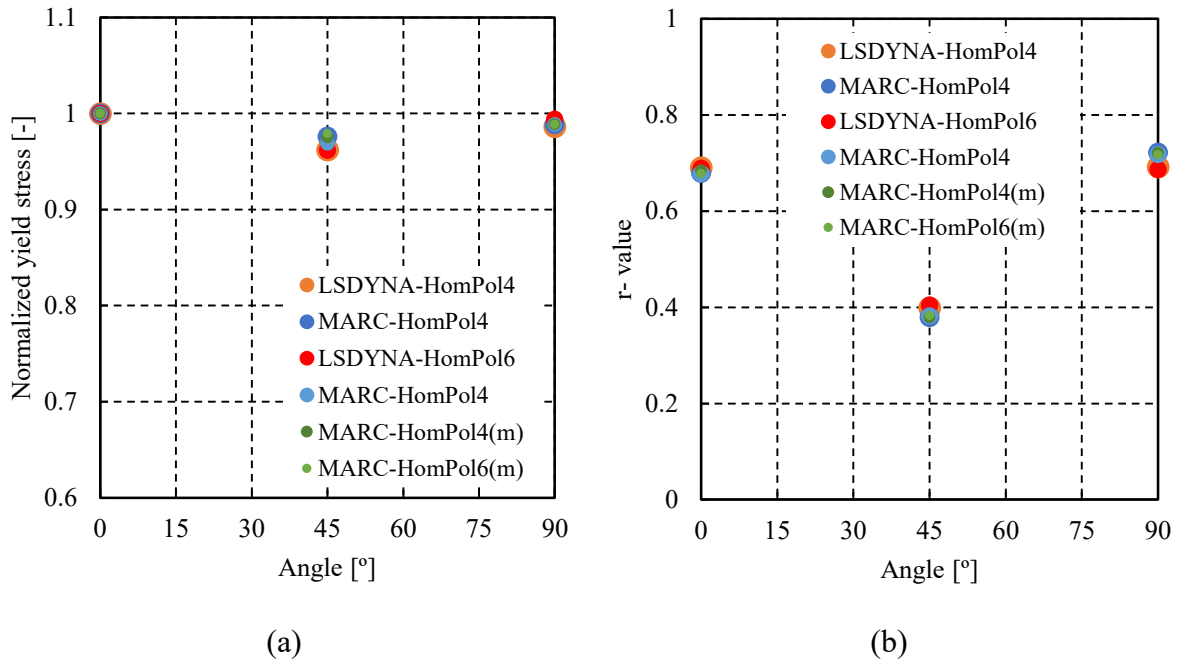
Figure 105 Predicted FEM results by HomPol4 and HomPol6 criterion with the anisotropy coefficients identified in Sections 7.2.2 and 7.2.3 (Table 23 and Table 24): (a) uniaxial tensile flow stresses, (b) Lankford coefficients (*r*-values). The label (m) corresponds to results obtained with MSC.MARC (multiplicative decomposition)

8.2 Results of phenomenological models identified with physical and virtual crystal plasticity tests

8.2.1 Yld2004-18p based on physical experiments and virtual tests with DAMASK

NTNU team performed two identifications for the Yld2004-18p yield criterion: using only mechanical data or considering also computer experiments, using DAMASK, as detailed in Sections 7.1.2.4 and 7.2.6 (anisotropy coefficients are given lines 2 and 3 of Table 28). Numerical simulations were computed with these sets of anisotropy parameters associated with the Voce hardening law (see Table 32) and a friction coefficient μ=0.09 in ABAQUS (implicit).

Figure 106(a) shows the comparison between the experimental and numerical punch force evolution with displacement, for both sets of parameters. The predicted drawing force agrees well with the experiments. The maximum value of punch force obtained from the simulations is similar to that in the experiment, but it occurs for a smaller displacement than in the experiment. After this peak point, both simulations underestimate the punch force, but the use of solid elements enables capturing the ironing effect. The comparison of the forces predicted by the two sets of parameters identified by NTNU shows that they present a good agreement; i.e. this variable is not sensitive to the calibration method of the constitutive model used in the analysis. The fact that the set of parameters identified based on the experimental data leads to a slightly higher value for the ironing force can be related with the fact that this model presents globally lower *r*-values (see Section 7.1.2.4), which justifies a slightly higher increase of thickness of the material initially located in the flange.

Figure 106(b) shows the experimental and simulated earing profiles at the end of the cup drawing. The set of parameters identified using both experimental and computer results, leads to 4 ears, with an amplitude lower than the experimental one; while the earing profile with the other set of parameters has a higher average level, a profile closer to 12 ears and very low amplitude. Thus, the prediction accuracy of the model using virtual tests in its identification process is higher than the one based only

109

on experiments. For this model, the amplitude of the ears increases for the identification performed with both mechanical and computer experiments although the amplitude of variation for the normalized yield stress is lower (see Section 7.1.2.4, Figure 40(a)).

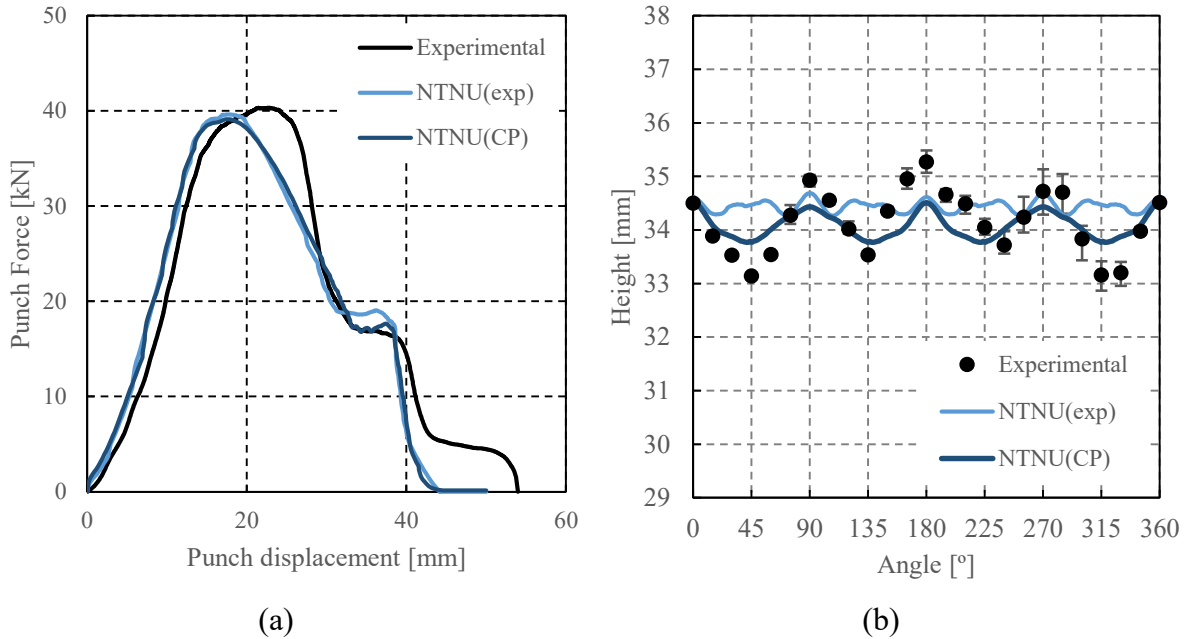(a)   (b)

Figure 106 Comparison between experimental and predicted results by Yld2004-18p criterion with the anisotropy coefficients identified based only in mechanical data or considering also computer experiments, as described in Sections 7.1.2.4 and 7.2.6 (Table 28): (a) punch force-displacement, (b) earing profile

8.2.2 Yld2000-2D based on virtual tests with VPSC

UGent team performed the numerical simulations with ABAQUS (implicit) considering the blank discretized with shell elements (see Table 9). The hardening Voce law and the phenomenological yield function Yld2000-2D, presented in Section 6.1.1, are implemented in ABAQUS (implicit) via a UMAT subroutine. The calibration of the yield locus is described in Section 7.1.2.5 (Table 19) and the hardening parameters are provided in Section 7.3, Table 32.

Figure 107(a) shows the punch force measured during the cup drawing process together with the one extracted from the simulation. The punch force magnitude during the initial stage of the experiment is well predicted by the numerical model. However, the FE analysis slightly underestimates the peak force and reaches a maximum earlier than in the experiment. The shell element adopted by UGent (S4R, see Table 9) leads to a clear underestimation of the ironing force, unlike other shell formulations (see e.g. Figure 71), which is certainly connected with the assumptions adopted to estimate the transverse strain.

Figure 107(b) shows the experimental and predicted earing profiles at the end of the cup drawing process. The FE model predicts the same number of ears as in the experiment. A quasi-perfect agreement is observed for the angles at which the highest and lowest heights are measured. On the other hand, the model cannot replicate the exact evolution of the measured profile. It is interesting to note that the minimum presents a shift towards the RD, similar to the one obtained with CPB06ex2 (see Figure 88(b)). This can be related with the trend observed for the in-plane distribution of the normalized yield stress for both models, which presents an extra inflexion point at a similar location

110

(see Figure 89 and Figure 108). Interestingly, all models that consider the Yld2000-2D (see also Figure 97(b)) underestimate the average cup height, whatever the parametrization adopted. The parametrization proposed by UGent leads to the best prediction of the number of ears and their amplitude.
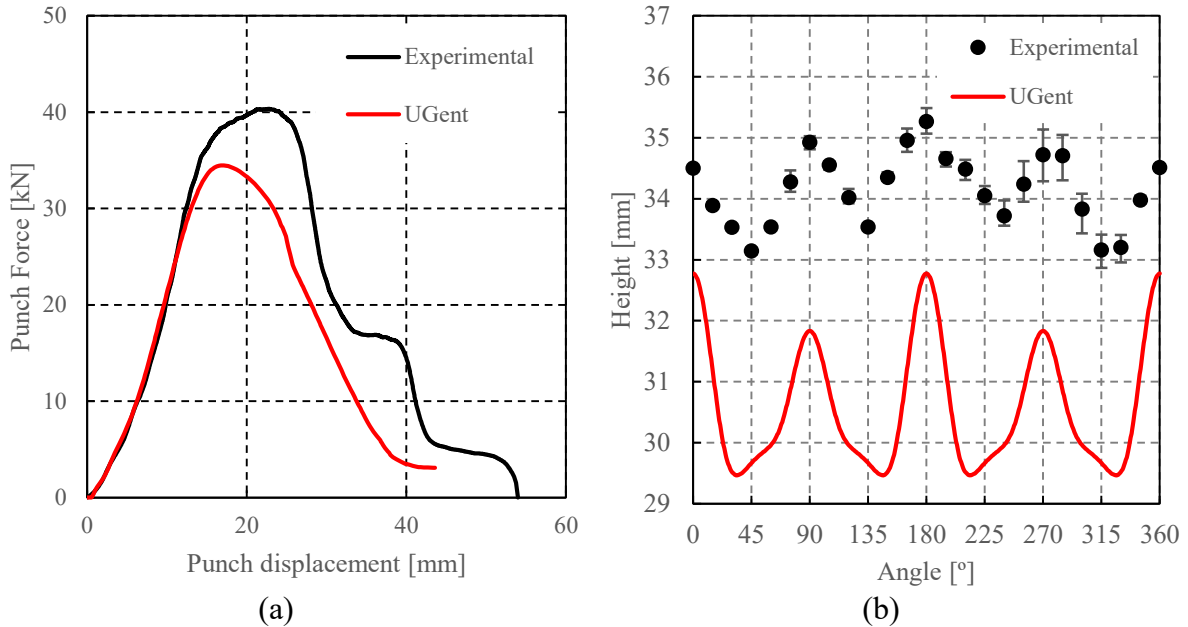

Figure 107 Comparison between experimental and predicted results by Yld2000-2D criterion, with the anisotropy coefficients identified by VPSC virtual tests, as described in Section 7.1.2.5: (a) punch force-displacement, (b) earing profile

It is important to mention that the shape of the yield function is calibrated using the data from the virtual experiments at 10% of effective plastic strain. This assumption is supported by the EBSD measurements performed after pre-straining that show that no significant texture evolution is observed (see Figure 6 and Figure 14). Besides, the parameter identification method used for the calibration of the anisotropic parameters for the phenomenological Yld2000-2d criterion, is performed giving more weight to the r-values rather than to the stress amplitude (see Section 7.1.2.5). This approach is chosen in order to get a better prediction of the earing profile. However, the inaccurate description of the yield strengths (see Figure 43) might have resulted in the underestimation of the global punch force.
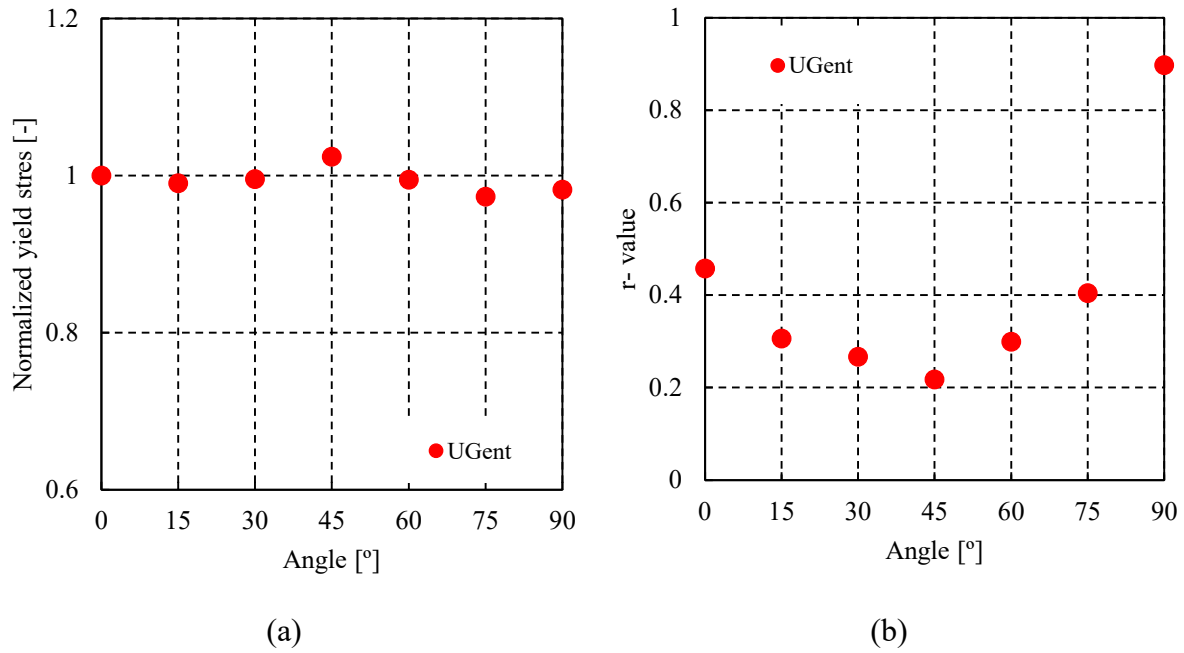
111

Figure 108 Predicted FE results by Yld2000-2D criterion, with the anisotropy coefficients identified by VPSC virtual tests, as described in Section 7.1.2.5: (a) uniaxial tensile flow stresses, (b) Lankford coefficients (*r*-values)

8.2.3 Caz2018singlecrys assuming or not a pure cube texture

As discussed in Section 6.2.2, a simplified approach was used by POSTECH based on the assumption that the AA 6016-T4 material has a pure cubic texture (i.e. 100% of the grains are with [100] along RD, and [001] along ND). POSTECH uses the single crystal law, Caz2018singlecrys (see Eq. (30), with crystal axes coinciding with (x,y,z) axes), to simulate the cup drawing. For this purpose, POSTECH implemented the single crystal model in the FE code ABAQUS explicit (subroutine VUMAT) in conjunction with a Voce hardening law (parameters in Table 32). They used their own set of anisotropy parameters (see Section 7.1.2.6, Table 20), solid elements (C3D8R), a coarse mesh (see Table 9 and Figure 28) and a friction coefficient $\mu = 0.1$.

The FE simulation results reported in Figure 109 for the POSTECH set of anisotropy parameters (see Table 20) predict 8 ears and the punch force evolution with displacement is overestimated for both the drawing and the ironing stage. As discussed in Section 7.1.2.6, for this set of anisotropy parameters the yield surface is not convex (see Figure 46 (b)).

As shown in Section 7.1.2.2, if the assumption of a pure cube texture is made for the AA 6016-T4 material, REEF identified in a different way the same single crystal law (i.e. did not impose $n_4 = 0$). The set of anisotropy parameters is given in Table 15-line 1. The implementation of the single crystal model was done in ABAQUS Standard, using a fully implicit integration algorithm for solving the governing equations. The punch force vs. displacement and earing profile obtained using this set of anisotropy coefficients, a Swift hardening law (parameters in Table 32), and this team's implementation are also shown in Figure 109. The predicted isocontours of the equivalent plastic strain for the full drawn cup are given in Figure 110. The FE REEF mesh for a quarter of the blank consisted of a refined mesh of 10900 solid elements (C3D8R), with three elements in the thickness direction and friction coefficient $\mu = 0.02$. Note that the predicted earing profile shows the same trends as the experimental one, namely 4 ears with maximum in cup height at 0° and 90° and a minimum cup height at 45°. Moreover, there is

correlation between the predicted *r*-values variation (see Figure 33(b)) and the predicted earing profile. Obviously, the assumption of ideal cube texture (which implies $r_0=r_{90}=1$) is not valid for the AA 6016-T4 material which has $r_0=0.525$ and $r_{90}=0.429$, hence a quantitative agreement for the ears amplitude cannot be expected.
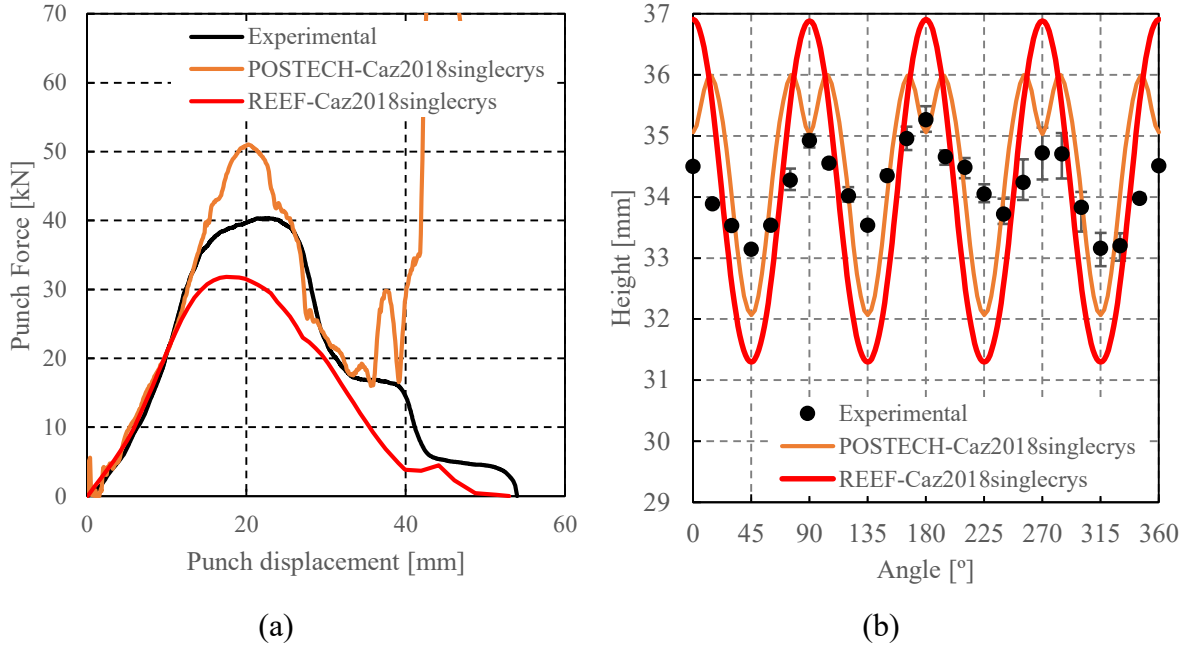

(a)　　　　　　　　　　　　　　　　　(b)

Figure 109 Comparison between experimental and predicted results by Caz2018singlecrys for the data set of Section 7.1.2.2 (Table 15 - REEF) and of Section 7.1.2.6 (Table 20 – POSTECH): (a) punch force-displacement, (b) earing profile
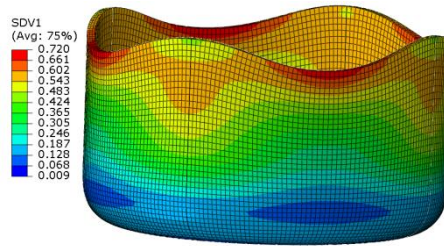

Figure 110 Predicted isocontours of equivalent plastic strain predicted by Caz2018singlecrys yield criterion with the anisotropy coefficients given in Section 7.1.2.2 (Table 15 - ideal cubic texture)

8.2.4 Facet-3D based on ALAMEL virtual tests

This section presents the results reported by KUL, using the Facet-3D model identified with ALAMEL, as described in Section 7.1.2.1. As mentioned in Section 5, the numerical simulation was performed with ABAQUS (explicit), using the complete model, with the blank discretized with continuum shell elements (SC8R). The blank initial position was offset (-0.3 mm in RD and 0.008 mm in TD, i.e. half of the cup height difference) to account for the asymmetry in the experimental earing profile. Figure 111 presents the comparison between the experimental and numerical punch force evolution with its displacement and the earing profiles. The evolution of the thickness along the cup circumferential

113

direction, at different heights, is shown in Figure 112. The use of a friction coefficient of 0.090 enables an accurate description of the drawing force as well as of the earing profile. Nevertheless, the ironing force is underestimated, although the contact algorithm selected (see Table 10) guarantees a maximum thickness value equal to the clearance between the die and the punch (see Figure 112). A previous study that compares the use of different types of elements implemented in ABAQUS indicates that continuum shell elements tend to predict slightly lower ironing forces than solid elements [Coe2018]. In this case, it is interesting to note that this constitutive model predicts a lower average thickness value for the higher cup heights (H = 25 and H = 30 mm), when compared with the ones predicted by other phenomenological models (see Figures 74, 83, 90 and 93), which can also help justifying the lower value predicted for the ironing force. Regarding the earing profile, the amplitude and average height are well captured, although the experimental normalized tensile yield stress values are not well predicted by ALAMEL and Facet-3D (see Figure 32(a)).
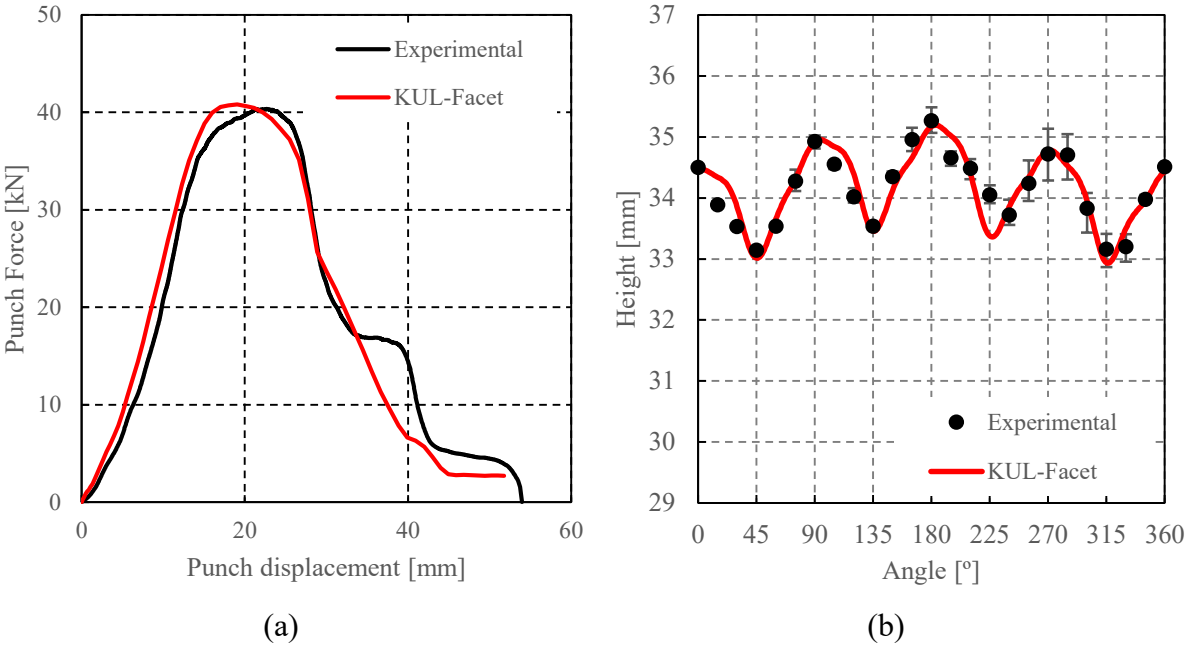

(a)   (b)

Figure 111 Comparison between experimental and predicted results by the Facet-3D model identified by ALAMEL, as described in Section 7.1.2.1: (a) punch force-displacement, (b) earing profile
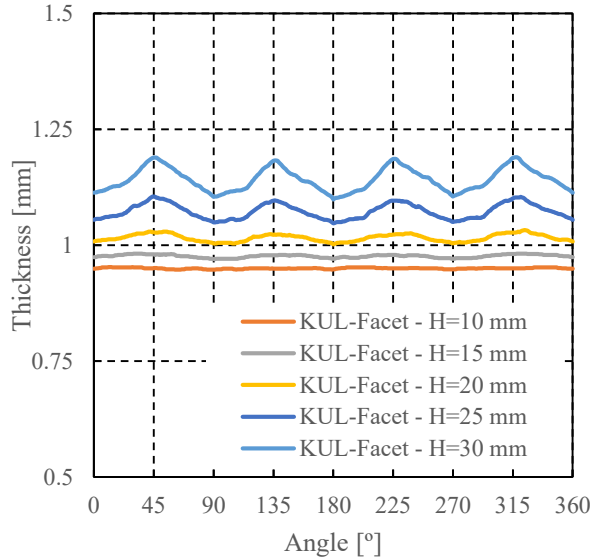
Figure 112 Evolution of the thickness along the cup circumference at different heights H = 15, 20, 25 and 30 mm from the cup bottom, by the Facet-3D model identified by ALAMEL (see Section 7.1.2.1)

8.3   Results with crystal plasticity based constitutive models

8.3.1   Caz2018polycrys based on Caz2018singlecrys

In the following are presented the cup drawing results obtained with Caz2018polycrys, the polycrystalline model based on the Cazacu et al (2018) single crystal criterion (Eq. (30) and the values of anisotropy coefficients corresponding to the actual texture, given in Table 15) and Swift isotropic hardening model (see parameters Table 16). As already mentioned, a polycrystalline aggregate is associated with each FE integration point (see Section 6.2.2 for more details). A friction coefficient of 0.02 was applied and a total of 10900 solid elements (ABAQUS C3D8R) have been used to mesh the quarter of the blank, resulting in a total of 2 725 000 grains in the FE simulation.

Figure 113(a) shows the predicted forming force as a function of the punch stroke in comparison with experimental data. The underestimation is consistent with the low friction coefficient used. The prediction of Caz2018polycrys model for the cup earing profile is shown in Figure 113(b). Note that the predicted cup-height profile is in good agreement with the experimental data. Specifically, it is a four-ear profile with ears located at RD and TD and a minimum cup height at 45° from RD, as observed experimentally. Moreover, the predicted average height is h_{avg}= 33.93 mm against h_{avg}= 34.10 mm experimentally (0.6% difference), the cup profile amplitude being of 2.61 mm against 2.29 mm experimentally (10% difference). Furthermore, Caz2018polycrys model predicts a maximum height of the cup of 35.39 mm against 35.27 mm experimentally (0.3% difference) and a minimum height of the cup of 32.78 mm against 32.99 mm experimentally (0.6% difference). In Figure 114, the predicted evolution of the wall thickness along the cup circumference, taken at different heights from the cup bottom, is presented.
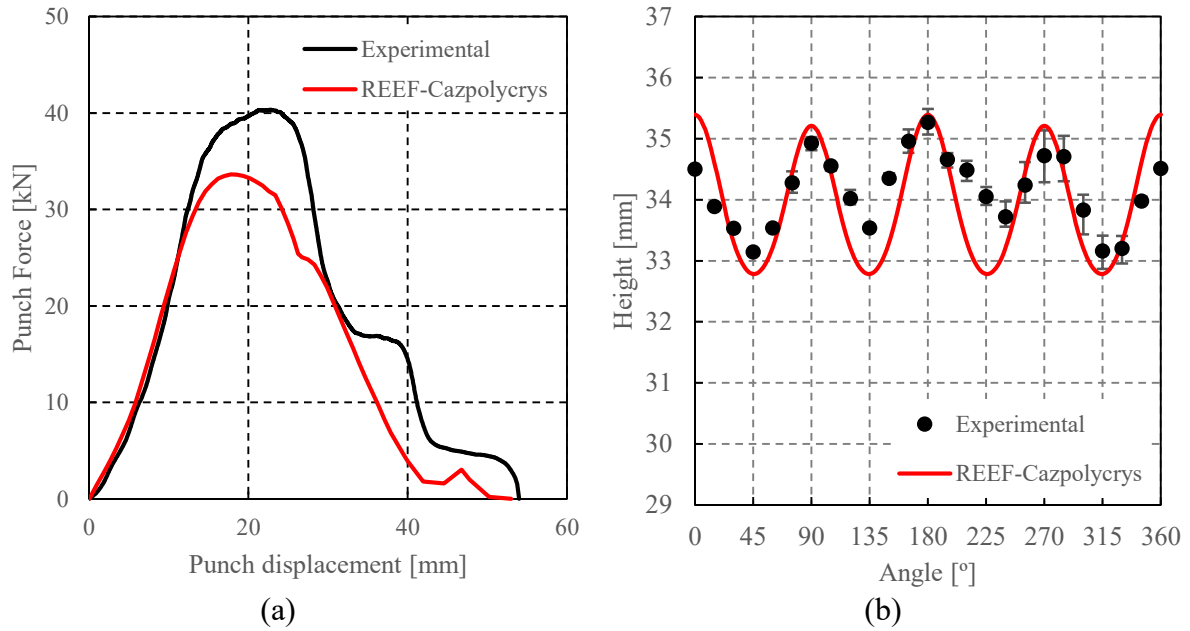
115

(a)   (b)

Figure 113 Comparison between experimental and predicted results by Caz2018polycrys model based on Caz2018singlecrys (Eqs. (30)-(32)): (a) punch force-displacement, (b) earing profile
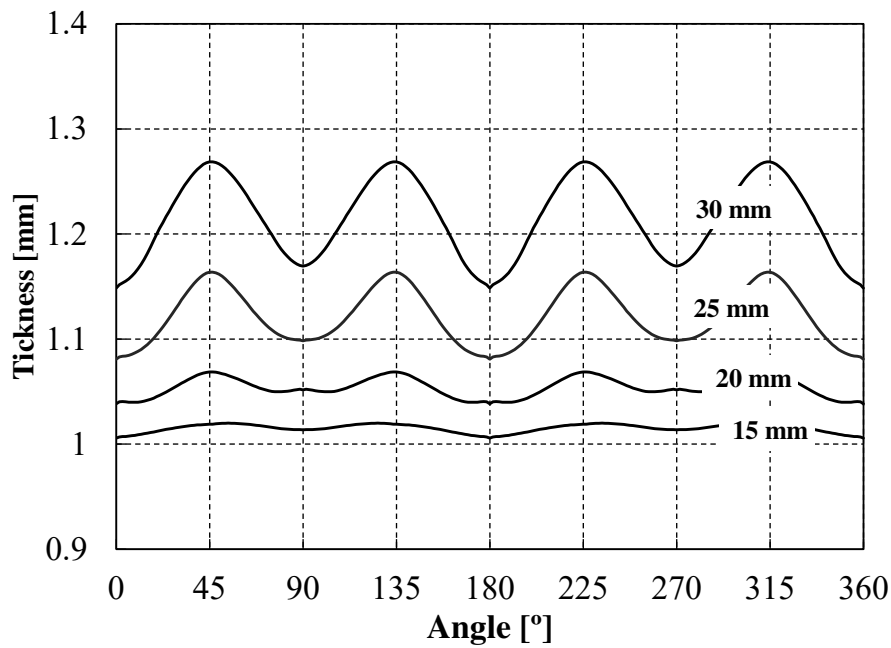
Figure 114 Evolution of the thickness along the cup circumference at different heights H = 15, 20, 25 and 30 mm, respectively from the cup bottom, by Caz2018polycrys model based on the Caz2018singlecrys model (Eqs. (30)-(32))

8.3.2 MINTY

In this section, the results obtained by ULiege using Minty (see Section 7.1.2.3) and the Swift hardening law are presented. According to the information given in Section 5, ULiege used solid elements and its own FE implicit software Lagamine, considering a constant friction coefficient of $\mu = 0.082$.

116

Figure 115(a) shows the predicted forming force as a function of the punch stroke in comparison with the experimental data. Despite the problems previously mentioned in Section 8.1.1.1, overall, the maximum drawing force is well predicted. The comparison with the results obtained with Lagamine for Hill48 yield criterion (see Figure 72) shows that the model adopting the Minty law leads to a slightly higher value for the maximum drawing force, which can be related with the selection of the Swift hardening law instead of Voce. Figure 115(b) presents the earing profile predicted with the model adopting the Minty law. As for Hill48 yield criterion (see Figure 72(b)), 4 ears are predicted with the same trend of the experimental ones. However, the average cup height is clearly underestimated by the model adopting the Minty law. In addition, the amplitude of the earing profile becomes higher, when compared with the one predicted by the Hill48 yield criterion. This change in amplitude can be explained by the increase in the amplitude of variation of the r-values in-plane distribution predicted by the model adopting the Minty law, when compared with the one obtained by Hill48 yield criterion (see Figure 73(b) and Figure 116(b)). In this context, it is interesting to mention that the Minty law and Caz2018polycrys model predict the same trend; the predictions for r-values for RD and TD are very close, with maximum differences being observed for the 45° orientation (see Figure 35(b) and Figure 116(b)).

(a)   (b)

Figure 115 Comparison between experimental and predicted results according to the MINTY law, as described in Section 7.1.2.3: (a) punch force-displacement, (b) earing profile
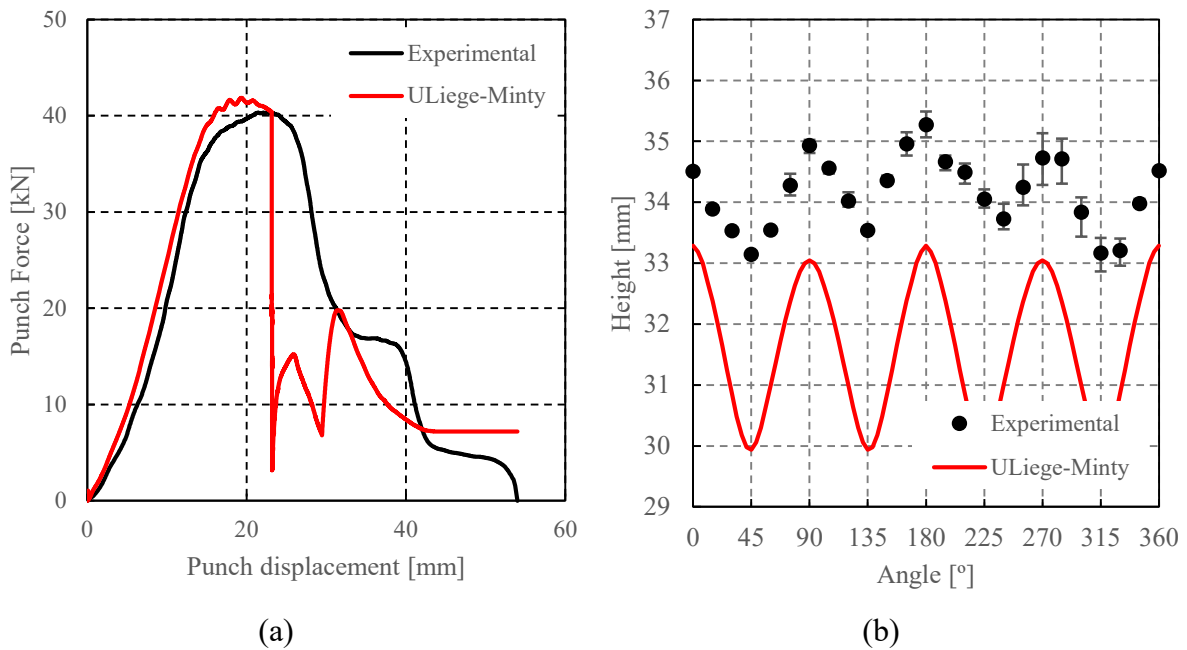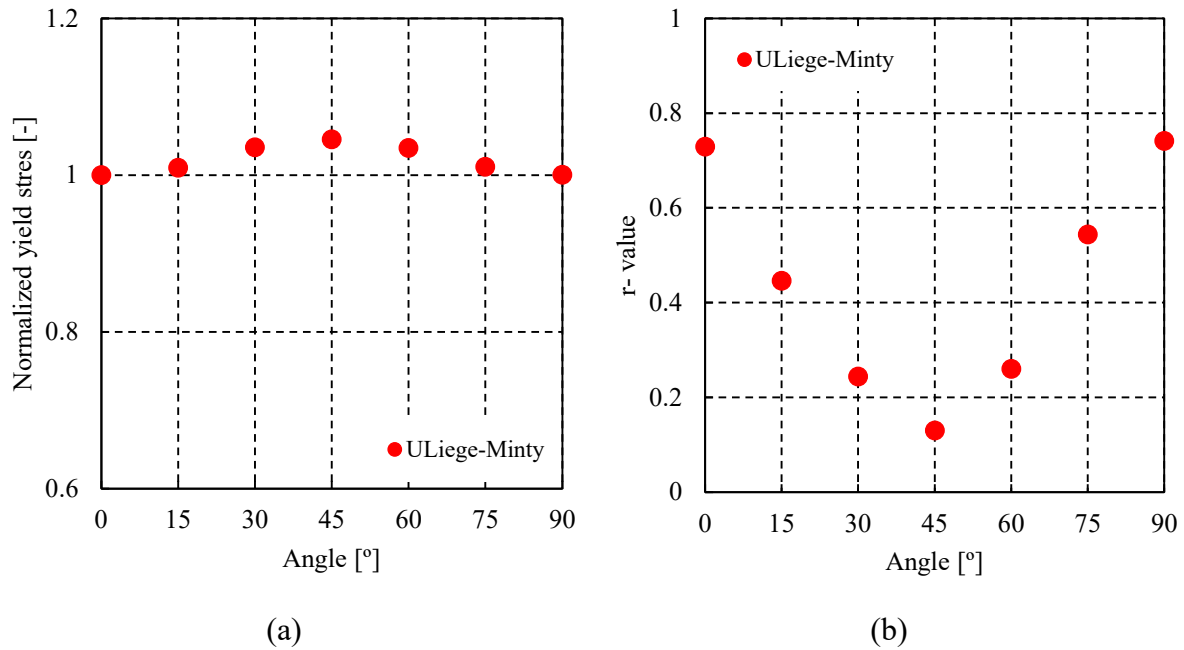
Figure 116 Predicted FEM results according to the MINTY law, as described in Section 7.1.2.3: (a) uniaxial tensile flow stresses, (b) Lankford coefficients (*r*-values)

8.4 Summary of the results and discussion

Here after, first the punch force and then the earing profile predictions are discussed.

Globally, all FE models enable the accurate prediction of the first peak of the punch force related to cup drawing, with the adjustment of the friction coefficient (within a reasonable physical range). Nevertheless, they show a considerable raise of the punch force during the ironing stage, particularly when using shell elements (except for ABAQUS: the S4R element used by UGent and SC8R element used by KUL). These results are summarized in Figures 117 and 118, which show the average of the maximum punch force during the drawing and the ironing stages, for each yield criterion/constitutive model and identification strategy adopted. Note that some models were selected by only one team, which justifies the lack of error bars.

Some teams (REEF, UCoimbra) that used solid elements did not perform any optimization of the friction coefficient and just select a low value (μ=0.02), which explains the underestimation of the drawing force (Figure 117). However, the teams using friction values from 0.05 until 0.1 and solid elements predicted the drawing force peak with higher accuracy than the teams that used shell elements, which all relied on friction values equal or higher than 0.07.

In Figure 118, the overestimation of the ironing force is observed for many participants and it is related with the strategies adopted to deal with transverse strains when using shell elements (different assumptions in LS-DYNA, PAMSTAMP and ABAQUS (S4R and SC8R), as detailed in Table 9). The lack of accuracy in the transversal strain prediction also explains the poor precision of shell elements of the thickness distribution along the cup circumference, for different heights.

Globally, the solid formulations clearly provide a more realistic ironing force (see Figure 118). Nevertheless, even for this type of elements, the ironing force tends to be overestimated, which seems to be related with the assumed tool rigidity. An elastic behaviour would slightly widen the drawing gap during ironing where very large surface pressures prevail and therefore a lower force is expected. The

118

improved accuracy of the ironing force and shape of the force curve are pointed by the simulations using an increased clearance (USakarya with Yld89, HomPoI4 and HomPoI6). Note that just based on these synthetic figures, one could enhance 3 interesting configurations:

- Yld2004-18p - ABAQUS implicit – solid element from NTU, with an identification based on 7 virtual tensile tests by Damask with an FFT approach, 7509 grains in a RVE and a physical tensile test in RD (see Section 8.2.1).
- FACET-3D – ABAQUS explicit - continuum shell from KUL, with an identification based on 200 virtual tests relying on 10 000 grains and the ALAMEL crystal plasticity model (see Section 8.2.4) although, the ironing force is underestimated and the start of the ironing stage occurs for higher values of punch displacement than in the experimental test (see Figure 111).
- MINTY – Lagamine implicit - solid element from ULiege, with an interpolation yield locus approach based on 1000 crystals and a simple Full Taylor plasticity approach (see Section 8.3.2); although, the start of the ironing stage is not correctly predicted and some issues still need to be further analysed.

This indicates that the use of crystal plasticity computations to complement physical tests in the identification of the parameters of phenomenological models may contribute to improve the prediction of the ironing force.

Regarding the punch force prediction, in conclusion, as the friction coefficient was not measured or suggested by the benchmark committee, most teams calibrated a constant Coulomb friction coefficient by fitting the experimental evolution of the punch drawing force. This has led to a very good description of the drawing force (see Figure 117) for models using solid elements. Nevertheless, using a constant friction coefficient does not enable to predict with great accuracy both the drawing and ironing force. While an evolving friction coefficient may help to further fine tune the predictions of the forces, improved prediction of the thickness at the top of the vertical wall may require consideration of the deformation of the forming tools. In practice, an easy and quick assessment of the friction coefficient for drawing or ironing stages seems difficult, due to experimental issues and the uncertainty related with the tools surface state and lubrication conditions. This topic as well as the reasons for the measured thickness being greater than the gap (see Section 3.5) clearly need to be addressed in future works. Within the next ESAFORM 2022 and Numisheet 2022 conferences, new studies on this benchmark will be published and, as all data will be public, the whole community will also be able to exploit it.
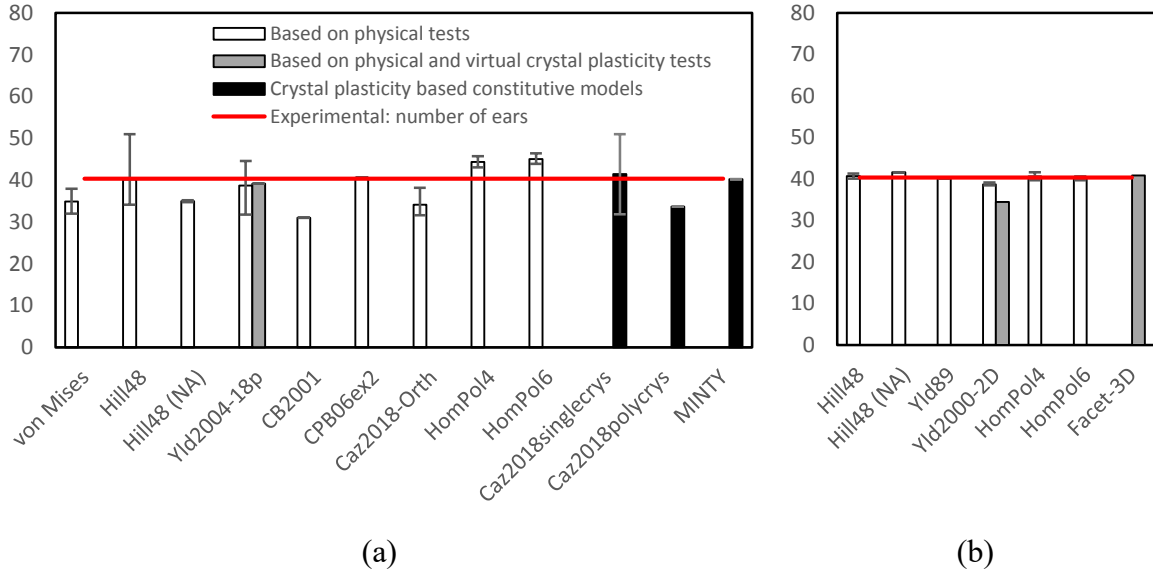
Figure 117 Maximum punch force predicted in the drawing stage in function of the yield criterion or constitutive model, for FE models using for the blank discretization: (a) solid (team used values from μ=0.01 up-to μ=0.100) and (b) shell elements (all teams used μ=0.07 or higher values)
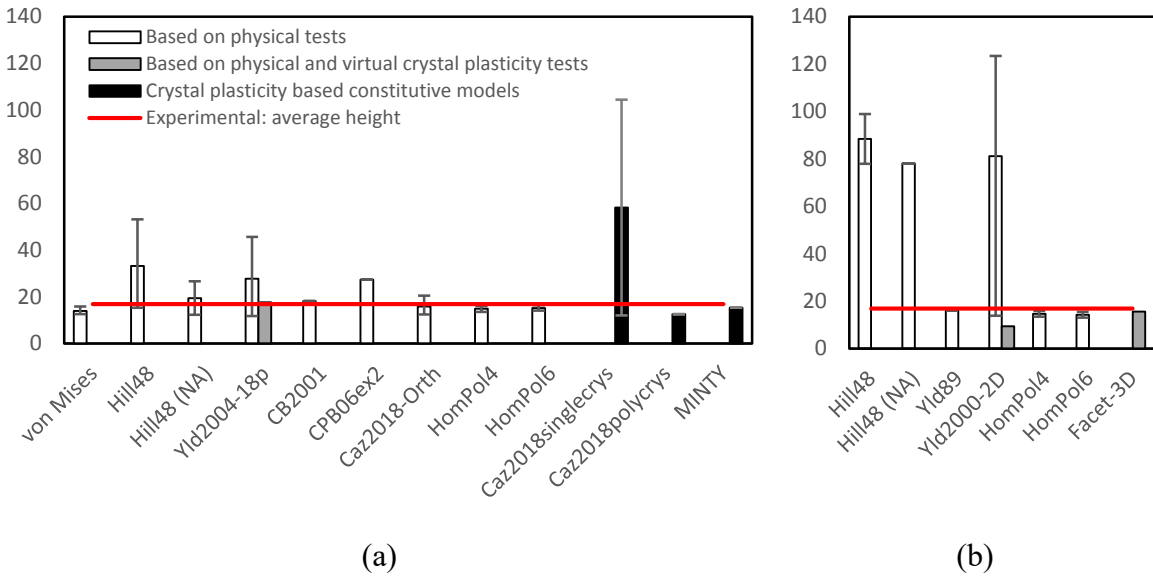

Figure 118 Maximum punch force predicted in the ironing stage in function of the yield criterion or constitutive model, for FE models using for the blank discretization: (a) solid and (b) shell elements

The number of ears, average height and average amplitude predicted by each FE model are presented in Table 35 and Table 36, for solid and shell/continuum-shell elements, respectively. In each table, the FE models are also separated taking into account the strategy used for the parameters identification. Table 35 and Table 36 also present the global error, evaluated as:

$$\text{Global error} = \left(\frac{n_{\text{avg}}^{\text{num}} - n_{\text{avg}}^{\text{exp}}}{n_{\text{avg}}^{\text{exp}}} \right)^2 + \left(\frac{h_{\text{avg}}^{\text{num}} - h_{\text{avg}}^{\text{exp}}}{h_{\text{avg}}^{\text{exp}}} \right)^2 + \left(\frac{a_{\text{avg}}^{\text{num}} - a_{\text{avg}}^{\text{exp}}}{a_{\text{avg}}^{\text{exp}}} \right)^2 , \qquad (72)$$

where n_{avg}, h_{avg} and a_{avg} represent the number of ears, average height and average amplitude, respectively, and the superscripts "num" and "exp", correspond to numerical and experimental results.

120

Global error values lower than 0.01 are highlighted in bold. In Figures 119-121, the average number of ears, average height and average amplitude were determined, for each yield criterion/constitutive model and identification strategy adopted.

Regarding the number of ears, most models that adopt a 3-D orthotropic yield function predict 4 ears (see Figure 119), as observed in the experimental results. Figure 120 shows that the average cup height is well predicted by all models, including the von Mises isotropic yield criterion. The fact that the Hill48, using solid elements, presents a higher amplitude of variation than most of the other models is related with the fact that it was selected by many teams, adopting different friction coefficient values and modelling strategies. Globally, the 2-D orthotropic yield functions (Yld89, Yld2000-2D, HomPol4 and 6) tend to underestimate the average height, particularly when combined with shell elements. The average amplitude of the ear profile is presented in Figure 121. It shows that 3-D orthotropic yield functions tend to predict values that are more accurate than 2-D orthotropic models, for which only shell elements can be used without additional assumptions (7 accurate average predictions out of 12 models *versus* 4 reasonable predictions out of 8 shell models).

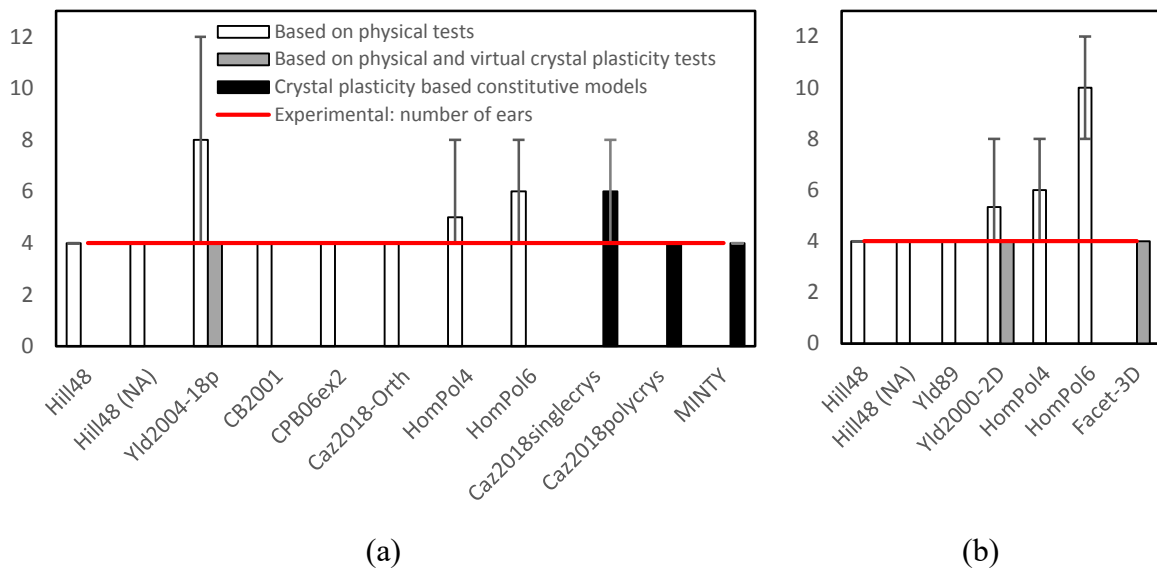(a)   (b)

Figure 119 Number of ears predicted in function of the yield criterion or constitutive model, for FE models using for the blank discretization: (a) solid and (b) shell elements
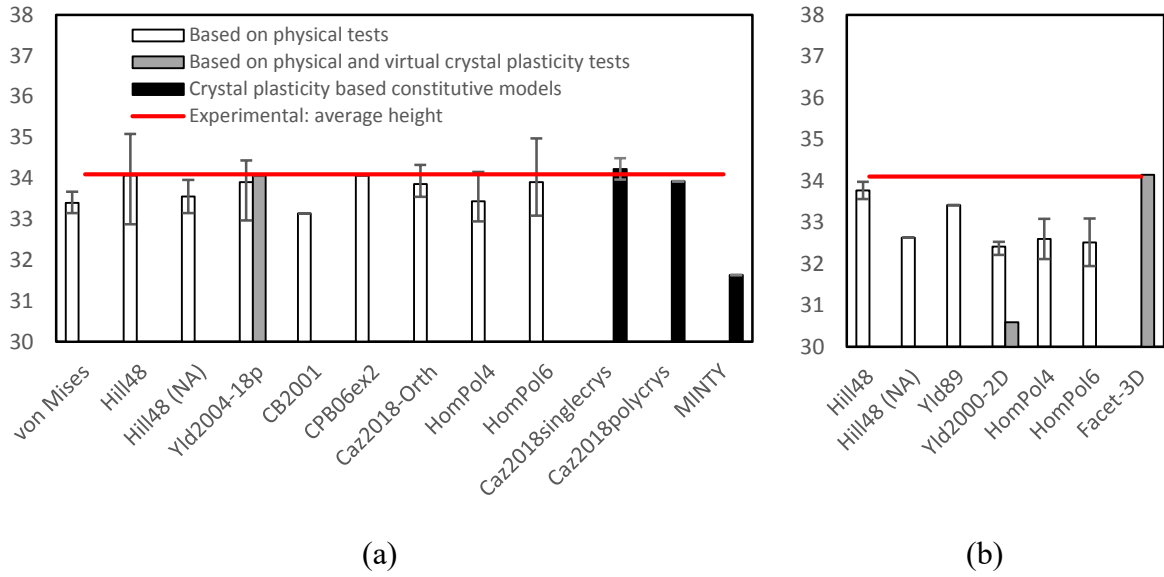
Figure 120 Average height of the cup predicted in function of the yield criterion or constitutive model, for FE models using for the blank discretization: (a) solid and (b) shell elements
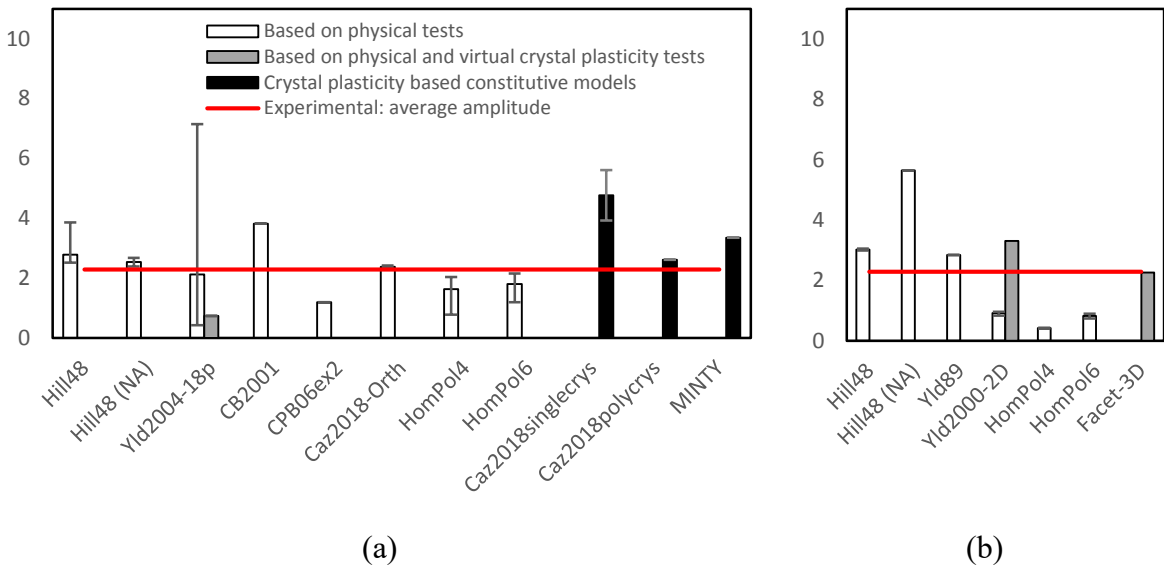
Figure 121 Average amplitude of the ear profile predicted in function of the yield criterion or constitutive model, for FE models using for the blank's discretization: (a) solid and (b) shell elements

As previously mentioned, it has been reported that there is a correlation between the earing profile and the *r*-values and the yield stresses directionalities (e.g. see [Yoo2011], [Caz2021]). Considering this assumption and based on the experimental data presented in Section 2, it is expected that all models that accurately predict the experimental *r*-values anisotropy will predict 4 ears, with maxima at RD and TD and minima at 45°. This is the case for the 3-D orthotropic yield functions of Hill48, CB2001, CPB06ex2 and Caz2018-Orth. Note also that all these 3-D orthotropic yield functions predict similar in-plane distributions for the *r*-values. Moreover, all these yield criteria predict a similar earing profile in agreement with the experimental data, in terms of both average height and locations of minima and maxima.

However, the results from each FE model that uses Yld2004-18p strongly varies:

- "Yld2004-18p – ABAQUS implicit - solid element (C3D8R) with NTNU implementation" predicts 12 ears (low amplitude) for the set of parameters based on physical experiments and 4 ears (medium amplitude) for the set based on crystal plasticity virtual experiments, see Figure 106;
- "Yld2004-18p – ABAQUS explicit -solid element (C3D8R) with POSTECH implementation" predicts 8 ears (low amplitude), see Figure 84;
- "Yld2004-18p - LS-DYNA explicit - solid element with the built-in implementation" used by USiegen predicts 4 ears with the data set of POSTECH (very high amplitude) and 12 with the set of parameters based on physical experiments from NTNU (very low amplitude), see Figure 85.

Moreover, for some sets of parameters, the predicted locations of the minima and maxima of the cup height are contrary to the experimental observations (see Table 35). This volubility of the results points a very strong sensitivity to the implementation as well as to the identification strategy adopted to determine the anisotropy parameters. It reminds also that just relying on a correct prediction of the *r*-values and the yield stresses directionalities is far from being a secure approach, as all the implementations and sets of coefficients enable an accurate description of those experimental results. Finally, for this specific yield criterion, only the set of parameters identified based on virtual crystal plasticity results and the implementation of NTNU in ABAQUS generates an acceptable result (Figure 106), although the earing amplitude is underestimated.

The results obtained with Hill48, associated flow rule, isotropic hardening and solid elements reported in Table 35 enable an accurate prediction of an earing profile with 4 ears, with the same location experimentally observed. Most teams used the set of parameters provided by UCoimbra (formula of second line of Table 21 and values of line 1 of Table 22), based on Lankford coefficients at 0°, 45° and 90° like advised in many deep drawing simulation guidelines. The variations in the results come mostly from different friction coefficient values, contact algorithms, mesh refinements, time integration strategies (explicit or implicit) and code selection. These differences generate some non-negligible dispersion in the results: average height [32.88; 35.07] mm; and amplitude [2.53; 3.86] mm, compared to experimental mean values of 34.1mm and 2.29 mm, respectively. Note that ULiege results provide the lowest average amplitude (closer to the experimental value), but a different set of parameters was used, identified giving the same weight to the Lankford coefficients and the yield stresses in 7 directions, obtained from UA tensile tests (values of line 3 of Table 22). The results of REEF and UCoimbra for two different friction coefficient values confirm that friction has a non-negligible impact on the average height but a small one on the average amplitude. In this context, if the results from ULiege are removed from the analysis, as well as the ones from UPorto, the dispersion in the amplitude reduces to [2.62; 2.69] mm.

The choice of using a non-associative Hill48 model was done by 3 teams: USiegen, UAalto and UPorto. However, a comparison between their results is not straightforward. UPorto simulation works with a fixed gap between the blank holder and the die, which can affect the material flow. Their identification methodology is based on Eq. (71), assuming the *r*-values and yield stress evaluated from UA tensile tests (see Table 4 and Table 5, respectively), which clearly allows predicting the experimental profile of both the uniaxial tensile yield stress and the Lankford coefficients (Figure 79). It predicts larger ear amplitude at 90° than in 0° (see Figure 78).

UAalto model not only takes into account a non-associated flow rule but also textural hardening: F, H, G and N anisotropic parameters for both yield criterion and flow potential (Table 31) evolve with the plastic strain. This assumption is based on an accurate analysis of the data collected during the tensile

tests in 7 directions, performed by UA, which can justify the evolution of the Lankford coefficients (see Figure 5(c)) and yield stress with the plastic strain. Nevertheless, the model extrapolates the evolution beyond the maximum tensile strain measured in the tests (maximum value of 0.3 in Figure 4), as shown for instance at 0.4 plastic strain in Figure 66. The model "Hill48(NA) - ABAQUS explicit - solid element C3D8R - Voce hardening law - μ=0.01" results are very accurate, for both earing average height and amplitude, as the associated global error 0.002 is among the smallest ones (see Table 35).

Finally, USiegen tested PAMSTAMP non-associated Hill48 model and found some unexpected results, regarding the value predicted for the yield stress at 45°, which lead to a very large earing amplitude. Some interaction with PAMSTAMP staff is ongoing to better understand where this issue comes from.

Concerning the amplitude of the ears obtained with the 3-D orthotropic yield functions that predict the correct number of ears, let us discuss the earing profile simulated with the FE code DD3IMP, using the same FE model and different yield functions. It can be seen that CB2001 (Figure 81) leads to an amplitude higher than Hill48 (Figure 72) while the Caz2018-Orth (Figure 91) presents an amplitude lower than Hill48 and closer to the experimental one. Finally, the CPB06ex2 (Figure 88) presents the lowest amplitude for the earing profile. This may be correlated with the amplitude of the in-plane variation of the normalized yield stresses predicted by each model. On the other hand, Yld2004 18p predicts extremely well the anisotropy in yield stresses irrespective of the set of the anisotropy coefficients. However, the set of coefficients for which a 4 ears profile is predicted, the earing amplitude is either 0.74 (set identified by NTNU) or 7.15 (set provided by organizers-POSTECH), i.e. much lower or much higher than the one obtained with Hill48 or the experimental one (see Figure 121 or 35).

The models that predict 8 ears (the 2-D orthotropic yield criteria HomPol4, HomPol6, Yld2000-2D) and the 3-D orthotropic yield criterion Yld2004-18p (POSTECH data set and NTNU based on physical experiments and simulations conducted with their own implementations in the FE code ABAQUS) have an earing amplitude much lower than Hill48 or the experimental one (see Figure 121 or Table 36). Note that all these yield criteria lead to a similar description of the in-plane distribution of the *r*-values.

The impact of using a pure isotropic hardening model (Swift) or mixed hardening (isotropic plus kinematic) model has been tested by USakarya, who uses HomPol4 and HomPol6 2-D orthotropic yield criteria, for both "LS-Dyna explicit - shell element" and "MSC.MARC implicit - solid element". Whatever the FE model adopted, the hardening model has a negligible effect on the punch force prediction. However, it affects the wall average height, as for Swift model wrinkling occurs while it disappears with the use of mixed hardening. The selected hardening law has a medium effect on the earing profile (see Figures 100, 101, 103, 104). However, the latter is also strongly dependent on the type of element. The use of solid element (MSC.MARC) with an additive or multiplicative decomposition of the deformation gradient also modifies the earing profile.

Within the simulations considering a pure isotropic hardening model, the participants selected either Swift or Voce laws. As shown in Section 7.3, the predicted stress-strain curves (see Figure 68) exhibit small variations, with a clear tendency to saturation with Voce law. This feature has a negligible effect on the stress-strain curve for the strain range present in tensile tests (maximum value of 0.25 at RD, in Figure 4). On the other hand, it would justify an effect on the force prediction in deep drawing cup case, since strain values from 0.4 to 0.9 appear in the wall (Figure 77). However, no FE model was tested strictly changing the hardening law by the participants, so it is not possible to quantify this effect neither on the force nor or on the earing profile.

Regarding the prediction of the evolution of the thickness along the cup circumference, at different heights, the results presented show that all FE models that predict 4 ears lead to similar trends, with

124

maximum at 45° and minima at RD and TD. Note that the earing profiles obtained with the FE code DD3IMP using the same FE model but different yield functions and associated flow rule, show different amplitudes of thickness variation along the circumferential direction (see Hill48 in Figure 74(e), CB2001 in Figure 83, CPB06ex2 in Figure 90 and Caz2018-Orth in Figure 93(a)), for each height. This result highlights the influence of the shape of the yield locus on the thickness predictions.

The use of crystal plasticity models to conduct virtual tests that complement the physical test data, used for identification of the anisotropy parameters of phenomenological models, seems to enable not only a better qualitative prediction of the punch force, but also of the earing profiles (see grey rectangles in synthesis Figures 119-121). This affirmation is confirmed:

- for solid element (ABAQUS implicit - C3D8R), by the predicted number of ears (Figure 119) and average height (Figure 120), when using Yld2004-18 (with NTNU identification based on DAMASK simulations). Nevertheless, the earing amplitude is underestimated (Figure 121) and, as previously pointed-out, this yield locus is very sensitive to the implementation.

-for shell element (ABAQUS implicit – S4R), by the predicted number of ears (Figure 119) and earing amplitude (Figure 121), when using Yld2000-2D (UGent identification based on VPSC simulations), but not by the average height (Figure 120). Although all the results indicate that this yield criterion tends to underestimate the average height (see Figure 97), the effect of choices such as, the low number of integration points through the thickness and the identification of anisotropic parameters based on virtual experiments for 0.1 strain could be investigated.

The ALAMEL crystal plasticity model used to identify the Facet-3D (ABAQUS explicit - SC8R continuum shell element) provides very interesting results in total agreement with both force and earing experimental results (see Figures 117-121 and the global error value).

If an ideal cube texture is assumed, although this specific orientation occurs only for 52% of the grains, the simulations using Caz2018singlecrys coupled with "ABAQUS C3D8R - solid element" and explicit (POSTECH) or implicit (REEF) strategies, predict 8 and 4 ears, respectively. Each team had its own identification procedure. Both simulations overestimate the earing amplitude and lead to a reasonable average height (with a higer accuracy for Reef approach).

The two polycrystal models that rely during the FE simulations on the single crystal behaviour (MINTY and Cazacu2018polycrys) lead to a correct description of the r-values, number of ears (Figure 119) and, for Cazacu2018polycrys, average height (Figure 120) and earing amplitude (Figure 121). For this latter model, the results, from the earing profile point of view, belong to the group of models with a low global error (≤ 0.02: Hill48 Lagamine, Hill48(NA) ABAQUS, Caz2018-Orth ABAQUS and DD3IMP, HomPol4 and HomPol6 MSC.Marc, Facet-3D ABAQUS, see Table 35).

The fact that none of the FE models that use shell elements attains the threshold of 0.01 for the global error (see Eq. (72)) can be related with the observation that such models cannot account for the occurrence of ironing. Regarding the FE models adopting solid or continuum-shell elements, three models present global error values lower than 0.002: the 3-D orthotropic yield functions Hill48(NA), using the identification strategy proposed by UAalto; and respectively, Caz2018-Orth, with the set of parameters provided by the organizers (REEF); and the Facet-3D model (identified with the approach of KUL) with a specific continuum-shell element. Nevertheless, it should be noted that some models might seem "penalized" because the respective teams did not seek to obtain the best possible prediction for the average cup height by fine-tuning the friction coefficient. The fact that different models can lead to similar results seems to highlight the robustness of the respective orthotropic yield functions and the experience of the analysts.

Table 35 FE prediction synthesis and error vs. experimental values for models using a blank discretization by solid elements. Global error values lower than 0.01 are highlighted in bold

					Number of ears	Average height (mm)	Average amplitude (mm)	
	Experimental result				4	34.1	2.29	
	Yield criterion	Code	Team	μ	Number of ears	Average height (mm)	Average amplitude (mm)	Global error
Phenomenological models identified based on mechanical data	von Mises	ABAQUS	REEF	0.020	0	33.15	0	2.001
		ABAQUS	REEF	0.070	0	33.62	0	2.000
		DD3IMP	UCoimbra	0.020	0	33.17	0	2.001
		DD3IMP	UCoimbra	0.070	0	33.67	0	2.000
	Hill48	ABAQUS	REEF	0.020	4	32.88	2.62	0.022
		ABAQUS	REEF	0.070	4	34.34	2.65	0.025
		DD3IMP	UCoimbra	0.020	4	33.42	2.62	0.021
		DD3IMP	UCoimbra	0.070	4	35.07	2.69	0.031
		Lagamine	ULiege	0.082	4	34.15	2.53	0.011
		ABAQUS	UPorto	0.050	4	33.25	3.86	0.472
		LSDYNA	USiegen	0.075	4	34.41	2.67	0.028
		PAMSTAMP	USiegen	0.075	4	35.09	2.64	0.024
	Hill48 (NA)	ABAQUS	UAalto	0.010	4	33.96	2.39	**0.002**
		ABAQUS	UPorto	0.050	4	33.15	2.68	0.030
	Yld2004-18p	ABAQUS	POSTECH[1]	0.100	8	34.00	0.43	1.660
		LSDYNA	USiegen(POSTECH)	0.075	4	34.22	7.15	4.498
		LSDYNA	USiegen(NTNU)[3]	0.075	12	32.97	0.52	4.599
		ABAQUS	NTNU(exp)[4]	0.090	8	34.44	0.43	1.662
	CB2001	DD3IMP	UCoimbra	0.020	4	33.14	3.82	0.449
	CPB06ex2	DD3IMP	UCoimbra	0.100	4	34.07	1.20	0.226
	Caz2018-Orth	ABAQUS	REEF	0.020	4	33.70	2.35	**0.001**
		DD3IMP	UCoimbra	0.020	4	33.54	2.42	**0.004**
		DD3IMP	UCoimbra	0.070	4	34.33	2.39	**0.002**
	HomPol4	MSC.MARC	USakarya(Iso)	0.100	4	32.94	1.71	0.065
		MSC.MARC	USakarya(Iso+KH)	0.100	4	33.20	2.02	0.015
		MSC.MARC	USakarya(Iso+m)[5]	0.100	8	33.45	0.78	1.436
		MSC.MARC	USakarya(Iso+KH+m)	0.100	4	34.16	2.04	0.012
	HomPol6	MSC.MARC	USakarya(Iso)[1]	0.100	8	33.09	1.70	1.067
		MSC.MARC	USakarya(Iso+KH)	0.100	4	33.28	2.15	**0.004**
		MSC.MARC	USakarya(Iso+m)[1]	0.100	8	34.98	1.20	1.227
		MSC.MARC	USakarya(Iso+KH+m)	0.100	4	34.29	2.16	**0.003**
Same + virtual tests	Yld2004-18p with DAMASK	ABAQUS	NTNU(CP)	0.090	4	34.06	0.74	0.458
		ABAQUS	POSTECH[1]	0.100	8	34.49	3.93	1.512

	Caz2018singlecrys	ABAQUS	REEF	0.020	4	33.97	5.61	2.103
CP	Caz2018polycrys	ABAQUS	REEF	0.020	4	33.93	2.61	0.020
	MINTY	Lagamine	ULiege	0.082	4	31.63	3.35	0.220

[1] Minima at 0°, 45° and 90° and maxima at 22.5° and 77.5°.

[2] Minima at 0° and 90° and maxima at 45°.

[3] Minima at 15°, 45° and 75° and maxima at 0°, 30°, 60° and 90°.

[4] Minima at 22.5° and 77.5° and maximum at 0°, 45° and 90°.

[5] Minima at 30° and 60° and maximum at 0°, 45° and 90°.

Table 36 FE prediction synthesis and error vs. experimental values for models using a blank discretization by shell elements. Global error values lower than 0.01 are highlighted in bold

					Number of ears	Average height (mm)	Average amplitude (mm)	
	Experimental result				4	34.1	2.29	
	Yield criterion	Code	Team	μ	Number of ears	Average height (mm)	Average amplitude (mm)	Global error
Phenomenological models identified based on mechanical data	Hill48	LSDYNA	USiegen	0.075	4	33.56	3.06	0.113
		PAMSTAMP	USiegen	0.075	4	33.97	2.99	0.094
	Hill48 (NA)	PAMSTAMP	USiegen	0.075	4	32.63	5.65	2.157
	Yld89	LSDYNA	USakarya	0.100	4	33.42	2.84	0.058
	Yld2000-2D	LSDYNA	USakarya	0.100	4	32.53	0.83	0.409
		LSDYNA	USiegen[2]	0.075	8	32.51	0.97	1.337
		PAMSTAMP	USiegen	0.075	4	32.22	0.94	0.349
	HomPol4	LSDYNA	USakarya (Iso)[2]	0.100	8	32.11	0.44	1.660
		LSDYNA	USakarya (Iso+KH)	0.100	4	33.08	0.40	0.683
	HomPol6	LSDYNA	USakarya (Iso)[1]	0.100	8	31.94	0.74	1.462
		LSDYNA	USakarya (Iso+KH)[3]	0.100	12	33.09	0.90	4.369
Same + virtual test	Yld2000-2D with VPSC	ABAQUS	UGent	0.070	4	30.59	3.31	0.208
	Facet-3D with ALAMEL	ABAQUS	KUL	0.090	4	34.15	2.26	**0.0001**

[1] Minima at 0°, 45° and 90° and maxima at 22.5° and 77.5°.

[2] Minima at 22.5° and 77.5° and maximum at 0°, 45° and 90°.

[3] Minima at 0°, 30°, 60° and 90° and maxima at 15°, 45° and 75°.

9. Conclusion

The finite element simulation of the cup drawing process of an AA6016-T4 aluminum alloy sheet sample , proposed in the ESAFORM benchmark 2021, has generated a huge collaborative work. Based on the result analysis, the following points are highlighted:

- No information was provided by the organizers regarding the friction value, except through the experimental evolution of the punch force during the cup drawing and the earing profile. It is a challenge for phenomenological models using a constant friction value, to predict both drawing and ironing forces (present in the experiment), while respecting the imposed clearance between the die and the punch. A close agreement with the experimental results

127

for the force signal is difficult, but possible, for simulations relying on solid elements. However, it is nearly impossible for the simulations using shell elements. Use of crystal plasticity computations to complement physical tests in the identification of the parameters of phenomenological models may contribute to improve the prediction of the ironing force.

- With the same set of experiments for the material parameter identification, trained scientists using the well-known Hill48 model, but different codes, meshes and element types have predicted quite similar earing profiles. This observation inspires confidence in the robustness of the FE implementation of this model in various codes. Seven participants out of eight have a global error for the earing profile smaller than 3% for this strong cube texture material. This observation shows that for this aluminium alloy, this criterion can lead to adequate predictions of the earing profile.

- Trying to enhance the FE prediction accuracy, numerous phenomenological orthotropic yield loci have been applied. Out of all these models, the 3-D Hill48 model with a non-associated flow rule and anisotropy parameters that evolve with the plastic strain [Lia2018] and the 3-D Caz2018-Ortho model [Caz2018a], which uses an associated flow rule and constant anisotropy parameters were highlighted. Both models predict earing profiles with less than 0.5% error.

- The 3-D orthotropic yield criteria which rely on experimental tensile yield stresses and Lankford coefficients in 7 orientations in their identification procedure are: Yld2004-18p, CPB06ex2, CB2001, and Caz2018-Orth. All these criteria predict with high accuracy the shape of the yield locus in the tension-tension quadrant as well as the plastic flow direction. About the anisotropy in yield stresses, compared to Hill48 and Caz2018-Orth yield criteria, CB2001 presents a small improvement, while Yld 2004-18p, and CPB06ex2 predict a better accuracy. Except Yld 2004-18p that predicts an earing profile with 4, 8 or 12 ears according its identification and implementation, the other criteria predict 4 ears, as observed experimentally. While CB2001 and CPB06ex2 have accuracy levels in the earing profile close to models that involve fewer parameters, Caz2018-Orth leads to a clear improvement in the predictions, with maximum and minimum cup height within 1% of the experimental values.

- It is to be noted that, for the identification of the parameters involved in various models, particular relevance was given by the participants to the description of the anisotropy of the Lankford coefficients, since it is known that it has a strong impact on the trend of the earing profile. This also highlights the importance of accurate experiments.

- No in-depth investigation about the choice of the hardening model has been performed. However, it appears that for the level of deformation reached in this cup drawing, both Swift and Voce isotropic laws can predict reliable results. Nevertheless, the interest of a mixed hardening approach is pointed by the HomPol4 and HomPol6 simulations.

- If 250 crystals, representative of the texture of the material, are used as input, simulations with Caz2018polycrys model, which uses Caz2018singlecrys for the description of the single crystal behaviour, lead to a good description of the material behaviour (tensile and shear tests, as well as the earing profile). However, a careful identification process of the five anisotropy parameters of Caz2018singlecrys model in three steps is applied, exploiting the seven uniaxial tests in directions 0°, 15°, 30°, 45°, 60°, 75°, and 90°.

- The Facet-3D yield locus is a very flexible function. For the benchmark material, 38 terms and a total of 154 non-zero coefficients are needed whereas for other systems with different initial textures, the total number of non-zero coefficients could be different. The most critical

requirement in the identification methodology proved to be the selection of the 10 000 discrete crystal orientations for the virtual experiments.

- The interest of using crystal plasticity to enhance the accuracy of the identification of a phenomenological model is a common idea. ALAMEL and Facet-3D cases confirm this approach but the use of VPSC to identify Yld2000-2D or DAMASK to identify Yld2004-18p are not so convincing. However, for Yld2000-2D, the element choice, number of integration points through the thickness and the low weight of the yield stress anisotropic in the identification process could explain the low accuracy. For Yld2004-18p, the sensitivity of the results to its implementation has been clearly pointed.

- The very basic Minty interpolation law with a set of 1000 representative crystals and a simple full Taylor assumption can describe all the trends in the earing profile but, probably at the cost of a higher CPU time for the deep drawing simulations than Facet-3D and Caz2018polycrys. Some issues in the predicted punch force evolution also suggest the need for further investigations.

- The identification methodology is a key point to generate reliable results. This article highlights how the careful parameter selection approach of some modelers led to accurate results. This also points out that this identification work request skilled scientists. The choice of a representative set of crystals, the analysis of Lankford coefficient evolution or not and, the need of pre-validation checks before performing the cup drawing simulations, require a larger training than applying simple analytical formula to identify Hill48 model, from constant Lankford coefficients in three directions.

- Looking at the benchmark from another point of view than the capacity to predict earing profile or force evolution, one could see six types of data. Tensile flow stress anisotropy, r-value anisotropy, yield locus (biaxial tests), earing profile, force evolution in cup forming and monotonic and reverse shear tests are available. It has been highlighted that none of the models could accurately describe the complete picture. For instance, the yield stress anisotropy under uniaxial loadings was not well predicted, particularly the one at 45°, by most of the models (including the ones based on crystal plasticity). Although, the very accurate description of the anisotropy of uniaxial yield stresses is not critical for the correct prediction of the earing profile, it is certainly relevant for other processes.

- The strong collaboration between experimental and numerical teams prevents the easy assumption, common for simulation teams, to just think that there is a problem in the experiments. Here, the interaction between the teams allowed fruitful discussions about clearance, defects in the blank positioning and measurements. The need for further investigation in tool deformation, contact modelling and friction measurements is itself a result from the benchmark.

CPU time is only presented in Table 33 and discussed in terms of exploiting polycrystalline models either in the cup drawing simulations or in the virtual predictions used to improve the identification of the optimal set of parameters for a phenomenological law. Two reasons justifies this choice.

The first one is the huge discrepancy in the meshes used to discretize the blank, from 1.344 (POSTECH), 2.128 (UPorto) to 55.560 elements (USiegen). This variation makes it impossible to assess the specific cost of a constitutive model. Choosing the mesh refinement is part of the modeller expertise and can,

129

indeed, affect the results accuracy. However, it is the responsibility of each FE user to perform a mesh convergence check.

The second reason is related with the fact that today, as pointed in the introduction, well-trained surrogate models can solve CPU issues and so the first priority is to know which models are the reliable ones.

This benchmark was also an opportunity to discover some issues related to the FE codes or their use. For instance, ULiege simulations using Lagamine present a non-physical drop in the punch force evolution; while the implementation of Hill48(NA) in the commercial code PAMSTAMP with shell elements leads to incoherent results, e.g. the FE prediction of the yield stress at 45° orientation is different from the experimental value. These difficulties highlight the importance of validating the FE models with simple tests or cup simulations and suggest the need for further investigations.

Last but not least, any scientist interested to work on this benchmark can contact Gabriela Vincze (gvincze@ua.pt) who will provide the data. Suggestions to ESAFORM board (current president livan.fratini@unipa.it) for an efficient platform of data exchange are welcome as the board has still to decide the best solution to share ESAFORM 2021 benchmark data and futur ones.

Do not hesitate to propose a benchmark in the following years (see the conditions on https://esaform.org/grants/).

10. Acknowledgement

11. Reference List

[Abe2013] Farid Abed-Meraim, Vuong-Dieu Trinh, Alain Combescure. New quadratic solid-shell elements and their evaluation on linear benchmark problems. Computing, 2013, 95 (5), pp.373-394. 10.1007/s00607-012-0265-1.

[Asa1985] Asaro, R. J., & Needleman, A. (1985). Overview no. 42 texture development and strain hardening in rate dependent polycrystals. Acta metallurgica, 33(6), 923-953.

[Bac2010] Bachmann, F., Hielscher, R., Jupp, P.E., Pantleon, W., Schaeben, H., Wegert, E., (2010). Inferential statistics of electron

backscatter diffraction data from within individual crystalline grains. Journal of Applied Crystallography 43, 1338e1355.

[Ban2010] D Banabic, F Barlat, O Cazacu, T Kuwabara (2010) Advances in anisotropy and formability International journal of material forming 3 (3), 165-189

[Bar1989] Barlat F, Lian K (1989) Plastic behavior and stretchability of sheet metals. Part I: A yield function for orthotropic sheets under plane stress conditions. Int J Plast. 5(1): 51-66

[Bar1991] Barlat F. Lege DJ. Brem JC (1991) A six-component yield function for anisotropic materials. Int. J. Plast. 7:693-712

[Bar1997a] Barlat F, Becker RC, Hayashida Y, Maeda Y, Yanagawa M, Chung K, Brem JC, Lege DJ, Matsui K, Murtha SJ, Hattori S (1997) Yielding description for solution strengthened aluminum alloys. Int. J. Plast. 13:385-401

[Bar1997b] Barlat F, Maeda Y, Chung K, Yanagawa M, Brem JC, Hayashida Y, Lege DJ, Matsui K, Murtha J, Hattori S, Becker RC, Makosey S (1997) Yield function development for aluminum alloy sheets. J. Mech. Phys. Solids 45:1727-176

[Bar2003] Barlat F, Brem JC, Yoon JW, Chung K, Dick RE, Lege DJ, Pourboghrat F, Choi SH, Chu E (2003) Plane stress yield function for aluminum alloy sheets—part 1: theory. Int. J. Plast. 19:1297–1319

[Bar2004] Barlat F., Cazacu O., Zyczkowski M., Banabic D., Yoon J.-W., Yield surface plasticity and anisotropy , In: Continuum Scale Simulation of Engineering Materials Fundamentals-Microstructures-Process Applications , (Editors: D. Raabe, L.-Q. Chen, F. Barlat, F. Roters), Wiley-VCH, Berlin, 2004, p. 145-185, ISBN 3-527-30760-5.

[Bar2005] Barlat F,Aretz H, Yoon J W, Karabin M E, Brem J C, Dick R E (2005) Linear transformation - based anisotropic yield functions, Int. J. Plasticity 21:1009-1039

[Bar2015] Barros PD, Neto DM, Alves JL, Oliveira MC, Menezes LF (2015) DD3IMP, 3D fully implicit finite element solver: implementation of CB2001 yield criterion. Rom J Tech Sci - Appl Mech 60:105–136

[Bla2001] Blau PJ (2001) The significance and use of the friction coefficient. Tribol Int 34:585–591. https://doi.org/10.1016/S0301-679X(01)00050-0

[Bro1989] Brown SB, Kim KH, Anand L (1989) An internal variable constitutive model for hot working of metals. Int J Plast 5:95–130. https://doi.org/10.1016/0749-6419(89)90025-9

[Bun1982] Bunge, H.J. (1982) Texture Analysis in Material Science. Butterworths, London.

[Caz2001] Cazacu, O., Barlat, F., 2001. Generalization of Drucker's yield criterion to orthotropy. Mathematics and Mechanics of Solids 6, 613-630.

[Caz2006]Cazacu, O., Plunkett, B., Barlat, F., 2006. Orthotropic yield criterion for hexagonal close packed metals. Int. J. Plasticity 22, 1171–1194

[Caz2018a] Cazacu O. (2018) New yield criteria for isotropic and textured metallic materials. Int J Solids Struct. 139:140, 200-210 doi: https://doi.org/10.1016/j.ijsolstr.2018.01.036.

[Caz2018b] Cazacu O, Revil-Baudard B, Chandola N (2018) A yield criterion for cubic single crystals. Int. J. Solids and Structures 151:9-19.

[Caz2019] Cazacu O, Revil-Baudard B, Chandola N (2019) Plasticity damage couplings: from single crystal to polycrystalline materials. Springer, Berlin Heidelberg

[Caz2021] Cazacu, O., Revil-Baudard, B., (2021) Plasticity of Metallic Materials: Modelling and Applications to Metal Forming, Elsevier, 500 pages, ISBN 978-0-12-817984-0

[Cha1986] Chaboche, J.L. (1986). Time independent constitutive theories for cyclic plasticity. International Journal of Plasticity. 2, 149-88.

[Cha2021] Chaker, A., Koubaa, S., Mars, J., A. Vivet & F. Dammak . An efficient ABAQUS solid shell element implementation for low velocity impact analysis of FGM plates. Engineering with Computers 37, 2145–2157 (2021). https://doi.org/10.1007/s00366-020-00954-8

[Che2020] Chen, L.; Zhang, H.; Song, M. Extension of Barlat's Yield Criterion to Tension–Compression Asymmetry: Modeling and Verification. Metals 2020, 10, 713. https://doi.org/10.3390/met10060713

[Chr2015] Christopher P d, Yannis P K (2015) Anisotropy of thin-walled tubes by a new method of combined tension and shear loading. Int. J. Plast. 71:87-112

[Chu2002] Chun, B.K., Jinn, J.T., Lee, J.K. (2002) Modeling the Bauschinger effect for sheet metals, Part I: theory. International Journal of Plasticity, 18, 571-95.

[Chu2005] Chung, K., Lee, M.G., Kim, D., Kim, C., Wenner, M.L., Barlat, F. (2005) Spring-back evaluation of automotive sheets based on isotropic – kinematic hardening laws and non-quadratic anisotropic yield functions, Part I: theory and formulation. International Journal of Plasticity. 21, 861-82.

[Coe2018] J. Coër, H. Laurent, M.C. Oliveira, P.-Y. Manach, L.F. Menezes, Detailed experimental and numerical analysis of a cylindrical cup deep drawing: pros and cons of using solid-shell elements, International Journal of Material Forming, 11, 357–373,

[Cop2019] Coppieters S, Hakoyama T, Eyckens P, Nakano H, Van Bael A, Debruyne D, Kuwabara T (2019) On the synergy between physical and virtual sheet metal testing: calibration of anisotropic yield functions using a microstructure-based plasticity model, Int. J. Mater. Form. 12:741–759

[Cor2012] Cora ÖN, Agcayaz A, Namiki K, et al (2012) Die wear in stamping of advanced high strength steels - Investigations on the effects of substrate material and hard-coatings. Tribol Int 52:50–60. https://doi.org/10.1016/j.triboint.2012.02.016

[Cou2021] Coulomb, C. A. (1821). Théorie des machines simples en ayant égard au frottement de leurs parties et à la roideur des cordages. Bachelier.

[Dru1949] Drucker D.C. (1949) Relation of experiments to mathematical theories of plasticity. J. App. Mech. 16:349–357

[Duc2003] Duchêne L (2003) FEM study of metal sheets with a texture based, local description of the yield locus. Ph. D. Thesis, Uliege, Liège, Belgium, available from http://hdl.handle.net/2268/135058

[Dun2012] Dunand M, Maertens A P, Luo M, Mohr D (2012) Experiments and modeling of anisotropic aluminum extrusions under multi-axial loading – Part I. Int. J. Plast. 36:34-49

[Ehs1957] Eshelby, J. D. (1957). The determination of the elastic field of an ellipsoidal inclusion, and related problems. Proceedings of the royal society of London. Series A. Mathematical and physical sciences, 241(1226), 376-396.

[Fro2021] Frohn-Sörensen, P., Cislo, C., Paschke, H., Stockinger, M., & Engel, B. (2021). Dry friction under pressure variation of PACVD TiN surfaces on selected automotive sheet metals for the application in unlubricated metal forming. Wear, 476, 203750.

[Gal2014] Galán, J., Verleysen, P., & Lebensohn, R. A. (2014). An improved algorithm for the polycrystal viscoplastic self-consistent model and its integration with implicit finite element schemes. Modelling and Simulation in Materials Science and Engineering, 22(5), 055023.

[Gal2020] Galán-López, J., & Hidalgo, J. (2020). Use of the Correlation between Grain Size and Crystallographic Orientation in Crystal Plasticity Simulations: Application to AISI 420 Stainless Steel. Crystals, 10(9), 819.

[Gal2021] Galdos, L., Otegi, N., Mendiguren, J., Trinidad, J., & Saenz de Argandoña, E. (2021). Contact pressure, sliding velocity and viscosity dependent friction behavior of lubricants used in tube hydroforming processes, Popups.Uliege.Be/Esaform21; Prof. Anne Marie Habraken ed.

[Gaw2013] Gawad, J., Van Bael, A., Eyckens, P., Samaey, G., Van Houtte, P., Roose, D. (2013). Hierarchical multi-scale modeling of texture induced plastic anisotropy in sheet forming. Computational Materials Science, 66, 65-83. doi: 10.1016/j.commatsci.2012.05.056

[Gor2020] Maysam B. Gorji, Mojtaba Mozaffar, Julian N. Heidenreich, Jian Cao, Dirk Mohr, On the potential of recurrent neural networks for modeling path dependent plasticity, Journal of the Mechanics and Physics of Solids, 143, 2020, 103972,

[Got1977] Gotoh M (1977) A theory of plastic anisotropy based on a yield function of fourth order (plane stress state). Int. J. Mech. Sci. 19:505-512

[Gro2008] Groche P, Nitzsche G, Elsen A (2008) Adhesive wear in deep drawing of aluminum sheets. CIRP Ann - Manuf Technol 57:295–298. https://doi.org/10.1016/j.cirp.2008.03.042

[Gro2014] Groeber, M. A., & Jackson, M. A. (2014). DREAM. 3D: a digital representation environment for the analysis of microstructure in 3D. Integrating materials and manufacturing innovation, 3(1), 56-72.

[Gro2000] Gronostajski, Z. (2000). The constitutive equations for FEM analysis. Journal of Materials Processing Technology, 106(1), 40–44.

[Hab2004a] Habraken A M, Duchêne L (2004) Anisotropic elasto-plastic finite element analysis using a stress–strain interpolation method based on a polycrystalline model. Int. J. Plasticity 20:1525-1560

[Hab2004b] Habraken, A. (2004). Modelling the plastic anisotropy of metals. Archives of Computational Methods in Engineering, 11,3-96.

[Han2010] Hanabusa, Y., Takizawa, H., Kuwabara, T., 2010. Evaluation of accuracy of stress measurements determined in biaxial stress tests with cruciform specimen using numerical method. Steel Research Int. 81 (9), 1376-1379.

[Han2013] Hanabusa, Y., Takizawa, H., Kuwabara, T., 2013. Numerical verification of a biaxial tensile test method using a cruciform specimen. J. Mater. Processing Technol. 213, 961-970.

[Her1954] Hershey A V (1954) The plasticity of an isotropic aggregate of anisotropic face centred cubic crystals. J. Appl. Mech. 21:241–249.

132

[Hos1973] Hosford, W.F., Allen, T.J., 1973. Twining and directional slip as a cause for strength differential effect.Met. Trans. 4, 1424–1425.

[Hos1993] Hosford, W.F., 1993. The Mechanics of Crystals and Textured Polycrystals. Oxford University Press, NewYork

[Hil1948] Hill R (1948) A theory of the yielding and plastic flow of anisotropic metals. Proc R Soc Lond Ser A 193A 1033:281–297

[Hil1998] Hill, R. (1998). The Mathematical Theory of Plasticity. Clarendon Press.

[Hol2013] Hol J (2013) Multiscale Friction Modeling for Sheet Metal Forming. University of Twente

[Hsu2020] Yu-Chuan Hsu, Chi-Hua Yu, Markus J. Buehler, Using Deep Learning to Predict Fracture Patterns in Crystalline Solids, Matter, Volume 3, Issue 1, 2020, Pages 197-211,

[Hut1999] Hutchinson, W.B., Lindh, E. & Bate, P. (1999) On the determination of textures from discrete orientation measurements. Proc. ICOTOM 12th, 35–39.

[ISO2014] ISO 16842: 2014 Metallic materials — Sheet and strip — Biaxial tensile testing method using a cruciform test piece.

[Kai1995] Kaiping, L., Habraken, A., & Bruneel, H. (1995). Simulation of Square Cup Deep Drawing with Different Finite Elements. Journal of Materials Processing Technology, 50(1-4), 81-91. http://hdl.handle.net/2268/32579

[Kar1993] A.P. Karafillis, M.C. Boyce, A general anisotropic yield criterion using bounds and a transformation weighting tensor, J. Mech. Phys. Solids 41 (1993) 1859-1886.

[Kaw1996] Kawka, M., Makinouchi, A., (1996). Plastic anisotropy in FEM analysis using degenerated solid element. Journal of Materials Processing Technology 60, 239-242.

[Kha2015] Khalfallah, A., Alves, J.L., Oliveira, M.C., Menezes, L.F., (2015) Influence of the characteristics of the experimental data set used to identify anisotropy parameters, Simulation Modelling Practice and Theory, 53, 15-44, doi: 10.1016/j.simpat.2015.02.007

[Kim2012] Kim YS, Jain MK, Metzger DR (2012) Determination of pressure-dependent friction coefficient from draw-bend test and its application to cup drawing. Int J Mach Tools Manuf 56:69–78. https://doi.org/10.1016/j.ijmachtools.2011.12.011

[Kuw2013] Kuwabara, T., Sugawara, F., (2013). Multiaxial tube expansion test method for measurement of sheet metal deformation behavior under biaxial tension for a large strain range. Int. J. Plasticity 45, 103–118.

[Kuw2017] Kuwabara T, Mori T, Asano M, Hakoyama T, Barlat F (2017) Material modeling of 6016-O and 6016-T4 aluminum alloy sheets and application to hole expansion forming simulation. Int. J. Plast. 93:164-186

[Leb1993] Lebensohn, R. A., & Tomé, C. N. (1993). A self-consistent anisotropic approach for the simulation of plastic deformation and texture development of polycrystals: application to zirconium alloys. Acta metallurgica et materialia, 41(9), 2611-2624.

[Lee2015] Lee JY, Barlat F, Lee MG (2015) Constitutive and friction modeling for accurate springback analysis of advanced high strength steel sheets. Int J Plast 71:113–135. https://doi.org/10.1016/j.ijplas.2015.04.005

[Lev1944] Levenberg, K. (1944). A method for the solution of certain nonlinear problems. Q. Appl. Math., 2, 164-168.

[Lia2018] Lian, J., Shen, F., Jia, X., Ahn, D.-C., Chae, D.-C., Münstermann, S., Bleck, W., 2018. An evolving non-associated Hill48 plasticity model accounting for anisotropic hardening and r-value evolution and its application to forming limit prediction. International Journal of Solids and Structures 151, 20-44.

[Liu2020] Liu W, Chen BK, Pang Y, Najafzadeh A (2020) A 3D phenomenological yield function with both in and out-of-plane mechanical anisotropy using full-field crystal plasticity spectral method for modelling sheet metal forming of strong textured aluminum alloy. Int J Solids Struct 193–194:117–133. https://doi.org/10.1016/j.ijsolstr.2020.02.008

[Liv2015] Livermore Software Technology Corporation (LSTC). Ls-Dyna® Keyword User's Manual Volume II-Material Models (2015) pp. 286-302

[LuL2015] Ju L, Mao T, Malpica J, Altan T (2015) Evaluation of lubricants for stamping of Al 5182-O aluminum sheet using cup drawing test. J Manuf Sci Eng Trans ASME 137:2–9. https://doi.org/10.1115/1.4030750

[MaJ2018] Ma J, Li H, Wang D, et al (2018) Tribological behaviors in titanium sheet and tube forming at elevated temperatures: evaluation and modeling. Int J Adv Manuf Technol 97:657–674. https://doi.org/10.1007/s00170-018-1985-y

[Nie2018] Nielsen C V, Bay N (2018) Review of friction modeling in metal forming processes. J Mater Process Technol 255:234–241. https://doi.org/10.1016/j.jmatprotec.2017.12.023

[Ope2021] Operations D (2021) The Interaction between the Sheet / Tool Surface Texture and the Friction / Galling Behavior on Aluminum Deep Drawing Operations

[Par2012] Park, T., Chung, K., 2012. Non-associated flow rule with symmetric stiffness modulus for isotropic-kinematic hardening and its application for earing in circular cup drawing. International Journal of Solids and Structures 49, 3582-3593.

133

[Pei1983] Peirce D, Asaro RJ, Needleman A (1983) Material rate dependence and localized deformation in crystalline solids. Acta Metall 31:1951–1976. https://doi.org/10.1016/0001-6160(83)90014-7

[Plu2008] B Plunkett, O Cazacu, F Barlat (2008) Orthotropic yield criteria for description of the anisotropy in tension and compression of sheet metals International Journal of Plasticity 24 (5), 847-866

[Pres2013] Pres, P., Stembalski, M., & Skoczynski, W. (2013). Determination of the friction coefficient as a function of sliding speed and normal pressure for steel C45 and steel 40 HM. Archives of Civil and Mechanical Engineering, 13.

[Rec2017] Recklin V, Dietrich F, Groche P (2017) In-situ-measurement of the friction coefficient in the deep drawing process. J Phys Conf Ser 896:. https://doi.org/10.1088/1742-6596/896/1/012027

[Rot2010] Roters F, Eisenlohr P, Hantcherli L, et al (2010) Overview of constitutive laws, kinematics, homogenization and multiscale methods in crystal plasticity finite-element modeling: Theory, experiments, applications. Acta Mater 58:1152–1211. https://doi.org/10.1016/j.actamat.2009.10.058

[Rot2019] Roters F, Diehl M, Shanthraj P, et al (2019) DAMASK – The Düsseldorf Advanced Material Simulation Kit for modeling multi-physics crystal plasticity, thermal, and damage phenomena from the single crystal up to the component scale. Comput Mater Sci 158:420–478. https://doi.org/10.1016/j.commatsci.2018.04.030

[Rov2018] Rovinelli, A., Sangid, M.D., Proudhon, H. et al. Using machine learning and a data-driven approach to identify the small fatigue crack driving force in polycrystalline materials. npj Comput Mater 4, 35 (2018).

[Saf1997] Saff, E.B., Kuijlaars, A.B.J. (1997). Distributing many points on a sphere. Mathematical Intelligence, 19, 5-11.

[Saf2014] Safaei, M., Lee, M.G., Zang, S.L., De Waele, W., 2014. An evolutionary anisotropic model for sheet metals based on non-associated flow rule approach. Computational Materials Science 81, 15-29.

[Sch2009] Schwarze M, Reese S (2009) A reduced integration solid-shell finite element based on the eas and the ans concept-geometrically linear problems. Isnt J Numer Meth Eng 80(10):1322–1355

[Sch2018] Shore, Diarmuid; Kestens, Leo; Sidor, Jurij; Van Houtte, Paul; Van Bael, Albert; 2018. Process parameter influence on texture heterogeneity in asymmetric rolling of aluminum sheet alloys. International Journal of Material Forming; 2018; Vol. 11; iss. 2; pp. 297 – 309

[Sch2021] Shisode M, Hazrati J, Mishra T, et al (2021) Modeling boundary friction of coated sheets in sheet metal forming. Tribol Int 153:106554. https://doi.org/10.1016/j.triboint.2020.106554

[Sen2021] Sener B, Esener E, Firat M (2021) Modeling plastic anisotropy evolution of AISI 304 steel sheets by a polynomial yield function. SN Applied Sciences 3(181)

[Sha2015] Shanthraj P, Eisenlohr P, Diehl M, Roters F (2015) Numerically robust spectral methods for crystal plasticity simulations of heterogeneous materials. Int J Plast 66:31–45. https://doi.org/10.1016/J.IJPLAS.2014.02.006

[She2021] Shen, F., Münstermann, S., Lian, J., 2021. Forming limit prediction by the Marciniak–Kuczynski model coupled with the evolving non-associated Hill48 plasticity model. J Mater Process Tech 287, 116384.

[Shi2021] Shisode M, Hazrati J, Mishra T, et al (2021) Modeling boundary friction of coated sheets in sheet metal forming. Tribol Int 153:106554.

[Sig2015] Sigvant, M., Hol, J., & Chezan, T. (n.d.). Friction modelling in sheet metal forming simulations: application and validation on an u-bend product, 8th Forming Technology Forum 2015: Advanced constitutive models in sheet metal forming, 135-142

[Soa2007] Soare SC, (2007). On the use of homogeneous polynomials to develop anisotropic yield functions with applications to sheet forming. University of Florida, Department of Mechanical and Aerospace Engineering. Ph.D. Thesis

[Soc1976] Society TR (1976) Bounds and self-consistent estimates for creep of polycrystalline materials. Proc R Soc London A Math Phys Sci 348:101–127. https://doi.org/10.1098/rspa.1976.0027

[Sou2019] Desenvolvimento de um Sistema de Controlo e Aquisição de Dados para Máquina Universal de Ensaios de Chapas Metálicas (in portuguese), João Paulo Sousa, MSc thesis (pp.46), Faculty of Engineering, University of Porto, 2019.

[Sto2002] Stoughton, T.B., 2002. A non-associated flow rule for sheet metal forming. International Journal of Plasticity 18, 687-714.

[Sto2009] Stoughton, T.B., Yoon, J.W., 2009. Anisotropic hardening and non-associated flow in proportional loading of sheet metals. International Journal of Plasticity 25, 1777-1817.

[Swi1952] Swift, H. W. (1952). Plastic instability under plane stress. Journal of the Mechanics and Physics of Solids, 1(1), 1–18.

[Tah2015] Taherizadeh, A., Green, D.E., Yoon, J.W., 2015. A non-associated plasticity model with anisotropic and nonlinear kinematic hardening for simulation of sheet metal forming. International Journal of Solids and Structures 69–70, 370-382.

[Tam2016] Tamai Y, Inazumi T, Manabe KI (2016) FE forming analysis with nonlinear friction coefficient model considering contact pressure, sliding velocity and sliding length. 227:161–168. https://doi.org/10.1016/j.jmatprotec.2015.08.023

134

[Tay1938] Taylor, G.I., 1938. Plastic strain in metals. J. Inst. Metals 62, 307–324.

[Tia2017] Tian H, Brownell B, Baral M, Korkolis YP (2017) Earing in cup-drawing of anisotropic Al-6022-T4 sheets. Int J Mater Form 10:329–343. https://doi.org/10.1007/s12289-016-1282-y

[Tom1984] Tome, C., Canova, G. R., Kocks, U. F., Christodoulou, N., & Jonas, J. J. (1984). The relation between macroscopic and microscopic strain hardening in FCC polycrystals. Acta metallurgica, 32(10), 1637-1653.

[Tot1992] Toth, L., Van Houtte, P. (1992). Discretization techniques for orientation distribution-functions. Textures and microstructures, 19 (4), 229-244.

[Trz2017] Trzepiecinski T, Lemu HG, Fejkiel R (2017) Numerical simulation of effect of friction directionality on forming of anisotropic sheets. Int J Simul Model 16:590–602. https://doi.org/10.2507/IJSIMM16(4)3.392

[Van1995] Van Houtte, P. (1995). MTM-FHM Software, Ver. 2. User Manual.

[Van2004] Van Houtte, P., Li, S., Engler, O., 2004. Modelling deformation texture of aluminium alloys using grain interaction models. Aluminium 80 (6),702–706.

[Van2005] Van Houtte, P., Li, S., Seefeldt, M., Delannay, L. (2005). Deformation texture prediction: from the Taylor model to the advanced Lamel model. International Journal of Plasticity, 21 (3), 589-624. doi: 10.1016/j.ijplas.2004.04.011

[Van2009] Van Houtte, P., Yerra, S.K., Van Bael, A. (2009). The Facet method: A hierarchical multilevel modelling scheme for anisotropic convex plastic potentials. International Journal of Plasticity, 25 (2), 332-360. doi: 10.1016/j.ijplas.2008.02.001

[Van2011]P. Van Houtte, J. Gawad, P. Eyckens, B. Van Bael, G. Samaey, D. Roose (2011) A full-field strategy to take texture-induced anisotropy into account during FE simulations of metal forming processes JOM 63 (11), 37-43

[Vin2013] Vincze, G., Barlat, F., Rauch, E.F., Tome, C.N., Butuc, M.C., Grácio, J.J., 2013. Experiments and modeling of low carbon steel sheet subjected to double strain path changes. Metall. Mater Trans. A44, 4475–4479.

[Vin2016] G. Vincze, M.C. Butuc and F. Barlat, "Mechanical behavior of TWIP steel under shear loading", Numisheet 2016, IOP Publishing, Journal of Physics: Conference Series 734, (2016), 032111, pp. 1-4.

[Vla2011] Vladimirov, I.N., Pietryga, M.P. & Reese, S. On the influence of kinematic hardening on plastic anisotropy in the context of finite strain plasticity. Int J Mater Form 4, 255 (2011). https://doi.org/10.1007/s12289-011-1038-7

[Voc1948] Voce, E., 1948. The relationship between stress and strain for homogeneous deformation.J. Inst. Met. 74, 537–562.

[WuL2020] Ling Wu, Van Dung Nguyen, Nanda Gopala Kilingar, Ludovic Noels,A recurrent neural network-accelerated multi-scale model for elasto-plastic heterogeneous materials subjected to random cyclic and non-proportional loading paths, Computer Methods in Applied Mechanics and Engineering,369,2020, 113234, https://doi.org/10.1016/j.cma.2020.113234.

[Yam2020] A. Yamanaka, R. Kamijyo, K. Koenuma, et al., Deep neural network approach to estimate biaxial stress-strain curves of sheet metals, Materials & Design (2020), https://doi.org/10.1016/j.matdes.2020.108970

[Yoo2011] Yoon JW, Dick RE, Barlat F (2011) A new analytical theory for earing generated from anisotropic plasticity. Int J Plast 27:1165–1184.